Fiber DFB Lasers for Sensor Applications

Erlend Rønnekleiv

December 30, 1999

Contents

Part I: Spatial Sensitivity and Intensity Distributions 7

Abstract

Fiber distributed feedback (DFB) lasers have been studied theoretically and experimentally, with emphasis on properties that are of importance for the use of these lasers in sensor applications, either as sensing elements or as sources for interrogation.

In the first part of the thesis we demonstrate a method for characterization of fiber DFB lasers which is based on scanning a heat-induced index perturbation along the cavity and recording the induced laser frequency shift. The experimental results reveal that the sensitivity of fiber distributed-feedback laser sensors with frequency read-out is highly localized near the grating phase-shift position. It is shown theoretically that the measurements give a good indicator for the intensity distribution in the cavity. Use of the characterization data to determine the grating coupling parameter κ, the polarization dependence of κ, and birefringence non-uniformities as well as identification of the order of longitudinal mode operation are discussed and demonstrated experimentally. Asymmetrically phase-shifted lasers with a highly directional output power are also investigated.

The second part deals with laser stability and noise. The measured laser frequency modulation noise ranges from 20 Hz/$\sqrt{\text{Hz}}$ at 1 kHz to 1.3 Hz/$\sqrt{\text{Hz}}$ at 1 MHz, with a sharp peak at the relaxation oscillation frequency near 220 kHz. $1/f$ noise is observed below 1 kHz. Negative feedback to the pump from a monitor detector reduces the intensity noise to the detection noise level, and removes the relaxation oscillation noise from the laser frequency. By comparing measured intensity and frequency fluctuations, we estimate the effective linewidth broadening factor at the relaxation oscillation frequencies of the in-

vestigated lasers to be between 2.1 and 3.8, as compared to typically between 3 and 7 for semiconductor lasers. The noise performance of four serially multiplexed fiber DFB lasers are found to be similar to that of the free running single lasers. We have also investigated the tolerance of fiber DFB lasers to external back-reflections before the onset of instabilities. The tolerable reflection coefficient is found to decrease with increasing external cavity lengths up to a few hundred meters, and to be proportional to the relative linewidth (quality factor) of the relaxation oscillation resonance. The tolerable length of Rayleigh backscattering fiber varies from 37 to 278 m. UV-induced saturable absorbers seem to play a role in degrading the laser stability.

The third part is devoted to a theoretical and experimental study of the polarization modes of the fiber DFB laser. A comprehensive model for steady state analysis of polarization mode competition (PMC) is presented. Effects of polarization dependent grating strength, back reflections, polarization dependent grating non-uniformities, twist, Faraday rotation, cross-saturation from serially multiplexed lasers, pump polarization fluctuations, as well as spatially and polarization dependent gain hole-burning are covered by the model. Regimes of single and dual polarization operation are identified and the modal output powers and differential gain contributions are investigated versus different types of polarization imperfections in the cavity. An experimental investigation of how the PMC and polarization beat frequency depend on localized transverse force perturbations, back reflections, and changes in pump polarization state is also carried out. Good agreement is obtained between the experiments and the simulation model. The noise fluctuations in the polarization beat frequency is also investigated. Use of a dual polarization laser as a transverse force sensor with a resolution in the order of 1–100 $\mathrm{nN}/\sqrt{\mathrm{Hz}}$ for interrogation frequencies above 20 Hz is demonstrated.

In the forth part we demonstrate the application of the fiber DFB laser for simultaneous static temperature and strain measurements, and as a hydrophone for the $0.1 - 1$ MHz frequency range. By measuring both the wavelength of one laser polarization modes and the polarization beat frequency we are able to determine the strain and temperature with accuracies of $\pm 3\mu\varepsilon$ and $-0.04°$C, respectively. These accuracies are limited by the accuracies of the equipment used to calibrate the sensor. For the fiber DFB laser hydrophone we demonstrate a noise equivalent pressure of $\sim$ 93 dB $\mu\mathrm{Pa}/\sqrt{\mathrm{Hz}}$. The angular responsivity at 800 kHz has a central lobe with a 3-dB width of 6.4°. This corresponds to an effective sensitive length of approximately 6mm, which is much shorter than the DFB grating length of 5 cm.

Acknowledgments

I wish to thank my supervisor Kjell Bløtekjær at NTNU for his guidance, and many stimulating discussions through the course of this work. I also wish to thank my colleague Jon Thomas Kringlebotn at Optoplan for introducing me to the field of fiber DFB lasers and their potential applications in sensing, and for inspiring discussions.

Part of the research (parts of the theory and all experiments in Chapters 2, 5, 6, 7, and 8) was carried out while I was a visiting researcher at the Optoelectronics Research Center at the University of Southampton during 1997. I would like to thank Dave Payne for formally inviting me to this stimulating scientific community, and Richard I. Laming and Michael N. Zervas for support, encouragement, and stimulating discussions. Morten Ibsen should be acknowledged for making the excellent DFB fiber gratings that I used in my experiments. Thanks go also to Oliver Hadeler for his collaboration with the work presented in Chapters 5 and 8. Gregory J. Cowle, the people at Fibercore, Guillaume Vienne, Sze Y. Set, Harald Geiger, and a number of other people should also be thanked for clarifying discussions and help with technical issues.

In Trondheim, the research has been conducted partly at NTNU and partly at Optoplan AS. Thanks go to Sigurd W. Løvseth, Dag Thingbø, and Jon Thomas Kringlebotn for collaboration with doing experiments and writing conference papers, and to Helge Engan, Helge Storøy, Bjørnar Langli, Johannes Skaar for interesting and clarifying discussions, and to supporting staff at NTNU and Optoplan for valuable help. Christian Poulsen and Ionas AS should be acknowledged for their flexible attitude to delivering specially designed fiber DFB lasers, and for lending us the laser array characterized in Chapter 3.

It has been of great help for me to have people read through and comment what I have written. Jon Thomas Kringlebotn and Kjell Bløtekjær have gone through and commented almost every chapter in the thesis. Michael N. Zervas, Morten Ibsen, Richard I. Laming, Sigurd W. Løvseth, Oliver Hadeler, Guillaume Vienne, Dag Roar Hjelme, and Morten Eriksrud have given useful comments to some of the chapters.

Finally, I acknowledge support from Optoplan AS, the Norwegian Research Council, and British Council to carry this work.

Chapter 1

Introduction

1.1 Background

The fiber sensor technology has developed during the past few decades much as a result of the rapid technological advances made for the telecommunication industry. Fiber compatible components and tools have become available, such as diode lasers, fusion splicers, fiber connectors, couplers, and amplifiers. The erbium doped fiber amplifier (EDFA) [1, 2] is often referred to as the most important single invention that has boosted the deployment of optical fiber technology for communication purposes. More recently, the fiber Bragg grating (FBG) technology [3, 4, 5, 6, 7] has developed to a commercial level. Due to their high degree of wavelength selectivity and simple in-fiber design, the FBG technology is expected to become essential in future wavelength division multiplexed (WDM) communication systems. FBGs are also attractive for broadband applications, such as dispersion compensation and EDFA gain flattening.

FBG lasers combine the EDFA and FBG technologies. There is a potential for the FBG lasers to become an important alternative as light sources for the telecommunications industry. They offer very narrow linewidths, low temperature dependence of the wavelength, and easy setting of the laser wavelength during production, and a large tuning range, which is favorable for dense WDM applications. The facts that they are in-fiber devices and that multiple FBG lasers can be pumped by a single pump laser may also be favorable.

FBG lasers can be divided into two categories depending on the grating geometry. The fiber distributed feedback (DFB) laser consists of a continuous Bragg grating written into an optical fiber containing a gain medium, such as

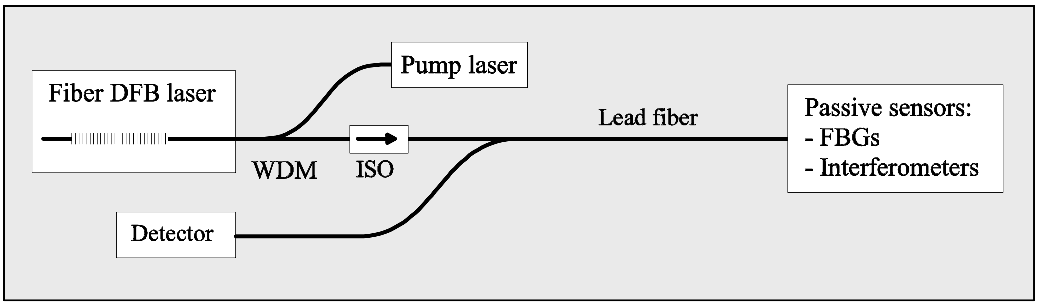

Figure 1.1. Fiber DFB laser used as source for interogation of passive fiber sensors. WDM, wavelength division multiplexer discriminating between the pump and laser wavelengths; ISO, optical isolator; FBGs, passive fiber Bragg gratings.

Er^{3+} ions [8]. This integration of the gain medium into the grating contrasts to the distributed Bragg reflector (DBR) geometry where two separate Bragg grating reflectors are separated by a gain section. If the spatial separation of the DBR gratings is comparable to or longer than the optical penetration depth into the gratings, there will be multiple cavity resonances within the grating reflection bandwidth. It is therefore known that DBR lasers tend to have problems with multiple longitudinal mode hopping or multimode operation, a problem that can be reduced by reducing the distance between the gratings. A DFB laser is essentially a DBR laser where the grating separation has been reduced to zero [9]. By introducing a π grating phase-shift at the center of the grating, the grating resonance is moved to the center of the grating reflection band, and the resulting DFB laser can operate very robustly in a single longitudinal mode.

This thesis is mainly focused on developing an understanding of Er-doped fiber DFB lasers with emphasis on their properties of importance for fiber-optic sensor applications.

Fig. 1.1 illustrates how a fiber DFB laser could be applied as a source for interrogation of passive FBG sensors or interferometric sensors. The very narrow linewidth combined with potentially very accurate strain or temperature tuning allows for interrogation of passive sensors over a large (several nm) optical wavelength range with high resolution.

Fiber DFB lasers can also be used as a sensor elements on their own [10, 11], as illustrated in Fig. 1.2. If the lasers are designed in such a way that the pump absorption per laser is not too high, multiple laser sensors (labelled DFB1 through DFBn in the figure) can be multiplexed in series on a single fiber. The interrogation system would usually monitor variations in the laser frequency, which gives a measure for strain and refractive index variations in the laser fiber. If the laser operates in two polarization modes the beat frequency

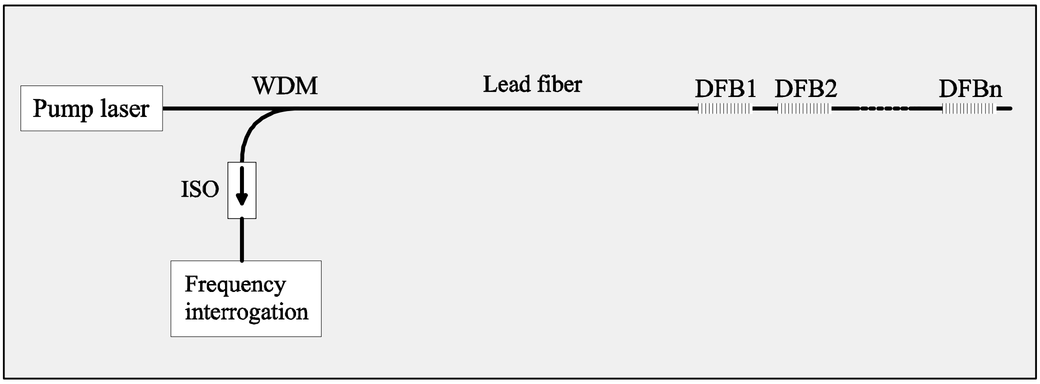

Figure 1.2. Fiber DFB lasers used as sensor elements. WDM, wavelength division multiplexer discriminating between the pump and laser wavelengths; ISO, optical isolator; DFB1 trorough DFBn, serially multiplexed fiber DFB sensor elements.

between the polarization modes can also be monitored, producing a measure of the birefringence in the laser cavity. The possibility of forming a true single point two-parameter sensor by combining laser frequency and polarization beat frequency interrogation is also attractive. For instance, this approach can be used to remove unwanted temperature dependence from the sensor readout.

The first single longitudinal mode fiber Bragg grating sensor lasers demonstrated in the literature were DBR lasers [12, 13, 14]. An important advantage of DFB over DBR sensor lasers is that the DFB lasers are less reluctant to longitudinal mode hopping due to non-uniform strain perturbations of the cavity. In many applications the shorter sensitive length of the fiber DFB laser will also be an desirable.

Fiber DFB laser sensors have many advantages in common with passive FBG sensors [15], such as compact in-fiber design, a highly localized sensitive region, and wavelength multiplexing capabilities. Both sensors types are based on interrogation of a shift in the FBG resonance frequency. The reflection bandwidth of a passive FBG may typically be in the order of 10 GHz, while the emission linewidth of fiber DFB lasers is typically in the order of $1 - 10$ kHz. Intuitively, this allows for an improvement of the interrogation accuracy by several orders of magnitude.

1.2 Thesis Outline

This thesis is divided into four parts with a total of 10 chapters. All chapters except for Chapters 1, 3, and 10 are reproductions of articles or papers that have been submitted to or are published in journals and conference proceedings. Each chapter should therefore be self contained, with its own abstract, introduction and conclusion.

In Part I a method for characterization of the longitudinal dependence of the sensitivity of the fiber DFB laser frequency to refractive index perturbations is investigated theoretically and experimentally. We show that the characterization results can reveal important information about the laser, such as the intensity distribution along the laser cavity, the grating strength, and the longitudinal mode of operation.

Part II is devoted to the investigation of laser noise and stability. Knowledge of the typical spectral distributions of the relative intensity noise and frequency noise of fiber DFB lasers is necessary in order to estimate the obtainable dynamic resolution of sensor systems employing these lasers. An understanding of the origins of the laser noise is essential if one wants to reduce the noise level further. We have found that external back reflections due to Rayleigh scattering or weak discrete reflections in the lead fiber may lead to instabilities in fiber DFB laser sensors that are connected to a long lead fiber like in Fig. 1.2.

In Part III the conditions for single or dual polarization mode operation of fiber DFB lasers is investigated. A comprehensive simulation model is introduced, which covers effects of gain hole-burning, several types of polarization dependent grating imperfections, as well as external back reflections. Simulation results are shown that illustrate the magnitudes of different types of polarization imperfection that can be tolerated in order to maintain dual polarization operation. Experimental results are presented which were obtained by applying polarization dependent external reflections to a dual polarization fiber DFB laser, and by applying a localized transverse force to the DFB phase-shift position which modifies the phase-shift birefringence. By monitoring the polarization beat frequency versus the transverse force, we demonstrate that the laser can be used as a very sensitive transverse force sensor. We also investigate the sensitivity of the polarization beat frequency to external back reflections, and the polarization beat frequency noise spectrum is measured.

In Part IV we demonstrate two applications of the fiber DFB laser as a sensor. The first application is of a dual polarization laser for simultaneous static strain and temperature measurements by interrogating both the laser wavelength shift and the polarization beat frequency shift. By using this technique we show that it is possible to eliminate the temperature sensitivity from the strain measurements and vice versa with a high degree of accuracy. The second application demonstrated is of a fiber DFB laser hydrophone for use in the $0.1 - 1$ MHz range. We investigate the sensitivity and angular directivity of the sensor, and compare the angular directivity with the spatial sensitivity distribution obtained with the characterization method introduced in Part I.

Finally, some concluding remarks are given in Chap. 10.

References

[1] R. J. Mears, L. Reekie, I. M. Jauncey, D. N. Payne, "Low-noise erbium-doped fibre amplifier operating at 1.54 μm", Electron. Lett., Vol. 23, pp. 1026-1028, 1987.

[2] A. Bjarklev, "Optical Fiber Amplifiers: Design and System Applications", (Archtech House, London, 1993).

[3] K. O. Hill, Y. Fujii, D. C. Johnson, and B. S. Kawasaki, "Photosensitivity in optical waveguides: Application to reflection filter fabrication", Appl. Phys. Lett., Vol. 32, pp. 647–649, 1978.

[4] G. Meltz, W. W. Morey, and W. H. Glenn, "Formation of Bragg gratings in optical fibres by transverse holographic method", Opt. Lett., Vol. 14, pp. 823–825, 1989.

[5] K. O. Hill and G. Meltz, "Fiber Bragg Grating Technology Fundamentals and Overview", J. of Lightwave Technol., Vol. 15, pp. 1263–1276, 1997.

[6] C. R. Giles, "Lightwave Applications of Fiber Bragg Gratings", J. of Lightwave Technol., Vol. 15, pp. 1391–1404, 1997.

[7] R. Kashyap, "Fiber Bragg Gratings", (Academic Press, London, UK, 1999).

[8] J. T. Kringlebotn, J. L. Archambault, L. Reekie and D. N. Payne, Er^{3+}:Yb^{3+}-codoped fiber distributed-feedback laser", *Opt. Lett.*, Vol. 19, pp. 2101-2103, 1994.

[9] G. A. Ball, W. H. Glenn, W. W. Morey, and P. K. Cheo, "Modeling of Short, Single-Frequency, Fiber Lasers in High-Gain Fiber", IEEE Photonics Technol. Lett., Vol. 5, pp. 649–651, 1993.

[10] J. T. Kringlebotn, W. H. Loh and R. I. Laming, "Polarimetric Er^{3+}-doped fiber distributed-feedback laser sensor for differential pressure and force measurements", Opt. Letters, Vol.21, pp. 1869–1871, 1996.

[11] J. T. Kringlebotn, "Optical fiber distributed feedback laser" (distributed feedback laser used as sensor), US Patent 5 844 927, UK Patent 2 299 203, NO Patent 302 441, Optoplan AS, 1996.

[12] G. A. Ball, W. W. Morey, and P. K. Cheo, "Single- and Multipoint Fiber-Laser Sensors", IEEE Photonics Technol. Lett., Vol. 5, pp. 267–*269*, 1993.

[13] G. A. Ball, G. Meltz, and W. W. Morey, "Polarimetric heterodyning Bragg-grating fiber-laser sensor", Opt. Letters, Vol. 18, pp. 1976–1978, 1993.

[14] K. P. Koo and Wanser, A. D. Kersey, "Fibre laser sensor with ultrahigh strain resolution using interferometric interrogation", Electron. Lett., Vol. 31, pp. 1180–1182, 1995.

[15] A. D. Kersey, M. A. Davis. H. J. Patrick, M. LeBlanc, K. P. Koo, C. G. Askins, M. A. Putnam, and E. J. Friebele, "Fiber grating sensors", J. of Lightwave Technol., Vol. 15, pp. 1442–1463, 1997.

Part I:
Spatial Sensitivity and Intensity Distributions

Chapter 2

Characterization of fiber distributed-feedback lasers with an index perturbation method[1]

Abstract — We demonstrate characterization of fiber distributed-feedback lasers by scanning a heat-induced index perturbation along the cavity and by measuring the induced laser frequency shift. The measured shift is shown to be a good indicator for the intensity distribution in the cavity, and the experimental results reveal that the sensitivity of fiber distributed-feedback laser sensors with frequency read-out is highly localized near the grating phase-shift position. Use of the characterization data to determine the grating coupling parameter κ, the polarization dependence of κ, and birefringence non-uniformities as well as identification of the order of longitudinal mode operation are discussed and demonstrated experimentally. Asymmetrically phase-shifted lasers with highly directional output are also investigated.

OCIS codes: 140.3430, 140.3510, 140.4780, 230.1480, 050.2770, 060.2370.

2.1 Introduction

The modal intensity distribution within distributed-feedback (DFB) lasers depends distinctly on the order of longitudinal-mode operation, as well as grating properties such as the grating amplitude and phase. Measurements of modal intensity distributions can therefore be an attractive tool for the characterization of such devices.

---

[1] This chapter is a re-edited version of [E. Rønnekleiv, M. Ibsen, M. N. Zervas, and R. I. Laming, "Characterization of fiber distributed-feedback lasers with an index perturbation method", Appl. Opt., Vol. 38, pp. 4558-4565, 1999].

Few experiments have been reported on spatially resolved measurements of the lasing conditions within DFB-cavities, and the understanding of the modal field distributions depends to a high extent on theoretical models that are based on idealized assumptions. Spatially resolved measurements of spontaneous side-emission from semiconductor DFB lasers have been demonstrated [1, 2]. These measurements confirm the existence of spatial gain hole burning, and that different modes have different spatial intensity distributions. However, little quantitative information on the properties of the devices could be deduced from these measurements.

Deduction of the intensity distribution along an Er^{3+} fiber DFB laser from measurements of the green side-emission generated from excited-state absorption of the 980-nm pump signal has been demonstrated [3]. This method relies on a good knowledge of the energy transitions involved in the fiber, and it seems to be restricted to laser operation close to threshold. The method cannot be used with other pumping schemes or gain media.

A heat-scan technique for characterization of a fiber grating device was first demonstrated by Margulis *et.al.* in [4]. They scanned a heating wire along a fiber used for optical second harmonic (SH) generation. By monitoring the SH generation efficiency versus heating position they were able to determine the spatial distribution of the amplitude of a Bragg grating which assisted the SH generation in the fiber. Characterization of the spatial distribution of the Bragg wavelength in a chirped fiber Bragg grating with a heat-scan technique has later been demonstrated in [5]. [2]

Spatially resolved measurement of the grating phase and amplitude in a high reflectivity passive fiber Bragg grating was recently demonstrated [6]. The measurements were made by scanning a small heat-induced index perturbation along the grating and recording of the change in transmission at a wavelength outside the grating stopband.

From microwave theory it is known that one can measure the intensity distribution in a resonant cavity by moving a small refractive-index perturbation along the cavity and measuring the resulting shift in resonance frequency [7, 8]. In this paper we apply this principle, to our knowledge for the first time, to characterize optical fiber DFB resonators. Parts of the experiments reported in this paper have earlier been presented in a conference paper [9].

---

[2] The references to [5] and [4] were not included in the Applied Optics version of this manuscript. We apologize for this omission.

2.2 Theory

2.2.1 Modal Intensity Distributions and Gain Thresholds

When interference between the forward- and backward-propagating field amplitudes E_+ and E_-, respectively, is taken into account, the local intensity inside an optical cavity can be expressed as:

$$|E_{loc}(z)|^2 = |E_0|^2 + 2|E_+E_-|\cos(2\pi zn\nu/c + \theta), \tag{2.1}$$

where ν is the resonating optical frequency, n is the refractive-index of the fiber, c is the speed of light in vacuum, $|E_0|^2 = |E_+|^2 + |E_-|^2$ is the mean intensity, $2|E_+E_-|$ is the standing wave intensity modulation amplitude, and θ is the standing wave modulation phase. $|E_0|^2$, $|E_+|^2$, $|E_-|^2$ and θ may all be slowly varying functions of z.

Figure 2.1 shows the theoretical intensity distributions of the fundamental mode and the first and second higher order mode pairs in a $L = 60$ mm index-coupled DFB structure, obtained by a T-matrix approach [15, 16, 17, 18].[3] The illustrated grating has a coupling coefficient of $\kappa = 230\ \text{m}^{-1}$ and a π grating phase-shift at the center. A uniform gain of 4.1×10^{-3} dB/m is required for lasing in the fundamental mode, whereas 22.0 dB/m and 31.5 dB/m are required for the first and second higher order mode pairs, respectively. The fundamental mode in this case is the mode operating at the Bragg resonance frequency ν_{Bragg}. For the illustrated κL-product of 13.8, the first and second higher-order mode pairs are found to operate at $\nu_{\pm 1} = \nu_{Bragg} \pm 1.086 v_g\kappa/(2\pi)$ and $\nu_{\pm 2} = \nu_{Bragg} \pm 1.111 v_g\kappa/(2\pi)$, respectively, i.e., close to the stopband edges of the uniform grating, defined as $\nu_{Bragg} \pm v_g\kappa/(2\pi)$.[4] Here v_g is the group velocity of the uncoupled waveguide.

In the more general case, one may consider an asymmetrically phase-shifted DFB laser of length L with the phase-shift positioned at $z = -\Delta L/2$ relative to the grating center $z = 0$. For such a laser the following approximations are valid, provided that the left and right sub-gratings are both relatively strong, i.e. $\kappa|L - \Delta L| \gtrsim 1$:

$$|E_0|^2 \approx P_0 \frac{\cosh\kappa(L \pm 2z)}{\cosh\kappa(L \mp \Delta L)}, \tag{2.2}$$

$$2|E_+E_-| \approx P_0 \frac{\sinh\kappa(L \pm 2z)}{\cosh\kappa(L \mp \Delta L)}, \tag{2.3}$$

---

[3] A more detailed description of the T-matrix DFB laser model is given in Chap. 6, which is a re-edited version of [18].

In the Applied Optics version of the present chapter, a wrong reference number was used for [18]. We have here also added references to some early papers [15, 16, 11] where T-matrixes for optical Bragg grating and DFB laser modelling are introduced.

[4] In the original paper, the factor $1/(2\pi)$ is missing in the expressions for the mode frequency spacing and the stop-band width. The expressions given here are correct.

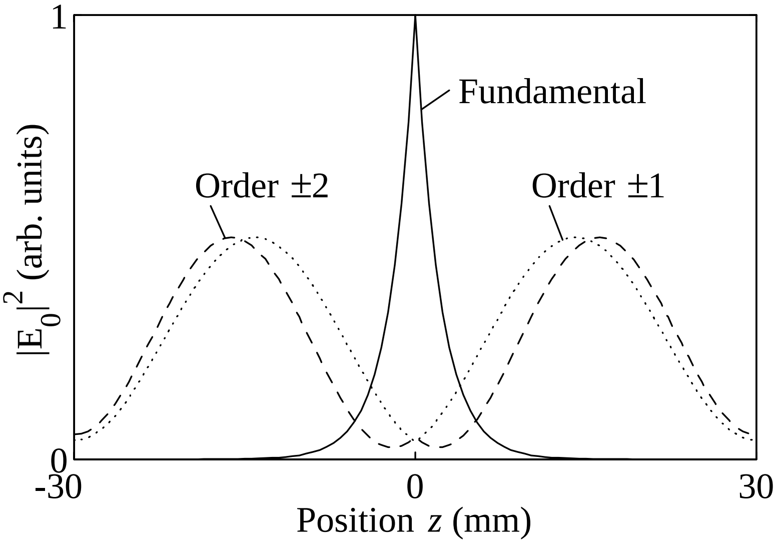

Figure 2.1. Theoretical intensity distribution $|E_0|^2$ in a 60 mm laser with $\kappa = 230\mathrm{m}^{-1}$ for the fundamental and first and second higher order modes.

where the upper signs apply for $-L/2 < z < -\Delta L/2$. P_0 is the intensity $|E_0|^2$ at $z = -\Delta L/2$.

Figure 2.2 shows the exact distributions of $|E_0|^2$, $2|E_+E_-|$, $|E_+|^2$, and $|E_-|^2$, calculated by the T-matrix approach, for an asymmetric laser with $\kappa L = 8$ and $\kappa\Delta L = 2$. As we explain in Subsection 2.2.2 below, the characterization method proposed in this paper produces a measure for the distribution of standing wave intensity amplitude $2|E_+E_-|$. From Fig. 2.2 and from expressions (2.2) and (2.3) one see that $|E_0|^2 \approx 2|E_+E_-| \approx \exp 2\kappa|z + \Delta L/2|$ at distances that are separated $\gtrsim \kappa^{-1}$ from the grating ends. This implies that the characterization method also produces a good estimate for the mean intensity distribution. It also implies that κ can be found easily from measurements of the exponential decay rate of $2|E_+E_-|$ or $|E_0|^2$ within the cavity.

The left to right output power ratio from the laser can be approximated from Eq. (2.2) as:

$$\frac{P_{left}}{P_{right}} = \frac{|E\left(-L/2\right)|^2}{|E\left(L/2\right)|^2} \approx \exp\left(2\kappa\Delta L\right) \tag{2.4}$$

An asymmetric π phase-shifted grating thus provides a simple way to make a laser with directional output power. This method was first demonstrated for fiber DFB lasers by movement of a thermally induced π phase-shift along a laser grating [10], yielding left to right output ratios of the order of 3–4.

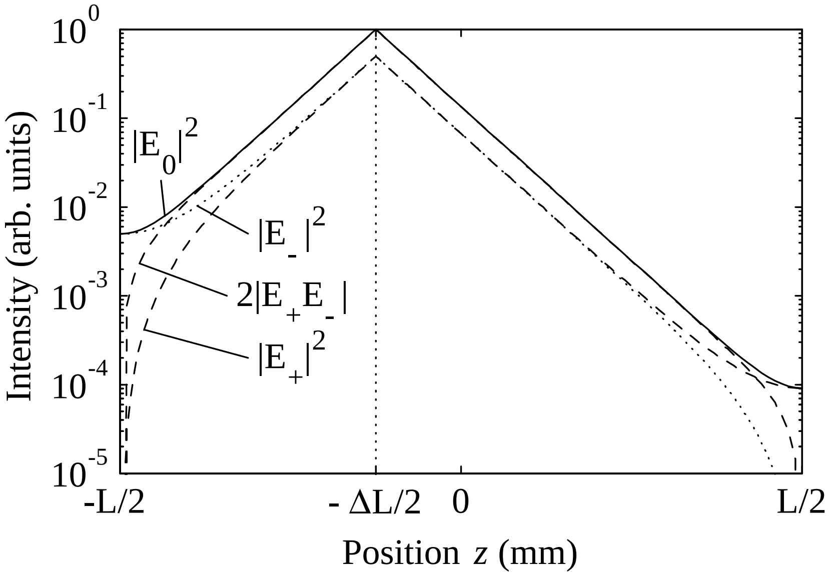

Figure 2.2. Theoretical distributions of $|E_+|^2$, $|E_-|^2$, $|E_+E_-|$ and $|E_0|^2 = |E_+|^2 + |E_-|^2$, calculated by the T-matrix approach, for an asymmetric laser with $\kappa L = 8$ and $\kappa \Delta L = 2$.

The method has also been discussed in a later publication [11]. The exact numerical calculations, assuming uniform gain distributions, show that Eq. (2.4) is a good approximation for grating parameters relevant for fiber lasers. For $\kappa(L - \Delta L) > 2$ and $P_{left}/P_{right} < 60$ dB the estimation error is within ±0.01 dB. For semiconductor lasers, $\kappa(L - \Delta L) > 0.5$ and $P_{left}/P_{right} < 20$ dB are more realistic, resulting in estimation errors that are within ±1.7 dB.

The intensity in the higher order modes may be interpreted as an interference between the two eigen-solutions of the coupled-mode equations. The difference in phase-propagation constants for these solutions result in sine-shaped intensity distributions at each side of the phase-shift discontinuity, as seen for the first and second order modes in Fig. 2.1. The number of peaks and troughs in the intensity distribution increases with the modal order.

For all modes the gain thresholds decrease with increasing κL. Our calculations show that grating phase imperfections generally reduces the threshold further for some of the higher order modes, while the fundamental mode threshold increases. Nonlinear index changes, which may for instance be due to self heating in the cavity, or to gain-dependent index changes, will contribute to such grating phase errors. Spatial gain hole-burning in combination with non-linear refractive-index changes may therefore lead to multiple-longitudinal-mode operation in high κL gratings, as discussed in other publications [1, 12].

In semiconductor lasers the gain differences that are due to hole-burning can be great, and multi-mode operation has been observed for grating strengths well below $\kappa L = 2.5$ [1, 2, 12].

Few studies have been made of the robustness of single longitudinal-mode operation in fiber DFB-lasers. Since the available single-pass gain in these lasers is relatively low, κL-products in the range from 5 to 10 are typically required to obtain threshold for the fundamental mode. For many applications it may be desirable to increase κL further. First, the sensitivity to external back reflections is expected to decrease with increasing κL [13]. Second, the Schawlow-Townes noise limit, which is believed to determine the laser phase noise at high frequencies [14], decreases with increasing κ and increasing L. Third, dual polarization lasers, which are interesting for polarimetric sensor applications, have been shown theoretically to be more robustly dual polarization for high κL-values [18]. In Subsection 2.3.4 of this paper we report on a DFB-laser with κ and L similar to the one modelled in Fig. 2.1 that was found to operate in a higher order mode. It is believed that the characterization method presented in this paper can be a useful tool for further investigations of longitudinal-mode competition in fiber DFB lasers.

2.2.2 Index-Perturbation Method

The index perturbation theory for resonant electromagnetic cavities [7, 8] states that a perturbation δn of the refractive-index within a small region δz of a cavity will result in a small shift $\delta\nu$ of the resonance frequency ν, given by:

$$\frac{\delta\nu}{\nu} = -\frac{\delta n \delta z \ \left|E_{loc}\left(z\right)\right|^2}{\int\limits_{Cavity} n\left(\hat{z}\right) \ \left|E_{loc}\left(\hat{z}\right)\right|^2 \ d\hat{z}}. \tag{2.5}$$

Here z is the position of the perturbation and $\left|E_{loc}\left(\hat{z}\right)\right|^2$ is the local intensity at position $\hat{z}$; *c.f.* Eq. (2.1). Equation (2.5) shows that $\delta\nu$ is proportional to the intensity at the perturbation point and to the induced round-trip phase perturbation $\delta\phi = 4\pi\,\delta n \delta z\,\nu/c$.

Both Cunliffe and Mathias [7] and Casimir [8] have deduced Eq. (2.5) (in slightly different 3-dimensional forms) for a gainless and lossless cavity medium with discrete and perfectly reflecting boundaries. This corresponds to zero net transport of energy within the cavity, implying that $|E_+|^2 = |E_-|^2$ everywhere. When the perturbed region is much larger than one standing wave period ($\delta z \gg nc/\nu$), $\left|E_{loc}\right|^2$ may therefore be replaced by $2|E_+E_-| = |E_+|^2 + |E_-|^2 = \left|E_0\right|^2$ in their treatment.

In a laser, there will always be transport of energy towards the output ports, i.e. $|E_+|^2 \neq |E_-|^2$. We have made exact numerical calculations of the perturbation sensitivity of the fundamental mode in π phase-shifted DFB lasers with varying κL-products. A T-matrix approach, which is valid for $\delta z \gg nc/\nu$, was used for the calculations. The results show an exact agreement with Eq. (2.5), provided that $2|E_+E_-|$ is substituted for $|E_{loc}|^2$ in Eq. (2.5). An intuitive way of understanding this result, is by observing that $2|E_+E_-|$ constitutes the non-propagating (or recirculating) portion of the cavity intensity, being independent on power transport to the output ports.

Only perturbations of the cavity volume at the boundary is discussed in the paper by Cunliffe and Mathias [7]. An interesting discussion of the case with almost degenerate modes is however included. Casimir [8] generalizes the derivation to also include perturbations of the refractive-index within the cavity.

We have investigated the validity of Eq. (2.5) for DFB lasers numerically by the T-matrix approach. Based on the conditions stated by Cunliffe and Mathias [7] and Casimir [8], the following limitations have been identified:

1. The perturbation magnitude should be small. In practice this means that the round-trip phase perturbation $\delta\phi$ should be well below 1 rad, and that $\delta\nu$ should be much smaller than the spacing to other cavity modes.

2. The perturbation must not, to the first order in $\delta\phi$, introduce coupling between laser modes. That is, the perturbation of the global field distribution must be small to the first order in $\delta\phi$. This will generally be true if the mode investigated is not close to degeneration with other modes.

The last condition is generally not well satisfied for the DFB modes. However, as mentioned above, the numerically calculated response for the fundamental mode of ideal DFB lasers are found to be in exact agreement with Eq. (2.5), independent on κL, when substituting $|2E_+E_-|$ for $|E_{loc}|^2$. This result is believed to be related to the symmetry of the higher order modes relative to the fundamental mode. That is: any frequency shift due to coupling to the $+1$ mode is exactly compensated by coupling to the -1 mode, etc. The perturbation responses for the first and second higher order modes have been calculated for κL-values ranging from 1 to 18, yielding deviations from Eq. (2.5) (with $|2E_+E_-|$ substituted for $|E_{loc}|^2$) that are maximum $\pm 6.5\,\%$ of the response at the most sensitive position. Also, non-ideal DFB structures that incorporate grating chirp or other non-uniformities, seem to have sensitivity distributions that are very similar to the actual intensity distributions.

Laser Number	Total length L (mm)	Assymmetry ΔL (mm)	Longit. mode order	Ratio P_{left}/P_{right}	Measured κ (m^{-1})	Wavelength (nm)	Fig.
1	40	0	0	1:1	230	1549	4
2	40	10	0	600:1	230	1549	4
3	50	0	0	–	230	1549	5
3 modified	45±1[a]	5±1[a]	0	33:1	230	1549	–
4	60	0	-1	–	–[b]	1533	6

Table 2.1. Overview of the Lasers Characterized in this Paper.

[a] The stated L and ΔL do not take into account possible annealing near the right-hand grating end during fusion splicing.

[b] The value of κ here is expected to be similar to the other lasers because the same UV-exposure level was used.

2.3 Experiments

2.3.1 Setup

The index perturbation sensitivities of four fiber DFB lasers, operating in the 1550-nm band and pumped at 1480 nm, were investigated using the setup shown in Fig. 2.3. An overview of the lasers is given in Table 2.1. Heat from a halogen lamp was focused onto a short length $\delta z = 1$–2 mm of the laser. Length δz determines the spatial resolution of the measurement. The bare fiber had been coated by black ink to improve the heat absorption. A fiber with an Er^{3+}–Yb^{3+}-doped core and a B–Ge-doped photosensitive ring outside the core [19] was used for the lasers.

To minimize effects of ambient temperature fluctuations, we placed the laser close to an aluminium surface. We monitored the lasing frequency by passing the laser output through a scanning Fabry-Perot cavity with a spectral resolution of 1.2 MHz and onto a detector. As the heating position was moved along the fiber, the heat was turned on and off with a shutter, and the resulting frequency shift was recorded.

The exact magnitude of the heat-induced round-trip phase-shift $\delta\phi$ could not be measured directly. $\delta\phi$ can, however, be determined from the measured distribution of $\delta\nu$, for instance by integration of both sides of Eq. (2.5) which thus eliminates the intensity from the expression.

The smallest frequency that could be resolved in the experiment was of the order of 10–30 MHz, limited by random fluctuations in the laser frequency, probably as a result of fluctuations in the ambient temperature and the pump power. Nonuniformities in the black ink coating or in the thermal contact be-

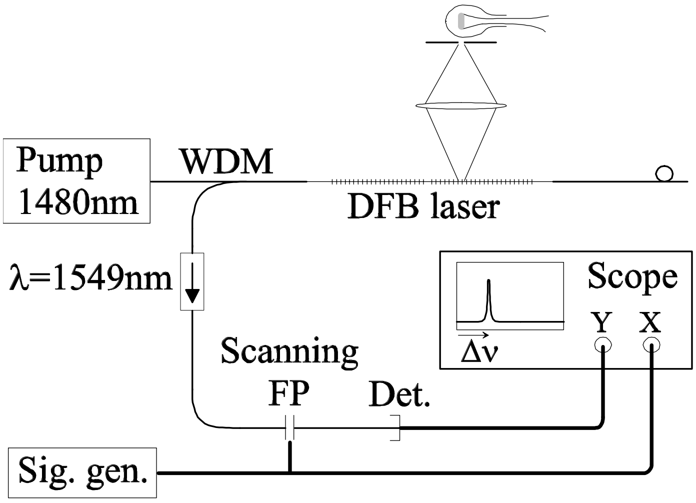

Figure 2.3. Setup for characterizing the phase perturbation sensitivity distribution: WDM, Wavelength division multiplexer; FP, Fabry-Perot interferometer; Det., detector; Sig. gen., signal generator.

tween the fiber and the aluminium may have caused some z dependence of $\delta\phi$.

2.3.2 Symmetric and Asymmetric Lasers

Figure 2.4 shows the measured heat perturbation responses, indicated as squares and circles, for the symmetric laser #1 and the asymmetric laser #2. Both devices lased in two polarizations at wavelengths close to 1549 nm. To within the measurement accuracy, no difference could be observed between the heat-induced perturbation responses of the two polarization modes.

In laser #2, the permanent grating phase-shift was offset by -5 mm from the center, giving a length difference $\Delta L = 10$ mm between the right and left sub-gratings. The corresponding shift in the peak response for that grating is clearly seen from the measurements.

Since the gratings were produced with equal UV-exposures, equal grating strengths are expected. That the grating strengths are equal is confirmed by the measured responses, which both decay exponentially from the phase-shift positions with decay rates corresponding to an effective grating strength of $\kappa = 230\ \mathrm{m}^{-1} \pm 10\,\%$. Calculated heating responses, assuming $\kappa = 230\ \mathrm{m}^{-1}$ and $\delta\phi = 0.53$ rad, are shown as curves in Fig. 2.4. From the UV spot-size used for the grating production, the extension of the permanently phase-shifted region is estimated to be less than 100 μm, which is much less than the $\delta z \approx 2$ mm spatial resolution of the measurements.

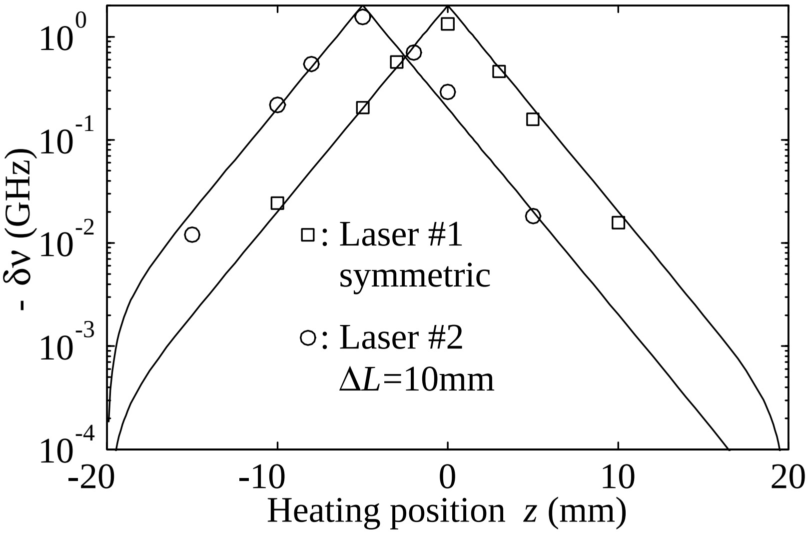

Figure 2.4. Laser frequency responses to heat scans measured for the symmetric laser #1 (squares) and asymmetric laser #2 (circles), both with 40-mm gratings. The lines show calculated responses for $\delta\phi$ =0.53 rad and κ =230 m^{-1}.

When a pump power of 83 mW at 1480 nm was launched into the lasers, the total left + right output powers were 470 μW from laser #1 and 30 μW from laser #2, corrected for losses in the wavelength-division multiplexer and the isolator. The left to right output power ratios were 1:1 for laser #1 and 600:1 ($\pm$10 %) for laser #2. The latter ratio is 6 times higher than predicted by expression (2.4), corresponding to a $\kappa\Delta L$ product that is 39 % higher than expected. The reason for this discrepancy is not clear, but it may be related to grating imperfections that cause nonideal intensity distributions in the regions near the grating ends. In these regions $\delta\nu$ was too small to be resolved by the measurements. Contributions to the power ratios from amplification outside the gratings should be ineligible, as the Er–Yb-fiber was spliced with good quality splices to standard telecom fiber less than 10 mm from the grating ends. The low power efficiency from the asymmetric device can be attributed to the short length and low reflectivity of the left-hand sub-grating [11], causing a higher threshold and reduced slope efficiency.

We obtained a better agreement with theory by cutting the symmetric 50 mm laser #3 (described in the next Subsection 2.3.3) 5$\pm$1 mm from its left end and fusion-splicing it back onto a standard telecom fiber. A total output power of 450 μW at 83-mW pump was obtained with a left-to-right output power ratio of 33. Assuming κ = 230 m^{-1}, this corresponds to an effective ΔL of 7.6

mm. The 2.6±1 mm increase in ΔL compared to what was cut off is probably due to excessive heating near the left-hand grating end during fusion splicing, annealing out the index modulation.

2.3.3 Polarization-Dependent Grating Strength

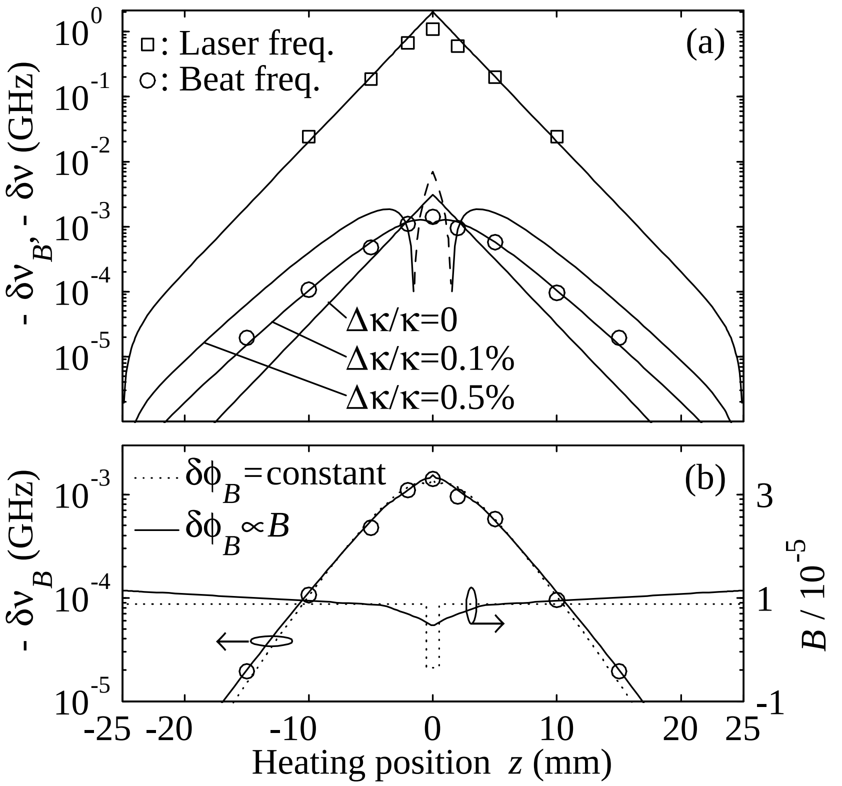

Figure 2.5. (a) Laser frequency and polarization beat frequency responses to heat scan measured for the dual polarization 50-mm DFB laser #3. Upper curve, the calculated laser frequency response $\delta\nu$. The other curves show calculated beat frequency responses $\delta\nu_B$ for three values $\Delta\kappa/\kappa$, assuming z-independence of B. Dashed curve indicates $-\delta\nu_B < 0$. (b) Measured (circles) and calculated (lines) beat frequency responses $\delta\nu_B$ for two different distributions of $B(z)$ when $\Delta\kappa = 0$. For all calculations in both (a) and (b) $\delta\phi$ =0.53rad and κ =230m^{-1} was assumed.

The squares in Fig. 2.5 (a) shows the measured response $\delta\nu$ of the laser frequency to a heat perturbation along symmetric 50-mm laser #3. This laser also operated in two polarizations operating at 1549 nm and produced under practically identical conditions to lasers #1 and #2. Again, the measured response fits the calculated response well when $\kappa = 230\ \mathrm{m}^{-1}$ and $\delta\phi = 0.53$ rad are assumed.

By replacing the Fabry-Perot interferometer in Fig. 2.3 with a polarizer and monitoring the detected signal on an rf spectrum analyzer, we measured the polarization beat frequency of laser #3 to be $\nu_B = 971$ MHz, corresponding to a birefringence of $B = n_y - n_x = 7.11 \cdot 10^{-6}$. The heat perturbation response $\delta\nu_B$ of the beat frequency was also measured and is plotted as circles in Fig. 2.5 (a).

Two contributions to $\delta\nu_B$ can be identified. The first contribution comes from the polarization dependence $\delta\phi_B$ of the heat-induced round-trip phase perturbation and should be proportional to $\delta\nu$. The second contribution arises from differences in the spatial distributions of the index perturbation sensitivities of the two modes, which corresponds to different shapes of the modal intensity distributions. This difference may either be due to a polarization dependence $\Delta\kappa$ of the grating coupling coefficient or to polarization dependent grating phase nonuniformities. Such phase nonuniformities are equivalent to a z dependence of the fiber birefringence B. Because the measured $\delta\nu$ and $\delta\nu_B$ are not proportional [*c.f.* Fig. 2.5 (a)], it seems clear that the difference in sensitivity distributions is significant in determining $\delta\nu_B$ for this laser.

If B is assumed to be z independent, the polarization dependence $\Delta\kappa$ of κ may be deduced from the measurements. The three bottom curves in Fig. 2.5 (a) show the calculated $\delta\nu_B$ for different (z independent) values for $\Delta\kappa/\kappa$. A good fit to the measured data is found for $\Delta\kappa/\kappa = 0.1\%$, corresponding to a Bragg modulation of the birefringence with an amplitude of $\Delta B = \Delta\kappa\lambda/\pi = 1.14 \cdot 10^{-7}$, where $\lambda = 1549$ nm.

Alternatively, if $\Delta\kappa$ is assumed to be zero, the z dependence of B can in principle be deduced from the measurements. One complicating question in this case is, however, to which degree $\delta\phi_B(z)$ will be dependent on $B(z)$. If variations in $B(z)$ arise from variable thermal stresses in the fiber [20], a proportional relation $\delta\phi_B \propto B$ is believed to be realistic. The temperature dependence of other possible contributions to $B(z)$, for example, UV-induced birefringence, is not so well understood, and it cannot be clearly determined whether $\delta\phi_B$ is z dependent.

Figure 2.5 (b) shows two different solutions obtained for $B(z)$, assuming either $\delta\phi_B \propto B$ or $\delta\phi_B =$ constant. A manual curve fitting procedure was used in which we adjusted the shape of $B(z)$ until the calculated curves for $\delta\nu_B$ matched the measured data to within reasonable error margins. For $\delta\phi_B =$ constant a second solution for $B(z)$ exists that is similar to the one shown but mirrored about the line $B = 0.71 \cdot 10^{-5}$. No similar second solution can be found for $\delta\phi_B \propto B$.

For simplicity, it was assumed that only n_x depends linearly on $B(z)$ in the calculations, while n_y was kept constant. This introduces grating phase errors in the x-polarized mode only, leading to a slightly wider spatial distribution of the index perturbation sensitivity for that mode. Practically the same solutions for $B(z)$ is obtained when we assume that both n_x and n_y are z dependent, provided that a small error in the permanent grating phase-shift at $z = 0$ is assumed.

The birefringence non-uniformities shown in Fig. 2.5 (b) are both larger in amplitude and much more localized than expected for the fiber used. UV-induced birefringence fluctuations of such a magnitudes are not likely, as the grating was produced by pulsed UV-laser scanning fiber technique in which the grating phase is directly controlled by the timing of the UV pulses relative to fiber's position as the fiber is scanned through a spot made from interfering UV-beams. This eliminates the need for extra UV-exposure in the phase-shifted region. It may therefore be concluded that the observed variations in $\delta\nu_B/\delta\nu$ most probably is due to a polarization dependence of the grating strength by 0.1 %, illustrated in Fig. 2.5 (a).

Note that the multiple solutions in Fig. 2.5 (b) imply that $\Delta\kappa$ cannot be easily deduced from measurements of $\delta\nu_B$ if $B(z)$ is not known in advance to some accuracy. Methods have been demonstrated for measuring fiber birefringence with potentially high spatial resolution [21] and could be used for this purpose.

UV-induced birefringence in low birefringence Ge-doped fibers ranging up to 8 % of the total index change, depending on the polarization of the UV beam, have been reported [22]. Similar values for $\Delta\kappa/\kappa$ should thus be possible. When we wrote the DFB-gratings characterized in this paper, the UV light was polarized approximately parallel to the fiber axis to minimize UV-induced birefringence. The remaining birefringence modulation ΔB, may be due to a small remaining component of the UV polarization orthogonal to the fiber axis, or to an asymmetric UV exposure of the photo-sensitized ring owing to the large amount of UV absorption in silica.

2.3.4 Higher-Order Mode Operation

The squares in Fig. 2.6 (a) show the measured response $\delta\nu$ of the laser frequency to heat perturbation along symmetric $L = 60$ mm laser #4 operating at 1533 nm. From the UV-exposure used, κ is expected to be 230 m^{-1} also for this laser, giving a rather large κL product of 13.8. It seems clear from the measurements that the laser operates in a higher order mode. We believed that the observed mode is of the first order, since the gain thresholds generally are expected to increase with modal order, *c.f.* Subsection 2.2.1. The relatively small width of the dip in $\delta\nu$ near $z = 0$ also supports this conclusion.

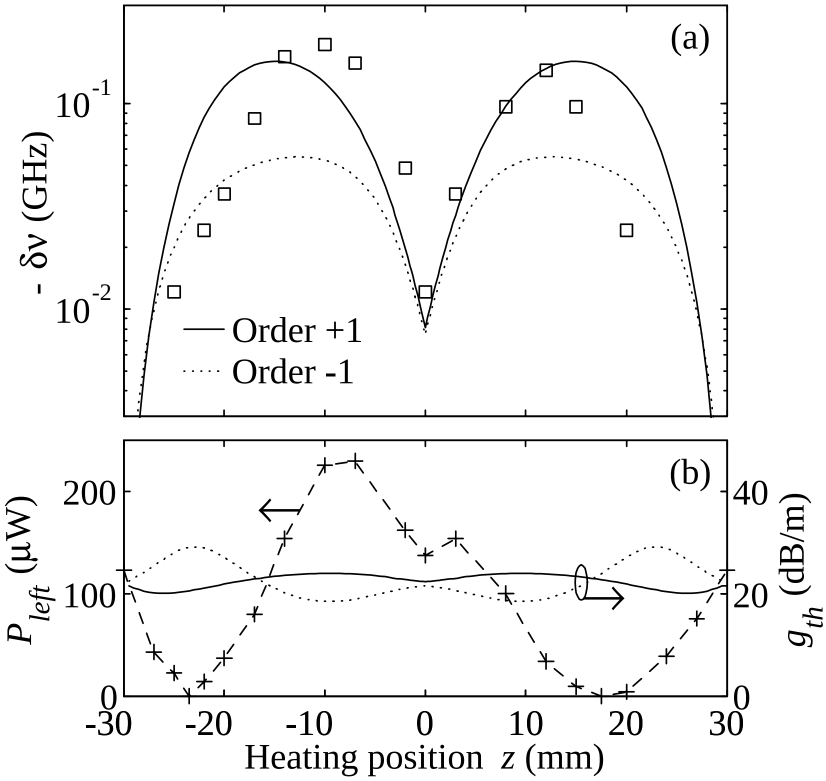

Figure 2.6. (a) Laser frequency response (squares) to heat scan measured for 60-mm DFB laser #4 with similar grating parameters to those characterized in Figures 3 and 4. Calculated responses of the +1- (solid curves) and −1- (dotted curves) order modes with $\delta\phi = 0.2$ rad are also shown. (b) Measured output power from the left end P_{left} (crosses) and calculated threshold gain for the +1 (solid curves) and -1 (dotted curves) order modes plotted versus heating position when $\delta\phi = 0.2$ rad.

The calculated frequency responses of the +1- and −1-order modes to a perturbation of $\delta\phi = 0.2$ rad are also shown in the figure. These responses are not identical, as they would be for much smaller perturbations. This difference is due to the very close frequency spacing of the first and second order modes, leading to a highly non-linear relationship between $\delta\phi$ and $\delta\nu$, *c.f.* requirement 1. in Subsection 2.2.2 [7]. When $\delta\phi$ increased, the calculated maximum value of the −1 mode response saturated towards 0.09 GHz for $\delta\phi \gtrsim 0.7$rad. This is well below the measured maximum of 0.19 GHz, indicating that the characterized mode is of the +1 order.

The left output power from the unperturbed laser was $P_{left} = 120\,\mu$W, corrected for losses in the wavelength-division multiplexer and isolator. However, P_{left} was found to be strongly affected by the position of the heat-perturbation, as can be seen from Fig. 2.6 (b) (crosses). At the heating positions $z = -23.5$ mm and +17.5 mm the laser is brought just below threshold while the power increases by 85 % compared to the unperturbed situation at $z = -8$ mm. This variation in output power with heating position may explain the discrepancy between theory and experiment in Fig. 2.6 (a), as the laser frequency is expected to decrease with increasing lasing power due to heating of the cavity from non-radiative losses at the lasing wavelength and conversion between pump and laser photon energies. The deviations between the measurements and the simulated +1-mode response in Fig. 2.6 (a) correlates well with the observed variations in output power. When we varied the lasing power by changing the pump power, a frequency shift of 0.87 MHz per μW of output power could be observed. Some of this shift may be due to non-radiative losses at the pump wavelength. The discrepancy from theory seen in Fig. 2.6 (a) corresponds to a shift of 0.4–0.6 MHz/μW.

The fundamental mode would also be expected to lase in this device, because the gain threshold for this mode should normally be much lower than for the higher-order modes. However, the fundamental mode could not be observed with the Fabry Perot interferometer, possibly partly because of asymmetric grating imperfections that could have caused most of the fundamental mode output power to exit at the right-hand end, which was not monitored in the experiment. The asymmetric shape of the measured response in Fig. 2.6 (a) supports this explanation. Competition with the higher order mode may also play a role in reducing the fundamental mode lasing power. Further, any losses within the cavity would reduce the slope efficiency much more for the fundamental mode than for the higher order mode because of the high cold-cavity Q factor of the fundamental mode.

The calculated threshold gain versus heating position for the +1 and −1 order modes are also shown in Fig. 2.6 (b). Again there is a qualitative agreement between the calculated +1-order mode threshold and the measured output power. The maximum gain of the fiber used, measured before UV-exposure and with 1480 nm pumping, was 15.2±1 dB/m at the laser wavelength. This is below the calculated and plotted threshold gains, which are in the range from 18 to 30 dB/m. Distributed grating phase errors may, however, bring the +1 order mode threshold down below 15 dB/m without changing the qualitative shape of the perturbation response. Such phase errors could arise from self heating owing to circulating high intensities in the fundamental mode near $z = 0$.

2.4 Conclusion

A heat-scan technique for characterization of DFB lasers has been demonstrated experimentally and investigated numerically and through comparison with an existing perturbation theory for electromagnetic resonators [7, 8]. Both the theory and the obtained numerical results indicate that the perturbation sensitivity will to a large extent be proportional to the modal intensity distribution.

Grating properties such as the coupling parameter κ, the polarization dependence $\Delta\kappa$ of κ, and the position of the grating phase-shift can be deduced from the measured heating sensitivity distributions ν and ν_B. Because the perturbation sensitivity depends on both the κ distribution and the grating phase distribution, one generally needs to know none one of these distributions is in general required to determine the other. For instance, to deduce $\kappa(z)$ from the measured $\Delta\nu(z)$ in Figs. 2.4 and 2.5, we had to assume a perfect grating phase. There is a similar relation between the abilities to determine $\Delta\kappa(z)$ or $B(z)$ from $\Delta\nu_B(z)$, as illustrated by the different beat-frequency simulations in Fig. 2.5 (a) and (b).

Without *a priori* knowledge of any of the grating parameters, the method still reveals the shape of the modal intensity distributions with good accuracy. This information is directly related to important topics such as the cold cavity Q factor, gain thresholds, pump efficiencies and non-linear effects such as gain hole burning, gain-dependent refractive-index changes and Kerr nonlinearities.

The experimental setup described in this paper is relatively simple, and easy to implement. Significant improvement in accuracy is however expected with a more refined setup. Better temperature stabilization of the laser, for instance by immersion of the laser into a liquid with a high specific heat capacity, would reduce both the random frequency noise and the systematic errors related to self-heating of the laser discussed in Subsection 2.3.4.

If the heat perturbation technique is to be used to characterize semiconductor DFB lasers, a much more localized heating spot would be required, because of the much smaller dimensions of the devices. This type of heating spot could be achieved by use of a focused laser beam for the heating. A relatively high heat-modulation frequency would probably be required to avoid broadening of the heated region by thermal diffusion.

An important application of the heat perturbation method is characterization of the spatial sensitivity distribution of fiber laser sensors with laser frequency readout, polarization beat frequency readout, or both [23]. Theoretically, the sensitivity of such DFB-lasers will decay from the center position proportionally to $\exp(-2\kappa|z|)$, giving an effective sensitive length of κ^{-1}. The sensitivity distribution of polarimetric sensors may, however, deviate significantly from the ideal case in the presence of a moderate polarization dependence of the grating strength or with non-uniform birefringence distributions, as illustrated by the simulated curves in Fig. 2.5.

2.5 Acknowledgment

This study was sponsored by Optoplan AS, the Norwegian Research Council and British Council. The Optoelectronics Research Center is an interdisciplinary research center funded by the Engineering and Physical Sciences Research Council, UK.

References

[1] L. J. P. Ketelsen, I. Hoshino, and D. A. Ackerman, "The Role of Axially Nonuniform Carrier Density in Altering the TE-TE Gain Margin in InGaAsP-InP DFB Lasers", IEEE J. Quantum Electron. **27**, 957–964 (1991).

[2] M. R. Phillips, T. E. Darchie, and E. J. Flynn, "Experimental Measure of Dynamic Spatial-Hole Burning in DFB lasers", IEEE Photonics Technol. Lett. **4**, 1201–*120*3 (1992).

[3] W. H. Loh, B. N. Samson and J. P. de Sandro, "Intensity profile in a distributed feedback fibre laser characterized by a green fluorescence scanning technique", Appl. Phys. Lett. **69**, 3773–*377*5 (1996).

[4] W. Margulis, I. C. S. Carvalho, P. M. P. Gouvêa, and B. Lesche, "Heat scan: a simple technique to characterize gratings in fibers", Opt. Lett. **18**, pp. 1016–*1018*, 1993.

[5] S. Sandgren, B. Sahlgren, A. Asseh, W. Margulis, F. Laurell, R. Stubbe, and A. Lidgard, "Characterization of Bragg gratings in fibers using the heat-scan technique", Electron. Lett. **31**, pp. 665–*666*, 1995.

[6] E. Brinkmeyer, G. Stolze, and D. Johlen, ”Optical space domain reflectometry (OSDR). for determination of strength and chirp distribution along optical fiber gratings” in *Bragg Gratings, Photosensitivity and Poling in Glass Fibers and Waveguides*, Vol. 17 of 1997 OSA Technical Digest Series, (Optical Society of America, Washington D.C., 1997).

[7] A. Cunliffe and L. E. S. Mathias, ”Some perturbation effects in cavity resonators”, Proc. Inst. Electron. Eng. **97**, 367–*3*76 (1950).

[8] H. B. G. Casimir, ”On the theory of electromagnetic waves in resonant cavities”, Phillips Res. Rep. **6**, 162–182 (1951).

[9] E. Rønnekleiv, M. Ibsen, M. N. Zervas and R. I. Laming, ”Characterization of intensity distribution in symmetric and asymmetric fiber DFB lasers”, in *Conference on Lasers and Electro-Optics*, Vol. 6, of 1998 OSA Technical Digest Series, (Optical Society of America, Washington D.C., 1997).

[10] J. T. Kringlebotn, J. L. Archambault, L. Reekie, and D. N. Payne, ”Er^{3+}:Yb^{3+}-codoped fiber distributed-feedback laser”, Opt. Lett., **19**, 2101–*210*3 (1994).

[11] V. C. Lauridsen, T. Søndergaard, P. Varming, and J. H. Povlsen, ”Design of Distributed Feedback Fibre Lasers” in *Proceedings of the European Conference on Optical Communications ’97*, (institution of Electrical Engineers, London, 1997) Vol. 3, pp. 39–42.

[12] H. Soda, Y. Kotaki, H. Sudo, H. Ishikava, S. Yamakoshi, and H. Imai, ”Stability in Single Longitudinal Mode Operation in GaInAsP/InP Phase-Adjusted DFB Lasers”, IEEE J. Quantum Electron. **QE-23**, 804–814 (1987).

[13] E. Rønnekleiv and O. Hadeler, ”Stability of an Er-Yb-doped fiber distributed-feedback laser with external reflections”, Opt. Lett. **24**, 617–619 (1999).

[14] G. A. Ball, C. G. Hull-Allen and J. Livas, ”Frequency Noise of a Bragg grating fibre laser”, Electron. Lett. **30**, 1229–*12*30 (1994).

[15] G. Björk and O. Nilsson, ”A New Exact and Efficient Numerical Matrix Theory of Complicated Laser Structures: Properties of Asymmetric Phase-Shifted DFB Lasers”, *J. Lightwave Technol.*, **LT-5**, pp. 140-146 (1987).

[16] M. Yamada and K. Sakuda, ”Analysis of almost-periodic feedback slab waveguides via a fundamental matrix-approach”, *Appl. Opt.*, **26**, pp. 3474-3478 (1987).

[17] G. P. Agrawal, A. H. Robeck, "Modeling of Distributed Feedback Semiconductor Lasers with Axially-Varying Parameters", *IEEE J. Quantum Electron.*, **24**, pp. 2407-2414 (1988).

[18] E. Rønnekleiv, M. N. Zervas and J. T. Kringlebotn, "Modelling of Polarization Mode Competition in Fiber DFB Lasers", IEEE J. Quantum Electron. **34**, 1559–*15*69 (1998).

[19] L. Dong, W. H. Loh, J. E. Caplen, J. D. Minelly and L. Reekie, "Efficient single-frequency fiber-lasers with novel photosensitive Er/Yb optical fibers", Opt. Lett. **22**, 694–*69*6 (1997).

[20] J. I. Sakai and T. Kimura, "Birefringence Caused by Thermal Stress in Elliptically Deformed Core Optical Fibers", IEEE J. Quantum Electron. **QE-18**, 1899–1909 (1982).

[21] A. Simon and R. Ulrich, "Evolution of polarization along a single-mode fiber", Appl. Phys. Lett. **31**, 517–521 (1977).

[22] T. Erdogan and V. Mizrahi, "Characterization of UV-induced birefringence in photosensitive Ge-doped silica optical fibers", J. Opt. Soc. Am. B **10**, 2100–*210*5 (1994).

[23] O. Hadeler, E. Rønnekleiv, M. Ibsen and R. I. Laming, "Polarimetric fiber distributed feedback laser sensor for simultaneous strain and temperature measurements", Appl. Opt. **38**, 1953–1959 (1999).

Part II:
Stability and Noise

Chapter 3

Frequency and Intensity Noise of Er-doped Fiber DFB Lasers

Abstract — The relative intensity (RIN) and optical frequency (ν_{rms}) noise of Er-doped fiber DFB lasers are investigated theoretically and experimentally. For a free running 1480-nm pumped fiber DFB laser with 170 μW output power we observe a typical RIN floor of -118 dB Hz$^{-1/2}$ for frequencies above 10 Hz, with a strong relaxation oscillation resonance peak reaching a peak value of -77 dB Hz$^{-1/2}$ at 222 kHz. The measured ν_{rms} ranges from 26 dB Hz/$\sqrt{\text{Hz}}$ at 1 kHz to 2 dB Hz/$\sqrt{\text{Hz}}$ at 1 MHz, with a sharp peak at the relaxation oscillation frequency. Below 1 kHz $1/f$ noise is observed in the laser frequency measurements. Negative feedback to the pump from a monitor detector reduces the RIN to the detection noise level, while the relaxation oscillation noise peak is removed from ν_{rms}. By comparing measured intensity and frequency fluctuations, we estimate the effective linewidth broadening factor at the relaxation oscillation frequencies of the investigated lasers to be between 2.1 and 3.8, as compared to typically between 3 and 7 for semiconductor lasers. The noise performance of four serially multiplexed fiber DFB lasers are found to be similar to that of the free running single lasers.

3.1 Introduction

The accuracy of optical sensors, such as interferometers, fiber Bragg grating sensors and high-resolution spectroscopic sensors, are in many cases limited by the accuracy by which the optical frequency of the interrogating source can be controlled or stabilized. Some of the most accurate sources known on the market today are ring-cavity Nd:YAG lasers [1] and Er:Yb-doped bulk glass lasers [2, 3]. Compared to single frequency fiber lasers these sources are relatively complicated to maintain and produce. They are also space consuming, and not easily tunable over large frequency ranges.

Fiber lasers can also be used as sensing elements, as demonstrated in [4, 5, 6], as well as in Chapters 7, 8, and 9. The optical pumping and frequency interrogation systems may then be situated far from the sensor lasers. The ultimate sensor accuracy will also in this case be limited by the intrinsic frequency noise of the lasers. It is therefore of interest to investigate the typical noise level of such lasers, and to investigate the origins of this noise in order to identify possible routes towards a further reduction of the noise.

Degrading of sensor accuracy due to source intensity noise can in principle be eliminated, for instance by monitoring the source power on a separate detector or by use of balanced interference detection schemes. However, these techniques tend to complicate the sensor design. Furthermore, parts of the laser frequency noise may actually arise from the intensity noise through thermal effects and the linewidth enhancement factor of the gain medium. Furthermore, It is therefore also of interest to investigate the intensity noise characteristics of the fiber DFB lasers.

This chapter is organized as follows: A theoretical framework for the study of laser noise and noise generating mechanisms is presented in Sec. 3.2. The aspects of thermally and acoustically induced noise in fiber DFB lasers are reviewed in Secs. 3.3 and 3.4, respectively. In Sec. 3.5 we characterize the sensitivity of the intensity and optical frequency of a fiber DFB laser to pump modulation, and we discuss the mechanisms causing this sensitivity. Measurements of the intensity and frequency modulation noise spectra from the lasers are presented in Sec. 3.6, while active noise suppression by applying negative feedback from the fiber laser output to the pump laser drive current is investigated in Sec. 3.7. The noise performance of serially multiplexed fiber DFB lasers is investigated experimentally in Sec. 3.8. Sec. 3.9 contains some concluding remarks.

3.2 Theory

A general theoretical framework for the study of laser intensity and frequency noise can be found in standard textbooks [7]. A purpose of this section is to define parameters and derive relations that can be related directly to the fiber DFB laser parameters.

3.2.1 Definitions of RIN, Frequency Noise, and Laser Linewidth

We let $A(t) = |A(t)| \exp(2\pi\nu(t))$ represent the complex optical field amplitude of the laser output as a function of time t, where $\nu(t) = \nu_0 + \Delta\nu(t) \ = \nu_0 + d\phi_s/(2\pi dt)$ is the instantaneous laser frequency. ν_0 is the mean laser frequency, while $\Delta\nu(t) = d\phi_s/(2\pi dt)$ represent the time dependent frequency fluctuations. $\phi_s(t)$ is the time-dependent optical phase fluctuations.

The relative fluctuations in the laser output power $P(t) = |A(t)|^2$ is defined as $RI = P(t)/P_o - 1$, where $P_o = \langle P(t)\rangle$ is the mean output power. The operator $\langle\cdot\rangle$ here means taking the average or expectation value. The relative intensity noise $RIN(f)$ (expressed in $\mathrm{Hz}^{-1/2}$) is defined by the relation $RIN^2(f) = \langle |RI^2(f)|\rangle$, which expresses the power spectral density of $RI(t)$ versus the electrical frequency f at which the noise is monitored.

The optical frequency noise $\nu_{rms}(f)$ (expressed in $\mathrm{Hz}/\sqrt{\mathrm{Hz}}$) is defined is defined by the relation $\nu_{rms}^2(f) = \langle |\Delta\nu^2(f)|\rangle$, which expresses the power spectral density of $\Delta\nu(t)$. The phase noise density ϕ_{rms} (expressed in $\mathrm{rad}/\sqrt{\mathrm{Hz}}$) is related to ν_{rms} by $\phi_{rms} = \nu_{rms}/f$.

The power spectral density $|A(\nu)|^2$ of the laser output field depends both on the phase $\phi_{rms}(f)$ and RIN noise spectra of the laser. In most cases, however, $\phi_{rms}(f)$ will dominate over the RIN. From Fourier theory we know that $|A(\nu)|^2$ is the Fourier transform of the auto-correlation function $\langle A(t)A(t+\tau)\rangle$. For the case where the RIN is negligible, Weissman shows in [8] that (for a noise process obeying Gaussian statistics) the auto-correlation function takes the form:

$$\langle A(t)A(t+\tau)\rangle = \left\langle |A(t)|^2 \right\rangle e^{-\Lambda(\tau)/2}, \tag{3.1}$$

where $\Lambda(\tau) = \langle [\phi_s\,(t+\tau) - \phi_s\,(t)]^2\rangle$ represents the variance of the interference phase that would arise in an interferometer with delay τ.

If we assume ν_{rms} to be independent on f (white noise), $\phi_s(t) = 2\pi \int_0^t (\nu(\hat{t}) - \nu_0) d\hat{t}$ represents a "random walk process". We then find:

$$\begin{aligned} \Lambda(\tau) &= \left\langle [\phi_s\,(t+\tau) - \phi_s\,(t)]^2 \right\rangle \\ &= \left\langle \left[\int_t^{t+\tau} 2\pi\nu\left(\hat{t}\right)\ d\hat{t} \right]^2 \right\rangle = 4\pi^2\tau\nu_{rms}^2. \end{aligned} \tag{3.2}$$

The laser coherence time τ_{coh} is often defined as the interferometer delay time τ for which $\langle A(t)A(t+\tau)\rangle$ has dropped to e^{-2} of its maximum value. (3.1) and (3.2) then implies:

$$\tau_{coh} = (\pi\nu_{rms})^{-2} \tag{3.3}$$

Inserting (3.2) into (3.1) and transforming to the frequency domain results in the following Lorenzian form of $|A(\nu)|^2$:

$$|A(\nu)|^2 = \frac{|A(\nu_0)|^2}{1 + (\nu - \nu_0)^2/\Delta\nu_{3dB}^2}, \tag{3.4}$$

where, $\Delta\nu_{3dB}$ is the laser full-width-half-maximum linewidth, defined as:

$$\Delta\nu_{3dB} = (\pi\tau_{coh})^{-1} = \pi\nu_{rms}^2. \tag{3.5}$$

In practice, (3.4) and (3.5) will produce good approximations for $|A(\nu)|^2$, provided that $\nu_{rms}(f)$ is flat up to a few octaves above $f = \Delta\nu_{3dB}$. More precisely stated: The contributions from deviations from a flat spectrum in $\nu_{rms}(f)$ to the integral $\int_0^\infty (\nu_{rms}(f)/f)^2\, df$ should be negligible.

For a free running fiber laser (without active feedback for intensity stabilization), RIN and frequency noise at the relaxation oscillation frequency f_r will usually lead to sidebands in the optical spectrum $|A(\nu)|^2$ at $\nu = \nu_0 \pm f_r$. For large relaxation oscillation amplitudes ($\gtrsim 10$ % modulation depth), higher order sidebands may also be observed at $\nu = \nu_0 \pm k\, f_r$, $(k = 1,\, 2,\, \cdots)$. Typically, $f_r = 100 - 500$ kHz for Er^{3+}-doped fiber DFB lasers. If the laser is self pulsing (100 % modulation depth), the effects of RIN on the shape of $|A(\nu)|^2$ will be significant, and (3.4, 3.5) will not be valid.

ν_{rms} will usually increase at low frequencies f due to ambient temperature drift, acoustical vibrations, etc. In semiconductor and solid state (Nd:YAG) lasers, $1/f$ noise processes of less understood origins are also known to play a role. Usually, one does not want to include the long-term frequency drift in the calculation of $\Delta\nu_{3dB}$. One solution to this problem is to maintain the definition $\langle A(t)A(t+\tau_{coh})\rangle = 1/e$ given above for the coherence time τ_{coh}, and use (3.5) as a definition for the 3-dB bandwidth. Alternatively, one may define $\Delta\nu_{3dB}$ as the full-width-half-maximum of $|A(\nu)|^2$ averaged over a specified recording time. With both definitions, ν_0 will be time-dependent on long time-scales.

3.2.2 Classification of Noise Sources

The origins of RIN and laser frequency noise can be classified into four categories:

1. *Spontaneous emission seeding* of the laser operation, represented by a white noise source of spectral power density e_{sp}^2 (W/Hz) radiating into the cavity. The complex field amplitude $e_{sp}(t)$ of the spontaneous emission is added to the existing field $M^{-1/2}A(t)$ in the cavity, where M is the laser mirror transmissivity to the output port. The resulting perturbations of the relative amplitude $RI/2$ and the phase ϕ_s are not correlated, but with equal rms magnitudes $e_{sp}(M/P_o)^{1/2}$. The field perturbations are

integrated over time due to the recirculation in the cavity every roundtrip time τ_{rt}. The field perturbations $d|A|/dt$ and $d\phi_s/dt$ resulting from this integration is called the Langevin force [7].

2. *Optical resonance frequency perturbations* of the cold cavity causing a direct contribution to $\Delta\nu$. By "cold cavity" we mean the cavity, including possible back reflections from the lead fiber, but excluding the effects of the active gain medium. The resonance frequency perturbations may originate from external thermal or mechanical perturbations.

3. *Loss perturbations* of the cold cavity, represented by a modulation Δa_{rt} of the roundtrip loss in absence of active gain (defined more precisely below). Such loss perturbations could originate from random fluctuations in saturable absorber losses, or by randomly varying external back reflections. The loss integrates over time into a RI contribution.

4. *Pump efficiency perturbations*, which may be due to fluctuations in the relative intensity RI_p, center wavelength, or polarization state of the pump. These fluctuations will lead to fluctuations Δg_{rt} in the roundtrip gain contributed from the active gain medium. (Δg_{rt} is defined more precisely below).

The RI and ν_s (or ϕ_s) observed at the output from the laser will generally be different from the input signals discussed above, due to feedback and interactions between the gain, loss, intensity, and resonance frequency. These interactions will be discussed in the following sub-sections.

3.2.3 A Model for the Interaction Between Gain and RI

The small-signal interaction between the active gain medium and the RI can be described by the following rate equations:

$$\begin{aligned}\frac{dRI}{dt} &= \frac{\Delta g_{rt} - \Delta a_{rt} + 2(M/P_o)^{1/2}e_{sp}}{\tau_{rt}} \\ \frac{d\Delta g_{rt}}{dt} &= \tau_{sat}^{-1}\Delta g_{rt} + (k_{slope}RI_p - RI)k_{sat}g_{rt}. \qquad (3.6)\end{aligned}$$

Here, g_{rt} is the contribution from the active gain medium to the field amplitude roundtrip gain coefficient of the laser (corresponding to the variable rtg_g in Chap. 6). At steady state we have $g_{rt} = a_{rt}$ where a_{rt} is the cold cavity roundtrip loss. Δg_{rt} and Δa_{rt} are the small-signal deviations of g_{rt} and a_{rt} from steady state.

$\tau_{sat} \equiv \partial\Delta g_{rt}/(\Delta g_{rt}\partial t)$ in (3.6) is the saturated lifetime of the gain medium for the given signal and pump intensities. It is convenient also to introduce the saturation frequency as $f_{sat} = 1/(2\pi\tau_{sat})$. For a two-level gain medium (like the 1480-nm pumped Er-laser) we have

$$\tau_{sat}^{-1} = 2\pi f_{sat} = \tau_{sp}^{-1} + (\sigma_{se} + \sigma_{sa})P_o/M + (\sigma_{pe} + \sigma_{pa})P_p, \qquad (3.7)$$

where τ_{sp}^{-1} is spontaneous and stimulated emission rate, σ_{xy} is the emission ($y = e$) and absorption ($y = a$) cross-sections (normalized with respect to the photon energy and the overlap with the mode cross section area) at the signal ($x = s$) and pump ($x = p$) wavelengths, and P_o/M and P_p are the signal and pump intensities inside the cavity, respectively.

k_{sat} in (3.6) is defined as $k_{sat} \equiv \partial\Delta g_{rt}/\partial RI$ where the differential should be evaluated at DC ($f \rightarrow 0$). For our two-level gain medium we have $k_{sat} = (1 + P_{sat}M/P_o)$ where P_{sat} is the saturation power of the gain medium for the given pump power. In the following we will assume that $k_{sat} \simeq 1$, corresponding to $P_o/M \gg P_{sat}$ which is believed to be valid for most fiber DFB lasers. k_{slope} is determined by the slope efficiency of the laser at DC, and is defined as

$$k_{slope} = RI(f \rightarrow 0)/RI_p(f \rightarrow 0). \qquad (3.8)$$

(3.6) can be transformed to the Fourier frequency domain by substituting $i2\pi f$ for d/dt. The resulting small-signal flow diagram is shown in Fig. 3.1 (a). A feedback loop from Δg_{rt} to RI and back to Δg_{rt} can be identified in the figure, with roundtrip transfer function:

$$\begin{aligned} H_0(f) &= \frac{-g_{rt}}{i\pi\tau_{rt}f(1 + if/f_{sat})} \\ &= \frac{-f_r^2 f_{sat}^{-1}}{if(1 + if/f_{sat})} \,. \end{aligned} \qquad (3.9)$$

Here,

$$f_r = \sqrt{\frac{g_{rt}f_{sat}}{\pi\tau_{rt}}} \qquad (3.10)$$

is the frequency at which $|H_0(f_r)| \simeq 1$. f_r is called the relaxation oscillation frequency. The magnitude and phase of $H_0(f)$ is illustrated in Fig. 3.1 (b) for values of f_{sat} and f_r that are typically expected in Er-doped fiber DFB lasers.

The transfer functions from the input signals RI_p, Δa_{rt}, and e_{sp} in Fig. 3.1 (a) to the output laser RI can be deduced from the flow diagram to be:

$$\begin{aligned} T_p(f) &= \frac{RI}{RI_p} &&= k_{slope}\frac{H_0(f)}{1 - H_0} \\ T_{loss}(f) &= \frac{RI}{\Delta a_{rt}} &&= \frac{-1}{i\pi\tau_{rt}f\,[1 - H_0(f)]} \\ T_{sp}(f) &= \frac{RI}{e_{sp}} &&= -2\,(M/P_o)^{1/2}\,T_{loss}(f) \,. \end{aligned} \qquad (3.11)$$

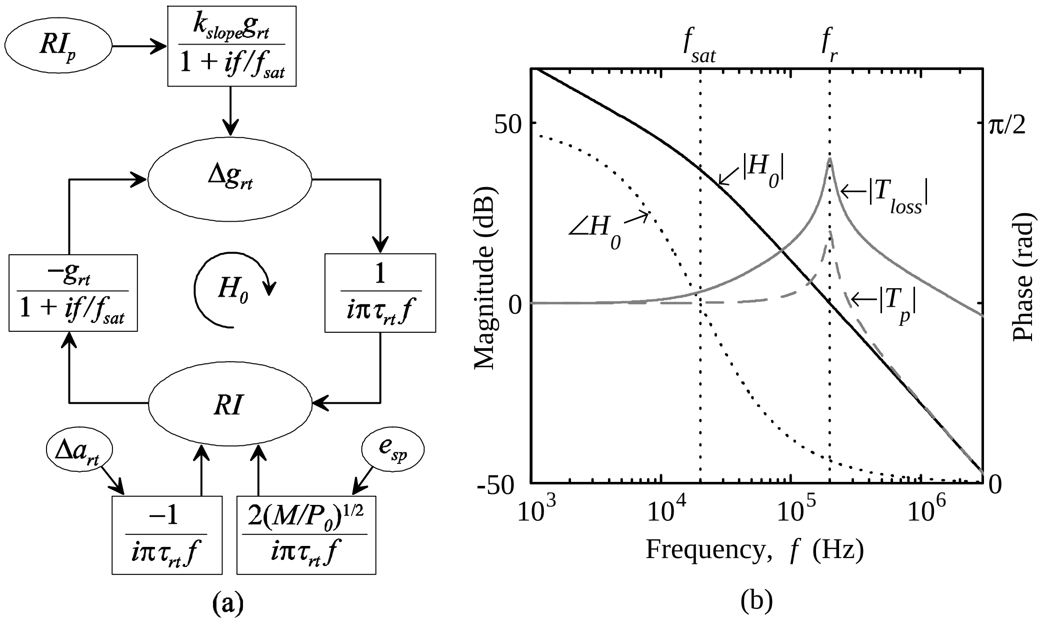

Figure 3.1. (a): Signal flow diagram illustrating the rate equations (3.6) in the frequency domain. (b): Phase and magnitude plots of the rondtrip transfer function $H_0(f)$ defined in (3.9); and arbitrarily scaled magnitude plots of the transfer functions T_p and $T_{loss} \propto T_{sp}(f)$ defined in (3.11). Parameters: $f_{sat} = 20$ kHz and $f_r = 200$ kHz.

The magnitudes of $T_p(f)$ and $T_{loss}(f) \propto T_{sp}(f)$ are illustrated Fig. 3.1 (b) with arbitrary scale factors. We see that the ratio between $T_{loss}(f)$ and $T_p(f)$ increases by 20 dB per decade for $f > f_{sat}$. Theoretical results recently published in [9] (for Er-doped lasers without ion clustering) are in qualitative agreement with Fig. 3.1 (b)[2].

The strong resonance in the transfer functions near $f = f_r$ is called the relaxation oscillation resonance. The strength of this resonance can be expressed by quality-factor Q_r, defined as the ratio of f_r to the 3-dB peak bandwidth of the transfer functions. For Er-doped fiber DFB lasers we will usually have $Q_r \gg 1$ (typically $Q_r > 8$), in which case the approximation $Q_r \approx [\angle H_0(f_r)]^{-1}$ is valid. Here, $\angle H_0(f_r)$ (expressed in radians) is the stability phase margin of H_0. From (3.9) and (3.10) we obtain

$$Q_r \approx f_r/f_{sat} = \sqrt{g_{rt}/(\pi\tau_{rt}f_{sat})}. \qquad (Q_r \gg 1) \qquad (3.12)$$

---

[2] The dB-scales in different figures in [9] are not consistent. Apparently the scales in the first two figures should be multiplied by a factor of two.

By combining (3.12) and (3.7) we find that the laser stability can be expected to improve with increasing pump power P_p, increasing output power P_o, and decreasing laser mirror transmissivity M.

Saturable absorber states, which are believed to originate from clustering of Er^{3+} ions in highly Er doped fibers [10], or from UV-induced life-time quenching of the Er^{3+} ions [11] (discussed in Chap. 5), will contribute with a second feedback path to the RI that acts in parallel with the path shown in Fig. 3.1. The saturable absorber losses decrease with increasing laser intensity. The resulting modified roundtrip transfer function (3.9) can be written as:

$$H_0(f) = \frac{-f_r^2 f_{sat}^{-1}}{if(1 + if/f_{sat})} + \frac{k_{s.abs}}{i\pi\tau_{rt} f}\,, \tag{3.13}$$

where $k_{s.abs} = \delta a_{rt}/\delta RI$ is a measure of the saturable absorber strength. The last term in (3.13) pulls the phase margin $\angle H_0(f_r)$ down by approximately $k_{s.abs}/(\pi\tau_{rt} f_r) \simeq k_{s.abs}\sqrt{g_{rt}/(\pi\tau_{rt} f_{sat})}$, and the stability of the laser is thus degraded by the saturable absorber. Although highly simplified,[3] we believe that (3.13) can be used to model the effects of saturable absorbers near $f = f_r$. More comprehensive models, requiring a detailed knowledge of the saturable absorber behavior (which we lack for the lasers studied in this chapter), are presented in [9, 10, 12]. Stability degradation due to saturable absorbers has been verified by several authors, including [10, 12]. On the other side, theoretical results in [9] indicate an improvement in stability (reduced Q_r) with increasing clustering fraction. There is no discussion in [9] of the reason for this unexpected result.

External feedback with time-delays that correspond to a significant phase shift at the relaxation oscillation frequency may also pull on the phase margin and cause degraded stability. Effects of external optical feedback and UV-induced saturable absorbers on laser stability will be discussed further in Chapters 4 and 5.

If the losses are dominated by the mirror transmissivities, and if both mirror transmissivities are equal to M (symmetric output), we will have $M = a_{rt} = g_{rt}$. For a discrete π phase-shifted DFB laser of length L we then have $M = 4\exp(-\kappa L)$, where κ is the index coupling parameter. Typical values for fiber DFB lasers may range from $M = 5 \times 10^{-6}$ to 5×10^{-3}.

The cavity roundtrip-time can be expressed as $\tau_{rt} = 2nL_c/c$, where L_c is the effective cavity length. For the π phase-shifted DFB laser it can be shown that $L_c \cong 1/\kappa$ (c.f. Chap. 1). If a distributed grating phase-shift is used, a length in the order of the extension of the phase-shift region should be added to the

---

[3] $k_{s.abs}$ will depend on the intracavity power P_o/M, and is expected to increase with P_o/M at low power levels. We expect $k_{s.abs}$ to saturate at high intracavity power levels, as the saturable absorber saturates. A frequency dependence of $k_{s.abs}$ is also expected for high frequencies f.

above value. Typical values for L_c may range from 3 to 15 mm, corresponding to roundtrip delays of $\tau_{rt} = 30 - 150$ ps.

3.2.4 Interactions with the Laser Frequency

In the following we discuss mechanisms related to the gain medium and the cavity loss dispersion that cause coupling or correlation between the intensity and frequency fluctuations in the laser.

Gain Medium Mechanisms

In semiconductor lasers, the linewidth enhancement factor α_g of the gain medium is known to play a dominating role in determining ν_{rms}. α_g relates refractive index changes to changes in the active gain in the cavity, and is defined by:

$$\alpha_g = \frac{dn'}{dn''} \tag{3.14}$$

where dn' and dn'' are changes in the complex refractive index $n' + in''$. The real and imaginary parts of the refractive index are related through the Kramers-Kronig relation.[4] Typical values for semiconductor lasers are $\alpha_g \sim 3 - 7$ [7]. α_g has been mentioned as a parameter of significance for longitudinal mode instabilities in semiconductor DFB lasers. We do not expect this to be the case for fiber DFB lasers, because the roundtrip gain magnitudes are generally orders of magnitude smaller than in semiconductor lasers. This means that the roundtrip phase-shift changes related via α_g to gain saturation will be small. There are still at least two reasons why the linewidth enhancement factor is of importance for fiber DFB lasers. First, the stability of the lasers in the presence of external reflection degrades with increasing α_g, as will be shown further down in this sub-section. Especially, the value of α_g at the relaxation oscillation frequency is of importance, as will become apparent in Chaps. 4 and 5. Second, the contribution from spontaneous emissions to the laser frequency noise ν_{rms} is proportional to α_g, as shown in Sec. 3.2.5.

Measured values of α_g in fiber lasers have to our knowledge not been reported in the literature. Simulation results for a saturated Er-doped amplifier reported by Alameh *et.al.* in [13] (based on theory published by Desurvire [14]) show the real and imaginary parts of the complex susceptibility for a few values of the saturating signal power P_s. Their results indicate that α_g increases when

---

[4] All physical (causal and stable) impulse responses must obey the Kramers-Kronig relations. However, both Desurvire [14] and Alameh *et.al.* [13] point out that the Kramers-Kronig relations are not valid for the complex susceptibility function they use to model saturation in Er^{3+}-doped amplifiers. This because the susceptibility function has poles in the right half of the complex s-plane, implying instability on time-scales longer than τ_{sat}. This must be due to approximations implicit in the model, as it cannot be true for the physical system.

the saturating signal power P_s or wavelength λ_s are increased. Their results indicate that α_g is roughly proportional to P_s for signal to saturation power ratios in the range $P_s/P_{sat} = 10 - 20$. (See Chapter 6 for a definition of P_{sat}.) For $P_s/P_{sat} \approx 20$ we estimate from [13] that α_g goes through zero around $\lambda_s = 1540$ nm, increasing to $\alpha_g \sim 2.3$ at 1550 nm and $\alpha_g \sim 4.4$ at 1560 nm. The main contribution to the calculated refractive index change seems to come from spectral hole-burning of the gain population for wavelengths close to λ_s. It should be noted that the results in [13] are derived for steady-state saturating conditions, i.e. for $f \ll f_{sat}$. Typical values for f_{sat} inside fiber DFB lasers are expected to be in the range from $5 - 160$ kHz (depending mostly on the grating strength). It is unclear to which degree the theory in [13] leads to representative values for α_g for $f > f_{sat}$. More comprehensive studies of the factors influencing on α_g could be useful, including studies of how α_g depends on f, P_s, P_{sat}, λ_s, pump wavelength, fiber composition (codopants), ion clustering, UV-induced lifetime quenching, etc.

α_g can be expressed in terms of the ratio between changes in the laser frequency ν and the cavity roundtrip gain $\Delta g_{rt} = \frac{1}{2}\tau_{rt} dRI/dt$, or alternatively in terms of the ratio between changes in the optical phase ϕ_s and the RI. From (3.14) we derive:

$$\alpha_g = 2\pi\tau_{rt}\frac{\partial\nu}{\partial g_{rt}} = \left\{\frac{2\,d\phi_s}{dRI}\right\}_{gain} \tag{3.15}$$

The subscript "*gain*" is used to indicate that only contributions to the differentials from the saturation of the gain medium is included. (3.15) indicates that we can estimate α_g from measurements of the correlation (or transfer function) between RI and ϕ_s ($= \Delta\nu/if$) provided that we can identify which fraction of the RI that originates from gain fluctuations. The direct input contributions to the RI from Δa_{rt} and e_{sp} in Fig. 3.1 (a) do not originate from the gain medium.

At the relaxation oscillation resonance frequency, the external input contributions to the RI will be amplified due to the feedback resonance by the quality factor Q_r, which is typically high in Er-doped fiber DFB laser ($Q_r \sim 8 - 50$). Therefore, the main contribution to RI in Fig. 3.1 (a) comes through the path from Δg_{rt}, and we can use the approximation $\Delta g_{rt} \approx i\pi\tau_{rt} f\, RI$. Inserting this approximation into (3.15) (with $\partial\nu/\partial g_{rt} = \Delta\nu/\Delta g_{rt}$) we obtain:

$$\alpha_g \simeq \frac{2\Delta\nu}{if\,RI} \quad \text{(relaxation oscillations, } Q_r \gg 1\text{)}, \tag{3.16}$$

where $\Delta\nu$ is the measured frequency shift.

More general formulas that can be used to express α_g in terms of the normalized correlation $\langle\Delta\nu^* RI\rangle/(\nu_{rms} RIN)$ between $\Delta\nu$ and the RI outside the relaxation oscillation resonance are deduced in [7]. However, due to the thermal effects discussed below, we expect $\langle \Delta\nu^* RI\rangle/(\nu_{rms} RIN)$ to depend heavily on which of the sources in Fig. 3.1 (a) that cause the RI. Care should therefore be taken when interpreting the results of applying these formulas to Er-doped fiber lasers.

Heating Mechanisms

Self heating from non-radiative losses of laser and pump energy will also contribute to a correlation between the RI and $\Delta\nu$. The relaxation of gain ions from the pump absorption level to the upper laser level is one source of self heating. Non-radiative losses at the pump and laser wavelengths are other possible sources. The self heating can be characterized by the ratio:

$$r_{th} = \frac{\Delta\nu_{th}}{RI}, \tag{3.17}$$

where $\Delta\nu_{th} = \frac{\delta n}{n\delta T}\Delta T$ is the thermally induced frequency shift, $\frac{\delta n}{n\delta T}$ is the effective thermal sensitivity (including effects of thermal stress and strain) of the refractive index n, and ΔT is the temperature change. For $f \ll f_r$, the fluctuations ΔP_{th} in the thermal power P_{th} produced in the core is expected to be proportional to the RI. At low frequencies f where the fiber core is in thermal equilibrium with the cladding and surroundings, we therefore expect a frequency independent proportional relation $\Delta\nu_{th} \propto \Delta T \propto -\Delta P_{th} \propto -RI$, and thus a frequency independent negative value for r_{th}.[5] Note, however, that the proportionality constant relating ΔP_{th} to RI depends on which of the self heating sources that dominate. This again depends on which of the input noise sources RI_p, Δa_{rt} and e_{sp} that dominates the laser noise.

For $f \gtrsim f_r$ a frequency independent proportionality between the RI and ΔP_{th} can no longer be assumed, partly because $T_p(f)$ becomes frequency dependent. It is also necessary to take Δg_{rt} into account as a significant source of fluctuations in the pump absorption rate. The thermal contribution $\alpha_{g,th}$ to α_g near $f = f_r$ can be expressed by combining (3.16) and (3.17) as:

$$\alpha_{g,th} = 2\pi\tau_{rt}\left\{\frac{d\nu}{dg_{rt}}\right\}_{thermal} \simeq \frac{2r_{th}}{if} \quad \text{(relaxation oscillations, } Q_r \gg 1\text{).} \tag{3.18}$$

Loss Dispersion Mechanisms

Fluctuations $\Delta\nu$ in the cavity resonance frequency due to refractive index perturbations that modify the effective cavity roundtrip phase-shift can in principle lead to laser intensity noise through the optical frequency dependence of

---

[5] The upper frequency limit for the condition of thermal equilibrium to be true depends on the nature of the heat sink. For an ideal heat sink with constant temperature at the fiber surface, we see from Fig. 3.6 that the upper frequency limit is about 100 Hz.

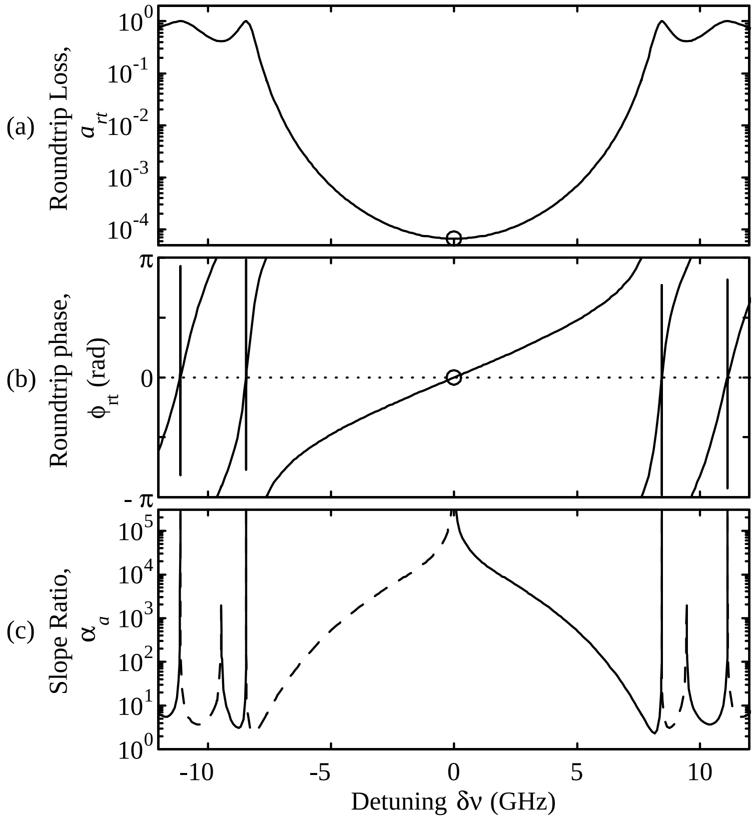

Figure 3.2. Roundtrip loss a_{rt} (a) and phase ϕ_{rt} (b) versus detuning $\delta\nu$ for an ideal 50 mm DFB laser with $\kappa L = 11$. Circles (○) indicate the laser operation point. (c) Ratio α_a (3.19) between the slopes of ϕ_{rt} and a_{rt}. Dashed lines indicate negative values.

the grating mirror transmissivities. Fig. 3.2 (a) shows the cavity roundtrip loss a_{rt} versus frequency detuning $\delta\nu$ for an ideal π phase-shifted fiber DFB laser of length $L = 50$ mm with a normalized index coupling coefficient of $\kappa L = 11$. The laser operation point at $\delta\nu = 0$ is indicated by a circle. We see that the loss is frequency independent at this point. Frequency perturbations will therefore not to the first order cause intensity noise in an ideally phase-shifted DFB laser.

Fig. 3.2 (b) shows the roundtrip phase $\phi_{rt}(\delta\nu)$ of the same laser. (The steep phase transitions at ±8.4 and ±11.1 GHz are due to higher order resonances of the DFB grating.) A change $\Delta\phi_{rt}$ in the effective grating phase-shift will cause ϕ_{rt} to move vertically in the figure by $\Delta\phi_{rt}$. The laser resonance frequency must still be at the zero-crossing $\phi_{rt}(\delta\nu) = 0$, and will thus move by $\Delta\nu = -\Delta\phi_{rt}/(d\phi_{rt}/d\delta\nu) = -\Delta\phi_{rt}/(2\pi\tau_{rt})$, since $d\phi_{rt}/d\delta\nu = \tau_{rt}$.

Inspired by (3.15) we define the "loss dispersion linewidth broadening factor" as:

$$\alpha_a = 2\pi\tau_{rt}\frac{\partial\nu}{\partial a_{rt}} = 2\pi\frac{d\phi_{rt}}{d\nu}\frac{\partial\nu}{\partial a_{rt}} = \left\{\frac{d\phi_{rt}/d\nu}{da_{rt}/d\nu}\right\}_{loss} \tag{3.19}$$

α_a is plotted for the ideal DFB laser in Fig. 3.2 (c).

In the presence of a small gain perturbation $\Delta\gamma$ (either due to loss, spontaneous emission or pump fluctuations), the interaction between α_a and α_g can be expressed by an effective linewidth enhancement factor $\alpha_{eff} = 2\pi\tau_{rt}\Delta\nu/\Delta\gamma$. At low frequencies $f \ll f_r$ we may assume $g_{rt} - a_{rt} = 0$, implying:

$$\Delta\nu\left\{\frac{\partial\nu}{\partial g_{rt}}\right\}^{-1} - \Delta\nu\left\{\frac{\partial\nu}{\partial a_{rt}}\right\}^{-1} + \Delta\gamma = 0.$$

Substituting $\partial\nu/\partial g_{rt}$ and $\partial\nu/\partial a_{rt}$ from (3.19) and (3.15) we obtain:

$$\alpha_{eff} = 2\pi\tau_{rt}\frac{\Delta\nu}{\Delta\gamma} = \frac{1}{\alpha_g^{-1} - \alpha_a^{-1}}. \tag{3.20}$$

The interaction between α_a and α_g will also affect the laser response to frequency perturbations. Assume that the laser is perturbed so that the frequency would change by $\Delta\nu_0$ for $\alpha_g = 0$ (for instance due to a perturbation of the cold cavity resonance frequency, or to spontaneous emission). The frequency change when the effect of α_g is taken into account is denoted $\Delta\nu$. Again assuming $g_{rt} - a_{rt} = 0$ we have:

$$(\Delta\nu - \Delta\nu_0)\left\{\frac{\partial\nu}{\partial g_{rt}}\right\}^{-1} - \Delta\nu\left\{\frac{\partial\nu}{\partial a_{rt}}\right\}^{-1} = 0.$$

implying:

$$\frac{\Delta\nu}{\Delta\nu_0} = \frac{\alpha_g^{-1}}{\alpha_g^{-1} - \alpha_a^{-1}} = \frac{\alpha_{eff}}{\alpha_g}. \tag{3.21}$$

The initial frequency perturbation $\Delta\nu_0$ is magnified by the ratio α_{eff}/α_g.

We see from (3.20) and (3.21) that α_a must be smaller than or comparable to α_g in magnitude in order to affect the laser noise significantly. From Fig. 3.2 (c) we see that this will not be the case for the ideal fiber DFB laser if it operates in the fundamental mode and within the grating stop band limits $|\delta\nu| < 7$ GHz. The figure indicates, however, that α_a may be of importance for lasers operating in higher order modes.

External reflections will cause ripple in the curves in Fig. 3.2 (a) and (b), and they will therefore contribute to α_a. If the external amplitude reflectivity is r_e with a delay τ_e that satisfies $\tau_{rt} \ll \tau_e < \tau_{coh}$, the frequency dependence of the roundtrip loss and phase can be approximated by:

$$\begin{aligned} \Delta a_{rt} &\simeq Mr_e \cos 2\pi\nu\tau_e \\ \Delta\phi_{rt} &\simeq 2\pi\Delta\nu\tau_{rt} + Mr_e \sin 2\pi\nu\tau_e. \end{aligned} \tag{3.22}$$

Here M is the mirror transmissivity to the laser port that is connected to the external cavity. α_a follows from (3.19) and (3.22) as:

$$\alpha_a = -\frac{1 + Mr_e\tau_e/\tau_{rt}\cos 2\pi\nu\tau_e}{Mr_e\tau_e/\tau_{rt}\sin 2\pi\nu\tau_e} \quad \text{(External reflection).} \tag{3.23}$$

For reflections satisfying $Mr_e\tau_e/\tau_{rt} \ll 1$ we have that $|\alpha_a^{-1}| \ll 1$ for all optical frequencies ν, implying that the back reflection is not of significance for the value of α_{eff}.

From (3.20) we see that $\alpha_{eff} \to \infty$ if $\alpha_a^{-1} \to \alpha_g^{-1}$. The maxima in $|\alpha_a^{-1}|$ with respect to ν occurs for $\cos 2\pi\nu\tau_e = -Mr_e\tau_e/\tau_{rt}$. The condition $\alpha_a^{-1} = \alpha_g^{-1}$ will occur at every second of these minima if:

$$Mr_e\tau_e/\tau_{rt} = \left(1 + \alpha_g^2\right)^{-1/2} \quad \text{(critical external reflection).} \tag{3.24}$$

At this and higher back-reflection levels $\alpha_{eff}(\nu)$ will go through singularities for certain values of ν, corresponding to mode-hopping between external cavity modes. Equation (3.24) is consistent with the external mode-hopping criterion $C \geq 1$ used in Chap. 5. The effect of external back reflections on the stability and the effective linewidth enhancement factor of semiconductor lasers is reviewed by Petermann in [15].

3.2.5 Schawlow-Townes Noise Limit

In Sec. 3.2.2 we mentioned that the spontaneous emission seeding of the laser operation causes a direct contribution to ϕ_{rms} with magnitude $M^{1/2}e_{sp}/(\pi\tau_{rt}f|A|)$. It can be shown that this magnitude must be multiplied by $(1+\alpha_{eff}^2)^{1/2}$ to incorporate the phase noise from the spontaneous emission induced fluctuations in Δg_{rt} at $f \ll f_r$. Using $\nu_{rms} = f\phi_{rms}$ we obtain the frequency noise due to spontaneous emission seeding of the laser operation as:

$$\nu_{rms} = \sqrt{1+\alpha_{eff}^2}\frac{e_{sp}\sqrt{M}}{\pi\tau_{rt}|A|} \quad (f \ll f_r, \text{ spontaneous emission}). \tag{3.25}$$

From (3.5) and (3.25) we obtain

$$\Delta\nu_{3dB} = \left(1+\alpha_{eff}^2\right)\frac{e_{sp}^2 M}{\pi\tau_{rt}^2 P_o} \quad (f \ll f_r, \text{ spontaneous emission}), \tag{3.26}$$

where $P_o = |A|^2$ is the laser output power.

The lowest possible value for e_{sp}^2 equals $2h\nu\, a_{rt}$, and is obtainable if the gain medium has the lowest possible doping concentration that will allow for threshold gain at full inversion. By inserting $e_{sp}^2 \geqslant 2h\nu\, a_{rt}$ into 3.26 we obtain:

$$\Delta\nu_{3dB} \geqslant \left(1+\alpha_{eff}^2\right)\frac{2h\nu\, a_{rt}\, M}{\pi\tau_{rt}^2 P_o} \qquad \text{(spontaneous emission)} \qquad (3.27)$$

(3.27) is known as the Schawlow-Townes noise limit (originally derived for $\alpha_{eff} = 0$), after A. L. Schawlow and C. H. Townes who were central in the early work on laser science from the late 1950's and onwards.

Typical fiber DFB lasers have values for the ratio $a_{rt}M/\tau_{rt}^2$ that are many orders of magnitude smaller than what is usually obtainable with semiconductor laser. This implies that smaller linewidths are obtainable with fiber DFB lasers. External cavity lasers, ring lasers, Fabry-Perot fiber lasers, or large bulk lasers may have much higher effective values for τ_{rt}, but the task of maintaining stable single longitudinal mode operation generally becomes more difficult as τ_{rt} increases. Frequency modulation noise densities which are believed to be dominated by spontaneous emission noise above $f \approx 3$ kHz have been reported for distributed back reflection (DBR) fiber Bragg grating lasers with relatively high cavity losses ($a_{rt}, M \sim 0.05$) [16].

With parameter values obtainable for fiber DFB lasers of $a_{rt} = M = 10^{-5}$, $\tau_{rt} = 50$ ps, $P_o = 250$ μW, $\alpha_{eff} = 3$, and $\nu = 194$ THz ($\lambda_s = 1550$ nm) we obtain $\Delta\nu_{3dB} \geqslant 0.13$ mHz. From slope efficiency considerations, and to allow for 1480-nm intraband pumping which allows for a maximum of about 75 % inversion, doping concentrations that are considerably higher than the theoretical requirement at full inversion may be desirable. In practical fiber DFB lasers, e_{sp}^2 may therefore be from 10 to 1000 times larger than the theoretical minimum of $2h\nu\, a_{rt}$ assumed in (3.27). The spontaneous emission induced frequency noise (3.26) of typical fiber DFB lasers is still believed to be well below other noise contributions, such as the fundamental thermal noise in the fiber index discussed in Subsec. 3.3.

3.2.6 Shot Noise

The shot noise, which is due to the quantization of the light into photons with energy $h\nu$, puts a lower limit to the detected RIN given by:

$$RIN = \sqrt{\frac{2h\nu}{P_o}} \qquad \text{(Shot noise).} \qquad (3.28)$$

A common method for optical frequency interrogation is by use of Mach-Zehnder or Michelson interferometers. When operated in quadrature with balanced detection, such interferometers can achieve a noise equivalent frequency shift $NE\nu$ due to the shot noise at the detectors of:

$$NE\nu = \frac{RIN \times f}{2\,|\sin(\pi\tau_i f)|} = \sqrt{\frac{h\nu}{2P_o}}\frac{f}{|\sin(\pi\tau_i f)|}\,, \qquad \text{(Interferometer shot noise)} \tag{3.29}$$

where τ_i is the interferometer delay and RIN is expressed by (3.28). For low frequencies $f \ll \tau_i^{-1}$ we have $NE\nu = RIN/(2\pi\tau_i)$. Thus, an interferometer with $\tau_i = 0.5$ μs (about 100 m single pass optical delay fiber) and a detected power of P_o of 1 μW will have a low-frequency $NE\nu$ of 160 mHz/$\sqrt{\text{Hz}}$.

$NE\nu$ according to (3.29) can be minimized for a given frequency f by choosing an interferometer delay τ_i that is an odd multiple of $(2f)^{-1}$. This produces an expression for what we believe is the fundamental shot noise limit of the optical frequency detection:[6]

$$NE\nu = \sqrt{\frac{h\nu}{2P_o}}f \qquad \text{(Shot noise)} \tag{3.30}$$

Note that $NE\nu$ according to (3.30) is proportional to f. It can be shown that the $NE\nu$ predicted by (3.30) can be obtained simultaneously for all frequencies f by heterodyne detection systems employing electrical beat-frequency interrogation of the optical detector output.

If an optical amplifier is used to increase the input power to the interrogation system, the lower limit for $NE\nu$ increases by at least 3 dB (depending on the amplifier noise figure) compared to the level predicted by (3.30), due to mixing with the amplified spontaneous emission.

3.3 Temperature Fluctuations

An important source of laser frequency noise is refractive-index fluctuations in the cavity due to temperature fluctuations. The resonance frequency of fiber lasers at 1550 nm has a temperature sensitivity of about −1 GHz/K (8 pm/K) [4], as verified in Chap. 8. There are three main sources of temperature fluctuations in the cavity: Ambient temperature fluctuations, self heating, and fundamental temperature noise due to random diffusion of thermal energy across the mode field boundary. Self heating will be treated in Sec. 3.5.

3.3.1 Ambient Temperature

The response of the laser to ambient temperature fluctuations is expected to decrease rapidly at frequencies above $\sim$ 1 kHz if the bare fiber is only in contact

---

[6] An alternative way of arriving at (3.30) is by assuming that the rms contributions from quantization to the relative amplitude $RIN/2$ and phase ϕ_{rms} noise signals are equal. Inserting (3.28) into $NE\nu = \phi_{rms}f$ $= 2RINf$ produces the result in (3.30).

with air. This is due to the limited thermal conductivity through the air-fiber interface and from the fiber surface to the core, as illustrated by Fig. 1 in [17]. If the fiber is surrounded by a material with higher thermal diffusivity than air the low-pass cut-off frequency of the response into the fiber may increase somewhat. On the other hand, a good heat sink will often act as an effective thermal low-pass filter on its own.

3.3.2 Fundamental Thermal Noise

If temperature is defined as the *expectation value* $\langle T\rangle = \langle E_{th}/C\rangle$ of the stored thermal energy E_{th} per unit heat capacity C, then the temperature of an object in thermal equilibrium with its surroundings must be independent of time. The effective refractive index of the fiber is, however, determined by the *instantaneous* temperature $T = E_{th}/C$ averaged over the mode power area $\pi MFD^2/8$ of the fiber. MFD is the mode-field diameter where the mode power density has dropped to e^{-2} of its maximum. Even for a fiber in perfect thermal equilibrium with its surroundings, there exists a thermal noise floor for the variance of the instant temperature fluctuation $\Delta T = T - \langle T\rangle$. This noise is caused by random diffusion of thermal energy in and out of the mode power area. Kingston [18] shows that this variance integrated over all frequencies f is given by:

$$\int_0^\infty \Delta T^2(f)df = \frac{k_b T^2}{C}\,, \qquad (3.31)$$

where $k_b = 13.81 \times 10^{-24}$ J/K is Boltzmanns constant. For our case of a fiber laser, C is the heat capacity of the effective mode power volume, given by:

$$C = \frac{L_c \pi MFD^2}{8} C_V\,, \qquad (3.32)$$

where $C_V = 1.67 \times 10^6$ J/(m^{3}K) is the specific heat capacity of silica.

The spectral power distribution $\Delta T^2(f)$ of this noise can be found by modelling the fiber as a collection of small heat capacities that are connected to their neighboring elements through thermal conductors. In analogy with the theory for thermal noise in electrical conductors, the random diffusion of heat can be represented as a heat (or "current") source Q_i in parallel with each conductor G_i with a white noise power spectral density $\langle Q_i\rangle = 4k_b T^2 G_i$. Due to the circular symmetry of the fiber, heat conduction and generation in the azimuthal direction will not contribute to ΔT. Heat conduction and generation in the longitudinal direction can also be neglected for $f \gg D/L_c^2$ where D is the effective thermal diffusivity of the combined fiber and surrounding materials. For a fiber with an infinite silica cladding, D/L_c^2 will be in the order of 3 – 40 mHz for typical fiber DFB laser cavity lengths. A numerical investigation into the shape of $\Delta T^2(f)$ and how it depends on fiber diameters, coating parameters, and heat sinking materials should be possible with typical available computer resources.

$\Delta T^2(f)$ is hard to compute analytically for the fiber geometry. An expression for the case of insulating border conditions at the fiber surface has been published by K. H. Wanser in [19]. The laser frequency noise magnitude derived from his formula may be expressed as

$$\nu_{rms}^2 = \left(\frac{\delta n}{n \delta T} + \frac{\delta \varepsilon}{\delta T} \right)^2 \nu_0^2 \, \Delta T^2(f) \ , \tag{3.33}$$

where

$$\Delta T^2(f) = \frac{k_b T^2}{2\pi k_c L_c} \times \ln \left\{ \frac{\left[\left(\frac{2}{\pi MFD} \right)^2 + \left(\frac{f}{c/n} \right)^2 \right]^2 + \left(\frac{f}{2\pi D} \right)^2}{\left[\left(\frac{2.405}{\pi d} \right)^2 + \left(\frac{f}{c/n} \right)^2 \right]^2 + \left(\frac{f}{2\pi D} \right)^2} \right\} . \tag{3.34}$$

Here, D the thermal diffusivity and $k_c = C_V D$ is the thermal conductivity of silica. $\delta\varepsilon/\delta T$ is the thermal expansion coefficient (ε = strain),[7] $n \approx 1.465$ is the refractive index, $c = 3 \times 10^8$ m/s is the speed of light in vacuum, d is the fiber diameter, and MFD is the modefield diameter. Typically, $d = 125\,\mu$m or $80\,\mu$m, while $MFD \approx 9.4$ μm for standard fiber, and 5.8 μm for high NA Er-doped fiber.

The derivation of (3.34) has not been published. Wanser takes thermal and optical material parameters for silica fiber from [20]: $k_c \approx 1.37$ W/(m K); $D \approx 0.82 \times 10^{-6}$ m^2/s; $(\delta n/(n\delta T) \approx 9.2 \times 10^{-6}$ K^{-1}; and $\delta\varepsilon/\delta T = 0.4 \times 10^{-6}$ K^{-1}. However, the temperature sensitivity of silica fibers generally accepted elsewhere in literature (and also verified in Chap. 8) $(\delta n/(n\delta T) + \delta\varepsilon/\delta T) \approx 5.2 \times 10^{-6}$ K^{-1} [4, 17] is only about one half of the value used in [19, 20]. Experimental results reported for the frequency range $f \sim 1 - 100$ kHz have been compared in [5, 21, 22, 23] with Wansers formula, using the material parameters as in [19, 20]. These experiments show noise floors which are similar in shape, and 1 – 3 dB *above* the theoretical predictions.

Numerical calculation of the integral on the left-hand side of eq. (3.31) with $\Delta T^2(f)$ inserted from (3.34) produces a result that is a factor of two smaller

---

[7] It can be argued that the fiber expansion will not be proportional to only the core temperature fluctuations ΔT for frequencies well above 1 kHz, because the temperature will not be correlated across the whole fiber cross-section at these frequencies. Consequently, we believe that the term $\delta\varepsilon/\delta T$ should be omitted from (3.33) at higher frequencies.

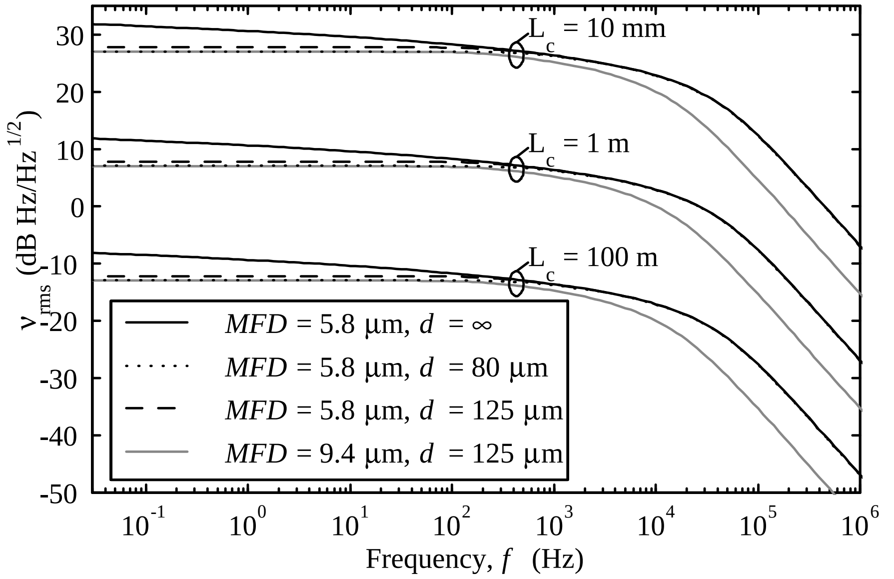

Figure 3.3. Fundamental thermal noise of the resonance frequency of fiber-optic cavities with length $L_c = 0.01$, 1 and 100 m, according to (3.33, 3.34) with 6 dB added for conformity with reported experiments.

than the right-hand side of eq. (3.31). This result is independent on the choice of material parameters. Since the shape of $\Delta T^2(f)$ predicted by (3.34) has been verified experimentally for $f > 1$ kHz, we believe that the discrepancy with (3.31) must either be due to a scaling error, or to an error in the frequency dependence of (3.34) (the logarithmic term) for $f < 1$ kHz.

In lack of better expressions, we will use (3.33, 3.34) in the following to illustrate the expected thermal frequency noise floor, using $(\delta n/(n\delta T)+\delta\varepsilon/\delta T) \approx 5.2 \times 10^{-6}$ K^{-1} and with 6 dB added for conformity with the previously reported experiments. Fig. 3.3 shows this noise floor for various values of L_c, d, and MFD. For $f > 100$ Hz the noise decreases by 20 dB/decade, while a strong dependence on MFD is observed at high frequencies, approaching $\nu_{rms} \propto (MFD)^{-2}$ for $f > 100$ kHz. This dependence on MFD is in agreement with (3.31, 3.32). For $f < 100$ Hz ν_{rms} increases with increasing fiber diameter. The results below 1 kHz should be used with care, however, since experimental evidence are not available for this regime.

According to [20], noise contributions due to direct interaction with thermal phonons will dominate over the temperature noise for $f \gtrsim 1$ MHz, increasing by 20 dB/decade towards a maximum around 500 MHz. The phonon contributions are not included in Fig. 3.3.

3.4 Acoustical Noise

The sensitivity of the laser to acoustical noise depends much on how it is mounted. If the laser is fixed in each end and strained, it will be sensitive to mechanical vibrations in the distance between the fixing points. The strain sensitivity of the laser is about 150 Hz/pε. If the laser is mounted with some slack, the problems with strain sensitivity should be reduced. However, high frequency vibrations in the supporting structure may still couple to compressional and flexural waves in the laser fiber. The sensitivity of a fiber with slack to mechanical perturbations has not yet to our knowledge been studied in the literature.

The sensitivity of the laser to pressure waves may also play a role. If the laser is submerged into a liquid, like water or oil, the sensitivity is expected to be $\sim$ 870 Hz/Pa if the fiber is axially constrained, and ~ -520 Hz/Pa if the fiber is free to expand [21]. At low frequencies (typically $f < 50$ kHz), the free expansion sensitivity should be used if the fiber is mounted with slack. At higher frequencies the treatment becomes more complex, as the acoustical wavelength for compression waves in the fiber becomes comparable to the fiber length.

The sensitivity of the fiber DFB laser to acoustical vibrations in air has been studied both theoretically and experimentally in [17], and was found to range from about 600 kHz/Pa at $f = 100$ Hz to about 2 kHz/Pa at $f = 7$ kHz. This implies that an acoustical noise amplitude of 20 dBA (200 μPa) at $f = 100$ Hz will cause a laser frequency noise amplitude of $\nu_{rms} = 120$ Hz. The acoustical sensitivity at low frequencies is dominated by adiabatic temperature changes induced by the acoustic compression of the air. The high sensitivity to acoustical noise at low frequencies can therefore easily be avoided by immersing the fiber into a liquid, which will not compress and heat significantly in response to acoustic waves.

3.5 Pump Fluctuations

In Sec. 3.2.3 it was shown that fluctuations in the relative pump intensity RI_p will cause laser RIN through the transfer function $T_p(f)$ (3.11). If saturable absorbers are present, the pump will also modulate the saturable absorber losses at the laser wavelength, causing additional RIN contributions through $T_{loss}(f)$. The pump induced RIN will lead to frequency noise according to the frequency to intensity noise ratio r_{th} (3.17) at low frequencies $f \ll f_r$ and according to the linewidth enhancement factor α_g (3.16) at $f \approx f_r$.

Fig 3.4 shows a typical measured response of the optical frequency shift $\Delta\nu$ and the relative laser intensity RI to modulation of RI_p for a fiber DFB laser.

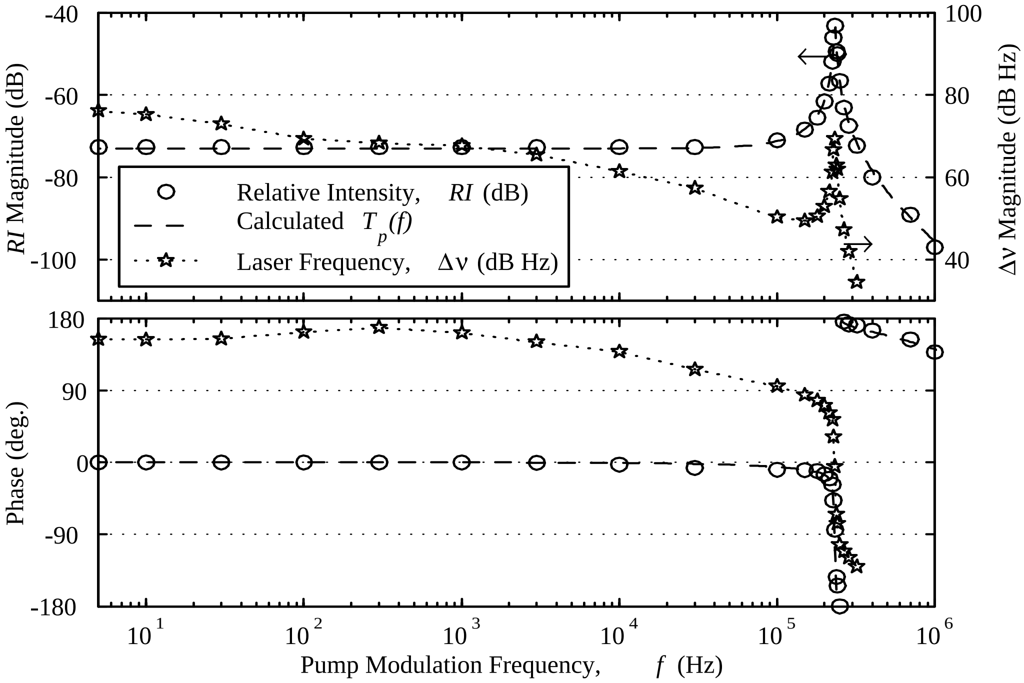

Figure 3.4. Response of the relative intensity RI and optical frequency $\Delta\nu$ of an Er-doped fiber DFB laser to pump modulation. The1480-nm pump power was modulated around its mean value of 60 mW with an rms amplitude of ~ 2.5 μW.

The pump power to the laser was modulated with an amplitude of about 2.5 μW rms by modulating the drive current to the pump diode, corresponding to a relative pump intensity modulation of $RI_p = -73.7$ dB.

The investigated laser was a sealed Er-doped fiber DFB laser (Ionas IFL01W1E-AD) operating at 1558 nm. The fiber laser was pumped with 60 mW at 1480 nm from a laser diode through a 1480/1550 nm wavelength division multiplexer (WDM). The output from the laser was about 170 μW copropagating with the pump, with a slope efficiency of ~ 3.3 μW/mW. The composition of the fiber laser heat sink is not known. The output from the 1550 nm branch of the WDM was passed through an isolator and split by a 10:90 fiber coupler.

The 90 % output from the 10:90 coupler was passed to a detector for monitoring of the RI. The 10 % output was passed to a Michelson interferometer with a dual pass path imbalance of 69 m ($\tau_i = 337$ ns). Balanced detection by subtracting the detected output power from one interferometer port from the output from the other port was used in order to minimize the sensitivity of the readout to laser RIN. In order to keep the interferometer in quadrature, the error signal generated at the balanced receiver output was fed back to a PZT optical phase modulator in one of the interferometer arms via a time-domain integrator filter. By adding the high-frequency ($f \gtrsim 1.5$ kHz) error signal to the low-frequency PZT signal (using proper scale factors), $\Delta\nu$ could be monitored from DC and up to $f > 1$ MHz. The plotted responses are calibrated to remove effects of the frequency responses of pump driver and detector electronics, as well as interferometer responses and fiber transmission delays.

The dashed line in Fig. 3.4 shows the pump response $T_p(f)$ calculated from (3.11, 3.13) with the parameters $k_{slope} = 1.18$, $f_r = 238$ kHz, $f_{sat} = 52$ kHz, $k_{s.abs} = 1.4 \times 10^{-5}$, and $\tau_{rt} = 1 \times 10^{-10}$ s ($\Leftrightarrow L_c = 10$ mm). Good fits to the measured RI magnitude can also be obtained with other combinations of f_{sat} and $k_{s.abs}$. The fit to the phase of the RI response for $f > f_r$ does, however, indicate that the chosen values f_{sat} and $k_{s.abs}$ are reasonable.

As mentioned in the introduction to this section, any modulation of the saturable absorber losses by the pump power modulation is expected to give a contribution to the pump modulation response that is proportional to $T_{loss}(f)$. From Fig. 3.1 (b) we see that the shape of the $T_{loss}(f)$ differs significantly from that of $T_p(f)$ at frequencies $f > f_{sat}$. It is therefore not possible to obtain a good fit to the measurements in Fig. 3.4 with our model if pump induced loss modulation is assumed to play a significant role.

Fig. 3.5 shows an expanded view of the relaxation oscillation peak. The relaxation oscillation resonance Q-factor is found from the measurements to be $Q_r = 31$, which is relatively high. Typical values measured for other lasers range from $Q_r = 10$ and upwards.

The shot noise induced RIN for our laser according to (3.28) is -148 dB Hz$^{-1/2}$. To avoid that pump-induced RIN dominates over shot-noise we then find from Figs. 3.4 and 3.5 that the requirements are $RIN_p < -148.7$ dB Hz$^{-1/2}$ at low frequencies $f \ll f_r$, and $RIN_p < -179$ dB Hz$^{-1/2}$ at $f = f_r$. To operate below the thermal noise floor for ν_{rms} predicted by (3.33) with $L_c = 10$ mm, the requirements become $RIN_p < -115$ dB Hz$^{-1/2}$ at $f = 100$ Hz and $RIN_p < -137$ dB Hz$^{-1/2}$ at $f = f_r$.

The shot-noise limitation of the effective RIN_p experienced by the fiber laser comes from the quantization of the absorbed pump energy. The shot noise statistics of this absorption gives an effective noise magnitude [in analogy with (3.28)] of $RIN_p = (2h\nu_p/P_{p,abs})^{1/2}$, where $h\nu_p$ is the pump photon energy and $P_{p,abs}$ is the pump power absorbed within the laser cavity by active gain ions. A simple estimate for the pump absorption would be $P_{p,abs} = 1550/1480 \times 2P_o$ $= 356$ μW, ignoring intracavity losses and assuming equal outputs from the two laser ends. The effective pump shot noise limitation then becomes $RIN_p =$ -151 dB Hz$^{-1/2}$. This is 28 dB below the requirement for shot-noise limited RIN at $f = f_r$ stated in the last paragraph. Consequently, stabilization the pump laser intensity is not sufficient to avoid that the RIN raises at least 28 dB above the shot noise limit at $f = f_r$.

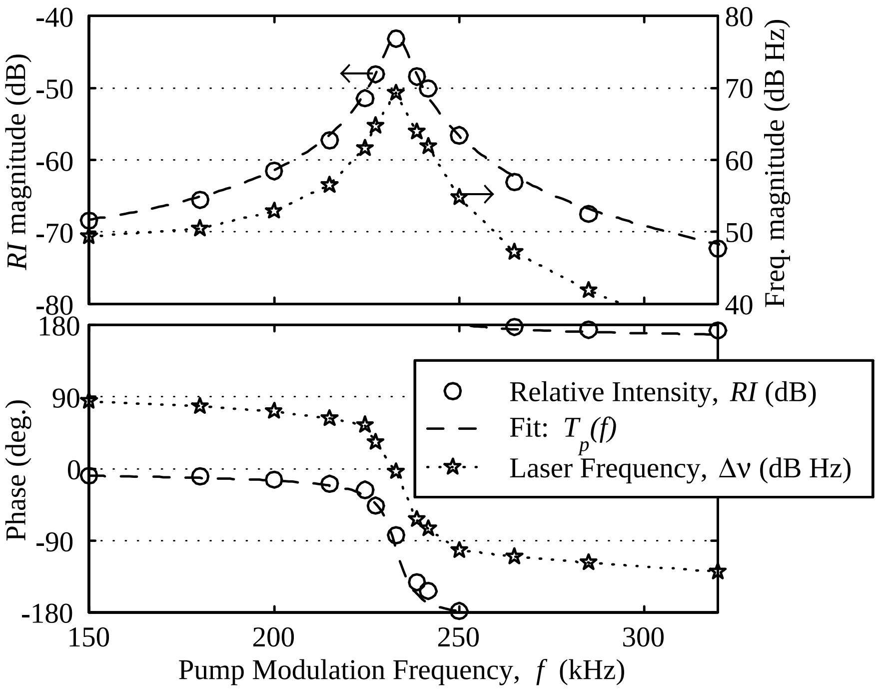

Figure 3.5. Expanded view of the relaxation oscillation peak in Fig. 3.4.

Fig. 3.6 shows the ratio $\Delta\nu/RI$ of the pump modulation responses. Circles illustrate the ratio between the measurements in Fig. 3.4. Black lines show measurements recorded with a low-frequency network analyzer.

As explained in Sec. 3.2.4, we expect the modulation P_{th} of the thermal power dissipated in the core of the laser fiber to be proportional to the pump induced RI at low frequencies $f \ll f_r$. The thermal response to step changes in the self heating of erbium-doped amplifier fibers have earlier been calculated numerically in [24]. However, it is hard to deduce frequency responses over a broad frequency range from those results. We have calculated numerically the expected frequency response $\Delta\nu_{th}$ to a modulation of P_{th}. The impulse response to heating was calculated in the time domain by a finite element method. The calculated impulse response were Fourier-transformed to produce the frequency response. Parameters used in the calculations were: core diameter $d_{core} = 5.4$ μm; mode field diameter $MFD = 5.8$ μm (Gaussian distribution); fiber diameter $d = 80$ μm; thermal conductivity $k_c = 1.37$ W/(m K); diffusivity $D = 0.82 \times 10^{-6}$ m^2/s; and fiber thermooptic coefficient $\delta n/(n\delta T) = 5.2 \times 10^{-6}$ K^{-1}. We believe that these parameters are representative for the investigated fiber.

The gray lines in Fig. 3.6 shows the calculated thermooptic frequency shift $r_{th} = \Delta\nu_{th}/RI$ fitted to the measurements by assuming a power dissipation

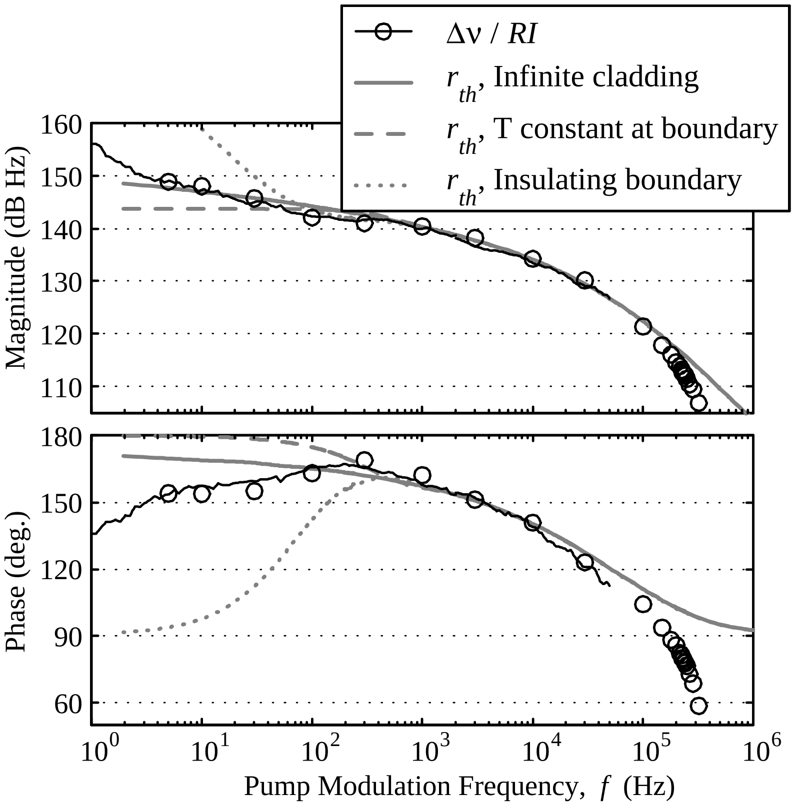

Figure 3.6. Black lines and circles: Ratio between the pump modulation responses $\Delta\nu$ and RI of the laser characterized in Fig. 3.4. Gray lines: Frequency response ν_{th} to 230 μW rms modulation of the heat absorbed in the core of a $L_c = 10$ mm long cavity, calculated for the fiber boundary conditions indicated in the legend text.

modulation amplitude of $RI \times 23$ mW/m. For a $L_c = 10$ mm laser cavity this corresponds to a dissipated power of $P_{th} = RI \times 230$ μW. If we assume that the thermal power dissipation is linear with intensity (as is verified for the fiber DFB laser investigated in Chap. 8), we may conclude that the DC thermal power dissipation in the laser cavity is close to 230 μW. The high value of the estimated P_{th} compared to the measured output power $P_o = 170$ μW indicates that power dissipation from the pumping process with ion relaxations to the upper laser level cannot be the dominating heating source. Remaining candidates are nonradiative absorption at the pump or laser wavelengths, due to some combination of saturable and non-saturable absorbers.

Three different simulated boundary conditions are illustrated in the figure, as indicated in the legend. The infinite cladding condition corresponds to immersing the laser into a medium with the same thermal properties (k_c and D) as silica. For the frequencies illustrated, the condition of constant temperature

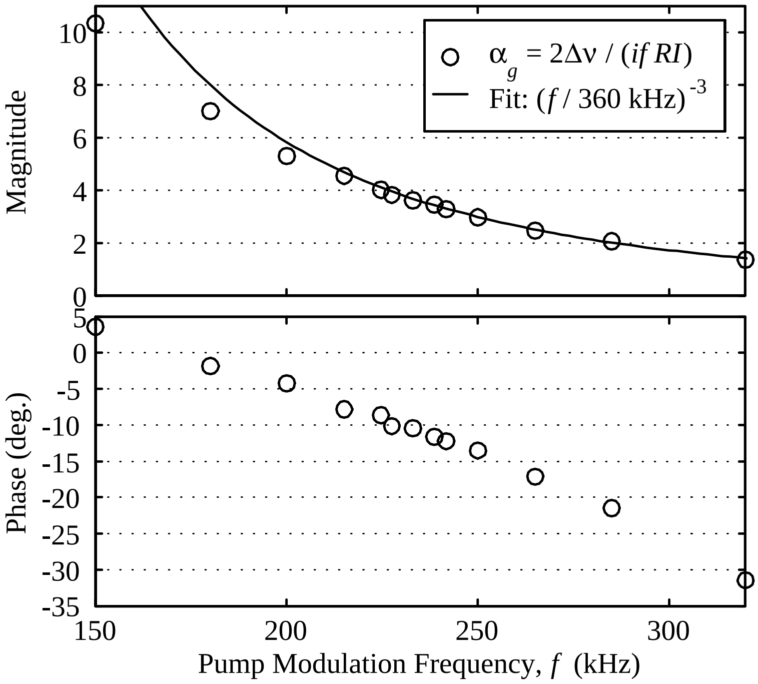

Figure 3.7. Circles: α_g according to (3.16) calculated from pump modulation measurements near the relaxation oscillation frequency $f_r = 238$ kHz. Line: Fit to a f^{-3}-dependence.

on the fiber surface should be a good approximation for a case where a good heat-sink (like aluminum) with high values for k_c and D is in contact with the fiber. The insulating boundary condition should approximate the effect of placing the fiber in a bad heat-sink such as air or a thick polymer coating. We see from the calculations that the boundary conditions become important for $f \lesssim 400$ Hz. The deviation between the measured response r_{th} and the calculated curves for $f < 400$ Hz in Fig. 3.6 are attributed to the thermal properties of the materials surrounding the fiber, which are not known. For 400 Hz $< f <$ 100 kHz, the agreement between measurements and calculations are reasonably good.

We see from Fig. 3.4 that the relaxation oscillation resonance starts to dominate the RI magnitude for $f > 100$ kHz. Fig. 3.7 shows the linewidth enhancement factor α_g near $f = f_r$ calculated according to (3.16) from the measured pump modulation responses in Fig. 3.4. The magnitude of $\alpha_g(f)$ fits well to an f^{-3} dependence in the frequency range $f = 200 - 320$ kHz, taking the value 3.5 at $f = f_r$. At lower frequencies a f^{-2} dependence is approached. The phase is about $-10°$ at $f = f_r$, decreasing with a slope of $-0.33°$/kHz. The observed frequency dependence of α_g cannot be described by a simple minimum-phase model, and we are not able to determine which mechanisms (spectral hole-burning through the Kramer-Kronig relations, different thermal mechanisms) that dominate.

Fluctuations in the pump center wavelength will also lead to fluctuations in the pumping efficiency, due to the wavelength dependence of the pump absorption cross section. We believe that pump wavelength fluctuations can be modelled as an equivalent RIN_p. The spectral dependence of the pump absorption is especially pronounced near 975 nm in Er:Yb-fibers [25]. However, due to the relatively slow energy transfer from the pump absorption state of Yb to Er, having a single-pole low-pass frequency around $\sim$ 1 kHz [3], the sensitivity to fluctuations in the pump center wavelength is still expected to be moderate. With 1480-nm pumping the response of the gain medium is much faster, as demonstrated by Fig. 3.4. However, the wavelength dependence of the pump absorption is significantly lower than around 975 nm. Until recently, available fiber pig-tailed diode pump lasers have been multi-moded both around 975 and 1480 nm, with mode spacings typically in the 100 to 500 GHz range. Fluctuations in the relative intensity distribution between the modes of these lasers may be a significant source of fiber laser noise. 975-nm pump lasers that are stabilized by external fiber grating reflectors are now commercially available and widely used for low-noise fiber amplifiers. Grating-stabilized 1480-nm pump lasers (intended for wavelength multiplexing of multiple lasers to obtain high pump powers) have recently been advertized as new products on the market.

In single polarization fiber lasers, fluctuations in the pump polarization state will introduce noise through the polarization anisotropies of the individual gain ions. In Chap. 7 the magnitude of the pump polarization hole-burning effect is described by the parameter η_p. It follows from the theory in the appendix to Chap. 7 that changes of the pump polarization state launched into a single polarization laser from being orthogonal to parallel to the laser polarization is equivalent to a change in the pump power by the factor $1 + \eta_p$. For the dual polarization Er-Yb doped 1480-nm pumped fiber DFB lasers investigated in Chap. 7 we estimate $\eta_p = 0.021$.

If the fiber laser is used as a sensor element with remote pumping and interrogation through a long lead fiber, the changes in pump polarization state may potentially become quite rapid (Hz to kHz range), due to poor isolation against temperature changes and mechanical vibrations. A way of eliminating noise from pump polarization fluctuations would be by depolarizing the pump, for instance with an active polarization scrambler that modulates the pump polarization state at a frequency well above the relaxation oscillation frequency of the fiber laser.

3.6 Noise Measurements

We have characterized the relative intensity and optical frequency noise spectra for the fiber DFB laser that was characterized with respect to pump modulation in Sec. 3.5. The interrogation system used for the noise measurements is identical to the system for monitoring of the RI and $\Delta\nu$ described in Sec. 3.5. Simultaneously recorded traces for the RIN and ν_{rms} are shown as gray curves Fig. 3.8. In Fig. 3.8 we also show the pump intensity noise RIN_p and the electrical noise floor of the interrogation system when no light is incident on the detectors.

A number of sharp noise spikes is observed in the RIN spectrum between $f =$ 9.5 Hz and 640 Hz. This is believed mainly to be due to acoustic pick-up in the $\sim$ 8 m lead fiber from the WDM to the fiber laser, modulating the polarization state of the pump, c.f. Sec. 3.5. Acoustical modulation of the polarization state of the signal reaching the interrogation system will also contributed to noise pick up, because of a small polarization dependence in the interrogation system originating from polarization dependent coupling ratios in the optical couplers used. The spikes in the measured RIN_p at 37, 50 100, and 150 Hz may also have originated from this kind of acoustical pick-up.[8]

Between $f = 10$ Hz and 30 kHz the measured RIN floor is essentially constant at -118 ± 1 dB Hz$^{-1/2}$. Shot noise according to (3.28), taking loss in the transmission from the laser to the detector into account, gives a RIN contribution of only about -145 dB Hz$^{-1/2}$. The dashed line in Fig. 3.8 (a) shows the spectral density $RIN = RIN_p T_p(f)$ expected according to (3.11, 3.13) to arise from a smoothened polynomial fit to the measured RIN_p. The parameters used are: $k_{slope} = 1.18$, $k_{s.abs} = 1.4 \times 10^{-5}$ (taken from the measurements in Sec. 3.5); $\tau_{rt} = 1 \times 10^{-10}$ s ($\Leftrightarrow L_c = 10$ mm, which is a typical number for Ionas lasers); as well as the fitted parameters $f_r = 222$ kHz, and $f_{sat} = 51$ kHz. We see that the pump-induced RIN is $\sim$ 5 dB lower than the measured RIN, indicating that other noise sources are dominating. Remaining candidates are fluctuations in the pump center wavelength λ_p, loss modulation Δa_{rt}, and spontaneous emission e_{sp}.

The dotted line in Fig. 3.8 (a) shows the spectrum $RIN = [RIN_p^2 T_p^2(f) + k_0 T_{loss}^2(f)]^{1/2}$ expected to arise from the measured RIN_p combined with white noise modulation of Δa_{rt} and e_{sp} described by the fitted parameter $k_0 = \Delta a_{rt}^2 + 4Me_{sp}^2/P_o = 8 \times 10^{-20}$. The fit to the RIN measurement is good.

The ratio ν_{rms}/RIN of the measured noise spectral densities in Figs. 3.8 (a) and (b) is illustrated by the black curve in Fig. 3.9. For comparison, The

---

[8] Fans and transformers in the laboratory instruments tend to produce vibrations at frequencies that are multiples of the 50 Hz line frequency.

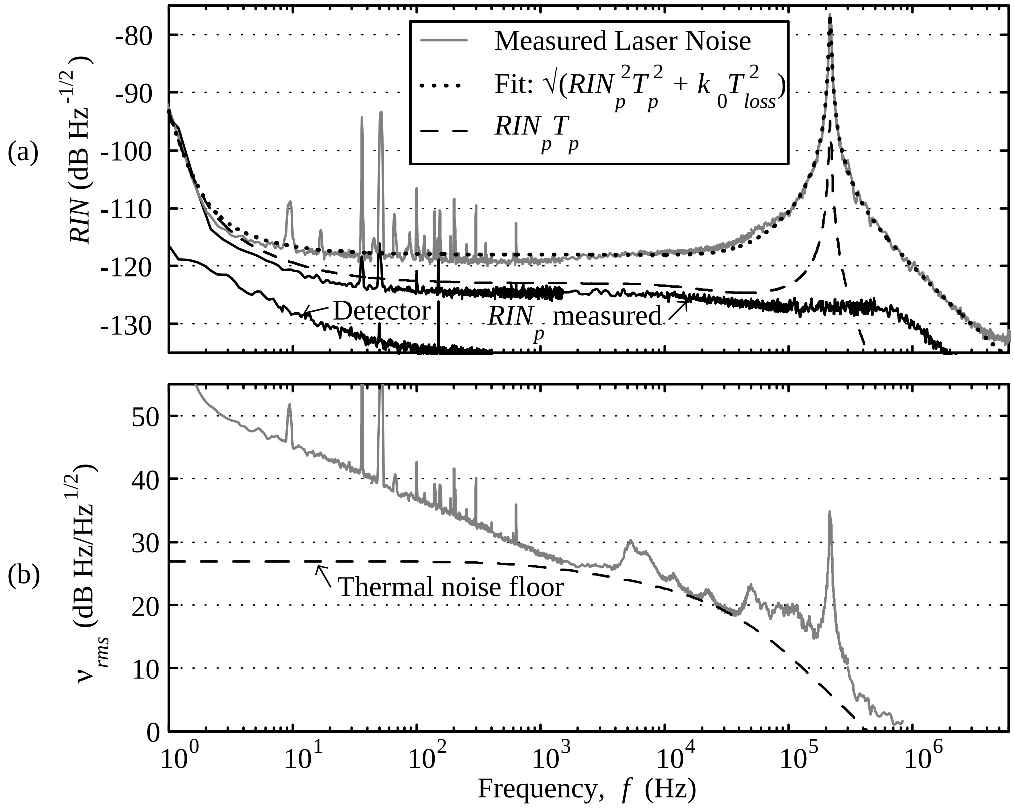

Figure 3.8. Solid gray curves in (a) and (b): fiber DFB laser RIN and ν_{rms} spectra, respectively. Solid black curves in (a): measured RIN_p and noise from detector electronics. Dashed and dotted lines in (a): expected noise from RIN_p only, and from a combination of RIN_p, Δrtl, and e_{sp}. Dashed line in (b): expected thermal noise according to (3.33, 3.34) with 6 dB added for conformity with reported experiments, using $L_c = 10$.

ratio $\Delta\nu/RI$ measured in the pump modulation experiment in Sec. 3.5 is indicated by open circles. The complex quantity $\langle\Delta\nu RI\rangle^*/RIN^2$ is also illustrated. $\langle\Delta\nu RI\rangle^*/RIN^2$ can be interpreted as the transfer function from the RI to the correlated component of $\Delta\nu$. (It may be useful in this context to recall the definitions $\nu_{rms}^2 = \langle\Delta\nu^2\rangle$ and $RIN^2 = \langle RI^2\rangle$.)

For frequencies below 100 kHz the measured $|\langle\Delta\nu RI^*\rangle/RIN^2|$ is typically 15 to 20 dB lower than ν_{rms}/RIN. This difference implies that only a $1-3$ % fraction of the frequency noise power ν_{rms}^2 originates from (is correlated with) the RIN.

If the laser RIN originated only from the effective value of RIN_p (including effects of pump wavelength fluctuations), $|\langle\Delta\nu RI^*\rangle/RIN^2|$ would equal the pump-induced $\Delta\nu/RI$ in Fig. 3.9. However, the measured $|\langle\Delta\nu RI^*\rangle/RIN^2|$ is

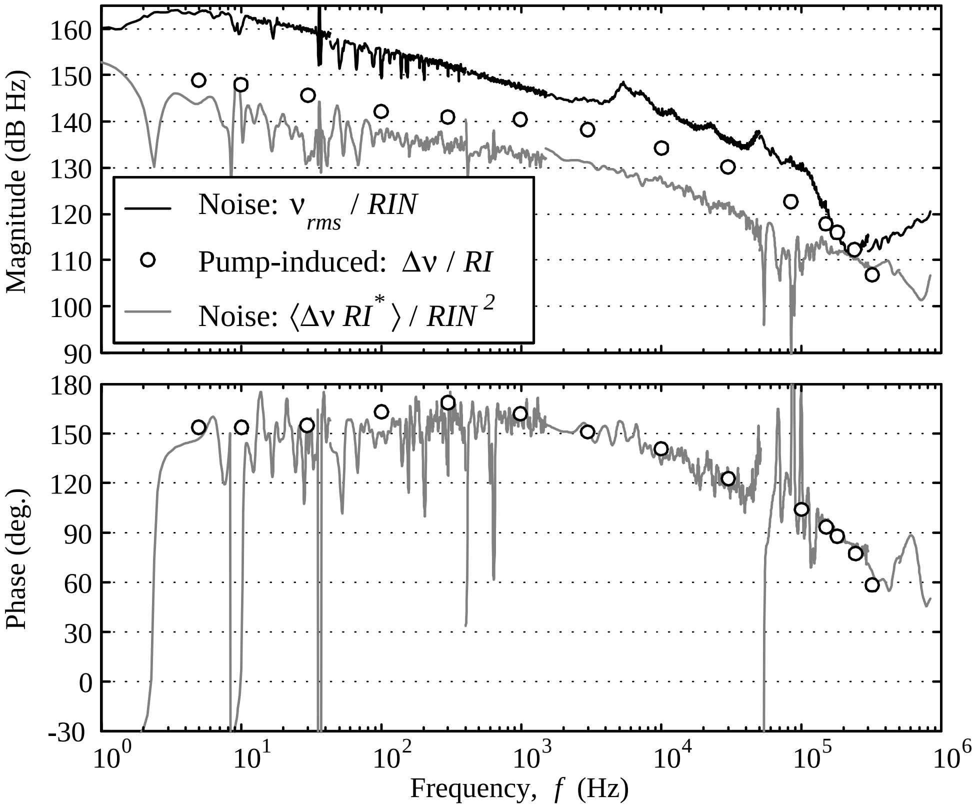

Figure 3.9. Ratio ν_{rms}/RIN from noise measurements; $\Delta\nu/RI$ from pump modulation response measurements; and "transfer function" $|\langle\Delta\nu RI^{*}\rangle/RIN^{2}|$ between the correlated components of RI and $\Delta\nu$ from the noise measurements.

4 to 9 dB lower than the pump-induced $\Delta\nu/RI$ at frequencies $f < 100$ kHz. The difference equals (to within the measurement accuracy) the difference observed in Fig. 3.8 (a) between the measured RIN and the calculated RIN_pT_p. This observation indicates that the difference between the measured RIN and the calculated RIN_pT_p originates from a noise source that produces frequency and intensity noise components with a ratio $\Delta\nu/RI$ that is far below the pump-induced $\Delta\nu/RI$. In other words, r_{th} (3.17) seems to be smaller for noise induced by random cavity loss modulation Δa_{rt} or spontaneous emission e_{sp} than for pump-induced noise. This verifies that pump wavelength fluctuations cannot be the origin of the measured excess RIN above RIN_pT_p in Fig. 3.8 (a). We are left with the candidates Δa_{rt} and e_{sp}.

The spontaneous emission power density from the fiber laser (outside the grating stop-band) was measured at threshold to be 3.5×10^{-21} W/Hz ± 2 dB. The spontaneous emission per unit length of fiber inside the laser cavity is not expected to change significantly above threshold. Assuming a total Er-doped fiber length of $\sim$ 60 mm we can thus estimate the spontaneous emission power launched into the laser mode as $e_{sp}^2 = 2L_c \times (3.5 \times 10^{-21}$ W/Hz$)/(60$ mm$) = 1.2 \times 10^{-21}$ W/Hz ± 2 dB. If the estimated $k_0 = 8.8 \times 10^{-20}$ in Fig. 3.8 originates only from spontaneous emission noise, with no significant contribution from loss modulation ($\Delta a_{rt} \approx 0$), then the estimated e_{sp}^2 corresponds to a laser mirror transmissivity of $M = k_0 P_o/(4e_{sp}^2) \approx -25 \pm 2$ dB. This corresponds to an effective κL of 7.2 ± 0.5, which is fairly low but still possible. If the loss modulation contributes significantly to the RIN, the value of κL may be much higher. A possible source of loss modulation could be random fluctuations in the saturable absorber inversion, for instance due to the shot-noise originating from quantization of the absorbed energy into photons.

The dashed line in Fig. 3.8 (b) shows the thermal noise floor according to Wansers formula (3.33, 3.34), using $L_c = 10$ mm, with 6 dB added (c.f. Sec. 3.3) for conformity with previously reported experiments. We see that the measured ν_{rms} touches down to this floor in several regions between 1 and 50 kHz. The noise peak in ν_{rms} between 4 and 15 kHz is believed to be due to acoustical noise in the lab. The small peak at 48 kHz coincides in frequency with the 1st order resonance of the PZT optical phase modulator in the interferometer. We do not know the explanation for the general increase compared to the predicted thermal noise for $f > 50$ kHz.

For $f < 1$ kHz a $1/f$ component is observed in ν_{rms}, with a slope of -8.6 dB per decade in f. The origin of this noise component is not understood. A similar $1/f$ noise component was observed in the beat frequency noise spectrum of a dual polarization fiber DFB laser characterized in Chap. 7.

A sharp increase in ν_{rms} can be observed near the relaxation oscillation frequency in Fig. 3.8 (b). This noise peak originates from the relaxation oscillation peak in the RIN spectrum, via the linewidth enhancement factor α_g. In Fig. 3.9 we see that the ratio of the rms noise magnitudes ν_{rms}/RIN, the pump-induced ratio $\Delta\nu/RI$, and the noise "transfer function" $|\langle \Delta\nu RI^* \rangle / RIN^2|$ become essentially equal near $f = f_r$. This is as expected from the discussion in Sec. 3.2.4 of α_g near $f = f_r$ according to (3.16).

The total optical power detected from the interferometer was ~ 8 μW, giving a shot noise equivalent frequency shift (3.29) at the investigated frequencies $f < 850$ kHz of $NE\nu \approx -22$ dB Hz$/\sqrt{\text{Hz}}$.

Fig. 3.10 shows a summary of the measured and theoretical frequency noise limits for the fiber DFB laser investigated in this section. The thermal noise curve is identical to that in Fig. 3.8 (b). The spontaneous emission noise is estimated from (3.25), with $e_{sp}^2 = 1.2 \times 10^{-21}$ W/Hz, $\tau_{rt} = 1 \times 10^{-10}$, $P_o = |A|^2 = 170$ μW, $M = -25$ dB ($\kappa L = 7.2$), and $\alpha_g = 3$. The illustrated spontaneous emission noise floor should be regarded only as an indication of

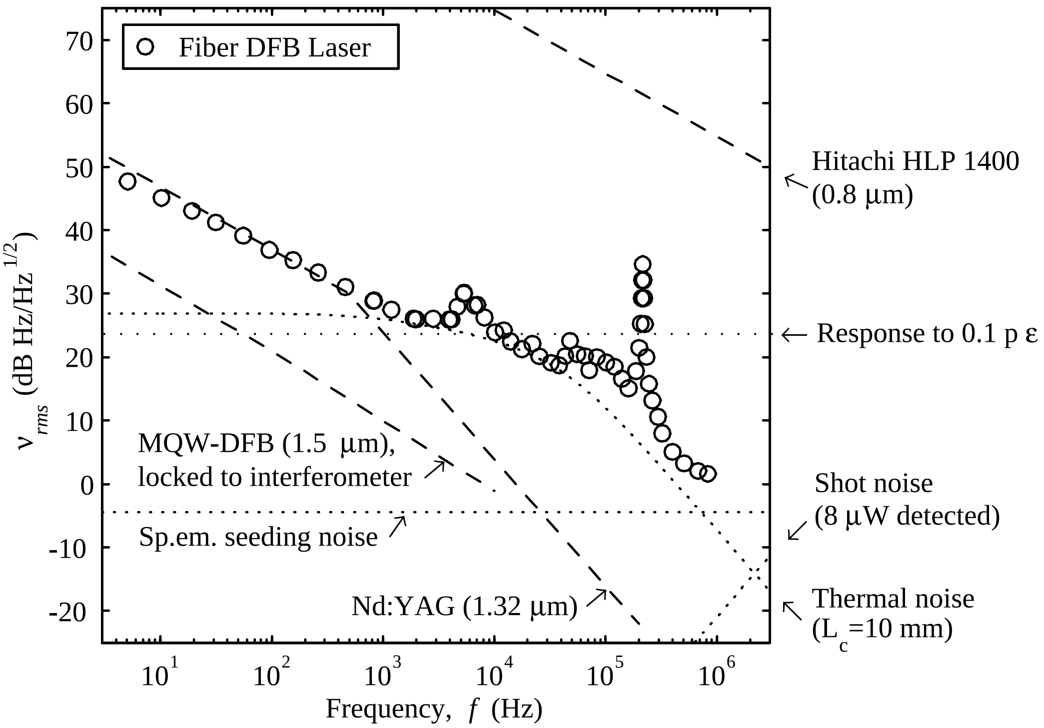

Figure 3.10. Sumary of measured and theoretical limits to ν_{rms}. Dotted lines illustrate the esitimated fundamental shot noise (3.30), thermal noise, and estimated spontaneous emission noise. Dashed lines: Published noise levels of a common 800 nm semiconductor laser, a Nd:Yag ring laser, and a tunable semiconductor MQW laser with active frequency stabilization.

the order of magnitude, since M and α_g are not known for this specific laser. If we assume $M = -46$ dB (corresponding to $\kappa L = 12$), the shot noise estimate decreases by 21 dB to -25.5 dB Hz/$\sqrt{\text{Hz}}$.

For comparison, results published for a relatively inexpensive 800 nm semiconductor laser [23], a tunable multiple quantum well (MQW) semiconductor DFB laser applying active frequency stabilization by feedback from an interferometer [26], and a Nd:YAG ring laser [1, 23] are also shown in the figure. We see that the $1/f$ noise level of the Nd:YAG laser is very similar to that of the fiber laser. The performance of the interferometer-locked MQW laser below 10 kHz is generally 15 dB better than that of the fiber DFB laser. It should be possible to obtain even better performances by locking a fiber DFB laser to a fiber interferometer.

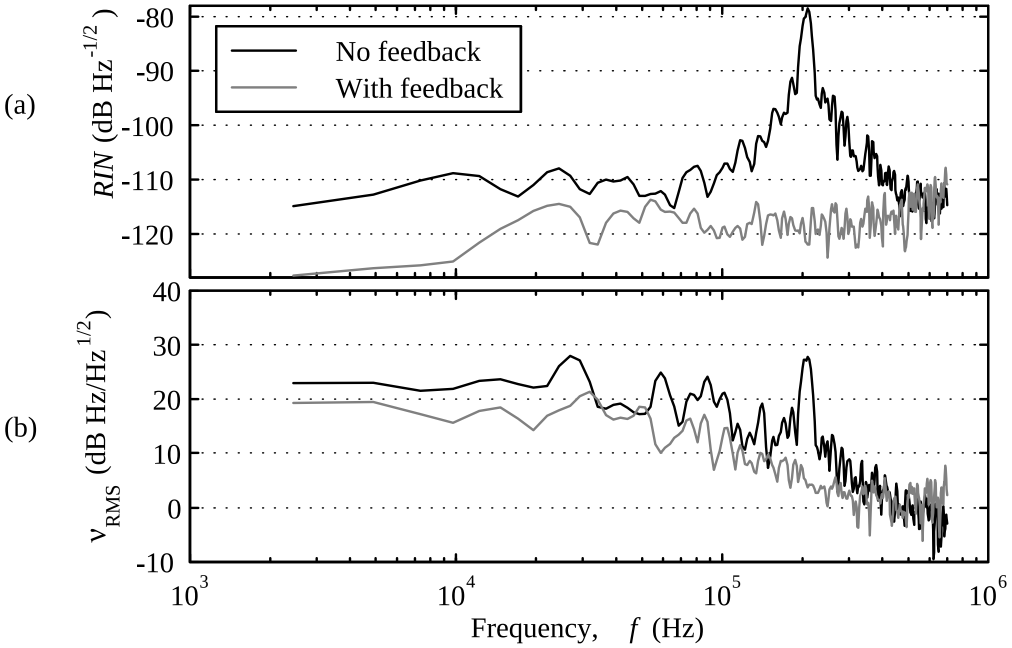

Figure 3.11. (a) RIN and (b) frequency noise ν_{rms} of a fiber DFB laser with and without RIN to pump feedback stabilization.

3.7 Noise Reduction by Feedback to the Pump Laser

RIN reduction for a single frequency Er-doped fiber Bragg grating laser by applying negative feedback from a monitor detector to the pump current has earlier been demonstrated in [27, 28]. To be able to investigate what happens to the laser frequency noise when such feedback is applied, we implemented a PID (proportional gain - integrator - differentiator) controller of the same type as used in [27] in a feedback path from the monitor detector to the pump drive current.

Fig. 3.11 shows the RIN and frequency noise ν_{rms} from a 50 mm long Ionas fiber DFB laser (not identical, but similar to the one investigated in the previous sections) which was pumped by $\sim$ 110 mW of 1480-nm power. The noise spectra were measured both for the cases with and without feedback to the pump. We see from Fig. 3.11 (a) that the relaxation oscillation peak near $f_r = 206$ kHz is effectively removed by the feedback. The RIN noise floor of ~ -118 dB Hz$^{-1/2}$ obtained with the feedback circuit is limited by noise generated in the monitor detector. With a better detector design we believe that the RIN would be limited by the shot noise at the monitor detector, which in our case with $\sim$ 50 μW of detected power would be -143 dB Hz$^{-1/2}$.

From Fig. 3.11 (b) we see that the relaxation oscillation peak in the frequency noise spectrum is also removed efficiently by the feedback. A small reduction in ν_{rms} by $\sim$ 2.5 dB is also observed for $f \lesssim 300$ kHz. We have not verified whether this noise reduction is a consequence of the feedback, or if it is only due to random fluctuations in the measurements. If the noise reduction is due the feedback, then this indicates that the contribution from pump noise to both RIN and ν_{rms} of the free running laser is more dominant for the present laser than for the laser investigated in the previous sections.

The ratio ν_{rms}/RIN of the free running laser in Fig. 3.11 at the relaxation oscillation peak $f_r = 206$ kHz equals 106.5 dB Hz. By inserting this ratio into (3.16) we estimate the effective linewidth enhancement factor at $f = f_r$ to be $\alpha_g \approx 2.1$ for this laser.

3.8 A Serially Multiplexed Fiber DFB laser Array

3.8.1 Introduction

An array with four serially multiplexed fiber DFB lasers pumped at 1480nm has been tested and evaluated at Optoplan with respect to output frequency noise and RIN noise. The array was on loan from Ionas AS in Denmark, and should be similar to the array investigated in [29]. A sensor laser array with 4 serially multiplexed single frequency Er-doped fiber lasers has earlier been demonstrated in [30]. We here present a more detailed characterization of the noise performance of the Ionas laser array, and investigate the effect of applying feedback to the pump from a detector that monitors the output from the array.[9]

The pump absorption in Er^{3+}-doped fiber DFB lasers pumped at 1480 nm can in principle be well below 0.05 dB (1.2 %), provided that splice losses do not dominate. This allows for serial multiplexing of a large number of fiber DFB lasers operating at different wavelengths, provided that interactions or reflections between the lasers do not make the laser operation unstable. Serial multiplexing of lasers is interesting both for multiplexing of fiber laser sensors and for making compact, low cost, and accurate multiple wavelength sources.

As mentioned in Secs. 3.2.3 and 3.2.4, back-reflections from external reflectors can degrade the laser stability. Back reflections may be caused by other fiber components, connectors, grating side-bands of serially multiplexed fiber DFB lasers, or by Rayleigh scattering. This constitutes a problem if one wants to create multiplexed fiber DFB laser sensor systems that are distributed over large distances ($>$ 30 to 300 m).

---

[9] This section is based on the Optoplan Report: "Test of Ionas fiber DFB laser array".

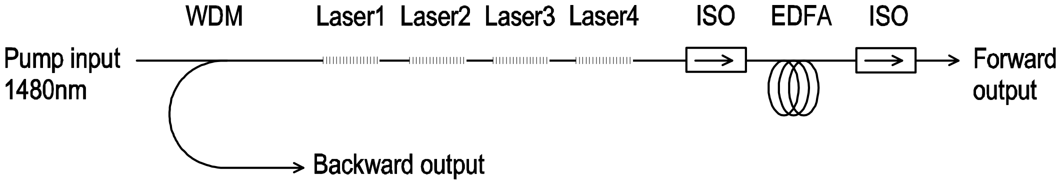

Figure 3.12. Laser array system on loan from Ionas AS. WDM, wavelength division multiplexer; ISO, optical isolator; EDFA erbium doped fiber amplifier.

We show in Chapters 4 and 5 that the tolerance to reflections from short distances ($\lesssim 10$ m) is reasonably high. This is promising for the possibilities of making a multiwavelength fiber DFB laser source without having to introduce isolators or attenuators between the lasers. However, one may suspect that the effect of having the power from each laser passing through all the other lasers, contributing to each others gain saturation, might introduce excess noise. Intensity noise in one laser may also be propagated to lasers further away from the pump via fluctuations in the pump absorption of the first laser. One may also fear that feedback mechanisms between the laser intensities could make the whole system start self-oscillating. One way of avoiding high feedback gains would be to make the outputs from each laser highly directional in the same direction as the pump by introducing asymmetries in the laser gratings. This type of configuration is used for the laser array investigated below.

It would be attractive if one was able to reduce the output RIN from the individual lasers in a fiber DFB laser array by applying feedback to the pump in a way similar to that demonstrated in Sec. 3.7. One may argue that it must be hard to control a multiple of independent signals (the RI of multiple lasers) by modulation of only one parameter (RI_p). We will here take a simple approach to the problem. Although we do not succeed in removing RIN from the array lasers, the results may provide some insight into the dynamics of the feedback system.

3.8.2 The Investigated Array

The laser array system contained four serially multiplexed Er-doped fiber DFB lasers, a 1480 / 1550 nm WDM, and an EDFA to boost the forward output power. Fig. 3.12 shows the system configuration. The WDM and the DFB lasers were packaged in a sealed box. The pump input port was spliced to a 1480nm diode laser with controller electronics built at Optoplan. The pump controller had options for either constant current operation or stabilization of the power from the fiber lasers by negative feedback via a PID-controller from a monitor detector to the pump laser. The monitor detector could either be connected to the forward or to the backward output ports from the array.

Laser1/2	$\lambda 1 = 1551.1$ nm
Laser1/2	$\lambda 2 = 1549.3$ nm
Laser3	$\lambda 3 = 1548.5$ nm
Laser4	$\lambda 4 = 1550.9$ nm

Table 3.1. Overview of the characterized lasers.

The laser wavelengths and the order of the lasers in the array, as specified from Ionas, is given in Tab. 3.1. The order of the first two lasers ($\lambda 1$ and $\lambda 2$) is not known.

3.8.3 Interrogation System

The wavelength demultiplexer system used to pick out the individual laser wavelengths received from the array is shown in Fig. 3.13. Two fibers with uniform Bragg gratings FBG1 and FBG2 inscribed were each mounted between a fixed point and a manual translation stage, allowing for independent strain-tuning of the grating center wavelengths. The strained lengths were between 50 and 70 cm. The position of the translation stages could be monitored on dial position meters. FBG1 was fixed with tape on an aluminum cylinder at each end, assisted by the friction of a few turns around the cylinders. The tuning repeatability for this grating was not very good (about ±50 pm), probably because the fiber was slipping on the cylinders. FBG2 was mounted with acrylate glue, resulting in better tuning repeatability.

When the grating stop band was strain-tuned over the laser wavelengths, fringes with peak-to peak amplitudes of 3 to 10 % of the DC level could be observed at the detector. This is probably due to reflections from the output detectors, implying that acoustically or thermally induced noise in the output fiber lengths may have induced extra RIN at the detectors. The influence of such acoustical and thermal noise is believed to be negligible at high frequencies. FBG1 could be tuned over the wavelengths $\lambda 1$, $\lambda 2$ or $\lambda 3$. FBG2 could be tuned to $\lambda 1$ or $\lambda 4$. In this way any two lasers could be monitored at the same time.

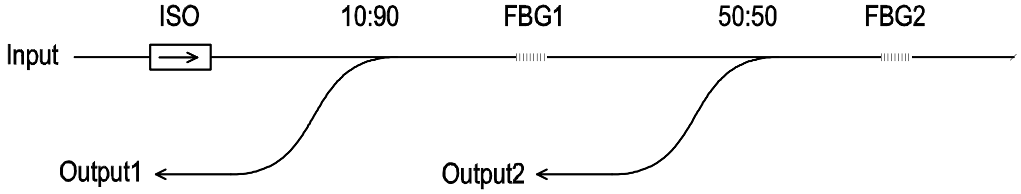

Figure 3.13. Wavelength demultiplexer. ISO, optical isolator; FBG1 and FBG2, strain tuned fiber Bragg gratings.

One of the two outputs from the demultiplexer was split by a 50:50 coupler and guided to a detector for RIN monitoring and to a Mach-Zehnder interferometer (MZ) with balanced detection for optical frequency noise monitoring. Active feedback to a PZT ring in one of the MZ arms was used to keep the DC interference phase in quadrature.

3.8.4 Output Power

With $\sim$ 140 mW of pump power entering the WDM, the total power from the forward output of the array was $\sim$ 10 mW. By inserting an optical band-pass filter (90 nm bandwidth) between the forward output and the detector it was verified that remaining pump power constituted less than 20 % of this power.

Tab. 3.2 shows the relative forward output powers from the different lasers, measured with the wavelength demultiplexer in Fig. 3.13.

The total backward output power with $\sim$ 140 mW pump was measured to $\sim$ 26 μW. According to Ionas, the lasers do not have equal output powers in both directions, and they are mounted such that they will give their maximum output power in the forward direction. This explains the low backward output power.

3.8.5 Performance without Feedback to the Pump

The RIN and frequency noise of the individual lasers were first measured with pump laser driver in a constant current mode. The pump power was set close to its maximum value of 140 mW. For each wavelength, the RIN and frequency noise spectra were recorded simultaneously. The results are shown in Fig. 3.14.

The relaxation oscillation resonance frequency f_r, the RIN and ν_{rms} at $f = f_r$, and the estimated α_g at $f = f_r$ according to (3.16) for each laser are summarized in Tab. 3.3. The lower peak noise densities for $\lambda 2$ compared to the other laser wavelengths may be explained by the lower Q-factor (inverse relative bandwidth) of the relaxation oscillation resonance in this laser compared to the others. For a given driving noise source (from pump fluctuations, vibrating back-reflectors etc.) the output peak noise power density should be proportional

Wavelength	Normalized output power (a.u.)
$\lambda 1$	1
$\lambda 2$	0.91
$\lambda 3$	0.66
$\lambda 4$	0.79

Table 3.2. Relative output powers.

Wavelength	f_r (kHz)	$RIN(f_r)$ (dB $\mathrm{Hz}^{-1/2}$)	$\nu_{rms}(f_r)$ (dB Hz/$\sqrt{\mathrm{Hz}}$)	α_g at $f = f_r$
$\lambda 1$	166	-74.8	33.0	2.4
$\lambda 2$	345	-85.3	27.6	2.6
$\lambda 3$	205	-70.0	31.5	3.8
$\lambda 4$	212	-74.6	37.2	3.6

Table 3.3. f_r, as well as RIN, ν_{rms}, and estimated α_g at $f = f_r$ for each laser wavelength

to the resonance Q-factor. If the resonances are affected by feedback between the intensities of the individual lasers, the lower Q-factor for $\lambda 2$ could be related to its large spacing in resonance frequency from the other lasers. It could also be related to its position as one of the first two lasers in the array counted from the pump input, since the first laser does not experience pump fluctuations caused by RIN fluctuations in lasers that are closer to he pump. However, a likely explanation for the variations in Q-factor is variations in the Q-factors of the solitary lasers (without effects of feedback).

3.8.6 Performance with Feedback to the Pump

Fig. 3.15 shows the RIN noise measured from the forward output when negative feedback was applied to the pump via the PID-controller. Again, the pump power was kept close to 140 mW. Both feedback from the forward [Fig. 3.15 (a)] and the backward [Fig. 3.15 (b)] outputs were investigated. In the latter case, the electronic gain of the feedback controller was increased by a factor of 71 compared to the former case, in order to partly compensate for the reduced DC power at the monitor detector. The dashed line shows the RIN noise at the feedback monitor detector. The peak in the monitor spectrum near 500 kHz is du to a relatively low stability phase margin of the electronic feedback loop.

By comparing Figs. 3.14 and 3.15 one see that the main effect of the feedback is to distribute the RIN-noise between the lasers. That is: When one laser oscillates at its resonance frequency, the feedback compensates in such a way that all four lasers starts oscillating at this frequency, but with such phases and amplitudes that the total monitor power is stabilized. Consequently, there is no significant overall improvement in the individual RIN noise levels due to the feedback. It is interesting, however, to observe that the relaxation oscillations of the laser $\lambda 2$ has been reduced very effectively by the feedback. This may be because of the relatively large separation of the relaxation oscillation frequency of this laser from the other resonance frequencies, meaning that the remaining three lasers are relatively insensitive to the feedback modulation of the pump power at the relaxation oscillation frequency of $\lambda 2$.

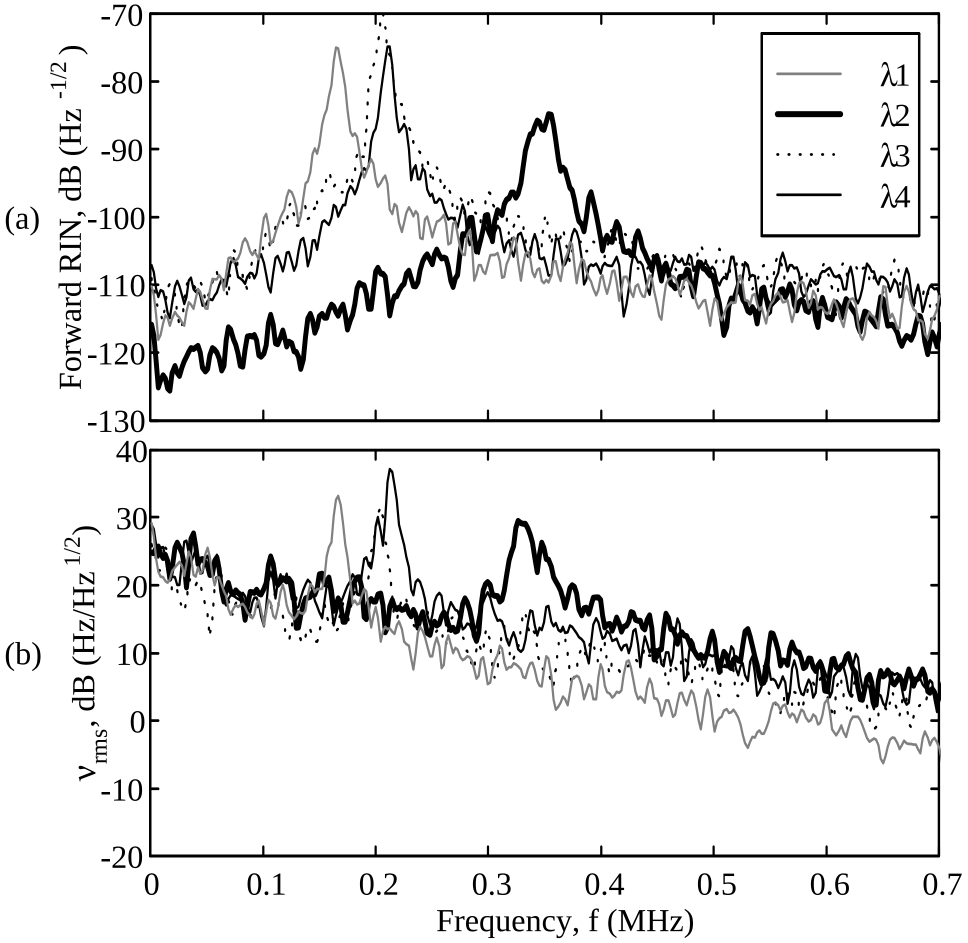

Figure 3.14. (a) RIN and (b) Frequency noise from the array lasers without feedback to the pump. The noise was measured from the forward output of the array.

The RIN at low frequencies of individual lasers with active feedback to the pump was also investigated. When feedback from the forward output was used, no striking noise phenomena could be observed (except for interference effects in the wavelength demultiplexer). However, when the feedback monitor was connected to the backward output, the forward output power was found to make abrupt changes by 10 to 15 % in amplitude at intervals of 1 to 10 s. The power changes occurred simultaneously and with the same sign at all laser wavelengths. The reason for this behavior is believed to be sudden changes in the lasing efficiency (or the forward to backward output ratio) of individual lasers. Such changes will cause the feedback electronics to change the pump power so that the backward output power is kept constant. This will, how-

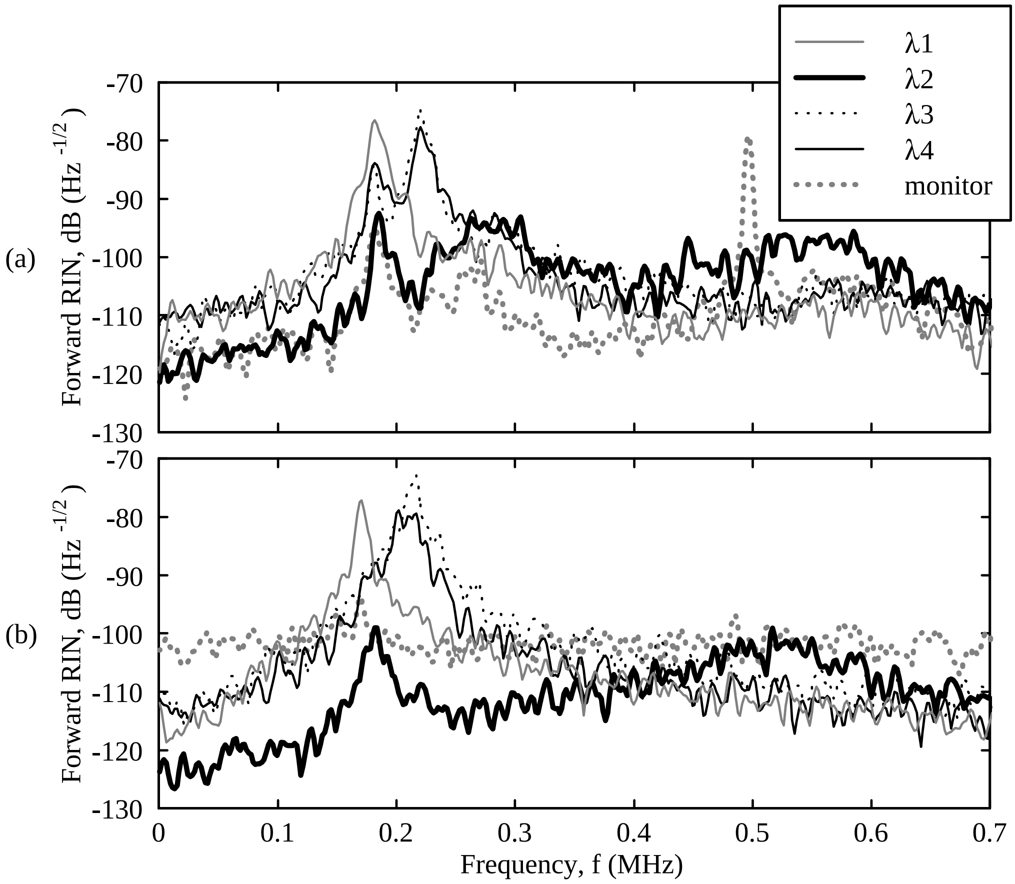

Figure 3.15. RIN with feedback to the pump from the (a) forward and (b) backward outputs of the array. The RIN of each laser was measured from the forward output of the array. The total RIN at the monitor detector is also illustrated.

ever, also cause changes in the remaining pump available for the EDFA, and amplification of the forward output changes for all wavelengths.

Fig. 3.16 shows the laser frequency noise measured with feedback to the backward output. Each of the spectra in Fig. 3.16 was measured simultaneously with the corresponding RIN spectrum in Fig 3.15 (b).

One may compare the noise measurements in Figs. 3.14 through 3.16 with the noise levels in Fig. 3.11 of a typical non-multiplexed Ionas fiber DFB laser with and without feedback to the pump. We see that without feedback to the pump, the RIN and frequency noise levels are similar for the single laser and the multiplexed lasers is Fig. 3.14. When feedback is applied, the RIN is dramatically reduced for the single laser, accompanied by a removal of the relaxation oscillation noise peak in ν_{rms}. This noise reduction is not achieved for the multiplexed lasers in Fig. 3.15.

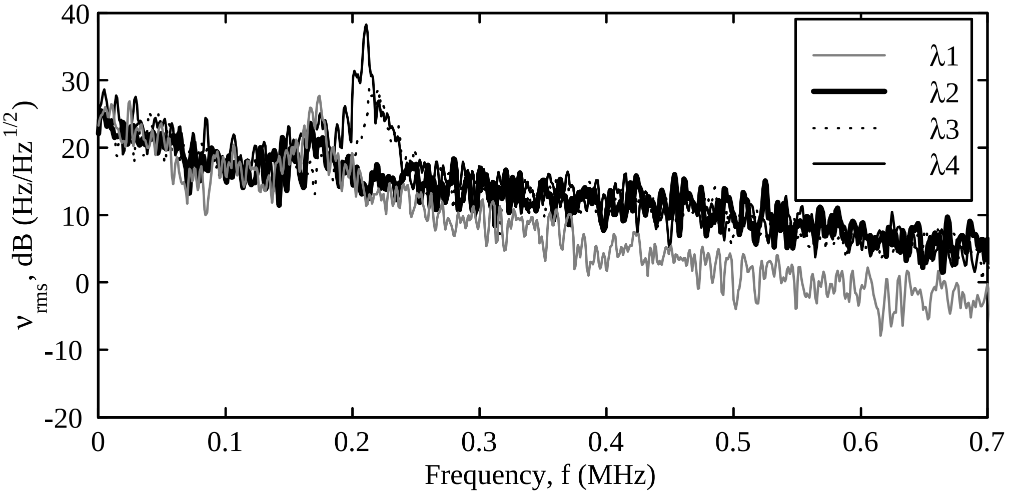

Figure 3.16. Frequency noise with feedback from the backward output of the array to the pump.

3.9 Conclusion

The origins of relative intensity noise RIN and optical frequency noise ν_{rms} in fiber DFB lasers has been studied both theoretically and experimentally. The correlation between intensity and frequency fluctuations has also been studied, in terms of the linewidth enhancement factor α_g and the self heating coefficient r_{th}.

The measured RIN ranges from a typical level of -118 dB Hz$^{-1/2}$ between $f = 10$ Hz and 30 kHz to a maximum of -78 dB Hz$^{-1/2}$ at the relaxation oscillation frequency f_r, and seems to be dominated either by random fluctuations in the cavity losses (possibly due to fluctuations in the saturable absorption), by spontaneous emission noise, or by a combination of the two noise sources. f_r varies between the investigated lasers from 166 to 345 kHz. Calculations indicate that the spontaneous emission induced noise (both RIN and ν_{rms}) can be reduced to negligible levels (3.22) if the laser mirror transmissivities are sufficiently low (effective $\kappa L \gtrsim 10$). Unfortunately, we do not know the mirror transmissivities for the investigated lasers.

A fundamental source of laser frequency noise ν_{rms} seems to be the random diffusion of thermal energy within the fiber cross-section. Above $f = 1$ kHz, except for near $f = f_r$, the measured ν_{rms} is typically 0 to 6 dB above the thermal noise floor expected from measurements of fiber interferometer noise published in [22, 23, 5, 21]. For a fiber DFB laser with a 10 mm effective cavity length, the expected thermal noise floor decreases from ~ 25 dB Hz/$\sqrt{\text{Hz}}$ at $f = 1$ kHz to ~ -5 dB Hz/$\sqrt{\text{Hz}}$ 1 MHz. The measured increase above this floor for $f \lesssim 50$ kHz is believed to be due to acoustical noise. Above $f = 50$ kHz, the origin of the excess noise is more unclear.

For $f < 1$ kHz an $1/f$ component is observed in ν_{rms}, which is qualitatively similar to the polarization beat frequency noise observed in Chap. 8 for a different laser. The origin of the $1/f$ noise has not been identified.

Near $f = f_r$ the optical frequency and intensity fluctuations are found to be highly correlated, and related by the linewidth enhancement factor $\alpha_g \simeq 2\nu_{rms}/(f\,RIN)$. A low value of α_g is thus desirable in order to reduce $\nu_{rms}(f_r)$. Low values of α_g are also expected to improve the lasers tolerance to external reflections, as will be further discussed in Chaps 4 and 5. Our measured values for α_g at $f = f_r$ range from 2.1 to 3.8, as compared to typically from 3 to 7 for semiconductor lasers. To our knowledge, this is the first time that values for α_g in a fiber laser is reported experimentally. Calculations reported in [13] (not including possible thermal contributions to α_g) indicate that α_g will depend strongly on the laser wavelength, going through zero somewhere near 1540 nm. α_g is also expected to depend on a number of other parameters, such as frequency f, pump power, and saturating signal power in the cavity (which is strongly dependent on κL). We observed a strong decrease in α_g with increasing f within the relaxation oscillation $\sim$ 25 dB bandwidth from 170 to 270 kHz..

At frequencies well below f_r the only laser noise contributions that depend on α_g are spontaneous emission induced frequency noise and noise due to cold cavity loss fluctuations. The coupling to ν_{rms} from RIN components that are induced by loss fluctuations or pump noise is believed to be dominated by thermal effects at these frequencies.

By comparing the pump modulation responses of the laser output power and the optical frequency shift we have determined the frequency response $r_{th}(f)$ of the Er-doped fiber to self heating from power dissipation in the core at frequencies below the relaxation oscillation peak ($f \lesssim 180$ kHz). Good agreement with theoretical calculations was found for $f > 400$ Hz. The theory shows that the fiber boundary conditions (heat sink), which were not known for the investigated fiber, are of great importance at lower frequencies.

The spontaneous emission induced frequency noise in fiber DFB lasers is typically many orders of magnitude smaller than in semiconductor lasers, due to the much lower effective laser mirror transmissivities and longer cavity roundtrip delays. Other noise sources, such as thermal fluctuations, are found to dominate in fiber DFB lasers. The huge difference in spontaneous emission noise levels explains why fiber DFB lasers have linewidths that are much smaller than semiconductor lasers.

We have verified that active stabilization of the laser RIN by feedback to the pump laser from a detector monitoring the fiber laser output power effectively removes the relaxation oscillation peak from the optical frequency noise spectrum.

The observation that single polarization fiber DFB lasers can be multiplexed along a single fiber with a common pump without significant degradation of the noise performance is promising for the possibility of performing multiple point distributed sensing with fiber DFB lasers. It is also promising for the possibility of making compact, low cost, and accurate multiple wavelength sources.

3.10 Acknowledgments

The author acknowledges Dag Thingbø at Optoplan AS for contributions to the design and implementation of the electronic circuits used in the experiments, and especially for designing and implementing the feedback circuit used in Secs. 3.7 and 3.8. Thanks go also to Jon Thomas Kringlebotn, Kjell Bløtekjær, Dag Roar Hjelme, and Sigurd Løvseth for inspiring and stimulating discussions, and for reading through and commenting on this manuscript, and to Ionas for lending us their laser array.

References

[1] K. J. Williams, A. Dandridge, A. D. Kersey, J. F. Weller, A. M. Yurek, and A. B. Tveten, "Interferometric measurement of low frequency phase noise characteristics of a diode pumped Nd:Yag ring laser", Electron Lett., Vol. 25, p. 774, 1989.

[2] T. L. Boyd, D. Klemer, P. A. Leilabady, J. Noriega, and M. Pessot, "A 1.55-μm Solid-State Laser Source for DWDM Applications", J. of Lightwave Tech., Vol. 17, pp. 1904–1908, 1999.

[3] S. Taccheo, P. Laporta, O. Svelto, and G. De Geronimi, "Intensity noise reduction in a single-frequency ytterbium-codoped erbium laser", Opt. Lett., Vol. 21, pp. 1747–1749, 1996.

[4] J. T. Kringlebotn, W. H. Loh and R. I. Laming, "Polarimetric Er^{3+}-doped fiber distributed-feedback laser sensor for differential pressure and force measurements", Opt. Letters, Vol.21, pp.1869–1871, 1996.

[5] K. P. Koo and Wanser, A. D. Kersey, "Fibre laser sensor with ultrahigh strain resolution using interferometric interrogation", Electron. Lett., Vol. 31, pp. 1180–1182, 1995.

[6] J. T. Kringlebotn, ”Optical fiber distributed feedback laser” (distributed feedback laser used as sensor), US Patent 5 844 927, UK Patent 2 299 203, NO Patent 302 441, Optoplan AS, 1996.

[7] T. Okoshi and K. Kikuchi, ”Coherent optical fiber communications”, (KTK Scientific Publishers, Tokyo, 1988), pp. 61–81.

[8] Y. Weissman, ”Optical Network Theory”, (Archtech House, 685 Canton Street, MA 02062, USA, 1992), pp. 142–152.

[9] H. L. An, E. Y. B. Pun, X. Z. Lin, and H. D. Liu, ”Effects of Ion-Clusters on the Intensity Noise of Heavily Erbium-Doped Fiber Lasers”, IEEE Phot. Technol. Lett., Vol. 11, pp. 803–805, 1999.

[10] F. Sanchez, P. Le Boudec, P. L. Francois, and G. Stephan, ”Effects of ion pairs on the dynamics of erbium-doped fiber lasers”, Phys. Rev. A, Vol. 48, pp. 2220–2229, 1993.

[11] J. Hübner, T. Feuchter, C.V. Poulsen, and M. Kristensen, ”Directly UV-written erbium doped waveguides”, in *Photosensitivity and Quadratic Nonlinearity in Glass Waveguides: Fundamentals and Applications*, OSA Technical Digest Series, Vol. 22, 1995.

[12] D. Marcuse, ”Pulsed Behavior of a Three-Level Laser With Saturable Absorber”, IEEE J. Quantum Electron., Vol. 29, pp. 2390–2396, 1993.

[13] K. E. Alameh, R. A. Minasian and Y. Zhao, ”A Numerical Model for the Complex Susceptibility of Saturated Erbium-Doped Amplifiers”, J. Quantum Electron., Vol. 33, pp. 855–860 (1997).

[14] E. Desurvire, ”Study of the Complex Susceptibility of Erbium-Doped Fiber Amplifiers”, J. of Lightwave Tech., Vol. 8, pp. 1517–1529, 1990.

[15] K. Petermann, ”External optical feedback phenomena in semiconductor lasers”, IEEE J. of Sel. Topics in Q. El., Vol. 1, pp. 480–487, 1995.

[16] G. A. Ball, C. G. Hull-Allen and J. Livas, ”Frequency Noise of a Bragg grating fibre laser”, Electron. Lett. **30**, 1229*–12*30 (1994).

[17] S. W. Løvseth, J. T. Kringlebotn, E. Rønnekleiv and K. Bløtekjær, ”Fiber DFB Lasers Used as Acoustic Sensors in Air”, Appl. Opt., Vol. 38, pp. 4821–4830, 1999.

[18] R. H. Kingston, ”Detection of Optical and Infrared Radiation”, (Springer-Verlag, Berlin, Germany, 1979), pp. 89–93.

[19] K. H. Wanser, "Fundamental phase noise limit in optical fibres due to temperature fluctuations", Electron. Lett., Vol. 28, pp. 53–54, 1992.

[20] W. H. Glenn, "Noise in Interferometric Optical Systems: An Optical Nyquist Theorem", IEEE J. Quantum Electron., Vol. 25, pp. 1218–1224, 1989.

[21] S. Knudsen, "Fiber-Optic Acoustic Sensors Based on the Michelson and Sagnac Interferometers: Responsivity and Noise Properties", Dr.ing. thesis, (Norwegian Univ. of Sci. and Tech. NTNU) 1996.

[22] K. H. Wanser, A. D. Kersey, and A. Dandridge, "Measurement of fundamental thermal phase fluctuations in optical fiber", in *Proceedings of 9th Optical Fiber Sensors Conference*, Florence, pp. 255–258, 1993.

[23] A. D. Kersey, "A Review of Recent Developments in Fiber Optic sensor Technology", Opt. Fiber Tech., Vol. 2, pp. 291–317, 1996.

[24] M. K. Davis, M. J. F. Digonet, and R. H. Pantell, "Thermal Effects in Doped Fibers", J. of Lightwave Tech., Vol. 16, pp. 1013–1023, 1998.

[25] O. Hadeler, M. N. Zervas, E. Rønnekleiv, and M. Berendt, "Temperature distribution along DFB fibre lasers", *IEE colloquium digest on Optical Fibre Gratings*, (IEE, Box 96, M. Faraday House, Stevenage, Herts. SG1 2SD, UK), 1999.

[26] M. Kuorogi, C. H. Shin, and M. Ohtsu, "A 250 Hz Spectral Linewidth 1.5 μm MQW-DFB Laser Diode with Negative-Electrical-Feedback", IEEE Phot. Tech. Lett., Vol. 3, pp. 496–498, 1991.

[27] G. A. Ball, G. Hull-Allen, C. Holton, and W. W. Morey, "Low Noise Single Frequency Linear Fibre Laser", *Electron. Lett.*, vol. 29, pp. 1623-1625, 1993.

[28] V. Mizrahi, D. J. DiGiovanni, R. M. Atkins, S. G. Grubb, Y.-K. Park, and J.-M. P. Delavaux, "Stable Single-Mode Erbium Fiber-Grating Laser For Digital Communication", J. of Lightwave Tech., Vol. 11, pp. 2021–2025, 1993.

[29] J. Hübner, P. Varming and M. Kristiansen, "Five wavelength DFB fiber laser source for WDM systems", *Electron. Lett.*, vol. 33, pp. 139-140, 1997.

[30] K. P. Koo and A. D. Kersey, "Noise and cross talk of a 4-element serial fiber laser sensor array", in *1996 Conf. on Optical Fiber Communications*, paper ThP2, Tech. Dig., pp. 266-267.

Chapter 4

Stability of Distributed Feedback Fiber Lasers with Optical Feedback[1]

Abstract — The tolerance of two fiber distributed feedback lasers to external back-reflection from discrete reflectors and to Rayleigh back-scattering has been investigated. The results show a reduced feedback sensitivity for the longer laser grating.

4.1 Introduction

Fiber distributed feedback (DFB) lasers used as sensor elements with optical frequency interrogation is an attractive high resolution alternative to passive Bragg grating sensors. Remote pumping and interrogation of such sensor lasers without the use of an optical isolator near the sensing point may be required. However, this will introduce Rayleigh back-scattering into the laser from the lead fiber. If in addition several laser sensors at different wavelengths are serially multiplexed along the same fiber [1], each laser may also experience discrete external reflections from the grating side-bands of the other lasers.

It is known that back-reflections into narrow linewidth semiconductor lasers may cause increased frequency noise, or even self pulsing. The tolerable back-reflection level of such lasers has been found to decrease with increasing external cavity length and with decreasing laser mirror reflectivity [2]. However, important laser parameters such as the frequency and relative linewidth (inverse Q-value) of the relaxation oscillation resonance and the coherence length

---

[1] This chapter contains a re-edited version of [E. Rønnekleiv and S. W. Løvseth, "Stability of Distributed Feedback Fiber Lasers with Optical Feedback", in *13th International Conference on Optical Fiber Sensors*, Proceedings of SPIE Vol. 3746, pp. 466-469, 1999].

of the solitary laser differ largely, typically by orders of magnitude, between semiconductor lasers and fiber DFB lasers. Therefore, few quantitative conclusions can be made about the back-reflection tolerance of fiber DFB lasers from existing work on semiconductor lasers.

In this paper we investigate the feedback attenuation required for stable operation of Er^{3+} fiber DFB lasers experiencing Rayleigh back-scattering or discrete end-reflection from fiber lengths ranging from $\sim$ 10 m to 13 km. We also discuss the possibility of improving the tolerance to back-reflections by increasing the DFB grating strength and/or by using a laser with asymmetric output characteristics.

4.2 Experiments and Results

Two Er^{3+} doped fiber DFB lasers, made by IONAS, Denmark, with grating lengths of 5 and 10 cm and nominal $\pi/2$ phase-shifts at the grating center have been investigated. In the following they will be denoted DFB1 and DFB2, respectively. From a heat scan measurement [3], the coupling coefficients were estimated to $\kappa = 170\ \mathrm{m}^{-1}$ for DFB1 and $\kappa = 150\ \mathrm{m}^{-1}$ for DFB2, giving total grating strengths of $\kappa l = 8.5$ and 15, respectively. Fundamental mode operation at the Bragg resonance frequency was verified for DFB1, while it was found that DFB2 could switch from the fundamental to a higher order longitudinal mode, depending on how the fiber was mounted. The higher order mode of DFB2 was found to be highly asymmetric, with a 15.8 dB ratio between the left and the right output power. When operating in the fundamental mode this ratio was 0.9 dB for DFB1 and 6.0 dB for DFB2. Both lasers were operating in only one polarization mode, and the laser wavelengths were 1551.1 nm for DFB1 and 1554.6 nm for DFB2.

The experimental setup is shown in Figure 4.1. The fiber laser was pumped at 1480 nm from the left through a 1480/1550 wavelength division multiplexer (WDM). Both lasers were pumped through their high output power ends. The output from the 1550 branch of the WDM was guided through a 50 dB optical isolator (ISO) and split by a 3 dB coupler, enabling the fiber laser frequency and the output power from the left to be measured simultaneously. The frequency was measured using a Mach-Zender interferometer (MZ), having an imbalance of 101.5 m and fringe sensitivity of 321 kHz/rad. A polarization controller (PC2) was used to optimize the interferometer response, and quadrature operation was ensured by feedback from the differential detector (D1 and D2) to a PZT stretcher inside the interferometer through a low-pass filter (LPF). The laser output power to the left was measured with detector D3, and was kept at 121 μW for DFB1 and 313 μW for DFB2 during all the experiments. The relative intensity noise (RIN) and frequency noise of the lasers without

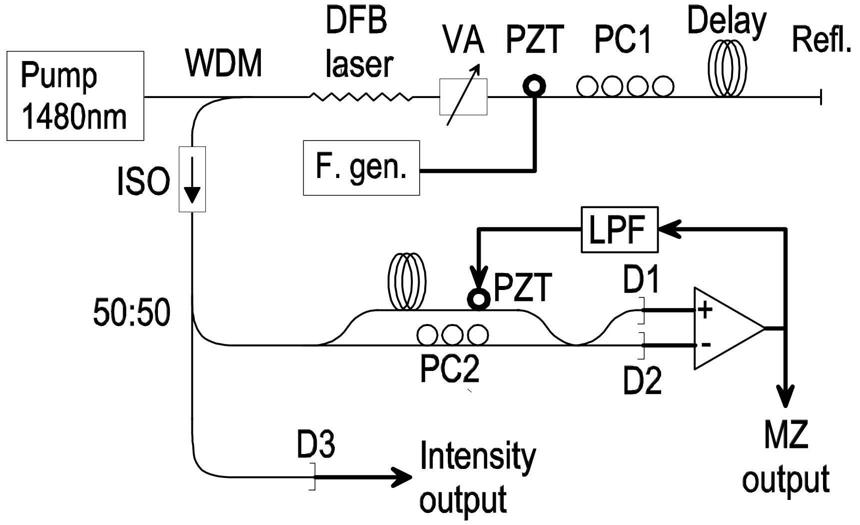

Figure 4.1. Experimental setup for investigation of DFB fiber lasers with optical feedback.

back-reflection in the frequency range from 2.4 to 930 kHz were measured to be 5.6 kHz and -36 dB (RMS values) for DFB1 and 6.5 kHz and -43 dB for DFB2. The 3 dB bandwidth and center frequency of the relaxation oscillations were roughly 8 kHz and 207 kHz for DFB1 and 18 kHz and 238 kHz for DFB2, respectively.

The right end of the fiber laser was connected through a variable optical attenuator (VA) to various fiber delay coils, ranging in length from a few meters to 13 km. By terminating the ends of the delay coils with bending losses, the effect of Rayleigh back-scattering at different attenuator settings could be investigated. To study the effect of back-reflection from a discrete point, we used a mirror with -0.75 dB reflectivity or a -14.5 dB cleaved fiber end reflector. The PZT phase modulator and the polarization controller (PC1) were used to control the phase and polarization of the feedback signal. Standard telecom fiber of varying fabricates were used in the delay coils, and the back-scattered Raleigh power per unit length may have varied by ±1 dB between the coils. The lengths and transmission losses were measured with an OTDR. Connector and splice losses were measured, and have been included in the stated attenuation values.

For Rayleigh scattering, one important parameter is the length of back-scattering fiber the laser can tolerate before the noise induced by back-reflection start to dominate over other noise sources. For longer lengths, it is interesting to know the attenuation required to maintain stable operation. The RMS frequency noise of DFB1 seemed unchanged for fiber lengths up to 37 m, but at 142 m the laser was self pulsing with excessive frequency noise. The noise of

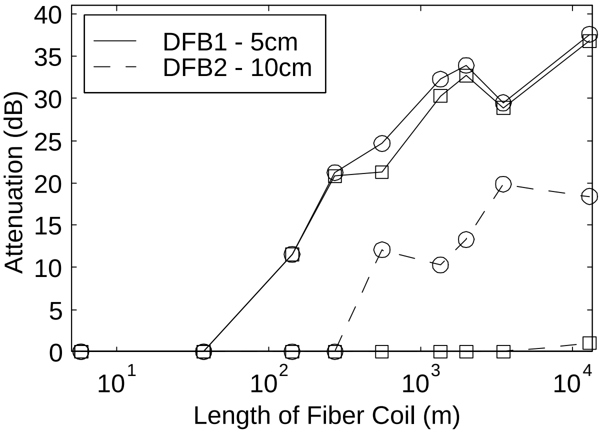

Figure 4.2. Attenuation needed for stable operation in frequency and intensity of DFB1 and DFB2 exposed to Raleigh scattering from fiber delay as a function of delay lengths. Curves with square markers (□) show the smallest attenuation measured to get CW operation (see main text), whereas curves with circular markers (○) show the smallest attenuation needed for max. ±20 kHz relaxation oscillation amplitude.

DFB2 seemed unchanged for lengths up to 273 m. With 13 km of fiber, RMS noise of 37 kHz with bursts of ±170 kHz could be observed. We also measured the attenuation needed between the delay fiber and the DFB fiber lasers to avoid frequency noise bursts with amplitudes exceeding ±20 kHz during a period of 12 s and the attenuation needed for continuous wave (CW) operation for the same duration. By CW operation we mean that the intensity should not have any noise with amplitude larger than 30 % of the DC value.

The results of the Rayleigh measurements are displayed in Figure 4.2. As seen from the figure, DFB2 is considerably more stable than DFB1 for fiber lengths above 100 m. At 13 km, the attenuation needed to avoid excess noise with DFB1 was 19.2 dB higher than with DFB2. DFB2 was only showing small signs of self oscillation at 13 km delay, with only 0.5 dB attenuation required for CW operation. DFB1, on the other hand, started self-oscillations for attenuation levels only slightly below those where the frequency noise started to increase, and at 13 km delay, 36.7 dB attenuation was needed for CW operation. Also note that the attenuation needed seems to approach saturation for the longest fiber delays from 2 to 13 km. This is expected, since the Rayleigh scattering feedback per fiber length levels will be lower far away from than close to the laser due to the fiber transmission losses. In addition, the longest lengths correspond to several relaxation oscillation periods [2].

As discussed by Petermann [2] and others, a discrete reflector will shift both the intensity, frequency, and linewidth of the laser, depending on the phase of the back-reflection. In a real sensor application, the phase of back-reflections

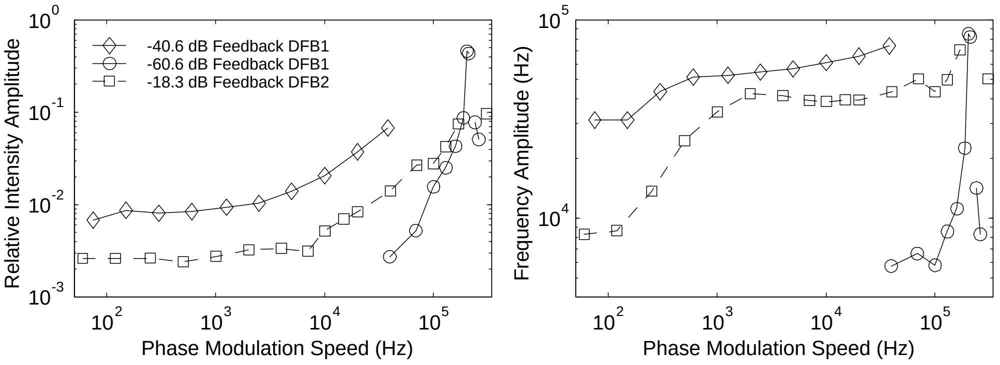

Figure 4.3. Laser intensity (left) and frequency (right) response as a function of phase modulation frequency of feedback from a distance of 28.5 m (DFB1) and 29.5 m (DFB2).

may drift at various speeds due to mechanical vibrations in the lead fiber. It is thus interesting to investigate how the laser frequency and intensity amplitudes vary with the phase modulation speed. Setting PC2 to the position of largest possible response, we measured this frequency response for a distance between the reflector and the fiber lasers of 29 meter. Phase modulation was obtained by driving the PZT ring in the delay with a triangular waveform. For phase modulations speeds far below the relaxation oscillation frequencies, this produced fringes in the laser frequency and intensity which easily could be measured with an oscilloscope. For larger phase modulation speeds, large relaxation oscillations were triggered and we had to estimate the frequency response from the Fourier spectra of the oscilloscope traces. The results are shown in Figure 4.3. Note that different feedback levels were used in the measurements, and that DFB1 starts to self-oscillate for modulation speeds close to the relaxation oscillation peak even at a feedback level less than -60 dB.

Similar to the Raleigh scattering case, we measured the largest feedback with less than 6 dB worst case increase in RIN, with less than ±20 kHz relaxation oscillation amplitude, and with CW laser operation. The two latter results are shown in Figure 4.4. The phase of the feedback was again modulated with the PZT, yielding comparable noise bursts at each fringe. The figure shows the feedback level for a phase modulation speed of 1 and 10 kHz for the frequency noise and 1 kHz for the CW limit measurements. The largest feedback levels for 10 kHz are slightly larger than for 1 kHz. The explanation is probably that the laser in the former case are shorter period of time in the unstable regime. The tolerable feedback seems to approach constant levels for delays longer than one relaxation oscillation period, corresponding to a fiber delay of roughly 500 m. This is in agreement with the theory for semiconductor lasers [2].

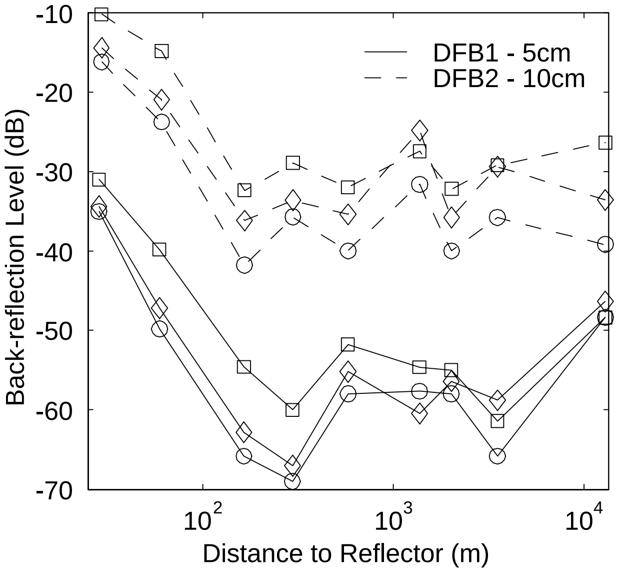

Figure 4.4. Maximum feedback allowed from discrete reflectors for stable operation in frequency and intensity of DFB1 and DFB2. Curves with circular (◯) and square (□) markers show the largest feedback allowed to get a maximum relaxation oscillation amplitude of ±20 kHz for a back-reflection phase modulation speed of 1 and 10 kHz, respectively. Curves with diamond (◇) markers show maximum feedback allowed for CW operation for a back-reflection phase modulation speed of 1 kHz.

4.3 Conclusion

We see from the measurements that the 10 cm DFB2 with $\kappa l \approx 15$ can tolerate back-reflection levels that are about 20 dB higher than the 5 cm DFB1 with $\kappa l \approx 8.5$. This is believed to be due to a weaker coupling of the laser modal power of DFB2 to the external cavity [2]. Since the longitudinal mode of operation in this laser during the experiment is not known, clear conclusions cannot be made about the reason for this weak coupling. If DFB2 was operating in its fundamental mode, an important reason is probably the increased intensity concentration near the phase-shift position for higher κl values [3]. In theory, an increase in κl by 6.5 corresponds to a reduction in coupling efficiency by $e^{-6.5}$, and the tolerable back-reflection level should thus be increased by $20\log_{10}(e^{6.5}) = 56$ dB.[2] Not included in this estimate are possible effects of non-linearities due to the high intensity inside high κl lasers, which may contribute to a reduced stability.

---

[2] In the conference proceding we wrote that the tolerable back reflection level is increased by 28 dB, which is wrong.

If DFB2 has been operating in the higher order mode, the improved tolerance to back-reflection should rather be explained by the 16 dB output asymmetry of this mode. This corresponds to an external cavity coupling coefficient that is 16 dB lower to the left than to the right, and the tolerable feedback level should thus be higher by 16 dB at the right side. In principle, asymmetric output lasers could be exploited by mounting the laser with the low output end pointing towards the source of back-reflections, i. e. the lead fiber. The expense of such a solution would be a reduced output power returned through the lead fiber.

The maximum length of Rayleigh back-scattering fiber that would give no excess noise without attenuation was found to be around 100 m for DFB1 and around 300 m for DFB2. DFB2 can however be made free from excess noise for all the investigated fiber lengths up to 13 km by introducing a 10 dB attenuator at the laser wavelength near the laser. Again, this would give a 10 dB reduction in output power.

References

[1] K. P. Koo and A. D. Kersey, "Noise and cross talk of a 4-element serial fiber laser sensor array", 1996 Conf. on Optical Fiber Communications, paper ThP2, Technical Digest, pp. 266-7.

[2] K. Petermann, "External optical feedback phenomena in semiconductor lasers", IEEE J. of Sel. Topics in Q. El., Vol. 1, pp. 480-7, 1995.

[3] E. Rønnekleiv, M. Ibsen, M. N. Zervas and R. I. Laming, "Characterization of intensity distribution in symmetric and asymmetric fiber DFB lasers", CLEO'98, Tec. Digest Vol. 6, CTuE6, (San Francisco), 1998.

Chapter 5

Stability of an Er–Yb-doped fiber distributed-feedback laser with external reflections[1]

Abstract — The maximum tolerable amplitude backreflection coefficient $r_{ext,c}$ into a fiber distributed feedback (DFB) laser before the onset of instabilities has been investigated. $r_{ext,c}$ was found to decrease with increasing external cavity lengths up to ∼320 m and to be proportional to the relative linewidth of the relaxation oscillation resonance. The tolerable length of Rayleigh backscattering standard telecom fiber was found to be 135-200 m. An observed degradation in the laser stability and slope efficiency at low pump powers is believed to be due to UV-induced saturable absorbers.

5.1 Introduction

Fiber distributed-feedback (DFB) lasers are attractive used as sensor elements with optical frequency interrogation because of their low level of frequency noise[2] and stable longitudinal mode operation. Remote pumping and interrogation of such sensor lasers through a long lead fiber may be required. For operational reasons, the use of optical isolators near the sensing point may be undesirable. Consequently, the laser will experience Rayleigh back-scattering from the lead fiber. If in addition several sensor lasers at different wavelengths

---

[1] This chapter contains a re-edited version of [E. Rønnekleiv, O. Hadeler, and G. Vienne, ”Stability of an Er-Yb-doped fiber distributed-feedback laser with external reflections”, Opt.. Lett., Vol. 24, pp. 617-619, 1999].

[2] ”low-frequency noise” in the original paper has been corrected to ”low level of frequency noise”

are serially multiplexed along the same fiber [1], each laser may also experience reflections from the grating side-bands of the other lasers. It is known that external backreflections can cause excess frequency noise or even self-pulsing in narrow linewidth semiconductor lasers [2]. This problem increases with decreasing laser mirror reflectivity and with increasing distance to the external reflector. However, important parameters such as the optical coherence lengths and the relaxation oscillation resonance Q-factors and center frequencies differ largely between semiconductor lasers and fiber DFB lasers. Therefore, few quantitative conclusions can be made about fiber DFB laser stability from existing work on semiconductor lasers.

5.2 Experiment

In this Letter we report on the tolerance of an Er–Yb-doped fiber DFB laser to external backreflections. The investigated laser operated at 1549 nm in two polarization modes and was pumped by a 1480-nm laser diode. We produced laser operation by writing a symmetric π phase-shifted grating of length L =40 mm into a UV-sensitized B–Ge doped ring enclosing the Er–Yb doped core of the fiber [3]. D_2-loading was used to enhance the UV-sensitivity. The grating coupling coefficient of the laser was measured by a heat-perturbation method [4] to be κ =230 m^{-1}±10%. Before UV exposure but after D_2-loading of the fiber, the fiber transmission spectrum was measured for various pump powers. From these measurements, the absorption (a_x) and gain (g_x) at zero and full inversion, respectively, at the laser signal ($x = s$) and pump ($x = p$) wavelengths were found to be $[\,a_s,\ a_p, g_s,\ g_p] = [11.7,\ 8.9,\ 15.9,\ 3.0]$ dB/m. The spontaneous emission power at full inversion was $P_{sp} = 4.1$ mW/m.

Figure 5.1 shows the measured left + right output power (crosses) emitted from the laser versus pump power. Curve A shows the theoretical output power, obtained from the measured gain parameters of the unexposed fiber and a DFB laser model described elsewhere [5]. The measured slope efficiency increases at low pump power and approaches a constant value of 0.7% above 40 mW. This indicates that bleachable absorbers are present which saturate for pump powers of >40 mW. We obtained a good theoretical fit (curve B) by assuming a lifetime reduction ("quenching") by a factor of $\zeta = 26$ for a fraction $\xi = 37.7$ % of the Er-ions, and unbleachable losses of $a_0 = 0.243$ dB/m. Here, ξ is essentially determined by the laser threshold, ζ by the position of the "knee" in the output power curve near 30 mW and a_0 by the slope efficiency at high pump powers.

It may be noted that higher slope efficiencies (>10%) could be obtained by pumping at 980 nm. However, the high pump absorption per laser in this case makes serial sensor multiplexing impossible. Moreover, the increased heat dissipation from the laser may disturb the sensor performance. For accurate

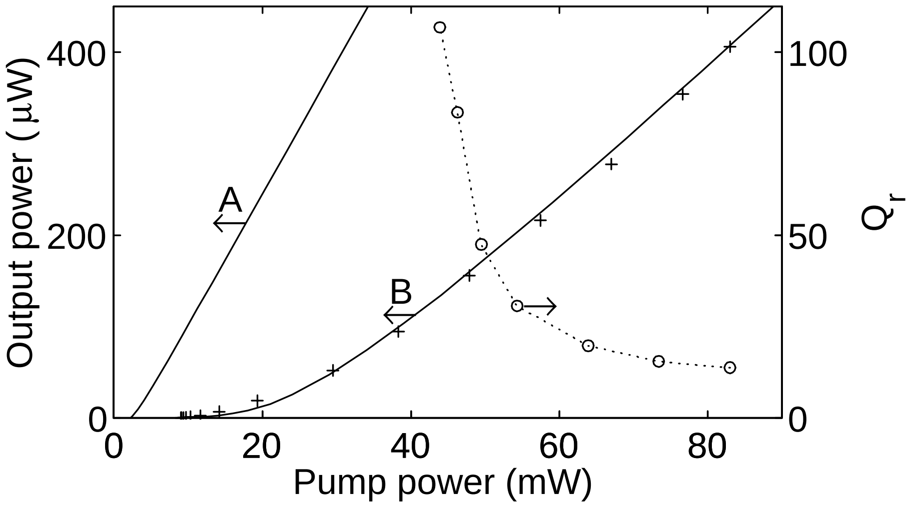

Figure 5.1. Measured laser output power (crosses) and relaxation oscillation Q factor Q_r (circles) versus pump power. Solid lines, theoretical output power assuming that A, $\xi = 0$, $a_0 = 0$; B, $\xi = 37.7\%$, $\zeta = 26$, $a_0 = 0.243$ dB/m.

interrogation of the laser as a sensor, the output power obtained with 1480 nm pumping is more than sufficient.

Before UV exposure the loss saturation versus bleaching power was measured for the laser fiber at 1535 nm. Parameter fitting to these measurements shows that less than $\xi_{\max} = 5$ % of the Er-ions were quenched by the factor $\zeta = 26$. The unbleachable losses were limited to $a_0 < 0.3$ dB/m. Moreover, the transmission spectrum versus pump power measurements show that the effective value of ξ does not vary significantly between 1535 nm and 1549 nm. Consequently, the majority of the bleachable absorbers seem to have been introduced during the UV exposure.

The relaxation oscillation resonance Q factor $Q_r = f_r/\Delta f_r$ of the solitary laser was also measured, and is shown by the open circles in Figure 5.1. Here, f_r is the peak frequency and Δf_r the 3-dB peak width of the intensity noise spectrum. Below a pump level of 40 mW the laser was self pulsing. Above 40mW a steep reduction in Q_r was observed, parallel with the bleaching of the UV-induced absorbers. It is known that bleachable absorbers can cause laser instabilities [6], and we believe that the bleachable absorbers play an important role in reducing the stability of the investigated laser at low pump powers. f_r followed a nearly linear dependence (±1.5 kHz) on the pump power from f_r=109 kHz at 42 mW to f_r=207 kHz at 83 mW.

Figure 5.2 shows the setup that we used to study the effects of backreflections. The laser was pumped from the left, and the left output power was guided

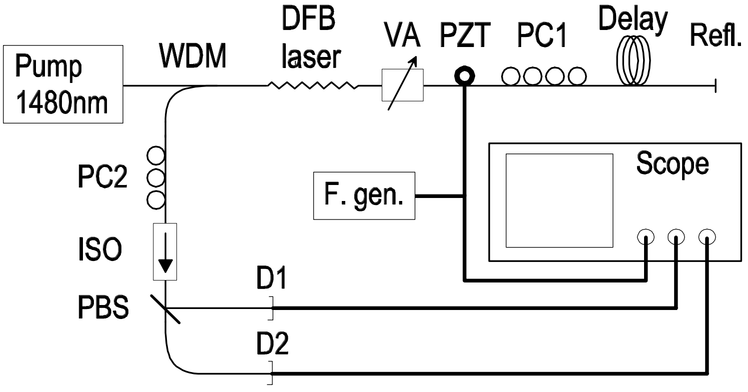

Figure 5.2. Setup for study of backreflection-induced self-oscillations: F.gen., function generator.

through a wavelength division multiplexer (WDM), a polarization controller (PC2), an isolator (ISO) and a polarization beam splitter (PBS) to detectors D1 and D2. PC2 was adjusted such that each detector received light from only one laser polarization mode. Backreflection into the right-hand end of the laser with variable attenuation, phase shift, polarization shift and delay was generated by use of a variable attenuator (VA), a piezoelectric fiber stretcher (PZT), a polarization controller (PC1) and a selection of delay coils with -14.5 dB cleaved end reflectors (Refl.).

With an external cavity length of $L_{ext} = 22.3$ m and a pump power of 83 mW, the effective external reflection coefficient r_{ext} seen by the laser was first adjusted to its critical value, $r_{ext,c} = -28.3 \pm 1$ dB, where relaxation oscillation noise bursts started to occur for worst-case settings of PC1 and the PZT voltage. By "worst-case" we mean that the noise amplitude was at its maximum. Figure 5.3 shows the evolution of the left output power P_{left} from the laser (recorded by D1 + D2) when the PZT was driven by a triangular waveform. The round-trip phase modulation ϕ_{ext} induced by the PZT is also shown in the figure. The periodic relaxation oscillation noise bursts are believed to be related to mode hopping or to unstable regimes at the transitions between external cavity modes [2]. For higher backreflection levels the laser was continuously self-pulsing. The deterministic dependence of P_{left} on ϕ_{ext} is believed to be due to a modulation of the effective right-hand mirror reflectivity of the laser.

When PC1 was in its worst case position, the power fluctuations of the two laser polarization modes were practically equal and in phase. This indicates equal backreflection phase shifts for the two polarizations. For other settings of PC1, the fast relaxation oscillations of the two polarizations would still be in phase, but the sign of the deterministic power oscillations could be made

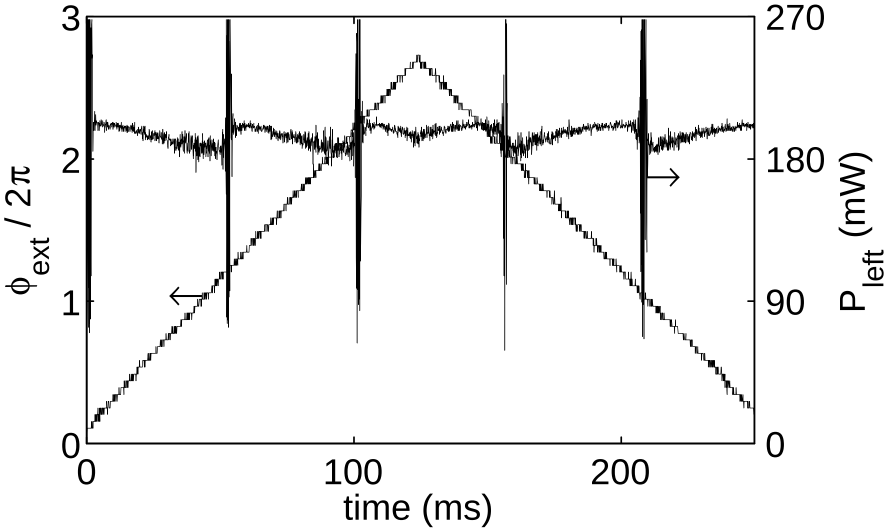

Figure 5.3. Scope traces of the left-hand output laser power P_{left} and of the phase modulation signal ϕ_{ext} applied to the PZT. $L_{ext} = 22.3$ m and $r_{ext} = r_{ext,c}$.

opposite for the two modes. For moderate phase modulation speeds ($d\phi_{ext}/dt <$ 5 rad/ms), $r_{ext,c}$ could be increased by at least 10 dB by adjustment of PC1. However, control of the reflected polarization to ensure stability is believed to be unrealistic in most real applications.

Figure 5.4 shows $r_{ext,c}$ measured for nine different combinations of L_{ext} and pump power, with worst-case settings of PC1. Simulation results reported for semiconductor lasers [7] show that $r_{ext,c}$ versus L_{ext} decreases steeper than −20 dB per decade for $L_{ext} < L_r = c/2nf_r$, and flattens out for longer lengths. Here, L_r corresponds to a feedback delay of one relaxation oscillation period, c being the speed of light in vacuum and n the refractive index of the fiber. The results in Figure 5.4 are in qualitative agreement with the simulations.

For L_{ext} =22.3 and 318 m the measurements satisfy $r_{ext,c} \propto Q_r^{-1}$ to within ±0.6 dB. This is expected, as it can be shown that the phase stability margin of the intensity feedback loop that causes the relaxation oscillation resonance of the solitary laser equals Q_r^{-1} (rad). For L_{ext} =1518 m the deviations from $r_{ext,c} \propto Q_r^{-1}$ are larger. This may be related to variations in the relaxation oscillation phase $\Phi = 2\pi L_{ext}/L_r$ of the external feedback when L_r changes (c.f. table in Figure 5.4).

The feedback parameter [2, 7] C can be written for a DFB laser as

$$\begin{aligned} C &= \sqrt{1+\alpha^2}\frac{2L_{ext}}{L_L}\,T_2\,r_{ext} \qquad (5.1) \\ &= \sqrt{1+\alpha^2}4\kappa\exp(-\kappa L)L_{ext}r_{ext}, \end{aligned}$$

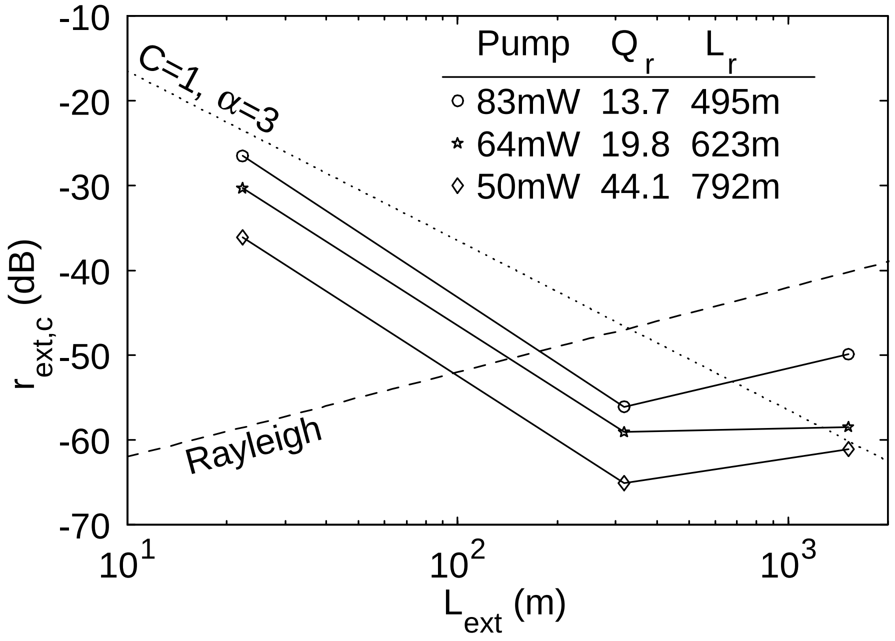

Figure 5.4. Measured critical external reflection coefficient $r_{ext,c}$ for several external cavity lengths L_{ext} and pump powers.

where $L_L = 2/\kappa$ is the effective round-trip path length of the laser, L the DFB-grating length, $T_2 = 4\exp(-\kappa L)$ is the power transmission coefficient of the right half of the grating, $\alpha = d\chi'/d\chi''$ the linewidth broadening factor and $\chi = \chi' + i\chi''$ the complex susceptibility of the gain medium. The limit $C = 1$ when assuming $\alpha = 3$ is shown in Figure 5.4. Below this line, only one external cavity mode solution will exist for any value of ϕ_{ext}, and mode-hopping cannot occur. Still, unlike the findings for semiconductor lasers [2, 7], self oscillations were observed for the laser that we investigated in this regime. This may partly be due to errors in the estimates for α and κ, which may cause significant errors in C. Moreover, it is believed that high-Q_r lasers like the one investigated can become unstable even for $C < 1$. This is because the laser stability margin Q_r^{-1} will be somewhat modified by the backreflection.

Simulation results reported for an Er-doped amplifier [8] indicate that α is proportional to the signal to saturation power ratio P_s/P_{sat}, approaching $\alpha \sim 3$ for $P_s/P_{sat} = 20$. For our laser an effective ratio $4 < P_s/P_{sat} < 20$ is estimated, depending heavily on the $\pm 10\%$ error margin of κ. Thermal effects may also contribute to the effective value of α, as the refractive index depends on the laser power through self-heating of the cavity.

We tested the tolerance to Rayleigh back-scattering by disconnecting the variable attenuator and splicing a coil with standard telecom fiber to the right-hand laser output. The coil end was terminated with bending losses. For 83-mW pump the laser was found to be stable with Rayleigh scattering from $\leq$135 m of fiber. At 135 m noise bursts could be observed in response to severe acoustical noise, such as clapping hands in the laboratory. Bursting or continuous self oscillations were observed for lengths of $\geq$200 m. The dashed line in Figure 5.4 corresponds to a typical Rayleigh back-scattering level of -72 dB/m. The cross-over point between this line and the straight line interconnecting the discrete reflection measurements is at 175 m, which is in good agreement with the Rayleigh measurements.

5.3 Conclusion

In conclusion, we have found that $r_{ext,c}$ has a proportional dependence on the stability margin Q_r^{-1} of the solitary laser, and decreases with increasing external cavity length for $L_{ext} < L_r$. Both the stability margin and the slope efficiency of the laser were found to decrease dramatically at pump powers below 60 mW. This is believed to be related to saturable absorbers introduced during the UV-exposure. The laser frequency noise was not measured in the present experiment. However, recent backreflection studies of similar fiber DFB lasers [9] have shown that the occurrences of excess frequency and intensity noise are highly correlated. One way of improving the tolerance to backreflections may be by increasing κL, as indicated by Eq. (5.1). There is, however, a limit to how high κL can be made before the laser tends to operate in higher order longitudinal modes [4]. Moreover, the effective value of α may increase as the intensity inside the cavity increases with κL, contributing to a reduced backreflection tolerance.

The authors acknowledge Morten Ibsen for providing the DFB grating for this experiment. The experimental part of this work was performed while all three authors were with the Optoelectronics Research Center in Southampton. E. Rønnekleiv acknowledges support from his employer Optoplan AS, the Norwegian Research Council and British Council. O. Hadeler acknowledges support through a CASE award from BICC plc, UK.

References

[1] K. P. Koo and A. D. Kersey, 1996 in *Optical Fiber Communications Conference (OFC)*, Vol. 2 of 1996 OSA Technical Digest Series (Optical Society of America, Washington, D.C., 1996), paper ThP2.

[2] K. Petermann, IEEE J. of Sel. Topics Quantum Electron., **1**, 480 (1995).

[3] L. Dong, W. H. Loh, J. E. Caplen, J. D. Minelly and L. Reekie, Opt. Lett., **22**, 694 (1997).

[4] E. Rønnekleiv, M. Ibsen, M. N. Zervas and R. I. Laming in *Conference on Lasers and Electro-Optics (CLEO)*, Vol. 6 of 1998 OSA Technical Digest Series (Optical Society of America, Washington, D.C., 1998), paper TuE6.

[5] E. Rønnekleiv, M. N. Zervas and J. T. Kringlebotn, IEEE J. Quantum Electron., **34**, 1559 (1998).

[6] D. Marcuse, IEEE J. Quantum Electron., **29**, 2390 (1993).

[7] N. Schunk and K. Petermann, IEEE Photon. Technol. Lett., **1**, 49 (1989).

[8] K. E. Alameh, R. A. Minasian and Y. Zhao, J. Quantum Electron., **33**, 855 (1997).

[9] E. Rønnekleiv and S. W. Løvseth, "Stability of Distributed Feedback Fiber Lasers with Optical Feedback", in *13th International Conference on Optical Fiber Sensors*, Proceedings of SPIE Vol. 3746, pp. 466-469, (1999).

Part III: Polarization Modes

Chapter 6

Modeling of polarization mode competition in fiber DFB lasers[1]

Abstract — A comprehensive model for steady state analysis of polarization mode competition in fiber distributed feedback (DFB) lasers is presented. Effects of polarization dependent grating non-uniformities, polarization dependent grating strength, coupling between the linear polarization states due to twist or Faraday rotation, back reflections, cross-saturation from serially multiplexed lasers, as well as spatially and polarization dependent gain hole-burning are covered by the model. Regimes of single and dual polarization operation are identified for different types of polarization imperfections in the cavity. The output powers of the individual modes and the magnitudes of the hole-burning mechanisms are also calculated and discussed.

Index Terms — DFB lasers, fiber lasers, gain hole-burning, laser mode competition

6.1 Introduction

The fiber distributed feedback (DFB) laser was first demonstrated in 1994 [1]. Since then, promising results have been obtained in understanding and improving the processes governing output power efficiency and output intensity

---

[1] This chapter contains a re-edited version of [E. Rønnekleiv, M. N. Zervas and J. T. Kringlebotn, "Modelling of Polarization Mode Competition in Fiber DFB Lasers", IEEE J. of Quantum El., Vol. 34, pp. 1559-1568, 1998] which has been modified to include the corrections and the extensions to theory contained in [E. Rønnekleiv, M. N. Zervas and J. T. Kringlebotn, "Correction to "Modelling of Polarization Mode Competition in Fiber DFB Lasers"", IEEE J. of Quantum El., Vol. 35, pp. ??, July 1999].

noise from these devices [2], [3]. Advances in fiber Bragg grating technology also indicates that it soon will be possible to produce high quality fiber DFB lasers with high reproducibility and yield.

One motivation for investigating polarization mode competition (PMC) in fiber DFB lasers is the possibility of using dual polarization fiber DFB lasers as sensor elements in polarimetric sensor applications. By measuring the beat-frequency between the polarization modes, the birefringence within the laser cavity can be determined with high accuracy [4]. However, as observed in [4], maintaining robust dual polarization operation in sensor lasers may be difficult due to non-uniformity of the birefringence changes introduced when the laser is brought into contact with the measurand.

Another motivation for this work is the requirement of single polarization operation in lasers for telecommunication applications. Single polarization has been observed in experiments [2], [3], [5]-[7], but the qualitative and quantitative understanding of the requirements for single or dual polarization operation is still poor.

Since Kogelnik *et. al.* introduced the DFB laser and applied the coupled mode theory to model such a laser in [8], much work has been dedicated to the modeling and understanding of semiconductor DFB lasers [9]-[11]. Much of this work is also relevant for fiber DFB-lasers. However, there are also important differences between semiconductor and fiber lasers, regarding waveguide geometries, gain medium properties and the maximum available grating strength (κL). These differences call for a separate treatment of fiber lasers, like in [12]. PMC has not been much discussed in relation to semiconductor lasers, since robust single polarization operation seems easily obtainable in the non-circular waveguide geometries used.

PMC in fiber DFB lasers depends on a number of parameters and effects. These include non-uniform birefringence, twist of the birefringence axes, polarization dependence of the grating strength, back reflections, gain cross-saturation from other lasers in serially multiplexed systems, as well as gain hole-burning effects. The work presented in this paper is aimed at obtaining a better understanding of these effects and how they affect the laser operation.

The organization of this paper is as follows: In Section 6.2 we generalize the DFB coupled mode equations to include polarization coupling from twist or Faraday rotation. The grating super-mode solutions are introduced and briefly discussed. Section 6.3 introduces the gain saturation model used in our simulations, and Section 6.4 presents a way of quantifying the contributions to PMC from various gain hole-burning mechanisms. In Section 6.5, simulation results are presented that illustrate the effects of various types of polarization imperfections on the requirements for single or dual mode laser operation. Section 6.6 contains some concluding remarks. Details on the calculations of the polarization gain hole-burning, spatial distributions of different gain hole-burning contributions, and a description of the numerical algorithm used for the simulations are given in Appendixes 6.A, 6.B, and 6.C respectively.

6.2 Coupled Mode Formulation

The electric field $\vec{E}\,(z,t)$ in a birefringent single mode fiber Bragg grating may be decomposed into the complex amplitudes of four intrinsic fiber modes. By "intrinsic" modes we mean the linearly polarized propagation modes when gain, loss and grating perturbations are removed. In vector notation we may write:

$$\vec{E}\,(z,t) = \mathbf{F}\,\vec{A}\,e^{i\omega t}\,; \quad \mathbf{F} = \begin{bmatrix} e^{-iK_Bz} & 0 & 0 & 0 \\ 0 & e^{-iK_Bz} & 0 & 0 \\ 0 & 0 & e^{iK_Bz} & 0 \\ 0 & 0 & 0 & e^{iK_Bz} \end{bmatrix}$$

with $\vec{A} = [\ r_x \quad r_y \quad s_x \quad s_y\ ]^T$. r and s represent the forward and backward propagating modal field amplitudes, respectively, and the subscripts x and y distinguish the polarization modes. Superscript T is used for matrix transposition. The phase of the elements of $\vec{A}$ are normalized with respect to the Bragg wave-number $K_B = \pi/\Lambda$, Λ being the grating period, through the diagonal matrix $\mathbf{F}$. ω, t and z denote frequency [rad/s], time and position along the fiber axis, respectively.

We assume K_B to be independent on z and express the propagation constants of the intrinsic polarization modes as

$$\beta_m = K_B + \Delta\beta_m + \delta\,; \quad m = x,\, y. \tag{6.1}$$

$\Delta\beta_m$ is the deviation due to birefringence and z-dependence of the refractive index. $\delta = (\omega - \omega_0)\,\partial\beta/\partial\omega$ (rad/m) is the detuning referenced to a nominal Bragg frequency $\omega_0 = K_B c/n$. c is the speed of light in vacuum and n is a nominal refractive index which is independent of polarization and position.

The polarization mode coupling originating from twist of the birefringence axes or Faraday rotation is deduced in [13] and [14]. A model for coupling between forward and backward propagating waves due to the index and gain gratings, including the effects of the mean gain or loss, is deduced in [11]. We here combine these effects in a 4-mode matrix coupling equation:

$$\frac{d\vec{A}}{dz} = \mathbf{C}_{tot}\vec{A}\,; \quad \mathbf{C}_{tot} = \mathbf{C} + \mathbf{G} + \mathbf{D}. \tag{6.2}$$

Here

$$\begin{aligned}
\mathbf{D} &= \begin{bmatrix} -1 & 0 & 0 & 0 \\ 0 & -1 & 0 & 0 \\ 0 & 0 & 1 & 0 \\ 0 & 0 & 0 & 1 \end{bmatrix} i\delta \\
\mathbf{G} &= \begin{bmatrix} g & 0 & g_{gr} & 0 \\ 0 & g+\Delta g & 0 & g_{gr}+\Delta g_{gr} \\ -g_{gr}^{*} & 0 & -g & 0 \\ 0 & -g_{gr}^{*}-\Delta g_{gr}^{*} & 0 & -g-\Delta g \end{bmatrix} \\
\mathbf{C} &= \begin{bmatrix} -d_x & r+\rho & i\kappa_x & 0 \\ -r-\rho & -d_y & 0 & i\kappa_y \\ -i\kappa_x^{*} & 0 & d_x & r-\rho \\ 0 & -i\kappa_y^{*} & -r+\rho & d_y \end{bmatrix}
\end{aligned}$$

and

$$d_m = i\Delta\beta_m - a\,.$$

For practical reasons we have divided the total coupling matrix $\mathbf{C}_{tot}$ into three parts. $\mathbf{D}$ contains the frequency dependence. $\mathbf{G}$ contains parameters that are dependent on the pumping and saturating fields, and $\mathbf{C}$ contains the remaining signal- and frequency-independent parameters.

g is the amplitude gain coefficient (resulting from the gain medium) and g_{gr} is the (complex) gain grating amplitude. Δg and Δg_{gr} are the gain and gain grating differences between the birefringence axes due to polarization hole-burning (PHB). a is the intrinsic loss coefficient and κ_m is the index coupling strength in the $m = x$ or y mode. The complex conjugation of κ_m in the lower left part of $\mathbf{C}$ is included for completeness only, since the assumption of a z-independent Bragg period means that κ_m can always be assumed to be real. The polarization coupling parameters r and ρ (rad/m) represent the twist rate of the birefringence axes and the Faraday rotation coefficient (in case of magnetic fields present), respectively. Note that in the case of twist, the field vector components of $\vec{A}$ refer to a twisted coordinate system that follows the birefringence axes of the fiber.

The general solution of (6.2) may be written as a linear combination of four grating "super-modes":

$$\vec{A} = \sum_{i=1}^{4} a_i\,\vec{u}_i e^{-(\gamma_i + i\zeta_i)z} \tag{6.3}$$

The eigenvectors $\vec{u}_i$ and propagation constants $-(\gamma_i + i\zeta_i)$ are the eigenvectors and eigenvalues of $\mathbf{C}_{tot}$. ζ_i may be interpreted as the difference between the spatial frequency of the super-mode and the Bragg wave-number K_B. γ_i is the modal attenuation coefficient. In general the eigenvalues occur in reciprocal pairs with opposite signs of ζ_i and γ_i.

With no cross-coupling between the polarization states (r, $\rho = 0$) the linear polarizations are decoupled, leading to two x- and two y-polarized super-modes. The full dispersion map of one such mode, in absence of any gain, loss or gain grating, was illustrated in [15]. Within the stop-band of each polarization, given by $|\delta + \Delta\beta_m| < \kappa_m$, there is a reciprocal set of two super-modes with $\zeta_i = 0$ and $\gamma_i = \pm\sqrt{(\delta + \Delta\beta_m)^2 + \kappa_m^2}$.

With the gain or loss magnitudes usually present in fiber DFB lasers (g, g_{gr}, $a \ll \kappa_m$), the modifications of the eigen-solutions in (6.3) are small. In an ideal half-period phase-shifted DFB laser operating in the fundamental longitudinal laser mode, the super-modes with $\gamma_i < 0$ will dominate to the left of the grating phase-shift and those with $\gamma_i > 0$ will dominate to the right. Since the laser operates at the center of the stop-band, the intensity will decay with an exponential rate of $2\gamma_{max} = \pm 2\kappa_m$ from the phase-shift position, where γ_{max} is the value of γ_i at the center of the stop band. This κ_m-dependence of the decay rate is important for the interpretation of simulation results in section 6.5

6.3 Gain Model

We have focused on Er-doped amplifier media, which can be modelled by the 2-level rate equations [16]. At a position z in the cavity the local amplitude gain is approximated as:

$$g_{loc}(\phi) = \frac{g_{unsat}}{1 + P_s/P_{sat}}; \quad g_{unsat} = \frac{a_p r_{wl} P_p}{P_{sat}} - a_s \tag{6.4}$$

with

$$\begin{aligned} P_{sat} &= \left(\left[g_p + a_p\right] r_{wl} P_p + P_{sp}/2\right) \left(g_s + a_s\right)^{-1} \\ P_s &= \sum_{m=1}^{N_m} \left(\left|\vec{R}_m\right|^2 + \left|\vec{S}_m\right|^2 + 2\,\mathrm{Re}\left(e^{i\phi} \vec{S}_m^{+} \vec{R}_m\right) \right). \end{aligned}$$

Here $\phi = 2K_B z$ describes the phase relative to the index grating. g_{unsat} is the unsaturated gain, P_{sat} is the saturation power at the signal wavelength, and P_p and P_s are the pump and signal powers. $\vec{R}_m = [r_x, r_y]_m$ and $\vec{S}_m = [s_x, s_y]_m$ are the right and left propagating fields of laser mode m, $m = 1..N_m$. This notation covers any number N_m of lasing modes. In the following sections, when only two polarization modes are involved, the letters $m = x, y$ will be used as mode indexes. $\vec{S}_m^{+}$ is the transposed conjugate of $\vec{S}_m$. The gain medium parameters

g_s, g_p, a_s and a_p represent signal and pump gain at full inversion and signal and pump absorption at zero inversion, respectively. $P_{sp} = n_{Er} h\nu_s/\tau_{sp}$ (W/m) is the spontaneous emission power per unit length of fiber at full inversion, with τ_{sp} being the spontaneous emission time, $h\nu_s$ the signal photon energy, and n_{Er} the ion concentration per unit fiber length. r_{wl} is the ratio of the pump wavelength to the signal wavelength.

The gain and gain grating coefficients g and g_{gr} that appear in (6.2) are given by the zeroth and first order Fourier components of $g_{loc}(\phi)$, respectively [17], [18]. Based on (6.4) we generalize the expressions in [17] and [18] to allow for multiple and arbitrarily polarized laser modes:

$$\begin{aligned} g &= g_{unsat}\left[(1+p_{tot})^2 - 4\left|p_c\right|^2\right]^{-1/2} \\ g_{gr} &= \frac{g_{unsat}}{2p_c^*}\left[1-(1+p_{tot})\left[(1+p_{tot})^2 - 4\left|p_c\right|^2\right]^{-1/2}\right]. \end{aligned} \tag{6.5}$$

Here

$$p_{tot} = \sum_{m=1}^{N_m} \frac{\left|\vec{R}_m\right|^2 + \left|\vec{S}_m\right|^2}{P_{sat}}; \quad p_c = \sum_{m=1}^{N_m} \frac{\vec{S}_m^{+}\vec{R}_m}{P_{sat}}.$$

Note that the gain grating coefficient g_{gr} has the same phase as the normalized standing wave power phasor p_c.

The pump absorption follows from the rate equations as:

$$a_{pump} = a_p - \frac{g_p + a_p}{g_s + a_s}(g + a_s). \tag{6.6}$$

Eqs. (6.4) to (6.6) cover the spatial hole-burning mechanisms. In addition, polarization hole-burning (PHB) should be included in the model. PHB effects in erbium-doped fiber amplifiers (EDFAs) have been studied in [19]-[22], and comprehensive ion anisotropy models as well as simplified approximate formulas are presented in [21] and [22]. However, those simplified formulas do not describe a reduction of the PHB magnitude at high gain compressions ($P_s/P_{sat} > 1$) predicted by the comprehensive models. Numerical implementation of the comprehensive ion anisotropy models (c.f. Appendix 6.A) indicates that the local gain difference between the polarization state of the saturating signal and the orthogonal state Δg_{loc} may be approximated by:

$$\frac{\Delta g_{loc}}{g_{unsat}} \approx \frac{\eta\, D_p\, P_s/P_{sat}}{(1+P_s/P_{sat})^2}. \tag{6.7}$$

Here D_p is the degree of linear polarization of the total power at the lasing wavelength, defined in our model by (6.8) below. η is a material parameter

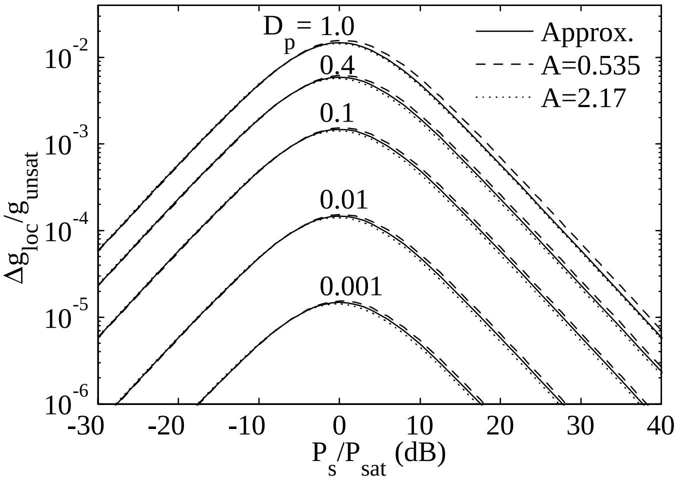

Figure 6.1. Normalized local PHB magnitude $\Delta g_{loc}/g_{unsat}$ versus normalized saturating power P_s/P_{sat} with various degree of linear polarization D_p. Solid lines: Approximation (6.7) with $\eta = 0.059$. Dashed/dotted lines: Model of Wysocki et. al. [15].

that depends on the magnitude of the ion anisotropy. When estimating η from PHB measurements on EDFAs, it is necessary to eliminate the effects of the random evolution of D_p along the EDFA, as well as the contribution to the measured EDFA saturation from pump absorption. Wysocki *et.al.* [21] have taken these effects have been taken into account when estimating the ion anisotropy parameter (ratio of ion cross-sections orthogonal and parallel to the optical axis of each ion, c.f. Appendix 6.A.) for an EDFA fiber to $A = 0.535$ or $A = 2.17$. Based on those estimates we estimate $\eta = 0.059$ in Appendix 6.A.

Fig. 6.1 illustrates the dependence of $\Delta g_{loc}/g_{unsat}$ on P_s/P_{sat} and D_p approximated by (6.7) with $\eta = 0.059$ (solid lines), and calculated from Wysocki's model [21] (dashed and dotted lines). The approximation error is within +10% and −18%. Note the drop in Δg_{loc} at high intensities. (6.7) may be reduced to $\Delta g_{loc} \approx \eta D_p(g_{unsat} - g_{loc})$ for $P_s \ll P_{sat}$, where g_{loc} is the saturated gain. This is consistent with previously published approximations.

In a dual polarization laser the saturating power will be only partly polarized, since the combined polarization state within the cavity oscillates at the beat frequency between the laser modes. The degree of polarization may vary spatially over a standing wave period if the standing waves in the two polarizations are not in phase. However, in those cases the spatial hole-burning effect on the PMC due to g_{gr} is expected to dominate over the PHB effects due to the polarization dependence Δg_{gr} of g_{gr}, and no significant error in the simulations should thus be introduced by ignoring this spatial modulation of D_p. For use in our model we therefore define an effective degree of polarization as the signed quantity in terms of the mean x- and y-polarized signal powers averaged over one standing wave period, denoted P_x and P_y:

$$\begin{aligned} D_p &\approx (P_x - P_y) / (P_x + P_y) \\ &= \frac{1}{p_{tot} P_{sat}} \sum_{m=1}^{N_m} \left(|r_{x,m}|^2 + |s_{x,m}|^2 - |r_{y,m}|^2 - |s_{y,m}|^2 \right) . \end{aligned} \tag{6.8}$$

As explained in Appendix 6.A, (6.7) leads to the following expressions for the polarization dependent gain parameters of (6.2) provided that D_p is does not vary over the standing wave period:

$$\begin{aligned} \Delta g &= \eta D_p \frac{\left(p_{tot} + p_{tot}^2 - 4 |p_c|^2 \right)}{\left[(1+p_{tot})^2 - 4 |p_c|^2 \right]^{3/2}} \\ \Delta g_{gr} &= \frac{\eta D_p}{2 p_c^*} \left\{ 1 + \frac{\left(8 |p_c|^2 + 4 |p_c|^2 p_{tot} - (1+p_{tot})^3 \right)}{\left[(1+p_{tot})^2 - 4 |p_c|^2 \right]^{3/2}} \right\} . \end{aligned} \tag{6.9}$$

It may be noted that PHB contributions due to the circularly polarized part of the saturating field, reported in [20], are not taken into account in (6.9). However, for the present simulations (Section 6.5) the field ellipticities are low or zero, and the omission of this effect should not affect the results significantly.

6.4 Quantitative measures of gain saturation

In earlier work [8]-[11] the single-pass gain parameter, defined as the gain experienced by a probe beam passing through the laser without interacting with the reflectors, was used to study and compare modal thresholds. This parameter, however, cannot reveal the important effect of gain hole-burning on multimoded laser operation.

An alternative measure for the threshold gain requirements of mode m is the contribution rtg_m from the gain medium to the total modal round-trip gain RTG_m (defined in Appendix 6.B). This parameter may be defined as:

$$rtg_m = \frac{P_{gain}}{P_c} \tag{6.10}$$

where P_{gain} is the power transferred from the gain medium to the laser mode and $P_c = \left| \vec{R}(z_c) \right| \cdot \left| \vec{S}(z_c) \right|$ is the geometric mean of the modal powers travelling in the right and left direction at the center z_c of the laser. rtg_m compensates exactly the cavity losses of any lasing mode.

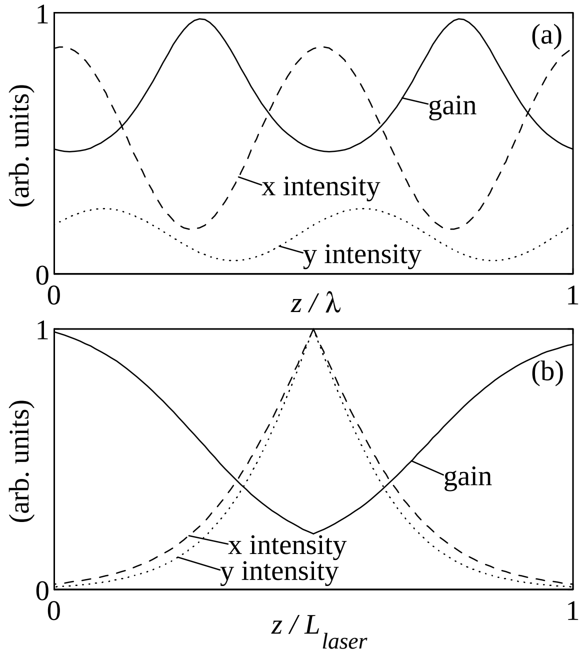

Figure 6.2. Examples of (a) local spatial hole-burning (LSHB) and (b) global spatial hole-burning (GSHB).

The difference $\Delta rtg_{total} = rtg_y - rtg_x$ between the gain contributed to the laser polarization modes ($m = x, y$) must be due to the spatial and polarization hole-burning mechanisms, i.e. different effective overlaps in space and polarization between the gain distribution and the modal intensity distributions. Three contributing hole-burning mechanisms have been identified:

Δrtg_p PHB contribution due to the polarization dependence of g and g_{gr} (c.f. (6.9)).

Δrtg_l Local spatial hole-burning (LSHB) contribution which is present if the two modal standing wave patterns have different phases relative to the gain grating. This situation is illustrated in Fig. 6.2 (a).

Δrtg_g $= \Delta rtg_{total} - \Delta rtg_p - \Delta rtg_l$. Global spatial hole-burning (GSHB) contribution, which is due to the different global overlaps of the modal field distributions and the gain, as illustrated in Fig 6.2 (b).

A more detailed description of how the hole-burning contributions are calculated is given in Appendix 6.B.

6.5 Simulation Results

A numerical approach, described in Appendix 6.C, has been used to compute the expected PMC behavior of fiber DFB lasers with different types of polarization imperfections. By polarization imperfections we mean asymmetries between polarization states that cause differences between the output powers of the two polarization modes. The expressions for mode-coupling, gain saturation and pump absorption described in Sections 6.2 and 6.3 were used for the calculations.

The basic structure to which the polarization imperfections were added was a $L = 70$ mm uniform grating with a π (half period) phase-shift in the center. The gain medium parameters used were $[g_s, g_p, a_s, a_p] = [22, 2.74, 20, 8]$ dB/m, $P_{sp} = 5.2$ mW/m, $r_{wl} = 0.961$, and $\eta = 0.059$. These numbers are representative for a highly Er-doped fiber pumped at 1480nm and lasing at 1540nm, with a maximum gain (when $P_p \to \infty$) at the laser wavelength of 11.3 dB/m, and with a pump saturation power of 2.95 mW. The intrinsic loss a was assumed to be zero. A pump power of $P_{p0} = 50$ mW launched from the left end ($z = 0$) was assumed for all the simulations.

Note that due to the scaling properties of the coupling equation (6.2), all results given in this section are valid for any scaling of the z-axis, provided that the normalized values for the detuning $\delta_m L$, gain medium parameters $g_s L, g_p L, a_s L$, $a_p L$ and the parameters contained in $\mathbf{C}L$ are all preserved.

The main results are plotted in Figs. 6.3-6.5, 6.7, 6.8, and 6.11, with the magnitudes of different polarization imperfections along the respective horizontal figure axes. Row (a) of these figures shows the regimes of grating strength κL that cause single and dual polarization operation. The single and dual mode thresholds computed were, except for the case with cross-saturation in Fig. 6.10, found to be quite insensitive to further increases of the pump power towards infinity.

In row (b) the magnitudes of the different gain hole-burning contributions at the border between the single and dual polarization regimes of row (a) are illustrated with curves for Δrtg_l, $\Delta rtg_l + \Delta rtg_p$ and Δrtg_{total}, c.f. Section 6.4. Note that Δrtg_g is given implicitly by the relation $\Delta rtg_{total} = \Delta rtg_l + \Delta rtg_p + \Delta rtg_g$.

In row (c) $\kappa L = 9$ is assumed. The absorbed pump power and the total output power (right+left) of both laser modes are plotted. The left to right output power ratio of the individual modes (not displayed) was found to be within 1 ± 0.002 in all cases, except for the case of back reflection in Fig. 6.9. In that case the left to right output ratios was within 1 ± 0.05 for back reflections below -32 dB.

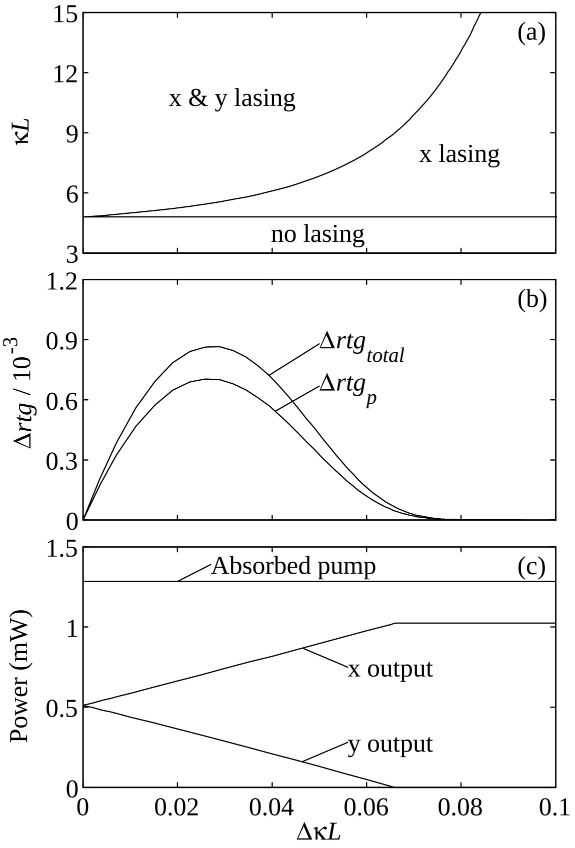

Figure 6.3. (a) Regimes of single and dual polarization operation, (b) differential gain contributions ($\Delta rtg_l = 0$ in this case) and (c) output power and absorbed pump power. All quantities are plotted against a polarization dependence of the grating strength $\Delta\kappa L$.

6.5.1 Polarization dependent grating strength

Fig. 6.3 illustrates how the PMC evolves with a polarization dependence of the grating strength, quantified by $\Delta\kappa L$ where $\kappa = \kappa_x$ and $\Delta\kappa = \kappa_x - \kappa_y$.

Fig. 6.3 (a) shows that the dual polarization threshold increases slowly at low polarization imperfection magnitudes. At higher magnitudes, $\Delta\kappa L \gtrsim 0.04$, the slope of the threshold starts increasing progressively. The single polarization threshold stays unchanged, as expected since the grating strength κ_x experienced by the first lasing mode is not changed.

From Fig. 6.3 (b) we see that the hole-burning contribution Δrtg_{total} to the differential round-trip gain at the dual polarization threshold increases towards a maximum at $\Delta\kappa L = 0.027$ and then decreases for higher imperfection magnitudes, approaching zero very rapidly for $\Delta\kappa L \gtrsim 0.06$. Δrtg_{total} is seen to be composed mainly from the PHB contribution Δrtg_p at low values of

$\Delta\kappa L$. The LSHB contribution is zero, since the phase of the modal standing wave intensity modulation is independent on the coupling parameter $\kappa_{x,y}$. The GSHB contribution $\Delta rtg_g = \Delta rtg_{total} - \Delta rtg_p$ contributes somewhat, due to the different spatial decay rates of modal intensities from the center of the cavity (c.f. the end of section 6.2).

The cold cavity round-trip loss rtg_{loss} for a mode may be expressed as the ratio between the total laser output power arising from that mode and the modal power travelling in one direction at the center of the grating. It can be shown (c.f. the end of Sec. 6.2) that

$$rtg_{loss} \approx 8\exp(-\kappa L)) \tag{6.11}$$

The difference in rtg_{loss} between the polarization modes due to $\Delta\kappa$ must equal Δrtg_{total}, which implies the following relation:

$$\Delta rtg_{total} \approx 8\Delta\kappa L\exp(-\kappa L). \tag{6.12}$$

Analysis of the dual polarization thresholds and total hole-burning magnitudes plotted in Figs. 6.3 (a) and (b) confirm the relation (6.12).

The evolution of the dual polarization threshold κL versus $\Delta\kappa L$ in Fig.6.3 (a) is decided by the condition that the gain difference due to the hole-burning must match the gain difference in (6.12). The available hole-burning contribution depends on the effective level of the saturating signal intensity P_s within the cavity. As mentioned in Sec. 6.2, P_s decays exponentially on a global scale from the central phase-shift position, with an exponential decay rate of $2\kappa_{x,y}$. This decay implies that most of the stored laser energy is concentrated near the center of the grating. It follows from (6.11) that the saturating power P_s at the central phase-shift position equals $4\exp(\kappa L)$ times the one way laser output power. P_s in the central region of the cavity thus increases exponentially with κL.

At small values of $\Delta\kappa L$ we see from Fig.6.3 (a) that the dual polarization threshold value for κL is close to the single polarization threshold. The effective saturation intensity in the cavity therefore increases relatively slowly in this regime, due mainly to the increase in laser output power as κL increases above the single polarization threshold. The increase in Δrtg_p with $\Delta\kappa L$ within this regime may be explained by the increase in PHB magnitude with increasing saturating power for $P_s/P_{sat} < 1$, as seen in Fig. 6.1.

The laser output power saturates when κL increases well above the single mode threshold. The effective saturating power in the cavity is then essentially proportional to $4\exp(\kappa L)$. Fig. 6.1 and (6.7) show that the PHB is inversely proportional to P_s/P_{sat} at high saturating powers, and Δrtg_p is therefore essentially proportional to $\exp(-\kappa L)$ at these high κL-values. By comparing with

(6.12) we see that the increase in the required Δrtg_{total} as $\Delta\kappa L$ increases can not be compensated solely by the PHB in this regime by increasing κL. Actually, the ratio $\Delta rtg_g/\Delta rtg_p$ increases with $\Delta\kappa L$ in Fig. 6.3 (b), confirming that the GSHB plays an increasingly important role as $\Delta\kappa L$ increases.

Analytic approximations like the one in (6.12) for the required hole-burning at dual polarization operation are not available for the other types of polarization imperfections discussed in the following sub-sections. However, as seen from (6.11), the round-trip loss of each laser mode in an ideal cavity decreases exponentially with increasing κL. It is therefore reasonable to believe that differential losses introduced by other types of polarization imperfections will also decrease rapidly with increasing κL.

Fig. 6.3 (c) shows that for $\kappa L = 9$ the laser will be single-moded, as required for a telecommunication CW-source, when $\Delta\kappa L > 0.066$. For birefringence sensors applications a polarization output power ratio smaller than 2 is a reasonable requirement, for which $\Delta\kappa L < 0.023$ is needed.

Polarization dependencies up to 8 % of the total photoinduced index change was reported in [23], depending on the polarization of the UV-exposure and on fiber properties. One may expect similar values for $\Delta\kappa/\kappa$ in a photoinduced grating. Even higher values for $\Delta\kappa/\kappa$ were reported in [24] for a fiber with high stress-induced birefringence. Control of the polarization of the UV-exposure thus seems to be important for controlling the PMC in fiber DFB lasers.

6.5.2 Polarization dependent chirp

Fig. 6.4 illustrates how PMC depends on chirp of the y polarization propagation constant β_y. This is equivalent to chirping of the y polarization Bragg wavelength while the x polarization Bragg wavelength is kept constant. Solid and dashed lines illustrate linear and square chirp, respectively, as given by (c.f. (6.1))

$$\begin{aligned} \Delta\beta_y &= \Delta\beta\,(z - L/2)/L && \text{(linear chirp)} \\ \Delta\beta_y &= 4\,\Delta\beta\,(z - L/2)^2/L^2 && \text{(square chirp).} \end{aligned} \tag{6.13}$$

The results in Fig. 6.4 are qualitatively similar to those shown for the polarization dependent grating strength in the previous section, except for he dual polarization threshold for the square chirped laser in Fig. 6.4 (a) which shows signs of saturating for $\Delta\beta L \gtrsim 5$. Unlike the case illustrated in the last section, there are also some contributions to Δrtg_{total} from LSHB in the chirped lasers, since the standing wave phase is affected by the polarization dependent variations of the propagation constant throughout the cavity.

Polarization dependent chirp may be due to any source of birefringence that is non-uniformly distributed along the fiber, such as UV-exposure (c.f. previous section), externally applied transverse forces, bending, internal stress in

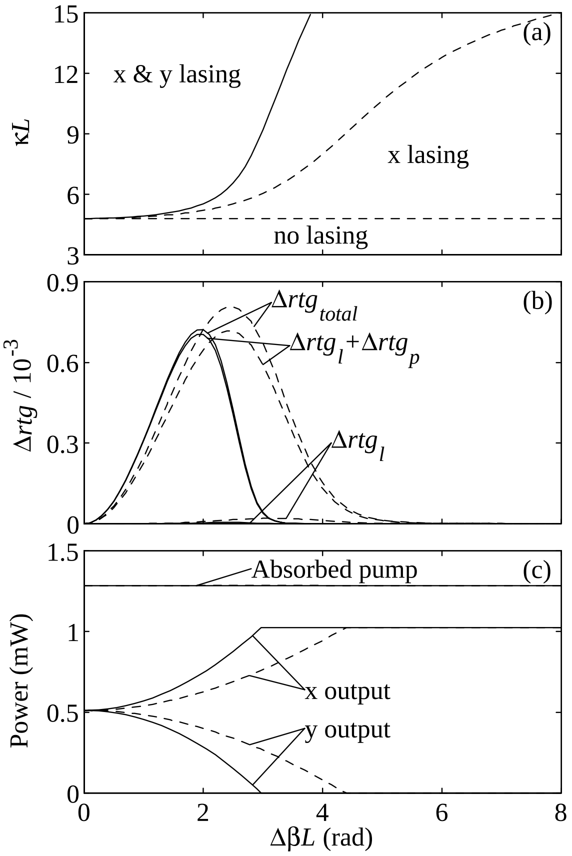

Figure 6.4. Same information as in Figure 6.3 plotted against linear chirp (dashed lines) and square chirp (solid lines) of β_y, c.f. eq. (6.13).

the fiber, or core ellipticity. In some sensor applications, where external forces are supposed to act on the fiber, the uniformity of some of these effects may be difficult to control. On the other hand, single polarization operation for telecommunication lasers may be achieved by manipulating the birefringence intentionally.

The assumption of chirp in only one axis, which has been used here, may not be realistic in many cases. Theoretical calculations of stress-induced birefringence suggest a ratio $\Delta\beta_y/\Delta\beta_x = -2.5$ for bending [14] and $\Delta\beta_y/\Delta\beta_x \sim -5$ for transverse forces applied externally to the fiber [14], [25], [26]. In the case of transverse forces, however, these calculations do not take common mode index change due to axial stress or coating effects into account, and experimental results have been published with differing $\Delta\beta_y/\Delta\beta_x$ ratios. In [4] a ratio of 50 was observed with an uncoated fiber DFB laser. Measurements on passive Bragg gratings show ratios of 7 for an uncoated fiber [27] and 1.37 for an acrylate coated fiber [28]. In the acrylate-coated case a significant chirp would

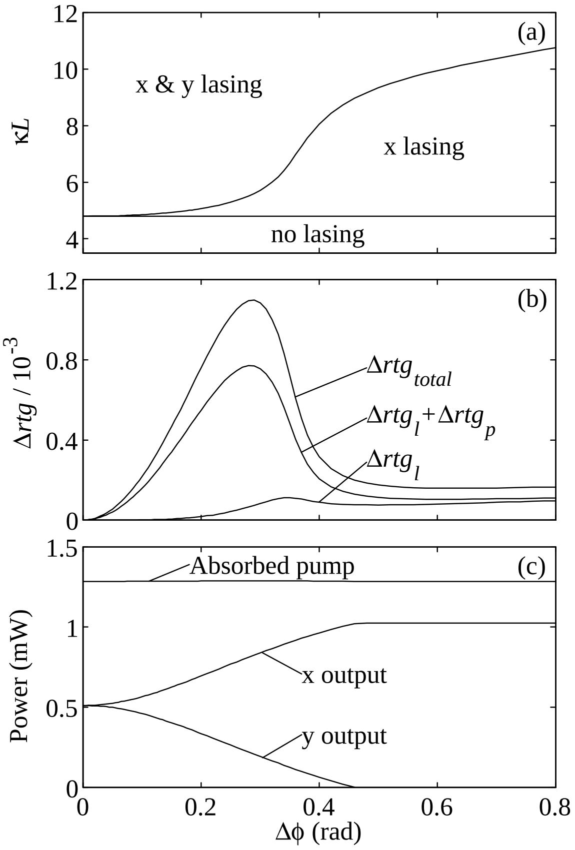

Figure 6.5. Same information as in Figure 6.3 plotted against a grating phase error $\Delta\phi$ in the y polarized mode localized to the center of the grating.

thus be imposed in both polarizations, and the curves in Fig. 6.4 would not be quantitatively representative.

According to the theory $\Delta\beta_y L = 1$ corresponds to a bending diameter of about 20mm or to axial forces in the order of 0.04N/mm in a fiber DFB laser of length $L = 70$ mm.

6.5.3 Polarization dependent phase error

Fig. 6.5 illustrates how PMC depends on a grating phase error (round-trip phase) $\Delta\phi$ in the y propagation mode only, localized at the center of the grating.

For comparison, the square chirp (dashed lines) in Fig. 6.4 can be viewed as a highly distributed phase error of magnitude $\Delta\phi \sim \Delta\beta L$. By comparing Figs. 6.4 (a) and 6.5 (a) we see that the dual mode threshold is much more sensitive to localized phase errors. The spatial hole-burning effects, though, are seen to be stronger in Fig. 6.5 (b) than in Fig. 6.4 (b).

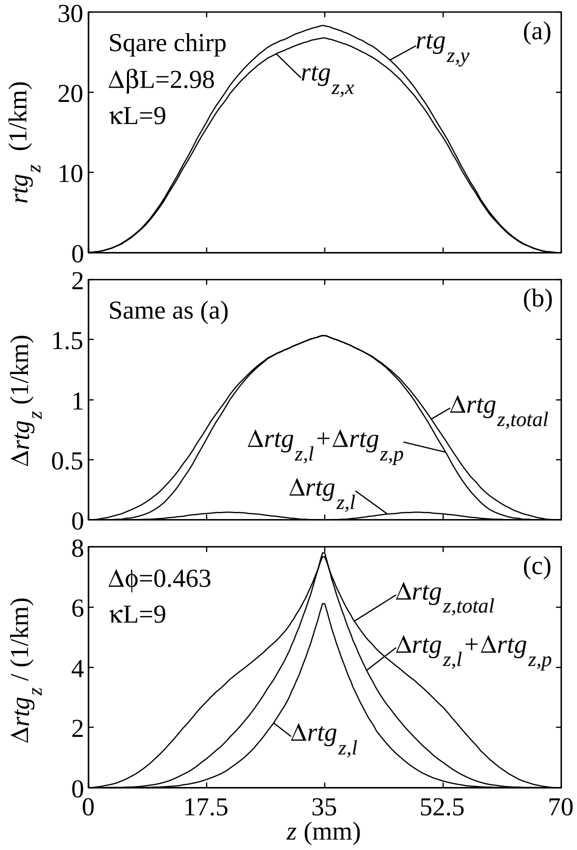

Figure 6.6. Spatial gain and differential gain contributions at the dual polarization threshold when $\kappa L = 9$. (a) Modal round-trip gain contributions for the square chirped laser illustrated with dashed lines in Fig. 6.4 (b). (b) Differential gain contributions for the same laser as in (a). (c) Differential gain contributions for the laser illustrated in Fig. 6.5 (b).

To give an indication of how the gain contribution per unit length to the individual modes may look like, the z-derivatives $rtg_{z,x}$ and $rtg_{z,y}$ of the modal gain contributions (i.e. the integrand of (6.15)) are plotted in Fig. 6.6 (a) for the square chirp case of (6.13) with $\Delta\beta L = 2.98$ and $\kappa L = 9.0$, i.e. at the dual polarization threshold of Fig. 6.5 (c). The relatively flat shapes of $rtg_{z,x}$ and $rtg_{z,y}$ indicate a strong saturation of the gain near the center, since the power penetration depth is only $(2\kappa)^{-1} = 3.9$ mm.

The z-distributions of the hole-burning contributions are illustrated in Fig. 6.6 (b) for the same laser as the one illustrated in Fig. 6.6 (a). Fig. 6.6 (c) shows the z-distributions of the different hole-burning contributions at the dual polarization threshold for a laser with a localized phase error, with $\kappa L = 9.0$ and $\Delta\phi = 0.463$. The relatively strong spatial hole-burning effect near the phase-shift position in Fig. 6.6 (c) may be explained by considering the phase of the standing wave pattern of the y-mode relative to the index grating, which close to the phase-shift position differs by $\pm\Delta\phi/2 = \pm0.2315$ rad from its ideal value. This causes significant LSHB contributions in the central region, and it also increases the effective power penetration depth of the y-mode, giving rise to significant GSHB contributions further away from the center, as is clearly seen in the figure.

In Fig. 6.6 (b) the LSHB and GSHB contributions are close to zero. This reflects that the phase difference between the standing waves of the two modes stays small throughout the central part of the grating, implying similar global intensity decay rates for the two modes in this region. The deviation in the of the y-index grating phase from an ideal non-chirped grating occurs mostly near the ends of the cavity, and the differential cavity loss is therefore mainly due to different intensity decay rates for the two modes in these end regions.

Polarization dependent phase-shifts can be achieved by post-exposure of a few millimeters of the fiber after grating inscription, and stable single polarization lasers have been reported by use of this technique [7]. If the length of the exposed section is comparable to or longer than the power penetration depth $(2\kappa)^{-1}$, effects of the spatial distribution of the phase error is believed play a significant role.

6.5.4 Combination of twist and polarization independent phase error

Fig. 6.7 illustrates how PMC depends on a uniform twist of the fiber birefringence axes by r (rad/m), combined with a polarization independent phase error of 0.2 rad located at the center of the grating. The solid and dashed lines illustrate cases where the normalized intrinsic birefringence $(\Delta\beta_y - \Delta\beta_x)L = 0.44$ and 4.4, respectively, corresponding to beat-lengths of 1m and 0.1m. "x" and "y" labelling of the polarization modes refers to the directions of the major axes of the modal fields at the center of the grating.

Without the phase error, the laser modes would have equal thresholds and output powers. With the error present, the dual mode threshold is seen to increase towards infinity when moderate twist is applied. Above $rL \sim 5$ the threshold decreases towards a minimum at $rL \sim 9$, while the gain difference contributions from LSHB and GSHB increase. The threshold variations are generally larger for the high birefringence case (dashed lines).

The results in Fig. 6.7 indicate that single polarization operation can be achieved by writing a uniform birefringent DFB laser with an intentional phase error, and then twisting the grating. This has earlier been demonstrated experimentally in [29]. There are, however, differences between the laser behavior reported in [29] and our simulation results. In the experiment no change in the output power was observed until an offset twist rate of $rL \approx 1$ was reached. No

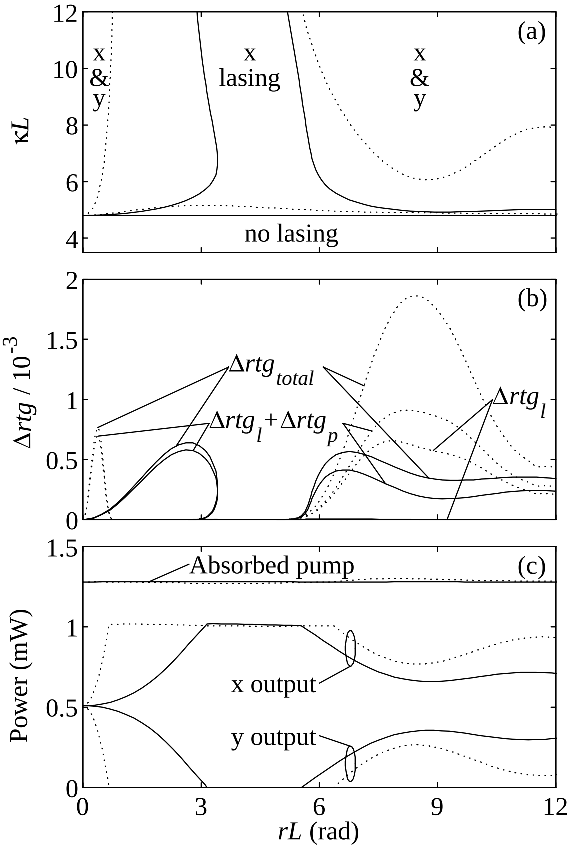

Figure 6.7. Same information as in Figure 6.3 plotted against twist rL assuming a polarization independent phase error of 0.2 rad at the center and intrinsic beat-lengths of 1m (solid lines) and 0.1m (dashed lines).

such effect is predicted from our simulations. Other differences in the shape of the output power versus twist rate may be related to different distributions of the grating phase errors in the experiment and the simulations. The changes in the beat frequency between the polarization modes observed in [29] are qualitatively similar to what we observed in the present simulations.

Fig. 6.8 shows (a) the z-dependence of the hole-burning effects, (b) the major axis orientations (MAO) of the forward and backward propagating modal fields $\vec{R}_m$ and $\vec{S}_m$, $m = x, y$ and (c) the ellipticity of the fields. The same parameters are assumed as for the laser illustrated with dashed lines in figure 6.7 (b), with $rL = 8.5$ and $\kappa L = 6.1$.

The plotted ellipticities are defined as the ratio of the minor to major axes, with positive sign for right hand rotation. The ellipticities are seen to be small (within ±0.11) throughout the grating. At the outputs the ellipticities are still

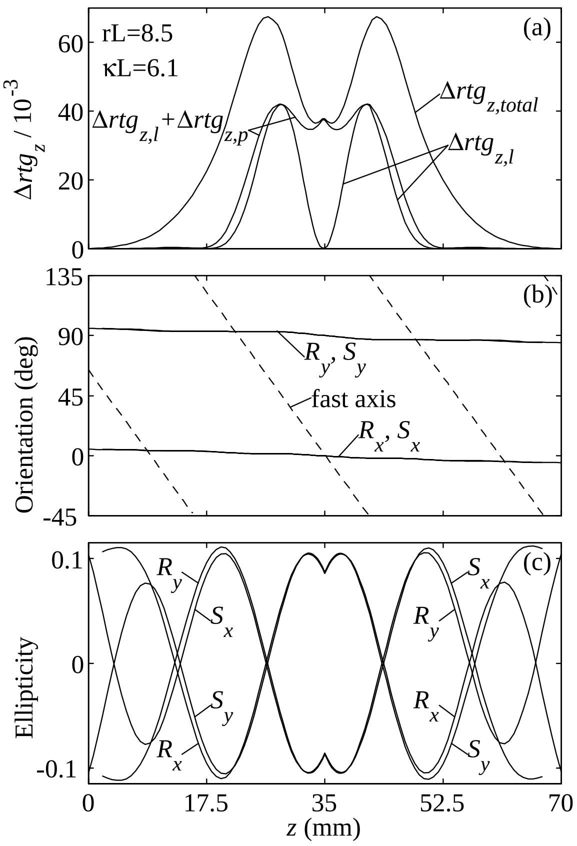

Figure 6.8. Spatial dependence of (a) differential gain contributions, (b) orientation of the major axes of $\vec{R}_m$ and $\vec{S}_m$, $m = x, y$, and (c) the ellipticity of $\vec{R}_m$ and $\vec{S}_m$ with $rL = 8.5$ for the laser illustrated with dashed lines in Figure 6.9 (b).

nonzero, though. This is in contrast to the findings for uniformly twisted Fabry-Perot lasers [30].

The MAO's are referenced to a non-twisted coordinate system. The orientation of the fast birefringence axis is included as a dashed line for reference. The MAO's are fairly constant throughout the grating. This means that throughout the grating each laser mode changes between propagating in the fast and slow intrinsic polarization modes. Consequently, the modal fields experience effectively positive and negative square chirps near the center of the grating. These effective chirp imperfections subtract and add to the polarization independent phase error of x- and y-modes, respectively, and thus explain why the polarization independent phase error changes the PMC behavior of the twisted DFB laser.

The rotation of the fast and the slow birefringence axes along the grating also "pulls" the two standing wave patterns out of phase with each other in certain

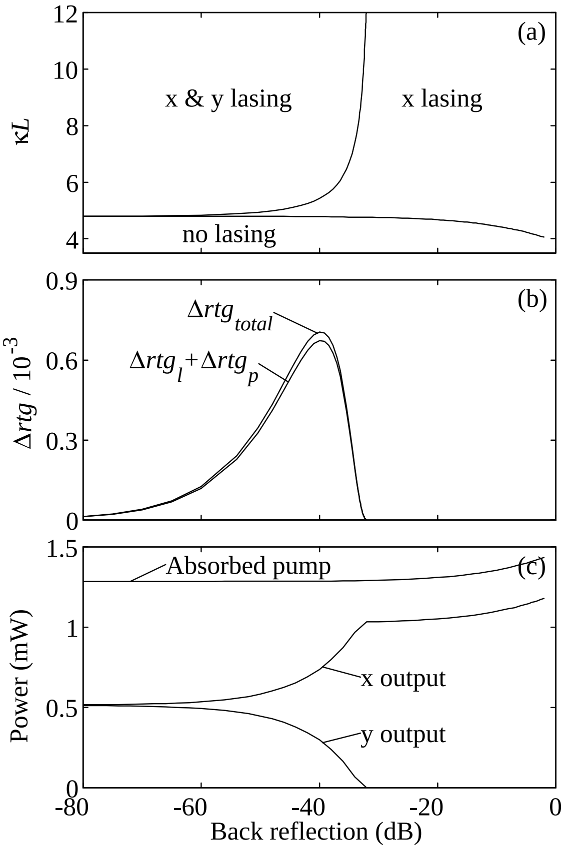

Figure 6.9. Same parameters as in Figure 6.3 plotted against back reflection level.

regions. This explains the high LSHB contribution in the regions around $z = 24$ mm and $z = 46$ mm.

Because of the stress-induced optical activity in silica fiber when it is twisted [14] the actual twist rate of the fiber will be $r_{act} \simeq 1.18r$, where r is the effective polarization coupling rate used in the simulations. Thus, the reference coordinates for Fig. 6.8 (b) will actually be twisted by $-0.18rL$ in a real silica fiber.

6.5.5 Back reflection

Fig. 6.9 shows how the PMC depends on back reflection into the right hand side ($z = 70$ mm) of the grating. The x and y output fields are assumed to be reflected with their polarization states maintained, while the phase-shift of the reflection differs by π between the two polarizations. The common reflection phase is selected such that the polarization output power ratio is maximized. It is believed that this combination of back reflection phases and polarization states represents a worst case with respect to the polarization output power ratio.

The dual mode threshold in Fig. 6.9 (a) increases only slightly up to a back reflection level of −40 dB. Above this level the dual polarization threshold increases very rapidly, and with the given worst case back reflection phases, dual polarization operation cannot be achieved only by increasing κL when the back reflections are stronger than −30 dB. The output powers shown in Fig. 6.9 (c) are sums of the modal output powers to the left and the output at the right-hand side of the added reflector. One see that for the illustrated case of $\kappa L = 9$, the polarization output power ratio is >1.09 for back reflections above −60 dB. In real systems, where the back reflection phases and polarizations may change due to vibrations and temperature variations, this would imply worst case ripples in the polarization output power ratio of more than ±9 %. Typical back reflection levels obtainable when an isolator is placed between the laser output and connectors/detectors may be from −60 to −70 dB.

As seen from Fig. 6.9 (a), single mode operation can in principle be achieved for any κL in a birefringent fiber by introducing a bare fiber end back reflection (-15 dB) positioned 1/4 beat-length from the grating, ensuring a back reflection phase difference of π between the polarization modes. Some kind of tuning would be required, however, to assure the correct common mode phase-shift between the reflector and the grating.

Fig. 6.9 (b) shows that PHB is the dominating hole-burning effect in this case, with a small negative contribution from GSHB.

6.5.6 Serial multiplexing, cross-saturation by passing power

Fig. 6.10 shows the PMC behavior when optical power at a wavelength close to the laser wavelength (but not resonating with the grating) is passing through the laser in the y polarization state. This corresponds to a situation where several dual polarization lasers are multiplexed along the fiber, for instance as birefringence sensor elements. In most such situations the passing power will, however, be somehow divided between the polarization states, so the simulations represent a worst case.

As indicated earlier, the modal power near the center of the laser, where most of the round-trip gain contribution originates, will typically exceed the output power by several orders of magnitude. From this argument, the DFB laser operation is expected to be quite tolerant to a passing saturating signal, both for single and dual polarization lasers. This is clearly confirmed for the dual polarization case in Figs. 6.10 (a) and (c). Also simulation of single polarization lasers (not illustrated here) shows a low sensitivity of the output power to cross-saturation.

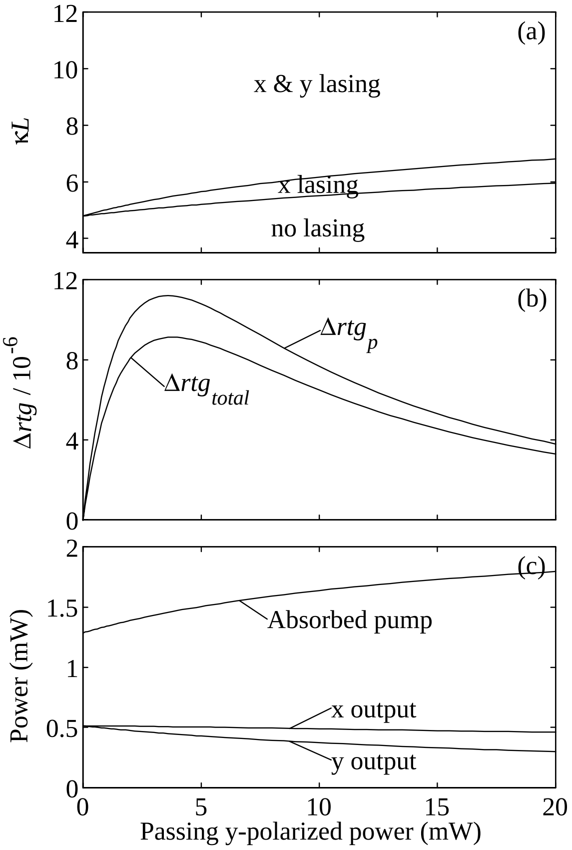

Figure 6.10. Same parameters as in Figure 6.3 plotted against passing cross-saturating power.

Serial multiplexing of DFB lasers should thus be possible as far as mean output power is concerned. This has also been demonstrated experimentally for single polarization lasers in [5] and [31]. Further studies are required to determine what happens to the dynamic behavior in terms of the total intensity noise and intra-modal intensity noise in multiplexed configurations.

The round-trip gain difference contributions in Fig. 6.10 (b) are much lower than in the previous cases (order of 10^{-6} as opposed to 10^{-3}). This is because the passing power does not change the cavity losses significantly.

6.6 Conclusion

A comprehensive model has been presented for multi-moded DFB lasers with arbitrary grating structures, including birefringence, twist and Faraday rotation. The model has been applied to investigate polarization mode competition in fiber lasers with certain polarization imperfections. The magnitudes of the polarization hole-burning effect and the local and global spatial hole-burning effects have been investigated, and it may be concluded that all these effects are of significance for the polarization mode competition behavior. The laser model may also be used to investigate longitudinal mode competition and fundamental mode thresholds in non-uniform gratings. More experimental work remains to be done to verify the validity of the model.

The grating model presented can also be applied to birefringent passive gratings, and it can readily be extended to include coupling between more than two modes propagating in each direction.

A simple approximation for the polarization dependence of the saturated gain has also been presented, which is believed to be valid both below and above the saturation power P_{sat}. From the approximation we are able to express the polarization dependence of the gain and gain grating parameters in the laser gain medium due to saturation from the laser power, including the standing wave modulation effects.

Promising techniques for achieving single polarization operation seem to be introduction of polarization dependent grating strength, polarization dependent grating phase errors located in the high intensity region of the cavity, twist of the birefringence axes combined with a non-ideal phase-shift, or back reflection into the laser with individually controlled phases for the two polarizations. Since unintended polarization imperfections, like back reflections, may work against the intended imperfections by favoring the mode that is not supposed to be lasing, extra margins should be added to the magnitudes of the intended imperfections.

If a dual polarization laser with stable polarization output power ratio is required, it may be necessary to include an isolator at the laser output to avoid mode competition noise caused by randomly varying back reflection phases.

In general, strong gratings (high κL) are found to be more tolerant to polarization imperfections, and relatively strong gratings should therefore be used when dual polarization lasers are required. There are, however, practical limits to how strong the gratings can be made. First, due to the high Q-factor of DFB's with high κL, even a small intrinsic fiber loss may reduce the slope efficiency significantly. Second, the gain thresholds of all longitudinal modes decrease with increasing grating strength. At the same time the global spatial hole-burning between longitudinal modes increases significantly. This may result in undesired multiple longitudinal mode operation.

Third, due to saturation of the UV-induced index-change, there is a limit to the κ-values that can be achieved. It may not be a good solution to increase κL by increasing L, since the impact of some of the grating imperfections, like twist, polarization dependent chirp, (and also polarization independent chirp) scale proportionally with L. Especially in birefringence sensor applications, where external forces are supposed to induce birefringence changes, maintaining uniform grating parameters along very long gratings may be difficult.

It is encouraging for sensor applications that serial multiplexing does not seem to affect the static solutions for modal output powers significantly. However, the influence of multiplexing on temporal intensity noise still needs more investigation.

6.7 Acknowledgments

The authors want to thank John Gregory Cowle for fruitful discussions and Kjell Bløtekjær for reading through and commenting the manuscript.

Appendixes:

6.A Background for the PHB Model

Two slightly different models have been presented in the literature for modelling the random orientation of ion cross-section anisotropies. Wysocki et. al. [21] assumes uniaxial gain of each ion, random orientations in three dimensions of the optical axes (OA) of each ion, and identical cross section anisotropies $A = \sigma_\perp/\sigma_\parallel$ for all ions where $\sigma_\perp$ and $\sigma_\parallel$ are the ion cross-sections for fields polarized parallel and orthogonal to the OA. Wagener et. al. [22] uses a simpler model with an "averaged" projected ion anisotropy ϵ, taking random ion orientations in only two dimensions into account. By fitting simulations to measurements of polarization hole-burning (PHB) in erbium doped amplifiers (EDFAs) at moderate signal intensities ($P_s < P_{sat}$), they estimate $A = 0.535$ or 2.17 and $\epsilon = 0.67$, respectively.

For moderate ion anisotropies it is found that (6.7) in Sec. 6.3 can approximate the local PHB calculated with the aforementioned models quite well. When comparing to Wysocki's model with $A = 0.535$ or 2.17, a best fit is obtained with $\eta = 0.059$, as illustrated in Fig. 6.1. For Wagener's model with $\epsilon = 0.67$, a good fit is obtained with $\eta = 0.039$. The difference in estimated η may be due to the fact that the two models are fitted to different experiments, and that Wagener assumes $D_p = 1$ everywhere along the test fiber, thus overestimating the EDFA PHB for the given ϵ.

The polarization dependent gain and gain grating coefficients to be used in the DFB coupled mode equations may be derived from (6.7) along the same lines as was used to derive (6.5) in Sec. 6.3: After expressing the ratio P_s/P_{sat} in (6.7) in terms of its mean value p_{tot} and its standing wave component $2Re\left(p_c e^{i\phi}\right)$, Δg and Δg_{gr} are derived as the zeroth and first order Fourier components of $\Delta g_{loc}\left(\phi\right)$. This leads to (6.9) in Sec. 6.3.

6.B Gain Medium Contributions to Round-trip Gain

The power transferred to a laser mode from the gain medium per unit length equals $g^r_{eff}|\vec{R}|^2 + g^s_{eff}\,|\vec{S}|^2$ where g^r_{eff} and g^s_{eff} are the effective power gains contributed to $\vec{R}$ and $\vec{S}$, respectively. By calculating $d|\vec{R}^2|\,/dz$ and $d|\vec{S}^2|\,/dz$ from (6.2) and extracting the terms that are due to the gain-medium, the following expressions are obtained:

$$\begin{aligned} g^r_{eff} &= 2\left\{g\left|r_x\right|^2 + \left(g+\Delta g\right)\left|r_y\right|^2 + \mathrm{Re}\left(r_x^* s_x g_{gr}\right)\right. \\ &\quad \left. + \mathrm{Re}\left(r_y^* s_y\left(g_{gr}+\Delta g_{gr}\right)\right)\right\}\,\left(\left|r_x^2\right| + \left|r_y^2\right|\right)^{-1}, \end{aligned}$$

$$\begin{aligned} g^s_{eff} &= 2\left\{g\left|s_x\right|^2 + \left(g+\Delta g\right)\left|s_y\right|^2 + \mathrm{Re}\left(r_x s_x^* g_{gr}^*\right)\right. \\ &\quad \left. + \mathrm{Re}\left(r_y s_y^*\left(g_{gr}^*+\Delta g_{gr}^*\right)\right)\right\}\,\left(\left|s_x^2\right| + \left|s_y^2\right|\right)^{-1}. \end{aligned} \qquad (6.14)$$

Not all of the power transferred from the gain medium contributes to the round-trip gain. For instance, at the grating ends the only contribution from the gain medium is to amplify the output signals. Numerical investigations indicate that the geometric mean of the forward and backward propagating powers $|\vec{R}(z)|\,|\vec{S}(z)|$ may be used in this context as a good estimate for the fraction of the laser power that is recirculated back into the cavity. The round-trip power contribution in (6.10) is thus calculated as:

$$\begin{aligned} P_{gain} &= \int_0^L \left(g^r_{eff}|\vec{R}(z)|^2 + g^s_{eff}\,|\vec{S}(z)|^2\right) \\ &\quad \cdot \frac{2\,|\vec{R}(z)|\,|\vec{S}(z)|}{|\vec{R}(z)|^2 + |\vec{S}(z)|^2}\,dz\,. \end{aligned} \qquad (6.15)$$

The PHB contribution to rtg_m, and thus Δrtg_p, is found by setting the polarization independent gain parameters g and g_{gr} to zero in (6.14).

The LSHB contribution to rtg_m, and thus Δrtg_l, is obtained as the difference between the actual rtg_m and the value for rtg_m obtained if the standing wave pattern is in exact antiphase with the gain grating, as it will always be in a uniform gain medium with only one laser mode. The latter value is obtained by replacing the $\mathrm{Re}\left(\cdot\right)$ function in (6.14) with $-\left|\cdot\right|$ (negative absolute value).

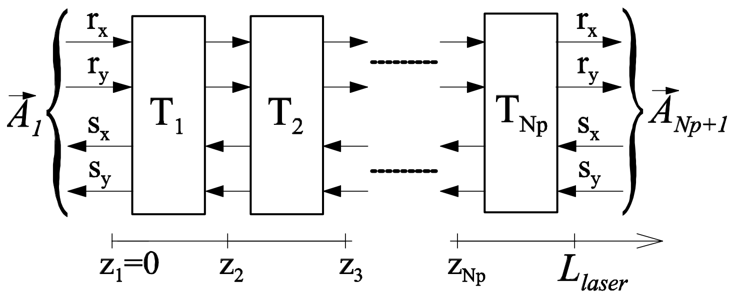

Figure 6.11. Finite element modelling by cascading of 4x4 T-matrixes.

6.C Numerical Model

In the numerical simulations we divide the grating into $q = 1..N_p$ sections along the z propagation axis. Each section may either be a grating section of length Δz_q, in which the coupling matrix $\mathbf{C}_{tot,q}$ is assumed to be constant, or it may be a localized ($\Delta z_q = 0$) perturbation like a phase-shift in the grating structure, reflection, loss or rotation of the birefringence axes.

$N_p = 80 - 120$ sections of variable length were used for the simulations, with shorter sections near the phase-shift position where the intensity and the gain parameters change rapidly. It was verified that further reductions in the section lengths did not give significant changes in the simulation results.

The transfer matrix $\mathbf{T}_q$ of section q is defined by [9]

$$\vec{A}_{q+1} = \mathbf{T}_q \vec{A}_q \tag{6.16}$$

where $\vec{A}_q$ is the field amplitude at the left of grating section q. The combined transfer matrix for several cascaded grating sections is computed as the product $\mathbf{T}_{p \cdots q} = \mathbf{T}_q \mathbf{T}_{q-1} \cdot \cdot \mathbf{T}_p$. This cascading of T-matrixes is illustrated in Fig. 6.11.

We assume the coupling parameters to be z-independent within each grating section. For sections with $\Delta z_q > 0$, $\mathbf{T}_q$ may thus be calculated as a product of three matrixes, the first matrix projecting $\vec{A}_q$ into the individual grating modes of (6.3), the second multiplying each mode component by $\exp(-(\gamma_i + i\zeta_i)\Delta z_q)$ and the third doing the reverse projection. This approach is similar to the matrix diagonalization approach presented in [9], and it can be easily extended to evaluate coupling between a larger number of modes.

For a localized perturbation the expression for $\mathbf{T}_q$ may be deduced from well known scattering (S-) matrix expressions [32], [33].

We want to calculate the steady state lasing condition for the DFB laser, taking gain saturation into account, when $m = 1..N_m$ specified modes are lasing. Let δ_m and ε_m denote the detuning and the stored cavity energy of

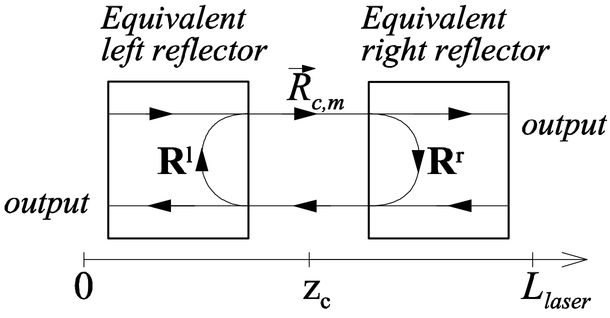

Figure 6.12. Model used for calculating the round-trip Jones-matrix of mode m in eq. (6.17).

mode m. Input parameters to our algorithm are the pump power P_{p0} (launched from left) and initial guesses for:

- the "laser state vector" $\vec{x} = [\varepsilon_1,\ \cdots,\ \varepsilon_{N_m},\ \delta_1,\ \cdots,\ \delta_{N_m}]$,
- the right propagating polarization states $\vec{R}_{c,1} \cdots \vec{R}_{c,N_m}$ ($\vec{R}_{c,m} = [r_x,\ r_y]_m^T$) of each mode at a specified center position z_c, and
- the gain distribution $\mathbf{G}_1 \cdots \mathbf{G}_{N_p}$ ($\mathbf{G}_i$ =gain matrix of the i'th subsection).

The round-trip matrix $\mathbf{RTM}_m$ for each laser frequency is calculated as the product of the effective Jones reflection matrixes at each side of z_c, see Fig. 6.12:

$$\mathbf{RTM}_m = \mathbf{R}^l\left(\delta_m\right) \mathbf{R}^r\left(\delta_m\right). \tag{6.17}$$

$\mathbf{R}^l$ and $\mathbf{R}^r$ are easily computed from the combined T-matrix of each subgrating. Out of the two eigenvalues of $\mathbf{RTM}_m$, the one with a corresponding eigenvector that projects onto $\vec{R}_{c,m}$ is identified as the round-trip gain RTG_m of mode m.

The criterion for a steady state solution is that RTG_m must equal one for all modes. An error gradient algorithm is used that searches for this condition by iteratively calculating improved values for $\vec{x}$ and recomputing the field and gain distributions. The T-matrix formalism outlined above and the gain model outlined in section 6.3 are used for this purpose.

The method outlined may also be adopted for calculating the threshold condition for mode N_m to start lasing, assuming modes $1 \cdots (N_m - 1)$ all have a lower threshold. For instance, the threshold pump power may be computed by assuming $\varepsilon_{N_m} = 0$ while substituting P_{p0} for ε_{N_m} in the definition of $\vec{x}$, i.e. $\vec{x} = [\varepsilon_1,\ \cdots, \varepsilon_{N_m-1},\ P_{p0},\ \delta_1,\ \cdots,\ \delta_{N_m}]$.

References

[1] J. T. Kringlebotn, J. L. Archambault, L. Reekie and D. N. Payne, Er^{3+}:Yb^{3+}-codoped fiber distributed-feedback laser", *Opt. Lett.*, vol. 19, pp. 2101-2103, 1994.

[2] L. Dong, W. H. Loh, J. E. Caplen, J. D. Minelly and L. Reekie, "Efficient single-frequency fiber-lasers with novel photosensitive Er/Yb optical fibers", *Opt. Lett.*, vol. 22, pp. 694-696, 1997.

[3] W. H. Loh, B. N. Samson, L. Dong, G. J. Cowle and K. Hsu, "Performance Characteristics of Single Frequency Er^{3+}:Yb^{3+} Codoped Fiber Lasers", 1997 *Conf. on Bragg Gratings, Photosensitivity, and Poling in Glass Fibers and Waveguides: Applications and Fundamentals*, sponsored by OSA/ACS, Williamsburg,VA, Tech. Digest vol. 17, pp. 132-134, paper BMC3-1.

[4] J. T. Kringlebotn, W. H. Loh and R. I. Laming, "Polarimetric Er^{3+}-doped fiber distributed-feedback laser sensor for differential pressure and force measurements", *Opt. Lett.*, vol. 21, pp. 1869-1871, 1996.

[5] J. Hübner, P. Varming and M. Kristiansen, "Five wavelength DFB fiber laser source for WDM systems", *Electron. Lett.*, vol. 33, pp. 139-140, 1997.

[6] M. Sejka, P. Varming, J. Hübner and M. Kristiansen, "Distributed feedback Er^{3+}-doped fibre laser", *Electron. Lett.*, vol. 31, pp. 1445-1446, 1995.

[7] H. Storøy, B. Sahlgren and R. Stubbe, "Single polarization fibre DFB laser", *Electron. Lett.*, vol. 33, pp. 56-58, 1997.

[8] H. Kogelnik and C. V. Shank, "Coupled-Wave Theory of Distributed Feedback Lasers", *J. Appl. Phys.*, vol. 43, pp. 2327-2335, 1972.

[9] G. Björk and O. Nilsson, "A New Exact and Efficient Numerical Matrix Theory of Complicated Laser Structures: Properties of Asymmetric Phase-Shifted DFB Lasers", *J. Lightwave Technol.*, vol. LT-5, pp. 140-146, 1987.

[10] M. Yamada and K. Sakuda, "Analysis of almost-periodic feedback slab waveguides via a fundamental matrix-approach", *Appl. Opt.*, vol. 26, pp. 3474-3478, 1987.

[11] G. P. Agrawal, A. H. Robeck, "Modeling of Distributed Feedback Semiconductor Lasers with Axially-Varying Parameters", *IEEE J. Quantum Electron.*, vol. 24, pp. 2407-2414, 1988.

[12] V. C. Lauridsen, T. Søndergaard, P. Varming and J. H. Povlsen, "Design of Distributed Feedback Fibre Lasers" in *Proc. ECOC 97*, vol. 7, paper WE1C, pp. 39-42, 1997.

[13] R. Ulrich and A. Simon, "Polarization optics of twisted single mode fibers", *Appl. Opt.*, vol. 18, pp. 2241-2251, 1979.

[14] J. I. Sakai, T. Kimura, "Birefringence and Polarization Characteristics of Single-Mode Optical Fibers under Elastic Deformations", *IEEE Journal of Quantum Electron.*, vol. QE-17, pp. 1041-1051, 1981.

[15] E. Peral and J. Capmany, "Generalized Block Wave Analysis for Fiber and Waveguide Gratings", *J. Lightwave Thechnol.*, vol. 15, pp. 1295-1302, 1997.

[16] C. R. Giles and E. Desurvire, "Modeling Erbium-Doped Fiber Amplifiers", *J. Lightwave Thechnol.*, vol. 9, pp. 271-283, 1991.

[17] M. Sargent III, W. H. Swantner and J. D. Thomas, "Theory of a Distributed Feedback Laser", *IEEE J. Quantum Electron.*, vol. QE-16, pp. 465-472, 1980.

[18] W. S. Rabinovich and B. J. Feldman, "Spatial Hole Burning Effect in Distributed Feedback Lasers", *IEEE J. Quantum Electron.*, vol. 25, pp. 20-30, 1989.

[19] V. J. Mazurczyk and J. L. Zyskind, "Polarization Dependent Gain in Erbium Doped-fiber Amplifiers", *IEEE Photon. Technol. Lett.*, vol. 6, pp. 616-618, 1994.

[20] V. J. Mazurczyk, R. H. Stolen, J.-S. Wang and C. D. Poole, "Observation of polarization hole burning in Er-doped fiber for circular polarization of the saturating signal", *1995 Conference on Optical Fiber Communications, Tech. Dig.*, pp. 49-50, paper TuJ7.

[21] P. Wysocki and V. Mazurczyk, "Polarization Dependent Gain in Erbium-doped Fiber Amplifiers: Computer Model and Approximate Formulas", *J. Lightwave Thechnol.*, vol. 14, pp. 572-584, 1996.

[22] J. L. Wagener, D. G. Falquier, M. J. Digonet, H. J. Shaw, "A Muller Matrix Formalism for Modelling Polarization Effects in Erbium-Doped Fiber", *J. Lightwave Thechnol.*, vol. 16, pp. 200-206, 1998.

[23] T. Erdogan and V. Mizrahi, "Characterization of UV-induced birefringence in photosensitive Ge-doped silica optical fibers", *J. Opt. Soc. Amer. B*, vol. 10, pp. 2100-2105, 1994.

[24] P. Niay, P. Bernage, T. Taunay, M. Douay, E. Delevaque, S. Boj and B. Poumellec, "Polarization Selectivity of Gratings Written in Hi-Bi Fibers by the External Method", *IEEE Photon. Technol. Lett.*, vol. 7, pp. 391-3, 1995.

[25] K. Okamoto, T. Hosaka, T. Edahiro, "Stress Analysis of Optical Fibers by a Finite Element Method", *IEEE J. Quantum Electron.*, vol. QE-17, pp. 2123-2129, 1981.

[26] Y. Namihira, "Opto-Elastic Constant in Single Mode Optical Fibers", *J. Lightwave Thechnol.* vol. LT-3, pp. 1078-1083, 1985.

[27] R. B. Wagreich, W. A. Atia, H. Singh and J. S. Sirkis, "Effects of diametric load on fibre Bragg gratings fabricated in low birefringent fibre", *Electron. Lett.*, vol. 32, pp. 1223-1224, 1996.

[28] L. Bjerkan, K. Johannessen, X. Guo, "Measurement of Bragg Grating birefringence due to transverse compressive forces" in *1997 Optical Fiber Sensors Conference,* Williamsburg, VA, Tech. Dig. vol. 16, paper OTuC7-1.

[29] Z. E. Haratjunian, W. H. Loh, R. I. Laming and D. N. Payne, "Single polarization twisted distributed feedback fibre laser", *Electron. Lett.*, vol. 32, pp. 346-348, 1996.

[30] H. Y. Kim, S. K. Kim, H. J. Jeong, H. K. Kim and B. Y. Kim, "Polarization properties of a twisted fiber laser", *Opt. Lett.*, vol. 20, pp. 386-388, 1995.

[31] K. P. Koo and A. D. Kersey, "Noise and cross talk of a 4-element serial fiber laser sensor array", in *1996 Conf. on Optical Fiber Communications*, paper ThP2, Tech. Dig., pp. 266-267.

[32] Y. Weissman, *Optical Network Theory.* Bostaon, MA: Archtech House, 1992, pp. 33-44.

[33] A. Yu and A. S. Siddiqui, "Systematic method for the analysis of optical fibre circuits", *Proc. Inst Elec. Eng.*, vol. 142, pp. 165-175, 1995.

Chapter 7

Polarization Characteristics of Fiber DFB Lasers Related to Sensing Applications[1]

Abstract — An experimental and theoretical investigation of dual polarization Er-doped fiber DFB lasers, and how the polarization mode competition and polarization beat frequency depend on localized transverse force perturbations, back reflections, or changes in pump polarization state is reported. Good agreement between the experiments and a comprehensive theoretical model is obtained. Use of a dual polarization laser as a transverse force sensor with a resolution in the order of 1–100 $\mathrm{nN}/\sqrt{\mathrm{Hz}}$ above 20 Hz is also discussed.

Index Terms — Fiber lasers, DFB lasers, Laser mode competition, Gain hole-burning, Optical fiber sensors.

7.1 Introduction

Fiber distributed feedback (DFB) lasers are attractive devices for both for telecommunication and sensing applications [1, 2, 3], due to their narrow linewidth, robust single longitudinal mode operation, compact in-fiber design, flexible and accurate wavelength selection in production, as well as easy tuning of the wavelength.

Robust single polarization sources are generally required for interrogation of interferometric and Bragg grating fiber sensors, as well as in telecommunication applications. A single polarization fiber DFB laser may also be used as a very

---

[1] Manuscript accepted for publication in Journal of Quantum Electronics. Minor revisions will be made prior to publication. Authors: Erlend Rønnekleiv, Morten Ibsen, and Gregory J. Cowle.

sensitive sensor element on its own, as the laser frequency is sensitive to strain, temperature and other perturbations that change the optical period of the DFB grating. Two methods for ensuring single polarization operation have been reported experimentally, which exploit the polarization dependence of the UV-induced index change. One is based on extra UV-exposure of a grating section to produce a distributed birefringent grating phase-shift [4, 5]. The other is based on inducing a polarization dependence of the grating coupling coefficient κ [6]. Another method reported in [7] is based on twisting a dual polarization fiber DFB laser to make it single polarization.

The polarization beat frequency of dual polarization fiber DFB lasers is sensitive to perturbations that change the fiber birefringence, such as temperature or lateral forces. Simultaneous monitoring of the beat and laser frequencies from such lasers allows for single point dual parameter sensors such as the force-temperature sensor demonstrated in [2] or the strain-temperature sensor demonstrated in [3]. For these applications, robust dual polarization operation of the laser is required.

In both single and dual polarization sensing applications the need for a direct physical contact or interaction between the laser and the measurand may lead to non-uniform birefringence along the DFB structure, which may in turn affect the polarization mode competition (PMC) within the laser. External back reflections and the state of polarization (SOP) of the pump are also expected to affect the PMC behavior of the lasers. In addition, back reflections will affect the polarization beat frequency. Many sensing applications will not allow the fiber laser sensor to be located close to the pump laser and optical isolators. Control with the pump SOP launched into the laser may therefore not be realistic, and isolation against external back reflections may be relatively poor. It is expected that problems due to drift in the pump SOP can be reduced or eliminated by scrambling the pump polarization. However, a polarization scrambling component would increase the complexity and cost of a sensor interrogation system, and it is therefore of interest to know if a sensor system can be operated without such scrambling.

The above mentioned problems call for a quantitative understanding of the mechanisms governing the PMC behavior and polarization beat frequency fluctuations in fiber DFB lasers. A comprehensive theoretical model was developed in [8] and several examples discussing the PMC behavior was given. One purpose of the present work is to verify the model experimentally, and to extend it to also cover pump induced polarization dependent gain (PDG). A further purpose is to investigate the dependence of the polarization beat frequency on localized lateral forces and external reflections. These investigations can reveal useful insight into the obtainable sensitivity for polarimetric fiber DFB laser sensors to lateral forces and the limitations set by external back reflection to the accuracy of polarimetric fiber DFB laser sensors in general.

7.2 The Investigated Lasers

Two dual polarization fiber DFB lasers operating at 1549 nm, in the following denoted DFBa and DFBb, have been investigated. The lasers consist of two consecutive uniform subgratings of lengths L_1 and L_2 with a localized π grating phase-shift in between. DFBa is symmetric with $L_1 = L_2 = 20$ mm, while DFBb is asymmetric with $L_1 = 17.4$ mm and $L_2 = 25$ mm. Both lasers were characterized with a heat perturbation technique in [9], verifying fundamental longitudinal mode operation and a grating coupling parameter of $\kappa = 230$ m^{-1} ±10%. In [9], DFBa and DFBb were named "laser #1" and "laser #3", respectively.

DFBa produced an output power of 205 μW ±10% in each direction when pumped from either end by 83 mW of 1480-nm pump power. Under the same pumping conditions, the asymmetric DFBb produced 395 μW ±10% from output port 1 (grating section L_1), and 11.5 μW ±10% from port 2 (grating section L_2).

The laser gratings were produced by UV exposure of a D_2-loaded fiber with an Er-Yb-doped core and a UV-sensitized B-Ge-doped ring outside the core [10]. Before UV exposure, but after D_2-loading of the fiber, the fiber transmission spectrum was measured for various pump powers. From these measurements, the absorption (a_x) and gain (g_x) coefficients at zero and full inversion, respectively, at the laser signal ($x = s$) and pump ($x = p$) wavelengths were found to be $[\,a_s,\ a_p, g_s,\ g_p] = [11.7,\ 8.9,\ 15.9,\ 3.0]$ dB/m. The spontaneous emission power at full inversion was $P_{sp} = 4.1$ mW/m.

Fitting of simulations to the measured slope efficiency of DFBa published in [11] indicates that the lifetime of a fraction $\xi = 38$ % of the Er-ions have been reduced (quenched) by a factor $\zeta = 26$ during the UV-exposure. In addition, an unbleachable loss of $a_0 = 0.24$ dB/m seems to be present. UV-induced quenching in Er^{3+}-doped glasses has earlier been reported in [12]. The slope efficiency of DFBb has also been measured, indicating very similar parameters for that laser: $\xi = 39$ %, $\zeta = 25$, and $a_0 = 0.24$ dB/m.

7.3 Response to Transverse Force

A polarization dependent phase-shift may be introduced in a fiber by applying a transverse force, resulting in stress-induced birefringence. We have investigated the sensitivity to transverse forces for a section of the same fiber that DFBa

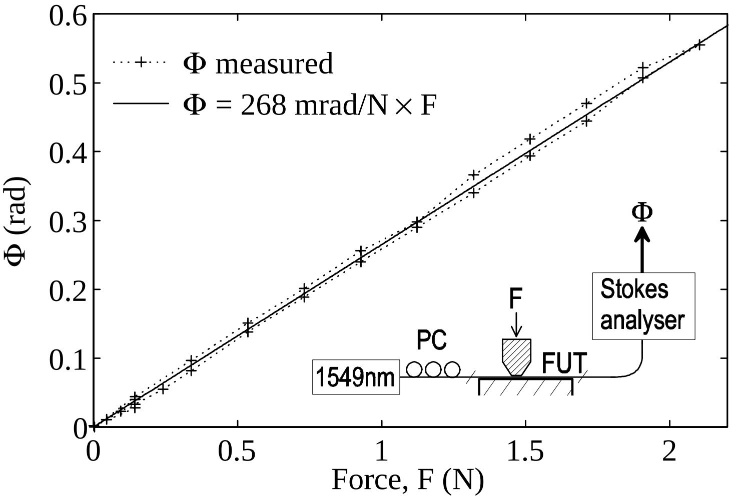

Figure 7.1. Polarization dependent phase shift Φ versus transversal force F applied to a section of the fiber used for the laser production. The measurement setup is illustrated in the inset drawing. PC, polarization controller.

and DFBb were made from, using the setup illustrated in the inset of Fig. 7.1. A variable force F was applied to a 1 mm section of the fiber under test (FUT). Polarized light at 1549 nm was launched from one end, and the resulting output SOP was monitored by a Stokes analyzer. After adjusting the input SOP so that the output SOP had maximum sensivity to the applied force, the difference Φ between the force-induced phase-shifts for optical fields polarized parallel and orthogonal to the force could be measured as the angular rotation of the output SOP on the Poincarè sphere. The result of this experiment is plotted in Fig. 7.1, showing a force sensitivity of $\Phi/F = 0.268 \pm 0.005$ rad/N. This value is somewhat less than the 0.29 rad/N indicated theoretically for silica fiber in [13] and experimentally in [2]. The hysteresis observed in Fig. 7.1 of ~ 70 mN may be due to hysteresis in the force monitoring arrangement.

Fig. 7.2 shows the setup used to investigate the sensitivity of DFBb to a polarization-dependent phase-shift induced by pressing on a ~ 1 mm section of the laser fiber close to the position of the permanent grating phase-shift. 83 mW of 1480-nm polarized pump power was launched into port 1 of the laser via a polarization controller (PC1) and a 1480 – 1550 nm wavelength division multiplexer (WDM). The laser output from port 1 was guided via the 1550-nm branch of the WDM through an isolator (ISO), a polarization controller (PC2) and a polarizing beam-splitter (PBS) to detectors Dx and Dy. To be able to monitor the PMC behavior of the laser, PC2 was adjusted so that Dx and Dy monitored the output powers P_x and P_y from the x- and y- laser polarization

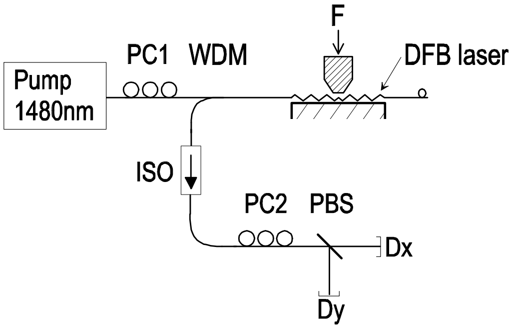

Figure 7.2. Setup for investigation of the laser response to a transverse force F applied near the grating phase-sift position.

modes, respectively. The given values for P_x and P_y have been corrected for losses measured between the laser output and the detector. Measurements were also made of the force-induced frequency shifts $\Delta\nu_x$ and $\Delta\nu_y$ of the x and y laser modes and the polarization beat frequency $\nu_b = |\Delta\nu_x - \Delta\nu_y|$. These frequency measurements were made by replacing Dx with a high finesse Fabry-Perot optical spectrum analyzer and connecting an RF spectrum analyzer to Dy. The state of PC2 was then adjusted so that the laser polarizations were mixed in the PBS, causing two separated peaks at the optical spectrum analyzer, and a distinct peak at the polarization beat frequency at the RF spectrum analyzer.

The measurements were first performed with the force applied parallel to the x polarization axis of the laser, and then repeated with the force parallel to the y polarization axis. The applied forces will be denoted F_x and F_y for the two cases, respectively. For each direction of the force, the modal output powers P_x and P_y were recorded versus the applied force. This measurement was repeated with PC1 adjusted first for maximum in P_x and then for maximum in P_y, corresponding to x and y polarized pump, respectively. Recordings of $\Delta\nu_x$, $\Delta\nu_y$ and ν_b versus the applied forces were also made.

Note that the direction of the x and y polarization states in the laser could not be measured directly in the experiment, due to random changes of polarization states between the laser and the PBS. The identification of the modes is therefore based on theoretical calculations of the birefringence due to transverse forces [13], from which we find that $\Delta\nu_x - \Delta\nu_y$ should increase with F_x and decrease with F_y.

Fig. 7.3 (a) shows the measured (markers) $\Delta\nu_x$, $\Delta\nu_y$ and $\Delta\nu_x-\Delta\nu_y$ versus F_x and F_y. No significant dependence on the pump polarization could be observed in the frequency measurements. For an ideal DFB laser grating, the frequency shift of mode $q = x, y$ due to a locally induced grating phase shift $\Delta\phi_q$ in the

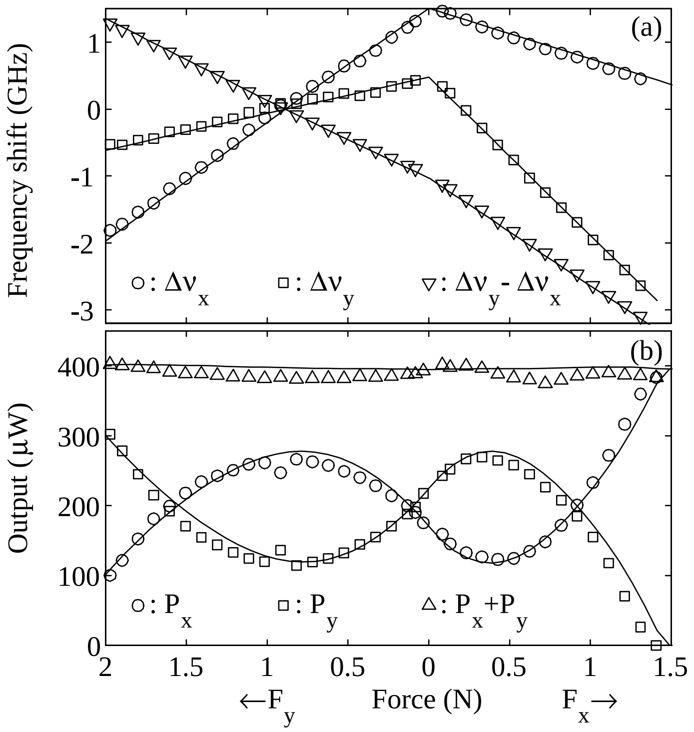

Figure 7.3. (a) Frequeny shifts $\Delta\nu_x$ and $\Delta\nu_y$, and polarization beat frequency $\Delta\nu_y - \Delta\nu_x$, plotted versus transverse force F_x or F_y applied parallel to the x or y birefringence axes of DFBb, respectively (c.f. Fig. 7.2). Responses to F_x are shown to the right and responses to F_y to the left. (b) Output powers P_x, P_y, and total output $P_x + P_y$. Markers and lines illustrate measurements and simulations, respectively.

q polarization propagation mode may be expressed as [9]:

$$\Delta\nu_q = -\frac{\kappa c}{4\pi n} \exp\left(-2\kappa|z|\right)\, \Delta\phi_q \tag{7.1}$$

Here, $c\kappa/(2n)$ is the inverse round-trip delay of the laser cavity at the grating phase-shift position $z = 0$, c is the speed of light in vacuum, n is the refractive index of the fiber, κ is the grating coupling coefficient, and $\exp\left(-2\kappa|z|\right)$ is the laser intensity dependence on the distance z from the grating phase-shift. The measured beat frequencies satisfy $d(\Delta\nu_y - \Delta\nu_x)/dF_x \approx -1.60$ GHz/N and $d(\Delta\nu_y - \Delta\nu_x)/dF_y \approx 1.16$ GHz/N. Taking into account that the forces are distributed over a 1 mm length and assuming $\kappa = 230$ m^{-1}, $n = 1.465$, and $|\Delta\phi_y - \Delta\phi_x| = 2\Phi = 0.536$ rad/N $\times F_q$ from Fig. 7.1, this indicates that F_x and F_y have been centered at effective distances $z = 0.5$ and 1.25 mm from the permanent π phase-shift position, respectively.

From the measured frequency shifts $\Delta\nu_x$ and $\Delta\nu_y$ of the individual modes and from (7.1), we estimate the sensitivity of the grating phase-shift to transverse force in the direction parallel to the optical polarization to be $k_\parallel = \Delta\phi_x/F_x = \Delta\phi_y/F_y = 0.255 \pm 0.04$ rad/N, and the sensitivity to orthogonal forces to $k_\perp = \Delta\phi_y/F_x = \Delta\phi_x/F_y = 0.791 \pm 0.04$ rad/N. Theoretical expressions for the sensitivities of the fiber refractive indices to transverse forces were derived by Sakai and Kimura in [13]. However, they did only take into account transverse stresses in the fiber, while effects of axial (z-directed) stress or strain were ignored. When we take these effects into account and use the same material parameters as in [13], we obtain $[k_\parallel,\ k_\perp] = [-0.031,\ 0.543]$ rad/N for a fiber that is axially constrained (no z-directed strain) and $[k_\parallel,\ k_\perp] = [0.175,\ 0.747]$ rad/N for a fiber that free to expand axially. As seen from the results, axial strain causes a polarization independent offset to $[k_\parallel,\ k_\perp]$. Our measurements indicate that this offset is even higher than calculated for the free axial expansion case. This high offset may be due to z-directed stress in the 1 mm long plastic surface (overhead copier grade foil) that was used to transfer the force to the fiber. If the transverse force is applied from relatively stiff surfaces over a longer length of the fiber, less axial strain is expected. This expectation is confirmed by results reported by Wagreich *et. al.* [14] from pressing on a 25 mm fiber section with a passive grating Bragg between polished aluminum plates. Their results correspond to $[k_\parallel,\ k_\perp] = [0.10 \pm 0.07,\ 0.62 \pm 0.15]$ rad/N at 1550 nm, which is close to what is expected theoretically for the axially constrained case.

The beat frequency measurements in Fig. 7.3 (a) demonstrates that the arrangement in Fig. 7.2 could be used as a very sensitive transverse force sensor. Dual polarization fiber DFB lasers used as transverse force sensors were first demonstrated in [2] by pressing on the full length of a 100 mm laser, producing a sensitivity of 96 MHz/N. The higher sensitivity of 1.6 GHz/N obtained here is due to the concentration of the force near the most sensitive region of the laser. Measurements of the fluctuations in ν_b when no perturbations were applied have been made for DFBa using a setup that will be described in the Sec. 7.4. Fig. 7.4 shows the noise spectral density $\nu_{b,rms}$ of the beat frequency versus interrogation frequency f. $\nu_{b,rms}$ decrease from 120 Hz/$\sqrt{\text{Hz}}$ at $f = 20$ Hz to 2.1 Hz/$\sqrt{\text{Hz}}$ at $f = 40$ kHz. In a sensor with a sensitivity of 1.6 GHz/N these noise levels would produce a noise floor (noise equivalent force) ranging from 75 to 1.3 nN/$\sqrt{\text{Hz}}$ in the same frequency interval, as illustrated by the right-hand axis in Fig. 7.4. The origin of $\nu_{b,rms}$ is not known, but it may be related to time varying back reflections to the laser, as will be discussed in Sec. 7.4.

Fig. 7.3 (b) illustrates the measured (markers) P_x, P_y and $P_x + P_y$ averaged over the two pump polarizations, and is believed to be representative for a situation with a scrambled pump polarization. Pump polarization dependence

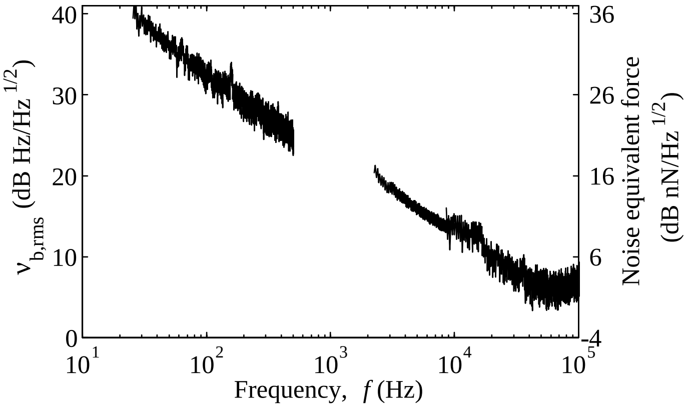

Figure 7.4. Measured beat frequency noise $\nu_{b,rms}$ for DFBa. The right-hand axis shows the corresponding noise equivalent force for a transverse force sensor.

will be discussed in Sec. 7.5. The total output power $P_x + P_y$ is seen to be fairly independent on F_x and F_y. The modal power difference $P_x - P_y$ decreases with F_x to a minimum at $F_x = 0.4$ N, and then increases until only the x-polarization is lasing at $F_x = 1.4$ N. The dependence on F_y is very similar, except for a sign-shift in $P_x - P_y$. This observed dependencies of P_x and P_y on F_x and F_y may be explained by assuming a negative polarization independent grating phase-shift error near $z = 0$. When a force is applied, this error is compensated most efficiently for the polarization axis orthogonal to the force (since $k_\perp > k_\|$), and the output power of the corresponding laser mode is favored. The mode polarized parallel to the force starts taking over about when the phase-shift error of the orthogonal mode is fully compensated near $F_x = 0.4$ or $F_y = 0.8$ N, and starts to increase in absolute value.

A complete degeneration of the laser modes as ν_b approached zero was not observed. Instead, ν_b went through a minimum value of $\nu_b \approx 14$ MHz at $F_y \approx 0.89$ N, while the polarization states of the laser modes were continuously transformed to their respective orthogonal states. This behavior may be explained by a small (<2°) misalignment between F_y and the birefringence axis, and is the explanation for the irregularities in the measured P_x and P_y near $F_y = 0.89$ N.

The lines in Fig. 7.3 (a) and (b) show simulation results obtained using the model described in Appendix 7.A and [8]. A depolarized pump ($D_{pp} = 0$) was assumed, and the polarization hole-burning (PHB) parameter was set to $\eta = 0.12$. The grating and gain parameters were assumed as described above, except for bias grating phase-shifts in the x and y polarization modes of $\Delta\phi_{x0} = -0.20$ rad and $\Delta\phi_{y0} = -0.18$ rad, respectively, which were added to the nominal π phase-shift at $z = 0$. Small adjustments were also made to ξ, ζ, and a_0 to maintain a good fit with the measured slope efficiency at $F_x = F_y = 0$. We see that the model produces a good fit to the measurements in Fig. 7.3. The model parameters that have been fitted to the measurements in Fig. 7.3 may be summarized as the force positions and the offset in $[k_\parallel, k_\perp]$ which are determined by the slopes of $\Delta\nu_x$ and $\Delta\nu_y$, $\Delta\phi_{x0}$ and $\Delta\phi_{y0}$ which are determined by the local maximum and minimum in $P_x - P_y$ and the offset in $P_x - P_y$ at $F_x = F_y = 0$, and η which is determined by the magnitude of $P_x - P_y$.

The observed local maxima and minima in $P_x - P_y$ could in principle be explained by assuming a UV-induced gain grating, which would be in phase with the index grating, instead of the bias grating phase errors. Such an effect would arise because the force-induced phase-shifts would cause the overlap between the standing wave intensity pattern and the gain grating to vary differently for the two laser polarizations. A UV-induced gain grating could either come from modulation of the unbleachable losses a_0 or modulations of the lifetime-quenched ion fraction ξ. However, the grating modulation amplitudes cannot exceed the estimated mean values for a_0 and ξ since negative background losses or ion fractions are not realistic. Simulations have shown that even with the maximum possible modulation amplitudes, bias phase-shifts $\Delta\phi_{x0}$ and $\Delta\phi_{y0}$ in the order of -0.12 rad must be assumed to achieve good fit with the measurements.

7.4 Response to External Back Reflections

Fig. 7.5 shows the setup used to investigate the sensitivity of DFBa and DFBb to back-reflections. 83 mW of 1480-nm pump was supplied to the laser through PC1 and the WDM in the same way as for the experiment in Fig. 7.2. Back-reflection into the forward port (right-hand side in figure) of the laser with variable attenuation, optical phase-shift and polarization state was generated by use of a variable attenuator (VA), a piezo-electric fiber stretcher (PZT) modulated at ~ 8 Hz by a function generator (F.gen.), a polarization controller (PC3), and a fiber end reflector (Refl.). A 10:90 coupler was inserted between the laser and the VA, and by connecting fiber connectors FC2 and FC3 the forward output power could be monitored through the 10% output port from the coupler. Alternatively, the backward output could be monitored through the WDM and isolator ISO1 by connecting FC1 to FC3. In the latter case FC2 was terminated with a fiber bend to avoid reflections. The detection system with ISO2, PC2, PBS, Dx and Dy is identical to that shown in Fig. 7.2, except for a tunable optical band-pass filter (BPF) with 1 nm bandwidth inserted between PC2 and the PBS to stop pump power from reaching the detectors.

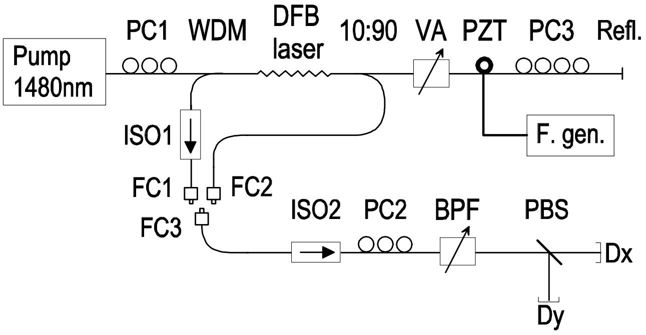

Figure 7.5. Setup for investigation of the laser polarization mode responses to back-reflections.

The observed dependencies of the modal output powers P_x and P_y on the dual-pass phase modulation Φ_{PZT} induced by the PZT was in agreement with the theoretically expected dependencies, indicated by the solid lines in Fig. 7.6. We maximized the amplitude of $P_x - P_y$ by adjusting PC3. It is believed that this corresponds to back reflection phases in the x and y polarizations that differ by π, while the reflected state of polarization is preserved for both laser modes. Thus, when Φ_{PZT} causes constructive interference between back reflected and intracavity signals for one mode, the other mode experiences destructive interference, and vice versa. The minima and maxima in output power versus Φ_{PZT}, denoted $P_{q,r,max}$ and $P_{q,r,min}$ where $q = x, y$ is the laser mode index, were then recorded as a function of back reflection level. This experiment was first performed with x-polarized pump ($r = x$) and then with y-polarized pump ($r = y$). To remove the pump polarization dependence, intrinsic differences in laser mode efficiencies, as well as polarization dependent measurement errors, we will in this section illustrate the averaged values $P_{max} = \overline{P_{q,r,max}}$ and $P_{min} = \overline{P_{q,r,min}}$, where the averages are taken over all possible combinations of q and r.

The markers in Figs. 7.7 (a) and (b) show the measured P_{max}, P_{min}, and $P_{max} + P_{min}$ plotted against back reflection level for the symmetric laser DFBa. (a) and (b) illustrate measurements made through the forward (FC2) and backward (FC1) ports, respectively. The PMC behavior is similar for the two directions, with P_{min}/P_{max} decreasing from >0.94 at <-55 dB reflection to zero at -24 dB.

The lines in Figs. 7.7 (a) and (b) show the simulated laser behavior, assuming phase and polarization of the back reflections as described above, depolarized pump ($D_{pp} = 0$), $\eta = 0.12$, and otherwise the parameters given for DFBa in Sec. 7.2. It can be seen that the agreement between measurements and simulations is good.

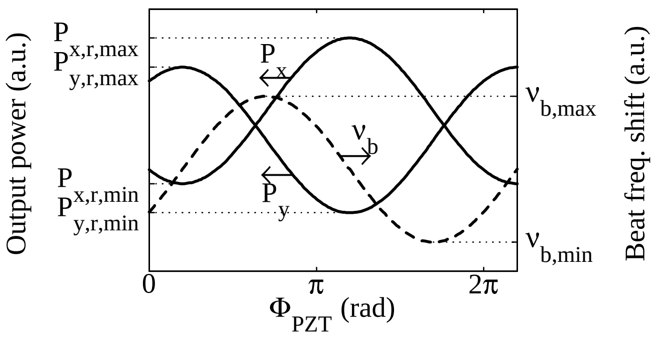

Figure 7.6. Dependence of modal powers P_x, P_y and the polarization beat frequency shift $\Delta\nu_b$ on the external cavity roundtrip phase-shift Φ_{PZT} induced by the PZT.

For polarimetric laser sensors relying on accurate readout of the polarization beat frequency ν_b, back reflection induced shifts in ν_b may contribute to measurement errors. We measured the back-reflection induced beat frequency shift for DFBa by adjusting PC2 so that the beat signal at $\nu_b \approx 970$ MHz was received at Dx (c.f. Fig. 7.5). The beat frequency was shifted down in an electronic mixer and passed to a 0-2 MHz frequency to voltage converter. The resulting voltage, monitored on an oscilloscope, was similar to the dashed line in Fig. 7.6. Fig. 7.7 (c) shows the measured (markers with error bars) and simulated (line) peak-to-peak beat frequency shift $\Delta\nu_b = \nu_{b,max} - \nu_{b,min}$. We see that $\Delta\nu_b$ exceeds the short term (~5 s) beat frequency drift of $\Delta\nu_b = \pm 10$ kHz observed in [3] when the back reflection level is > -50 dB. Rayleigh back scattering from ~ 60 m of standard single mode fiber is sufficient to produce this back reflection level. The observed beat frequency drift could, however, also be due to random temperature fluctuations or bad isolation against discrete reflectors. If the laser is used as a transverse force sensor or as a temperature sensor [3], $\Delta\nu_b = \pm 10$ kHz would correspond to readout errors of ± 6 μN or ± 6 mK, respectively.

The noise floor $\nu_{b,rms}$ at higher interrogation frequencies, seen in Fig. 7.4, may also be due to unintended back reflections with random phase. Fluctuations in back reflection phase can be caused by fluctuations in the mean laser frequency or by thermally or mechanically induced fluctuations in the optical path lengths to the reflecting points.

$\Delta\nu_b$ may be approximated analytically by:

$$\Delta\nu_b = \nu_{b,max} - \nu_{b,min} \simeq \frac{\kappa c}{\pi n} rT \left(1 + \alpha_B^2\right)^{1/2}, \tag{7.2}$$

where r is the external amplitude reflectivity, T is the power transmissivity of the grating section (or laser mirror) between r and the DFB phase-shift position, $\alpha_B = \delta(\Delta\phi_x - \Delta\phi_y)/\delta\Delta rtg_{total}$ is the linewidth enhancement factor for the beat frequency, and $\delta(\Delta\phi_x - \Delta\phi_y)$ and $\delta\Delta rtg_{total}$ are changes in

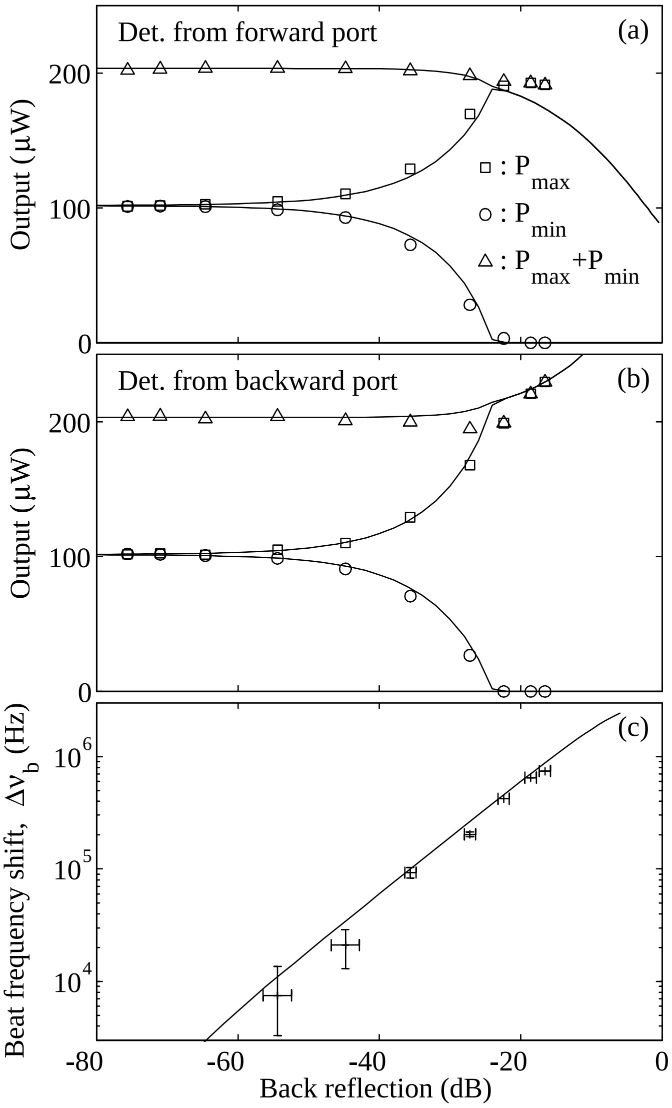

Figure 7.7. Measured (markers) and simulated (lines) response of DFBa to back-reflection into the forward port (c.f. Fig. 7.5). (a) and (b) illustrate modal output powers from the forward and backward ports, respectively. (c) shows the peak to peak modulation of the polarization beat frequency.

the polarization dependencies of the grating phase shift and the cavity roundtrip amplitude gain [8a], respectively, due to PHB. $T \simeq 4\exp(-2\kappa L_1)$ for an ideal grating section of length L_1. (7.2) is a valid approximation provided that $rT \ll 1$ (weak reflection), $\pi\Delta\nu_b\tau_{ext} \lesssim 1$ (no external cavity-mode hopping) where τ_{ext} is the external cavity roundtrip time, and $\tau_{ext} \ll \tau_{coh}$ where τ_{coh} is the laser coherence time. All these conditions were satisfied in our experiment. For our gain medium α_B is not known, and $\alpha_B = 0$ was therefore assumed for the simulations in Fig. 7.7 (c). The discrepancy between simulations and measurements indicates that the actual rT-product may have been 10 to 40 % higher than the value used for the simulations, corresponding to an underestimate of κL_1 by 1 to 4 %. This estimation error is well within the ±10 % uncertainty of the κ measurement [9].

Fig. 7.8 shows the measured (markers) and simulated (lines) response of DFBb to back reflections. (a) and (b) illustrate outputs from port 1 and 2, respectively, with back reflection into port 1. (c) illustrates output from port 1 with back reflection into port 2. The simulation parameters are the same as in Fig. 7.2. Again, the agreement between simulations and measurements is seen to be good.

The ratio T_1/T_2 of the laser mirror transmissivities of DFBb at port 1 and 2 equals the port 1 to port 2 output power ratio of 15 dB. The curves in Fig. 7.8 (c) are shifted by approximately two times this ratio (30 dB) relative to the curves in Figs. 7.8 (a) and (b). Thus, the PMC behavior is similar when the power fraction reflected back into the cavity is similar, i.e. $(rT_1)^2 = (rT_2)^2$. Note, however, that this relation is valid only when comparing the sensitivities of one laser to back reflection through two different ports. The tolerable back reflection into either port is not generally expected to drop so efficiently if both T_1 and T_2 are reduced simultaneously. This is because a reduced cavity loss implies an increase in the intensity inside the cavity, while the PHB effect is expected to decrease with increasing signal intensity [8b].

The minimum output degree of polarization (DOP) $(P_{max} - P_{min})/(P_{max} + P_{min})$ is seen from Figs. 7.7 and 7.8 to be fairly independent on output direction for both DFBa and DFBb. This observation illustrates that the relative change of the output transmissivities for the two modes caused by the back reflection is small within the dual polarization regime.

7.5 Dependence on Pump Polarization

The markers in Fig. 7.9 show the measured pump polarization dependence of the transverse force measurements that were first presented in Fig. 7.3 (b). The solid and dashed lines show simulation results obtained when we assume an effective pump PHB parameter of $\eta_p = 0.021$ and otherwise simulation

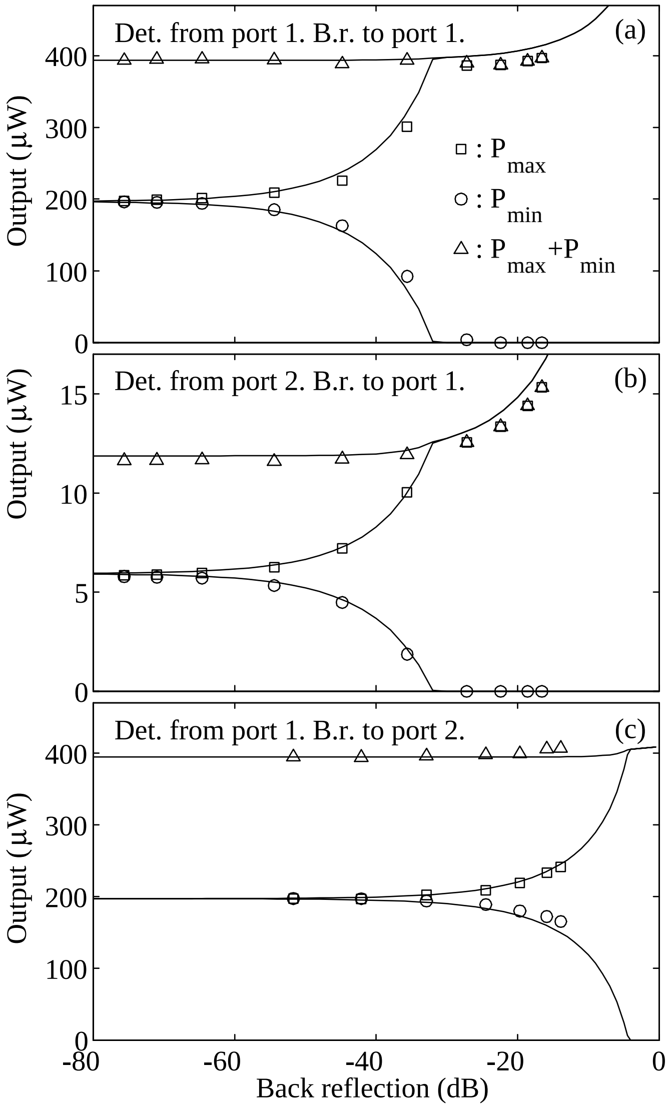

Figure 7.8. Measured (markers) and simulated (lines) response of DFBb to back-reflections (c.f. Fig. 7.8). The monitored port and the port experiencing back reflections are indicated in each sub-figure.

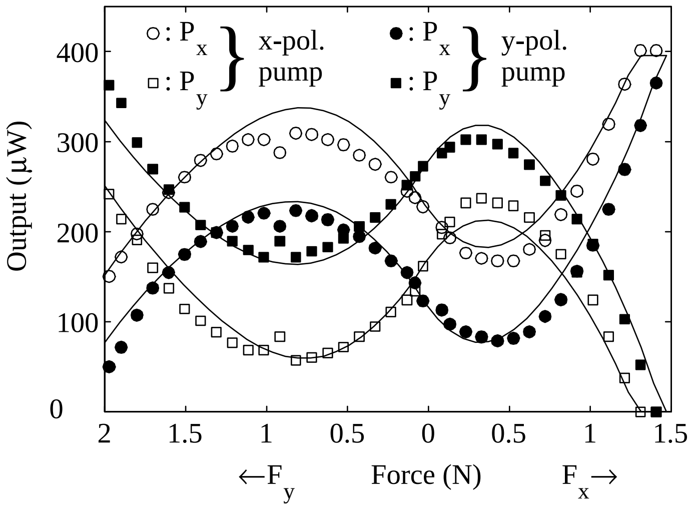

Figure 7.9. Pump polarization dependence of the measurements in Fig. 7.3 (b). Open and filled markers illustrate measurements with the pump aligned with the x and y polarizations, respectively.

parameters that are identical to those used in Fig. 7.3 (including $\eta = 0.12$). We see that the pump PHB model produces fairly good agreement with the measurements.

The markers in Fig. 7.10 show the measured pump polarization dependence of the back reflection measurements that were first presented in Fig. 7.7 (a). The open markers show $P_{q,r,max}$ and $P_{q,r,min}$ (c.f. Fig. 7.6), averaged over all possible combinations (q, r) where the mode r favored by the pump polarization is identical to the mode favored by the back reflection (q for P_{max} and opposite of q for P_{min}), i.e.: $P_{max} = (P_{x,x,max} + P_{y,y,max})/2$ and $P_{min} = (P_{y,x,min} + P_{x,y,min})/2$. The filled markers illustrate the opposite situation when the pump polarization and back reflection favor different modes, i.e.: $P_{max} = (P_{x,y,max} + P_{y,x,max})/2$ and $P_{min} = (P_{x,x,min} + P_{y,y,min})/2$. This averaging should eliminate effects of intrinsic differences in laser mode efficiencies, as well as polarization dependent measurement errors. The lines in Fig. 7.10 show the simulation results obtained with $\eta_p = 0.021$ and otherwise identical parameters to those used in Fig. 7.8 (including $\eta = 0.12$). Again, there is good agreement between theory and measurements.

The pump polarization dependencies of the remaining back reflection measurements, first presented in Figs. 7.7 (b) and 7.8 (a,b,c), were also found to be in good agreement with the simulations.

The PHB model used for the simulations is described in Appendix 7.A. It is based on an ion anisotropy model described in [15] where the Er ions are assumed to have uniaxial gain, random orientation of their optical axes (OA)

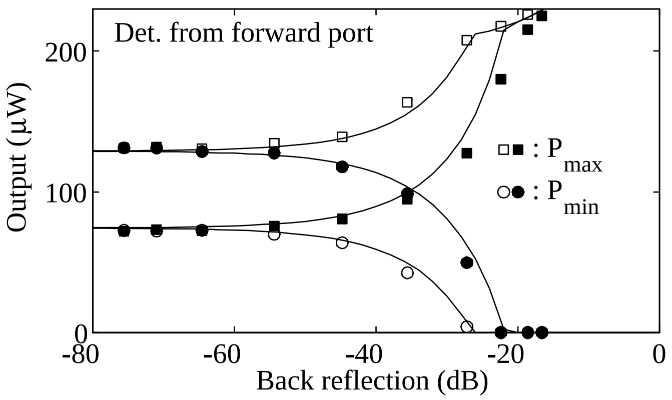

Figure 7.10. Pump polarization dependence of the measurements in Fig. 7.7 (a). Open and filled markers illustrate measurements with the pump aligned with the laser mode that is favored and disfavored by the back-reflection, respectively.

and ion cross section anisotropies defined by $A = \sigma_{\perp}/\sigma_{\|}$, $\sigma_{\perp}$ and $\sigma_{\|}$ being the ion cross-sections for fields polarized parallel and orthogonal to the OA. $\eta_p = \eta$ would be expected if the ion anisotropies were identical at the pump and signal wavelengths. However, our measurements indicate $\eta_p \approx 0.18\eta$. This reduced sensitivity to pump PHB may be due to a cross-section anisotropy that is closer to $A = 1$ at 1480 nm than at 1549 nm, or to a low correlation between the ion anisotropies at the two wavelengths for individual ions.

Fig. 7.11 shows the local PDG contributions from signal and pump PHB predicted by our model, plotted versus the signal power P_s for fully polarized pump and laser signals. The pump power and gain medium parameters are the same as for the simulations in Figs. 7.9 and 7.10. We see that both the signal and the pump induced PDG have maxima near the saturation signal power $P_{sat} = 15.5$ dBm. The signal induced PDG scales proportionally with the signal DOP, which is essentially constant throughout the cavity, and equal to the output DOP $D_p = (P_x - P_y)/(P_x + P_y)$. Similarly, the pump induced PDG is proportional to the pump DOP D_{pp}. It is found from Figs. 7.9 and 7.10 that D_p increases with about 0.5 in the dual polarization regimes when D_{pp} is reduced by 2 by changing from x-polarized to y-polarized pump. To maintain lasing in both polarizations, any difference in round-trip gain contributed from the gain medium must be maintained when D_{pp} and D_p changes. This condition is satisfied when the sum of the integrals over z of the signal and pump induced PDG contributions, weighted by the intensity distribution $P_s(z)$, is unchanged. The calculated laser power distribution for DFBa, averaged over one standing wave period, $\overline{P_s}(z)$, is illustrated with z referenced to the right-hand axis in Fig. 7.11. (The power distribution for DFBb has also been calculated, and was

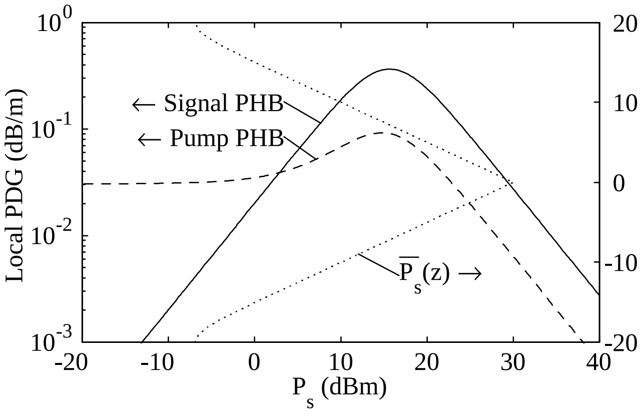

Figure 7.11. Contributions to the local signal PDG originating from signal PHB (solid line) and pump PHB (dashed lines), plotted against signal power P_s for a pump power of $P_p = 83$ mW. The pump and signal are assumed to be fully polarized. The calculated laser power distribution $\overline{P_s}(z)$ in DFBa is also shown. Parameters: $D_{pp} = -D_p = 1$, $\eta = 0.12$, $\eta_p = 0.021$, $[a_s, a_p, g_s, g_p] = [11.7, 8.9, 5.9, 3.0]$ dB/m, $P_{sp} = 4.1$ mW/m, $\xi = 39$ %, $\zeta = 25$.

found to be similar in peak magnitude and exponential decay rate to that of DFBa.) We see from the figure that most of the integrated PDG contributions will originate from the region -7 mm $< z < 7$ mm. In this region $\overline{P_s}(z) \gtrsim P_{sat}$, and the pump PHB is suppressed relative to the signal PHB by a factor that is close to $\eta_p/\eta \approx 0.18$.

In lasers with mirror transmissivities $T_1$and T_2 that exceeds the mirror transmissivities the investigated lasers by more than 15 dB, the peak cavity intensity will be more than 15 dB lower for similar output powers. We see from Fig. 7.11 that the ratio between the pump and the signal PHB magnitudes is higher in this case. Therefore, the PMC is expected to be more sensitive to the pump DOP in high mirror transmissivity lasers.

7.6 Conclusion

We have investigated how the polarization mode competition, polarization beat frequency, and individual modal frequencies in fiber DFB lasers depend on localized transverse force induced birefringence, back reflections and pump polarization. Theoretical results obtained from a comprehensive simulation model show good agreement with the measurements. Since the model parameters are obtained from independent informations that were extracted from a variety of measurements, the validity of the model is believed to be well verified.

The decrease in PHB at high saturating powers predicted by the model (c.f. Fig. 7.11) could not be checked very well by the presented measurements, however, since the peak intensity in laser cavities have been similar in all the measurements. The theory describing PHB effects at lower saturating powers have been verified from experiments in earlier publications [15]. The signal PHB parameter $\eta = 0.12$ estimated from the present measurements is twice as high as the value estimated in [8b] from measurements reported in [15] on erbium doped fiber amplifiers. Our higher value for η may be due to different compositions for the laser and the EDFA fibers, or it may be related to the grating fabrication process, including D_2-loading and UV exposure.

We have shown how the gain model presented in [8] can be extended to cover effects of PHB at the pump wavelength. The estimated pump PHB parameter $\eta_p = 0.021$ is significantly smaller than η, allowing for stable dual polarization operation independent on pump polarization. Fluctuations in the pump polarization are found to cause variations in the laser output degree of polarization D_p by ±0.25.

We have shown that the transverse force sensitivity of a dual polarization fiber DFB laser sensor can be increased significantly compared to the sensitivity achieved by pressing uniformly along the whole length of the laser by concentrating the force to within a distance shorter than $1/2\kappa$ from the grating phase-shift position. Eq. (7.1) predicts that the sensitivity can be enhanced by a factor of κL (typically 10) in this way. In our experiment we measured a transverse force sensitivity of 1.6 GHz/N, with good linearity over the full dynamic range of ~ 1.5 N. The dynamic range is limited by fading of one of the laser modes as the polarization dependence of the grating phase-shift increases.

We have found that possible UV-induced loss gratings, either formed by lifetime-quenched ions or by unbleachable losses, will influence how the PMC depends on a polarization dependent grating phase-shift. The effects on the PMC of such a loss grating is similar to the effects of a polarization independent bias in the grating phase-shift. There exist clear indications, both from investigations of the laser slope efficiencies and relaxation oscillation stability margins, that UV-induced lifetime-quenching is present in the investigated lasers [11]. It is not, however, verified to which degree the quenching has a grating component.

The tolerable external back reflection level to maintain dual polarization operation is found to be -24 dB for the symmetric DFBa. This limit is expected to increase with increasing η. It is not expected to depend much on the grating strength κL, provided that κL is well above its threshold value for lasing [8b]. For the asymmetric DFBb, the tolerable back reflection level was -32 dB at the high output port and -4.4 dB (simulated) at the low output port.

The beat frequency noise has been measured for one of the lasers to decrease from 120 to 2.1 $\mathrm{Hz}/\sqrt{\mathrm{Hz}}$ between 20 Hz and 40 kHz. For a force sensor this corresponds to a noise equivalent force ranging from 75 and 1.3 $\mathrm{nN}/\sqrt{\mathrm{Hz}}$. If the DC temperature sensitivity reported in [3] is assumed to be valid up to 40 kHz, a noise equivalent temperature fluctuation between 75 and 1.3 $\mu\mathrm{K}/\sqrt{\mathrm{Hz}}$ is found. The sensitivity to external temperatures is, however, expected to decrease above 100 Hz due to the limited radial thermal conductivity of the fiber. The source of the observed noise floor has not been identified. Beat frequency noise contributions from Schawlow-Townes noise, shot-noise, and fundamental temperature noise are all estimated to be below 0.1 $\mathrm{Hz}/\sqrt{\mathrm{Hz}}$. The results in Fig. 7.7 (c) indicate that external back reflections with random phase fluctuations may be a significant noise source. Such phase fluctuations could either originate from optical path length fluctuations in the external cavity, or from common-mode laser frequency noise.

7.7 Acknowledgment

The first author acknowledges K. Bløtekjær, S. W. Løvseth and J. T. Kringlebotn for valuable help with reading through and commenting earlier versions of this manuscript. This work was sponsored by Optoplan AS, Norwegian Research Council and British Council. The ORC is an EPSRC (UK) funded interdisciplinary Research Centre.

Appendix:

7.A Modifications to the Gain and PHB Models

The gain model used for the simulations in this paper is based on the model derived in [8]. The gain coupling matrix $\mathbf{G}$ has been slightly modified, taking the form:

$$\mathbf{G} = \begin{bmatrix} g_x & 0 & g_{gr,x} & 0 \\ 0 & g_y & 0 & g_{gr,y} \\ -g_{gr,x}^* & 0 & -g_x & 0 \\ 0 & -g_{gr,y}^* & 0 & -g_y \end{bmatrix} \tag{7.3}$$

with

$$\begin{aligned} g_x &= g - (1 - D_p)(\Delta g_s + \Delta g_p) \\ g_y &= g + (1 + D_p)(\Delta g_s + \Delta g_p) \\ g_{gr,x} &= g_{gr} - (1 - D_p)(\Delta g_{gr,s} + \Delta g_{gr,p}) \\ g_{gr,y} &= g_{gr} + (1 + D_p)(\Delta g_{gr,s} + \Delta g_{gr,p})\,. \end{aligned} \tag{7.4}$$

Here, g_q and $g_{gr,q}$ are the gain and gain grating coefficients, respectively, in the $q = x, y$ polarization propagation modes. $g_x - g_y = \Delta g_s + \Delta g_p$ and $g_{gr,x} - g_{gr,y} = \Delta g_{gr,s} + \Delta g_{gr,p}$ are the polarization dependencies of the gain and gain gratings due to polarization hole burning (PHB) at the signal (subscript s) and pump (subscript p) wavelengths. D_p is the linear degree of polarization (DOP) of the lasing signal, defined by [8a] (8). The main modification to the form of $\mathbf{G}$ compared to [8] is that the pump polarization dependent parameters Δg_p and $\Delta g_{gr,p}$ have been included. A further modification is that the polarization dependent gain (PDG) components in (7.4) are divided between the x and y modes (through the factors $(1 \pm D_p)$) in a way such that the energy conservation budget, taking into account pump absorption, signal gain, and spontaneous emission, is satisfied independent on D_p.

Lifetime quenching of a fraction ξ of the ions by a factor ζ is modeled by assuming two gain media numbered $k = 1, 2$ with ion concentrations $n_k = w_k N$. $w_1 = (1 - \xi)$, $w_2 = \xi$, and N is the total ion concentration. The local saturated amplitude gain $g_{loc,k}$ for medium k, may be expressed according to [8a] as:

$$\begin{aligned} g_{loc,k}(\phi) &= n_k N^{-1} g_{unsat,k} \left(1 + P_s(\phi)/P_{sat,k}\right)^{-1} \\ g_{unsat,k} &= w_k \left(a_p r_{wl} P_p / P_{sat,k} - a_s\right) \\ P_{sat,k} &= \left[(g_p + a_p) r_{wl} P_p + P_{sp,k}/2\right] (g_s + a_s)^{-1} \end{aligned} \tag{7.5}$$

Here, $g_{unsat,k}$ is the mean unsaturated gain and P_{sat} is the saturation power. P_p is the pump power, and $P_s(\phi) = \sum_{q=x,y} |\vec{R}_q + \vec{S}_q \exp(i\phi)|^2$ is the total saturating power where $\vec{R}_q$ and $\vec{S}_q$ are the right and left propagating fields of the $q = x, y$ lasing modes. P_{sp}, g_s, g_p, a_s, and a_p are the gain medium parameters without quenching, as defined in Sec. 7.2, $P_{sp,1} = (1 - \xi) P_{sp}$, and $P_{sp,2} = \zeta \xi P_{sp}$. $r_{wl} = 1480/1549$ is the ratio of the pump wavelength to the signal wavelength. The gain g_k and gain grating $g_{gr,k}$ coefficients of each gain medium may be expressed as

$$g_k = \frac{g_{unsat,k}}{R}; \quad g_{gr,k} = g_k \frac{R - a}{b^*},$$

with

$$a = 1 + \frac{P_t}{P_{sat,k}}, \quad b = \frac{2P_c}{P_{sat,k}}, \quad R = \sqrt{a^2 - |b|^2}, \tag{7.6}$$

$$P_t = \sum_{q=x,y} \left|\vec{R}_q\right|^2 + \left|\vec{S}_q\right|^2, \quad P_c = \sum_{q=x,y} \vec{S}_q^{+} \vec{R}_q. \tag{7.7}$$

$\vec{S}_q^{+}$ is the conjugate transpose of $\vec{S}_q$.

An expression for the local signal induced polarization dependence of the gain due to the ion cross section anisotropies was deduced in [8b] (1):

$$\Delta g_{loc,k}(\phi) = \frac{D_p \eta g_{unsat,k}\, n_k(\phi)}{N} \times \frac{P_s(\phi)/P_{sat,k}}{\left(1 + P_s(\phi)/P_{sat,k}\right)^2}. \tag{7.8}$$

Here, η is the PHB parameter at the signal wavelength. (7.8) may be expressed as $\Delta g_{loc,k} = f_k(\phi)$ where

$$f_k(\phi) = v \frac{c + \mathrm{Re}\left\{be^{i\phi}\right\}}{\left(a + \mathrm{Re}\left\{be^{i\phi}\right\}\right)^2}, \tag{7.9}$$

$v = w_k \eta D_p\, g_{unsat,k}$, $c = a - 1$, and a and b are defined by (7.6). The zeroth and first order Fourier components of $f_k(\phi)$ are:

$$\begin{aligned} F_{0,k} &= \frac{1}{2\pi}\int_0^{2\pi} f(\phi)\, d\phi = v\frac{aB^2c - B^4}{QB^2}, & (7.10) \\ F_{1,k} &= \frac{1}{2\pi}\int_0^{2\pi} f(\phi)\, e^{-i\phi} d\phi = vb^* \frac{aB^2 - a^3 - B^2c + Q}{QB^2} & (7.11) \end{aligned}$$

respectively, where

$$B = |b| \text{ and } Q = \left(a^2 - B^2\right)^{3/2}.$$

The signal induced polarization dependence of the gain and gain grating coefficients are found as $\Delta g_s = F_{0,1} + F_{0,2}$ and $\Delta g_{gr,s} = F_{1,1} + F_{1,2}$, respectively

The pump induced PDG may be modeled on basis of the same theory [8b] that was used to arrive at (7.8) by assuming the existence of ion cross-section anisotropy also at the pump wavelength. We first exchange the roles of the pump and the signal in (7.5) and (7.8) by exchanging $\Delta g_{loc,k}$, P_s, g_s, a_s, g_p, a_p, r_{wl}, $P_{sp,k}$, η, and D_p with $\Delta g_{loc,p,k}$, P_p, g_p, a_p, g_s, a_s, r_{wl}^{-1}, $P_{sp,k}/r_{wl}$, η_{p0}, and D_{pp} respectively, where, $\Delta g_{loc,p,k}$ is the polarization dependence of the (negative) gain at the pump wavelength. η_{p0} depends on the ion anisotropy at the pump wavelength in the same way as η depends on the ion anisotropy at the signal wavelength [8b]. $D_{pp} = (P_{px} - P_{py}) / (P_{px} + P_{py})$ is the linear DOP of the pump signal, where P_{px} and P_{py} are the x- and y-polarized components of P_p, respectively. The resulting PDG at the signal wavelength may be written $\Delta g_{loc,s,k} = r_1 r_0 \Delta g_{loc,p,k}$, where $r_0 = (g_s + a_s) / (g_p + a_p)$ is the conversion factor from pump to signal gain changes, and r_1 accounts for the possibility that the cross section anisotropies of individual ions at the two wavelengths may not be fully correlated. After some algebraic manipulation, the local PDG may be written on the form $\Delta g_{loc,s,k} = f_k(\phi)$ if the parameters a, b, c and v in (7.9) are redefined as:

$$\begin{aligned} a &= 1 + (P_t + P_{sp,k}/2)\, P_0^{-1}, & b &= 2P_c P_0^{-1} \\ c &= \left(P_t + \frac{r_0 a_p\, P_{sp,k}/2}{r_0 a_p - a_s} \right) P_0^{-1}, & P_0 &= r_{wl} P_p r_0^{-1} \\ v &= -w_k \eta_p\, D_{pp}\, (r_0 a_p - a_s) & \eta_p &= r_1 \eta_{p0}. \end{aligned} \tag{7.12}$$

P_t and P_c are defined by (7.7). The pump induced portion of the polarization dependence of the gain and gain grating coefficients Δg_p and $\Delta g_{gr,p}$, respectively, may thus be calculated, after substituting (7.12) into (7.10, 7.11), as $\Delta g_p = F_{0,1} + F_{0,2}$ and $\Delta g_{gr,p} = F_{1,1} + F_{1,2}$.

References

[1] M. Ibsen, A. Fu, H. Geiger and R.I. Laming, "All-fibre 4 x 10 Gbit/s WDM link with DFB fibre laser transmitters and a single sinc-sampled fibre grating dispersion compensator", Electron. Lett., Vol. 35, pp. 982-983, 1999.

[2] J. T. Kringlebotn, W. H. Loh and R. I. Laming, "Polarimetric Er^{3+}-doped fiber distributed-feedback laser sensor for differential pressure and force measurements", Opt. Letters, Vol.21, pp.1869-71, 1996.

[3] O. Hadeler, E. Rønnekleiv, M. Ibsen and R. I. Laming, "Polarimetric fiber distributed feedback laser sensor for simultaneous strain and temperature measurements", Appl. Opt., Vol. 38, pp. 1953-1958, 1999.

[4] H. Storøy, B. Sahlgren and R. Stubbe, "Single polarization fibre DFB laser", El. Letters, Vol. 33, pp. 56-8, 1997.

[5] J. I. Philipsen, M. O. Berendt, P. Varming, V. C. Lauridsen, J. H. Povlsen, J. Hübner, M. Kristensen, B. Pálsdóttir, "Polarisation control of DFB fibre laser using UV-induced birefringent phase-shift", El. Letters, Vol. 34, pp. 678-9, 1998.

[6] M. Ibsen, E. Rønnekleiv, G. J. Cowle, M. O. Berendt, O. Hadeler, M. N. Zervas, and R. I. Laming, "Robust high-power (>20 mW) all-fiber DFB lasers with unidirectional and truly single polarization outputs" in *Proc. to Conference on Lasers and Electro-Optics (CLEO) 1999*, pp. 245-246, paper CWE4, Baltimore, USA, 1999.

[7] Z. E. Haratjunian, W. H. Loh, R. I. Laming and D. N. Payne, "Single polarization twisted distributed feedback fibre laser", El. Lett., Vol. 32, pp. 346-8, 1996.

[8] a) E. Rønnekleiv, M. N. Zervas and J. T. Kringlebotn, "Modeling of Polarization Mode Competition in Fiber DFB Lasers", IEEE J. Quantum Electron., Vol. 34, pp. 1559-69, 1998.
b) E. Rønnekleiv, M. N. Zervas and J. T. Kringlebotn, "Correction to "Modeling of Polarization Mode Competition in Fiber DFB Lasers"", IEEE J. Quantum Electron., Vol. 35, pp. 1097-1100, 1999.

[9] E. Rønnekleiv, M. Ibsen, M. N. Zervas, and R. I. Laming, "Characterization of fiber distributed-feedback lasers with an index perturbation method", Appl. Opt., Vol. 38, pp. 4558-4565, 1999.

[10] L. Dong, W. H. Loh, J. E. Caplen, J. D. Minelly and L. Reekie, "Efficient single-frequency fiber-lasers with novel photosensitive Er/Yb optical fibers", Opt. Lett., Vol. 22, pp. 694-6, 1997.

[11] E. Rønnekleiv and O. Hadeler, "Stability of an Er-Yb-doped fiber distributed-feedback laser with external reflections", Opt. Lett., Vol. 24, pp. 617-619, 1999.

[12] J. Hübner, T. Feuchter, C.V. Poulsen, and M. Kristensen, "Directly UV-written erbium doped waveguides", in *Photosensitivity and Quadratic Nonlinearity in Glass Waveguides: Fundamentals and Applications*, OSA Technical Digest Series, Vol. 22, 1995.

[13] J. I. Sakai, T. Kimura, "Birefringence and Polarization Characteristics of Single-Mode Optical Fibers under Elastic Deformations", IEEE J. of Q. El., Vol. QE-17, pp. 1041-51, 1981.

[14] R. B. Wagreich, W. A. Atia, H. Singh and J. S. Sirkis, "Effects of diametric load on fibre Bragg gratings fabricated in low birefringent fibre", El. Letters, Vol. 32, pp. 1223-4, 1996.

[15] P. Wysocki and V. Mazurkzyk, "Polarization Dependent Gain in Erbium-doped Fiber Amplifiers: Computer Model and Approximate Formulas", J. Lightwave Technol., Vol. 14, pp. 572-84, 1996.

[16] M. Sargent III, W. H. Swantner and J. D. Thomas, "Theory of a Distributed Feedback Laser", IEEE J. of Q. El., Vol. QE-16, pp. 465-72, 1980.

[17] W. S. Rabinovich and B. J. Feldman, "Spatial Hole Burning Effect in Distributed Feedback Lasers", IEEE J. of Q. El., Vol. 25, pp. 20-30, 1989.

Part IV: Sensor Applications

Chapter 8

Polarimetric distributed feedback fiber laser sensor for simultaneous strain and temperature measurements[1]

Abstract — We report the application of a dual polarization distributed feedback (DFB) fiber laser as a strain and temperature sensor. By measurement of the absolute wavelength of one polarization as well as the polarization beat frequency, strain and temperature were determined simultaneously. The sensor has an accuracy of $\pm 3\mu\varepsilon$ and $\pm 0.04°\mathrm{C}$. Self-heating of the DFB fiber laser as a function of pump power was measured with this sensor.

OCIS codes: 060.2370, 280.3420.

8.1 Introduction

Fiber-optic Bragg grating sensors are a promising device for measuring strain and temperature in a variety of structures. Bragg gratings are written noninvasively into optical fibers [1, 2] making the sensor head very compact. The measurands are wavelength encoded, offering high accuracy and wavelength division multiplexing capabilities of several sensors. However, as the grating wavelength is a function of strain and temperature, the elimination or compensation of this strain-temperature cross-sensitivity has become of great technological interest in recent years.

---

[1] This chapter is a re-edited version of [O. Hadeler, E. Rønnekleiv, M. Ibsen and R. I. Laming, "Polarimetric fiber distributed feedback laser sensor for simultaneous strain and temperature measurements", Appl. Opt. Vol.38, pp. 1953–1959 (1999)].

Several techniques have been developed and demonstrated to separate the strain and temperature response of fiber Bragg grating sensors. These include compensating temperature drifts by employing two independent sensors, [3] the first one subject to strain and temperature and the second one subject to temperature only. Careful packaging and positioning of the sensors is required for ensuring that the temperature difference between the two sensors remains constant and that the second sensor does not experience any strain. A more compact design can be achieved by use of a single Bragg grating sensor capable of measuring strain and temperature simultaneously. By superimposing two gratings at different wavelengths, such a sensor has been demonstrated [4] making use of the different strain and temperature responses at the two grating wavelengths. The measurement errors were ±10 $\mu\varepsilon$ and ±5 °C. Although such a sensor needs two light sources at widely separated wavelengths, Sudo et al. [5] have reported a sensor with a Bragg grating written into birefringent fiber where the grating wavelengths of the two orthogonal polarizations responded differently to strain and temperature. The maximum measurement errors of that polarimetric sensor were ±20 $\mu\varepsilon$ and ±2 °C. Alternatively, the thermal response of a grating strain sensor can be canceled by use of a chirped grating in a tapered fiber [6]. However, the elimination of the temperature response might limit the practicality of this strain sensor for structural monitoring because it is impossible to discriminate between mechanically and thermally induced expansion.

A common disadvantage of the above-mentioned passive fiber Bragg grating sensors is that only a small fraction of the spectrally broadband light incident on a narrow-band grating is reflected. This limits the signal-to-noise ratio and therefore the resolution of the sensor. In general, active fiber grating sensors, i.e., sensors where gratings form part of a fiber laser, offer a higher accuracy than passive Bragg grating sensors. The laser intensity is concentrated in a spectral band that is several orders of magnitude narrower than the bandwidth of a passive grating. The laser cavities of distributed Bragg reflection (DBR) fiber lasers are formed by either a broadband mirror and a grating or two gratings at the same wavelength. Typical DBR fiber laser are between a few centimeters and several meters long. Melle et al. [7] reported a DBR fiber laser strain sensor with a resolution of ±5.4 $\mu\varepsilon$, limited by the electrical noise of the interrogation system. However, in this case, the sensor resolution potentially suffers from mode hopping of these highly multimoded lasers caused by nonuniform environmental changes along the cavity length [7, 8]. Multiplexing of as many as three DBR fiber laser sensors was demonstrated with negligible cross talk between the sensors in [9].

A DBR fiber laser may operate in orthogonal polarization modes if birefringent fiber or birefringent gratings are used in the laser cavity. For lasers with a sufficiently small birefringence, the beat frequency between the two polarization modes can be measured with a commercial rf spectrum analyzer. External perturbations such as strain and temperature change the birefringence [10] and therefore the polarization beat frequency. Kim et al. [10] demonstrated a polarimetric fiber laser sensor for measuring either strain or temperature. Because of its multimode operation, the rf spectrum exhibited a number of beat frequencies between different longitudinal and polarization modes. The accuracy of the sensor was limited by the broad linewidth of the polarization beatsignal ($\sim$ 1.2 MHz). A DBR fiber laser that was lasing only in two orthogonal polarization modes was demonstrated by Ball et al. [12]. The linewidth of the polarization beat signal was less than 2.5 kHz. Compared with multimode lasers, signal processing becomes much simpler as only one polarization beat frequency is present. Also, the narrow linewidth of the polarization beat signal leads to a higher measurement resolution.

For single-mode operation, DBR fiber lasers must not be longer than a few centimeters and the grating bandwidth has to be below -0.2 nm. The short length usually limits the pump absorption and therefore the output power. Distributed feedback (DFB) fiber lasers are an alternative to DBR fiber lasers with the advantage that they consist of only one grating written into rare-earth-doped fiber. They offer single-mode operation without mode hopping and kilohertz linewidth [13]. With a grating length of -50 mm, DFB fiber lasers are very compact. Furthermore, as most of the laser intensity is concentrated in the center of the grating, the sensitive region is only $\sim$5-10 mm long, [14] making it ideal for point sensing. Multiplexing of five DFB fiber lasers has been demonstrated [15], but only few investigations into lasing stability and sensor accuracy have been carried out. In low birefringent fiber a DFB fiber laser can operate on two orthogonal polarization modes with a ftequency separation between the two modes sufficiently small so that the polarization beat signal can be measured very accurately with a commercial rf spectrum analyser. A birefringent DFB fiber laser operating stably in two polarization modes was employed in [16] as a polarimetric sensor for separately measuring lateral forces and temperature.

In this paper, we demonstrate a similar polarimetric DFB fiber laser sensor for strain and temperature measurements. By measuring both the polarization beat frequency and the absolute wavelength of one polarization, we determined both measurands simultaneously.

8.2 Theory

The wavelengths of the two orthogonal polarization modes of a DFB fiber laser are given by

$$\lambda_{x,y} = 2n_{x,y}\Lambda, \tag{8.1}$$

where $\lambda_{x,y}$ denotes the wavelength of the two orthogonally polarized laser modes, $n_{x,y}$ are the refractive indices of the fiber, and Λ is the grating pitch. For a low birefringent fiber with $n_x \approx n_y \approx n$, the polarization beat frequency becomes

$$\Delta\nu = cB/\left(2n^2\Lambda\right) \tag{8.2}$$

where $B = n_x - n_y$ is the birefringence and c is the velocity of light. Generally, the strain and temperature dependence of $\lambda_{x,y}$ is given by

$$\delta\lambda_{x,y}/\lambda_{x,y} = (1 - p_e)\ \delta\varepsilon|_{\varepsilon=const} + (\alpha + \xi)\ \delta T|_{\varepsilon=const}, \tag{8.3}$$

where p_ε is the strain-optic coefficient, α is the linear thermal expansion coefficient, and ξ is the thermooptic coefficient. Typical values for silica fiber quoted in the literature are $p_\varepsilon = -0.22$, $n_x = 1.46$, $\alpha \approx 0.5 \times 10^{-6}$ K^{-1}, and $\xi \approx -8.5 \times 10^{-6}$ K^{-1} [16, 17].

Asymmetrical transverse stress introduces birefringence in the fiber. This stress can build up in noncircular symmetric fibers during fabrication owing to the different thermal contraction of core and cladding. For temperatures below −350 °C, the birefringence reduces linearly with increasing temperature as the glass softens.[10]. Theoretical and experimental research [18] has shown that the birefringence is also strain dependent. Both Ball et.al. [10] and Huang et.al. [18] have shown that the strain and temperature dependence of the birefringence is caused by a complex interplay between fiber asynimetries and the different mechanical and thermal properties of the core and cladding. However, the theory proposed [18] is not detailed enough to describe exactly the strain dependence of the birefringence in fibers in which core and cladding have different mechanical properties. Leaving the exact birefringence mechanisms aside, it follows from Eq. (8.2) that $\Delta\nu$ of a birefringent DFB fiber laser changes with strain and temperature according to

$$\begin{aligned}\frac{\delta(\Delta\nu)}{\Delta\nu} &= \left[\frac{1}{B}\frac{dB}{d\varepsilon} - (1 + 2p_\varepsilon)\right] \delta\varepsilon|_{T=const} \\ &\quad + \left[\frac{1}{B}\frac{dB}{dT} - (\alpha + 2\xi)\right] \delta T|_{\varepsilon=const}\end{aligned} \tag{8.4}$$

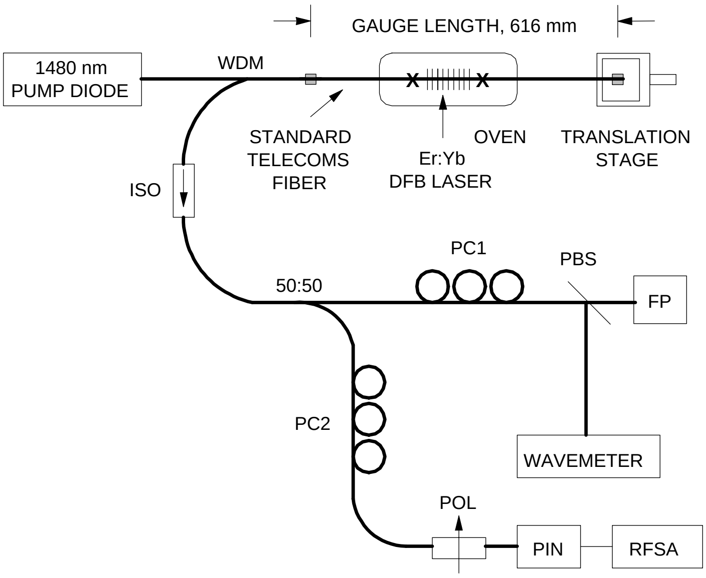

Figure 8.1. Experimental arrangement: WDM, wavelength division multiplexer; ISO, isolator; 50:50, coupler; PC1 and PC2, polarization controllers; PBS, polarizing beam splitter; POL, polarizer; FP, Fabry-Perot spectrometer; PIN, photodiode; RFSA, rf spectrum analyzer.

The responses $\delta\lambda_{x,y}$ and $\delta(\Delta\nu)$ of the DFB fiber laser to strain and temperature [Eqs. (8.3) and (8.4)] can be written in matrix form as

$$\begin{aligned}\begin{bmatrix}\delta\lambda_{x,y}\\ \delta\Delta\nu\end{bmatrix} &= \begin{bmatrix}k_{11} & k_{12}\\ k_{21} & k_{22}\end{bmatrix}\begin{bmatrix}\delta\varepsilon\\ \delta T\end{bmatrix}\\ &= \mathbf{K}\begin{bmatrix}\delta\varepsilon\\ \delta T\end{bmatrix} \qquad (8.5)\end{aligned}$$

For a well-conditioned matrix **K**, i.e., det $\mathbf{K} \neq 0$, Eq. (8.5) can be inverted. Strain and temperature can then be determined simultaneously by measurement of either $\delta\lambda_x$ or $\delta\lambda_y$ and $\delta\Delta\nu$.

8.3 Experimental Arrangement

The experimental arrangement is shown in Fig. 8.1. A 45 mm long DFB fiber laser was written in an uncoated fiber consisting of an Er^{3+}:Yb^{3+}-doped silica core, a B-Ge-doped silica photosensitive ring around the core, and a silica cladding. The grating coupling coefficient was $\kappa \approx 230$ m^{-1}, and the grating phase shift was positioned asymmetrically 20 mm away from the pump input end. The laser operated near $\lambda = 1550$ nm. Standard telecommunication fiber was spliced to both sides of the laser, approximately 5 mm away from the grating ends. With cyanoacrylate used to bond the coated telecommunication fiber to a fixed metal post and a manual translation stage, the gauge length of the strain sensor was defined. Each bonded region was 10-15 mm long. The gauge length was $l_g = 616$ mm. An oven, consisting of a 150 mm × 15 mm × 15 mm aluminium block and a Peltier element, was used to heat the DFB fiber laser. A duct (3 mm × 3 mm) along the longitudinal axis of the aluminium block accommodated the DFB fiber laser. Care was taken so that the laser did not touch the aluminium block, preventing unwanted strain caused by friction. Furthermore, twist in the fiber was avoided so that additional birefringence was not introduced. The temperature of the aluminium block was regulated with a commercial temperature controller. The thermistor of the control loop was placed -10 mm away from the edge of the Peltier element. The real temperature of the aluminium block was measured with a thermocouple next to the thermistor. The thermocouple had a resolution of ±0.1 °C, and the temperature controller kept the temperature of the oven to within this resolution. The oven was isolated by 5-15-mm-thick polystyrene. The thermal expansion of the fiber was constrained by the two fixing points of the fiber. Therefore temperature changes of the fiber section in the oven induced thennal stress along the whole length of fiber. The stress related strain was $l_h \alpha \delta T \,/\, l_g$, where l_h is the length of the fiber section in the oven.

The DFB fiber laser was pumped by a 1480-nm diode laser and gave an output power of 430 μW for 82 mW of pump power. The output of the DFB fiber laser was split into two arms by a 50:50 coupler. One arm was used to measure the wavelength $\lambda_{x,y}$ of one polarization with a wavemeter. The polarization controller PC1 was used to align the polarization axes of the laser output parallel to the axes of a fiber-pigtailed polarizing beam splitter (PBS) so that only the x polarization (labeling of the polarization axes is arbitrarily) was incident on the wavemeter. The alignment of the polarization axes was monitored at the second output of the PBS with a scanning Fabry-Perot spectrum analyzer with a free spectral range of 6 GHz and a resolution of 1.2 MHz. The polarization controller PC1 was adjusted until the signal from the x polarization vanished on the Fabry-Perot trace. Measuring $\delta\lambda_{x,y}$ of only one polarization leads to a greater accuracy than measuring the change of the mean wavelength of both polarizations. The latter method could suffer from relative intensity fluctuations between the two polarization modes. As external perturbations of the lead fiber change the polarization state at the input of the PBS, active polarization control or the use of polarization- maintaining fiber should be considered. At the other output of the coupler, the two polarization modes were mixed in a polarizer. The resulting beat signal was detected with a photodiode and the frequency measured with an rf spectrum analyzer. A

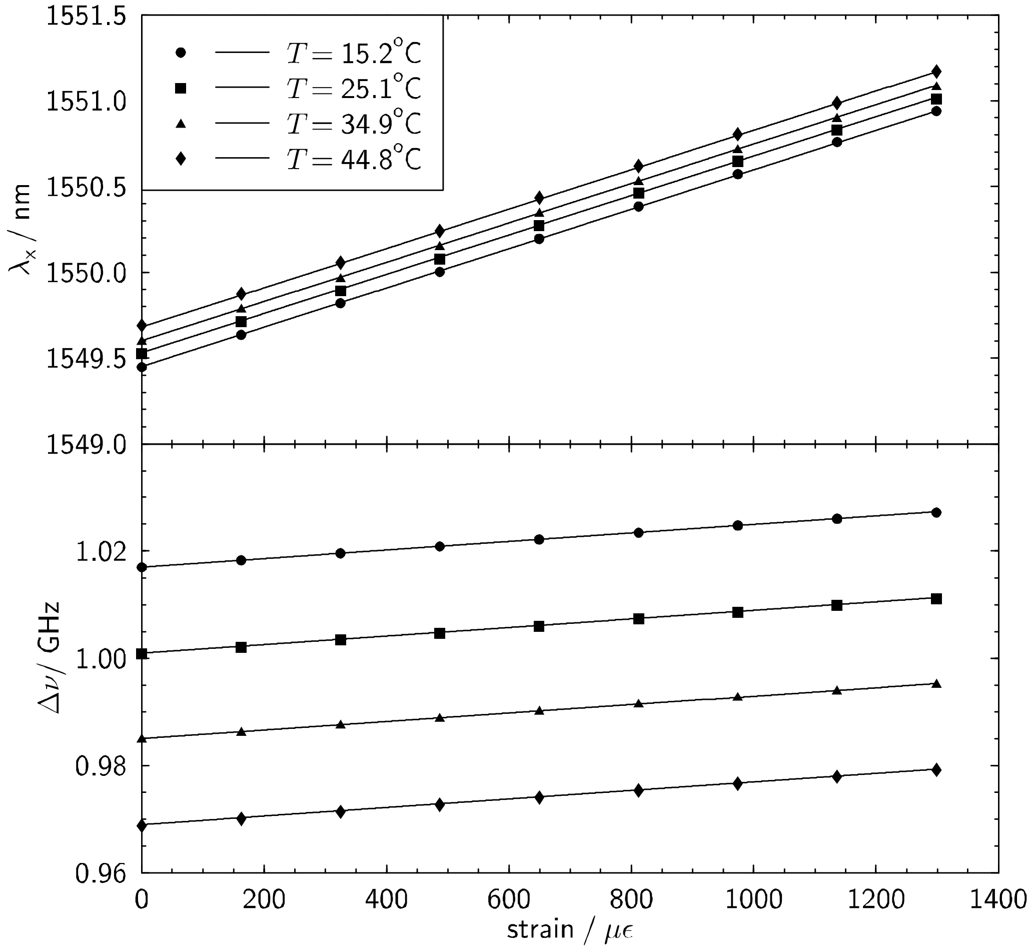

Figure 8.2. Wavelength of x-polarization and polarization beat frequency as a function of strain.

polarization controller (PC2) was used to optimize the signal amplitude on the rf spectrum analyzer.

8.4 Results

The wavelength λ_x of the unstrained DFB fiber laser at room temperature was measured to be 1549.5 nm whilst the polarization beat frequency was $\Delta\nu \sim 1$ GHz with a linewidth of $\sim$ 10 kHz. Inserting $\Delta\nu$, $\lambda_x \approx 2n\Lambda$, and $n = 1.46$ into Eq. (8.2) leads to a birefringence of $B \approx 7.5 \times 10^{-6}$. This birefringence is a combination of the intrinsic fiber birefringence and the birefringence induced by the inscription of the DFB grating. The polarization beat frequency of our DFB fiber laser is approximately 2.3 times bigger than in a previous experiment

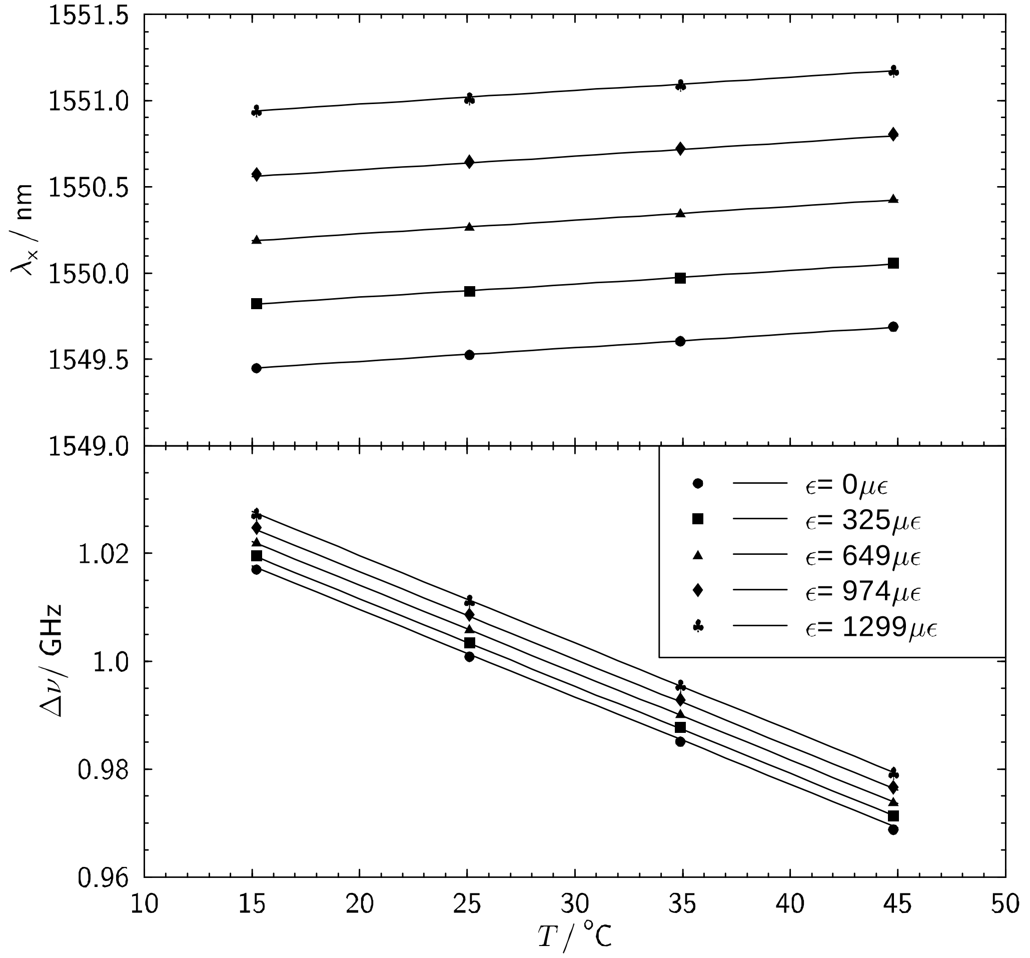

Figure 8.3. Wavelength of x-polarization and polarization beat frequency as a function of temperature. Data of only five strain levels is shown for clarity of the graph.

[16]. This can be attributed to the different fibers used for the two lasers as the grating writing process was essentially the same.

The sensor was calibrated by measurement of λ_x and $\Delta\nu$ at four different temperatures with nine strain levels each. The standard deviation of each measurement was estimated to be $\sigma(\lambda_x) \approx \pm 1$ pm and $\sigma(\Delta\nu) \approx \pm 10$ kHz. The results are shown in Figs. 8.2 and 8.3. Two planes, $\lambda_x(\varepsilon, T)$ and $\Delta\nu(\varepsilon, T)$, were fitted to the data, yielding the following regression coefficients and their standard deviation:

$$\begin{aligned}
k_{11} &= (1.147 \pm\ 0.002)\ \mathrm{pm}/\mu\varepsilon,\\
k_{12} &= (7.946 \pm\ 0.065)\ \mathrm{pm}/^{\circ}\mathrm{C},\\
k_{21} &= (7.946 \pm\ 0.043)\ \mathrm{kHz}/\mu\varepsilon,\\
k_{22} &= (-1.623 \pm\ 0.002)\ \mathrm{MHz}/^{\circ}\mathrm{C}.
\end{aligned}$$

Note that the numerical equality of k_{12} and k_{21} is pure coincidence.

The analysis of the residuals showed that the deviations of the wavelength measurements from the fitted straight line arose mainly from an uneven motion of the translation stage, which defined the strain. This limits the accuracy of the regression coefficients k_{11} and k_{12}. The resolution (±0.1°C) of the thermocouple used to measure the oven temperature corresponds to $\delta\Delta\nu = \pm 162$ kHz. The residuals of the beat frequency measurements and the resulting standard deviation of the regression coefficients k_{21} and k_{22} are due mainly to this limited resolution of the temperature measurement. The analysis of the residuals showed no sign of nonlinear strain or temperature response of the sensor. Therefore it can be concluded that any cross-sensitivity between strain and temperature is negligible. Combination of the calibration errors, i.e., the errors of $\mathbf{K}^{-1}$, and the accuracies of the wavelength and polarization beat frequency measurements, $\sigma(\lambda_x)$ and $\sigma(\Delta\nu)$, yields, for this strain and temperature sensor, an accuracy of $\pm 3\ \mu\varepsilon$ and ±0.04 °C. The reproducibility of the strain measurements was $\pm 2.5\ \mu\varepsilon$, which is in agreement with the position reproducibility of the translation stage. Although the telecommunication fiber was coated, no slipping or creep of the fiber was observed. However, at higher strain levels or over longer periods, slipping and creep are potential problems that one can solve by choosing appropriate glues and by using either uncoated fiber or harder coatings. The thermal stress induced by the rise of the fiber temperature from room temperature (25 °C) to 45 °C led to a strain of $-2.4\ \mu\varepsilon$, which lies within the accuracy of the sensor. A possible calibration error of the thermometer is not included in the above stated accuracy of the sensor. The resolution of this strain and temperature sensor is limited by the accuracy of the wavelength and the beat frequency measurements. The accuracy of the wavelength measurement is practically limited by the wavemeter used, in this case ± 0.1 pm. The accuracy of the beat frequency measurement is limited by the linewidth of the beat signal, which, in turn, depends on the linewidth of the DFB fiber laser.

The strain dependence $\delta\lambda_x/\lambda_x = k_{11} \times \delta\varepsilon/\lambda_x = 0.74\delta\varepsilon$ is in good agreement with theoretical predictions from Eq. (8.3) of $\delta\lambda_x/\lambda_x = 0.78\delta\varepsilon$. The temperatare dependence $\delta\lambda_x/\lambda_x = k_{12} \times \delta T/\lambda_x = 5.1 \times 10^{-6} K^{-1}$ is smaller than $8.5 \times 10^{-6} K^{-1}$, the value commonly quoted for silica fiber in the literature. This discrepancy probably arises from the rare-earth doping of the fiber, as the

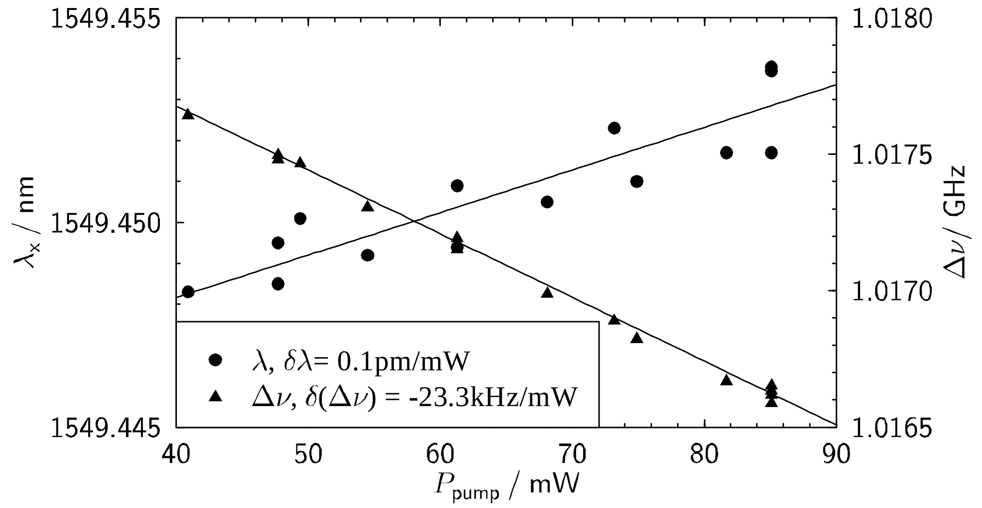

Figure 8.4. Wavelength of x-polarization and polarization beat frequency as a function of pump power at 1480 nm.

value is similar to $4.9 \times 10^{-6} K^{-1}$, which is calculated from the results published by Kringlebotn et.al. in [16]. From the beat frequency measurement $\Delta\nu$, it can be concluded that the birefringence increases with strain. Additional asymmetric stress is probably induced in the strained fiber owing to different mechanical properties of the core, the B-Ge-doped ring, and the cladding. The decrease of $\Delta\nu$ with increasing temperature is expected from theory. The slope $\delta\Delta\nu/\delta T$ depends on the actual thermal properties of the fiber used.

Self-heating of the DFB fiber laser sensor, which is a function of pump power, is a potential source of error. Since the laser intensity is concentrated in the center of the grating and decreases exponentially toward the ends [14], the temperature varies accordingly. Measuring λ_x and $\Delta\nu$ yields a weighted mean or an effective temperature of the DFB fiber laser. While the unstrained fiber was in free air in the oven, the pump power was increased from 40 to 85 mW. Figure 8.4 shows λ_x and $\Delta\nu$ as a function of pump power. The data points lie within the aforementioned accuracy. Fitting two straight lines to the data and using the calibration constants k_{12} and k_{22} reveals that the effective temperature increased by 0.014 ± 0.001 °C/mW. So that the aforementioned accuracy of ± 0.04 °C is not exceeded, the pump power must not vary by more than ± 3 mW. Although the output power of commercial pump lasers can easily be stabilized to within this limit, variable losses in the lead fiber could potentially cause larger variations. Further investigations on how the pump and lasing intensifies heat the fiber will be carried out in a separate experiment.

8.5 Conclusion

In conclusion, we have demonstrated an active polarimetric strain and temperature sensor based on a birefringent DFB fiber laser. The achieved accuracy of simultaneous measurements of strain and temperature was $\pm 3\ \mu\varepsilon$ and ± 0.04 °C, respectively. This accuracy was limited by the equipment used to calibrate the sensor, so an improved accuracy should be obtainable. No cross-sensitivity between strain and temperature was observed; the sensor responded linearly to both measurands. The DFB fiber laser operated robustly in two linear polarizations, and it is hoped that multiplexing of several such devices will lead to simple, easy to install, and reliable fiber sensor networks. For industrial applications the sensor can potentially be protected by, e.g., tubes of ~ 50 mm length and ~ 1 mm diameter. Mass fabrication of DFB fiber lasers would result in a low-cost sensor head. The expensive parts of the sensor, the pump laser, and the signal processing unit could be shared between several sensor networks. The use of a digital ftequency counter or a voltage-controlled oscillator locked to the polarization beat frequency would reduce the costs of the signal processing unit. Self-heating of the fiber laser as a function of pump power has also been measured. Pump power fluctuations that could be caused by variable losses in the lead fiber should be kept below ± 3 mW so that the previously mentioned accuracy of the temperature measurements is not exceeded.

8.6 Acknowledgement

O. Hadeler acknowledges the support through a Co-operative Award in Science and Engineering, award from BICC Cables Limited, and the useful discussions with the staff at BICC in Helsby, United Kingdom. The Optoelectronies Research Centre is an interdisciplinary research center funded by the United Kingdom Engineering and Physical Science Research Council.

References

[1] G. Meltz, W. W. Morey, and W. H. Glenn, "Formation of Bragg gratings in optical fibers by a transverse holographic method," Opt. Lett. **14**, 823-825 (1989).

[2] K. O. Hill, B. Malo, F. Bilodeau, D. C. Johnson, and J. Albert, "Bragg gratings fabricated in monomode photosensitive optical fiber by UV exposure through a phase mask," Appl. Phys. Lett. **62**, 1035-1037 (1993).

[3] A. D. Kersey, T. A. Berkoff, and W. W. Morey, "Fiber-optic Bragg grating strain sensor with drift-compensated high-resolution interferometric wavelength-shift detection," Opt. Lett. **18**, 72-74 (1993).

[4] M. G. Xu, J. L. Archambault, L. Reekie, and J. P. Dakin, "Discrimination between strain and temperature effects using dual-wavelength fibre grating sensors," Electron. Lett. **30**, 1085-1087 (1994).

[5] M. Sudo, M. Nakai, K Himeno, S. Suzaki, A. Wada, and R. Yamauchi, "Simultaneous measurement of temperature and strain using PANDA fiber grating," in *Optical Fiber Sensors*, Vol. 16 of 1997 OSA Technical Digest Series (Optical Society of America, Washington, D.C., 1997), pp. 170-173.

[6] M. G. Xu, L. Dong, L. Reekie, J. A. Tucknott, and J. L. Cruz, "Temperature-independent strain sensor using a chirped Bragg grating in a tapered optical fibre," Electron. Lett. **31**, 823-825 (1995).

[7] S. M. Melle, A. T. Alavie, S. Karr, T. Coroy, K Liu, and R. M. Measures, "A Bragg grating-tuned fiber laser strain sensor system," IEEE Photonics Technol. Lett. **5**, 263-266 (1993).

[8] G. A. Ball, W. W. Morey, and P. K Cheo, "Single- and multi- point fiber-laser sensors," IEEE Photonics Technol. Lett. **5**, 267-270 (1993).

[9] A. T. Alavie, S. E. Karr, A. Othonos, and R. M. Measures, "A multiplexed Bragg grating fiber laser sensor system," IEEE Photonics Technol. Lett. **5**, 1112-1114 (1993).

[10] S. C. Rashleigh, "Origins and control of polarization effects in single-mode fibers," J. Lightwave Technol. **LT-1**, 312-331 (1983).

[11] H. K Kim, S. K. Kim, and B. Y. Kim, "Polarization control of polarimetric fiber-laser sensors," Opt. Lett. **18**, 1465-1467 (1993).

[12] G. A. Ball, G. Meltz, and W. W. Morey, "Polarimetric heterodyning Bragg-grating fiber-laser sensor," Opt. Lett. **18**, 1976-1978 (1993).

[13] J. T. Kringlebotn, J. L. Archambault, L. Reekie, and D. N. Payne, "Er^{3+}:Yb^{3+}-codoped fiber distributed-feedback laser," Opt. Lett. **19**, 2101-2103 (1994).

[14] E. Rønnekleiv, M. Ibsen, M. N. Zervas, and R. I. Laniing, "Characterization of intensity distribution in symmetric and asymmetric fiber DFB lasers," in *Conference on Lasers and Electro-Optics*, Vol. 6 of 1998 OSA Technical Digest Series (Optical Society of America, Washington, D.C., 1998), p. 80.

[15] J. Hübner, P. Varming, and M. Kristensen, "Five wavelength DFB fibre laser source for WDM systems," Electron. Lett. **33**, 139–140 (1997).

[16] J. T. Kringlebotn, W. H. Loh, and R. I. Laming, "Polarimetric Er^{3+}-doped fiber distributed-feedback laser sensor for differential pressure and force measurements," Opt. Lett. **21**, 1869-1871 (1996).

[17] H. Singh and J. S. Sirkis, "Simultaneously measuring temperature and strain using optical fiber microcavities," J. Lightwave Technol. **15**, 647-653 (1997).

[18] S.-Y. Huang, J. N. Blake, and B. Y. Kim, "Perturbation effects on mode propagation in highly elliptical core two-mode fibers," J. Lightwave Technol. **8**, 23-33 (1990).

Chapter 9

Intrinsic Distributed Feedback Fibre Laser High Frequency Hydrophone[1]

Abstract — We demonstrate for the first time a distributed feedback fibre laser used as a hydrophone for acoustic frequencies ranging from 0.1 to 1MHz.

9.1 Introduction

Fibre optic interferometric hydrophones have been under development for more than 20 years as an alternative to conventional piezoelectric based hydrophones, and are attractive due to light weight, multiplexing capabilities, and high resolution, making them attractive for hydrophone arrays. Interferometric sensors are based on coils of optical fibre with dimensions mainly limited by the minimum coiling diameter, which is typically 15-20 mm. Smaller sensor dimensions are normally required for high frequency ($>$100 kHz) acoustic sensing to avoid extremely directive sensors. Also operation in space-restricted areas will require small sensor dimensions.

Distributed Bragg reflector (DBR) fibre laser sensors with interferometric readout have been demonstrated for high resolution strain measurements [1]. DBR lasers are based on one fiber Bragg grating (FBG) reflector at each end of an erbium-doped fibre. They are susceptible to mode-hopping and typically will have effective sensor lengths of several centimetres, which may be too

---

[1] This chapter contains a re-edited version of the submitted manuscript [D. Thingbø, E. Rønnekleiv and J. T. Kringlebotn "Intrinsic Distributed Feedback Fibre Laser High Frequency Hydrophone", submitted to the Topical Meeting on Bragg Gratings, Photosensitivity, and Poling in Glass Waveguides, to be held in Florida, USA, 1999]

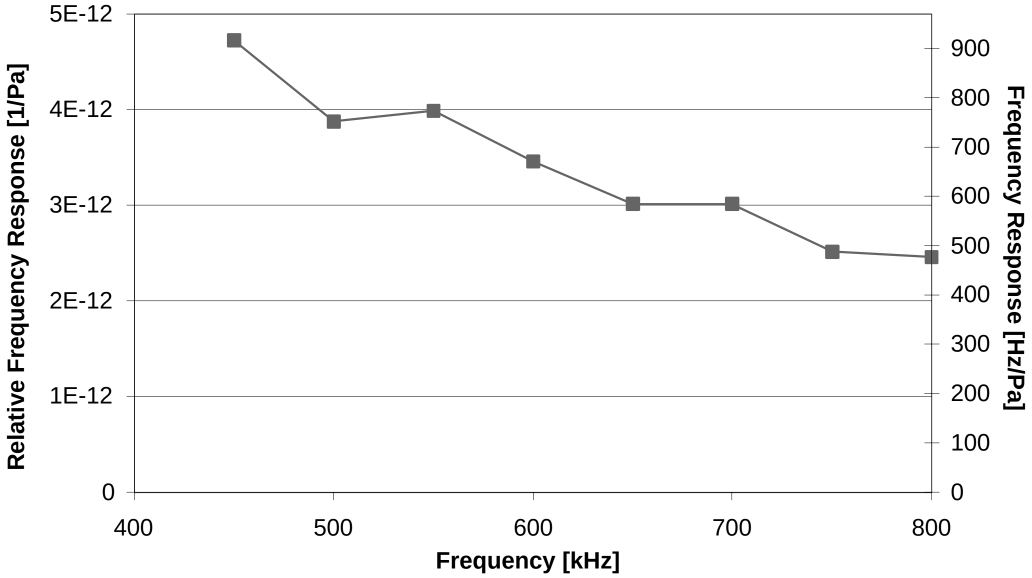

Figure 9.1. Relative and absolute frequency responsivity of the DFB fibre laser sensor.

long for high frequency acoustic sensing. DFB fibre lasers, [2] consisting of a single phase-shifted FBG written into a rare-earth doped fibre, should be very attractive for acoustic sensing owing to i) their robust single mode operation, ii) an extremely narrow linewidth (1-10kHz), providing low noise, and iii) a very short sensitive length [3].

We here demonstrate a DFB fibre laser used as a hydrophone for acoustic measurements in the frequency range of 0.1 to 1 MHz. The frequency response, directivity, and noise spectrum are measured.

9.2 Experimental results

A 5 cm-long erbium-doped, acrylate coated DFB fibre laser with 80 mm diameter and an optical linewidth of $\sim$ 10 kHz (produced by Ionas, Denmark) was placed in a large water tank with 1.1 m diameter, $\sim$ 65 cm from the acoustic source, made from a broad-band (0.1 - 2.2 MHz) 15 mm diameter PVDF-disk. The acoustic source emitted bursts of 30-40 sine-periods to allow gated detection without interference with reflections from the walls of the tank. The acoustic field was directed normally to the fibre laser axis. The source was calibrated up to 800 kHz, using a calibrated probe hydrophone. The fibre laser was remotely pumped by a 1480-nm diode laser through a WDM and the back-propagating fibre laser light was directed through the WDM and into an unbalanced (ΔL = 18 m) Mach-Zender interferometer with manual polarisa-

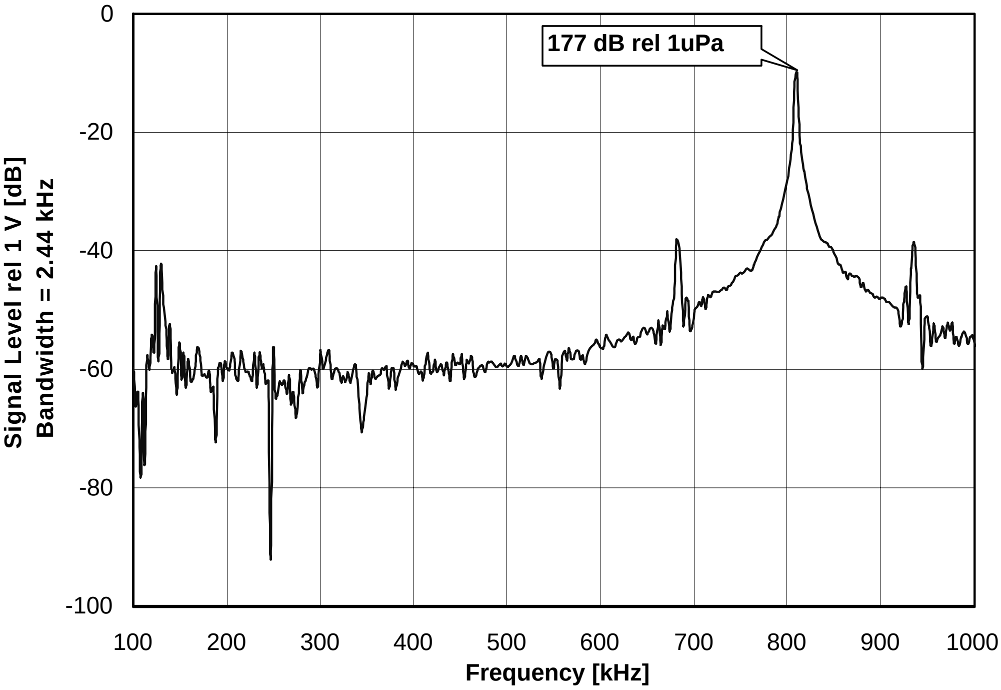

Figure 9.2. Output power spectrum of the sensor with an applied signal at 800kHz.

tion control and DC quadrature control by feedback to a piezo-electric fibre stretcher.

Fig. 9.1 shows the measured relative frequency response, $\Delta\nu/(\nu\delta P)$ and absolute frequency response $\Delta\nu/\Delta P$ of the DFB fibre laser acoustic sensor used as a hydrophone between 400 and 800 kHz, where ν is the laser frequency. The measurement is in good agreement with the expected relative frequency response of $\sim 4.5 \times 10^{-12}$ Pa^{-1} for a high frequency (axial constrained) optical fibre hydrophone [4]. The $\sim$ 6 dB/octave roll-off in the frequency response can be due to a slight misalignment of acoustic wave-front relative to the fibre axis, as the width of the angular responsivity (see Fig. 9.4) is highly frequency dependent.

The output power spectrum of the sensor with an applied signal of 177 dB rel. 1 mPa at 800 kHz is shown in Fig. 9.2. From this we have derived a noise equivalent acoustic pressure of $\sim$ 93 dB rel. 1 μPa/$\sqrt{\text{Hz}}$ (50 mPa/$\sqrt{\text{Hz}}$) at 800 kHz. This noise floor is determined by receiver noise, and can be reduced by 10-20 dB by optimising the electronic receiver and the receiver interferometer. The noise will then be determined by the fundamental thermal frequency noise of the fibre laser [1]. As seen in Fig. 9.2 the noise spectrum has a peak around 130 kHz (with a bandwidth of $\sim$ 10 kHz), due to the laser relaxation oscillations, which is also causing side-band peaks around the signal at 800 ± 130 kHz.

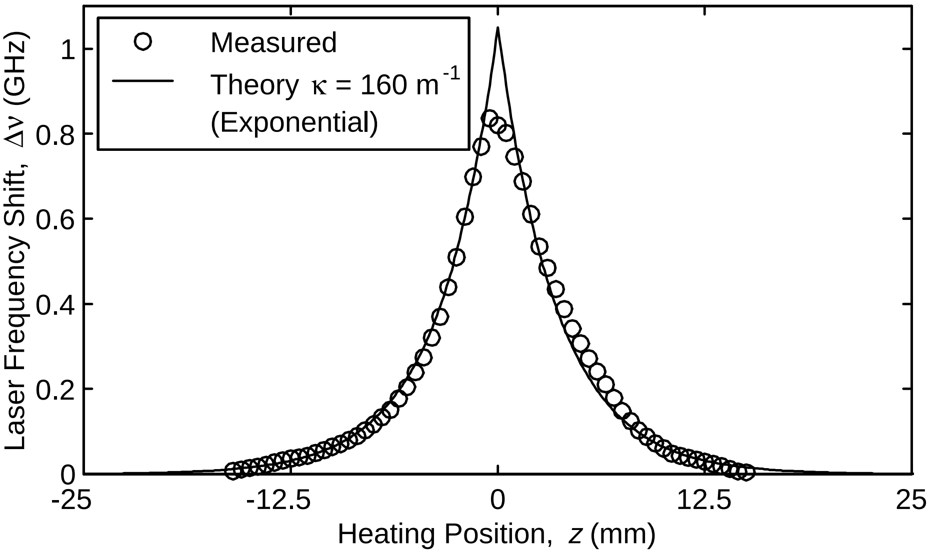

Figure 9.3. Spatial sensitivity dustribution of the fiber DFB laser measured with a heat perturbation technique.

The acoustic sensor is omnidirectional in the plane normal to the fibre axis owing to the symmetrical (cylindrical) shape of the fibre. When the acoustic wave is incident at an angle Φ relative to the fibre axis (as shown in the inset of Fig. 9.4) the response has an angular dependence, determined by the effective sensitive length (aperture) of the sensor.

Fig. 9.3 shows the spatial sensitivity distribution of the laser, measured by sacnning a heat source with an extension of about 1.5 mm over the laser fiber and measuring the resulting laser frequency shift. A good fit to the exponential distribution $\delta\nu \propto \exp(-2\kappa|z|)$ expected theoretically for an ideal discrete π phaseshifted DFB laser with grating strength $\kappa = 160$ m^{-1} is observed, except for is a rtelatively flat region close to $z = 0$. This flat region is attributed to the distributed nature of the grating phase-shift. The aperture, defined as the distance between the points where the sensitivity has dropped to 1/2 of its peak value, is 6.7 mm.

Fig. 9.4 shows the measured angular responsivity of the DFB fibre laser sensor at 800 kHz, which has a narrow central lobe with a 3-dB width of 6.4°. This width will decrease with increasing acoustic wavelength, which at 800 kHz is close to 2 mm. The angular responsitivity expected from the spatial characterization measeurements, calculated by taking a Fourier transform of the measurements in Fig. 9.3, is also shown i n the figure, along with a Lorenzian curve corresponding to the ideal theoretical curve in Fig. 9.3. The central lobe of the angular measurements is similar to the calculated curves.

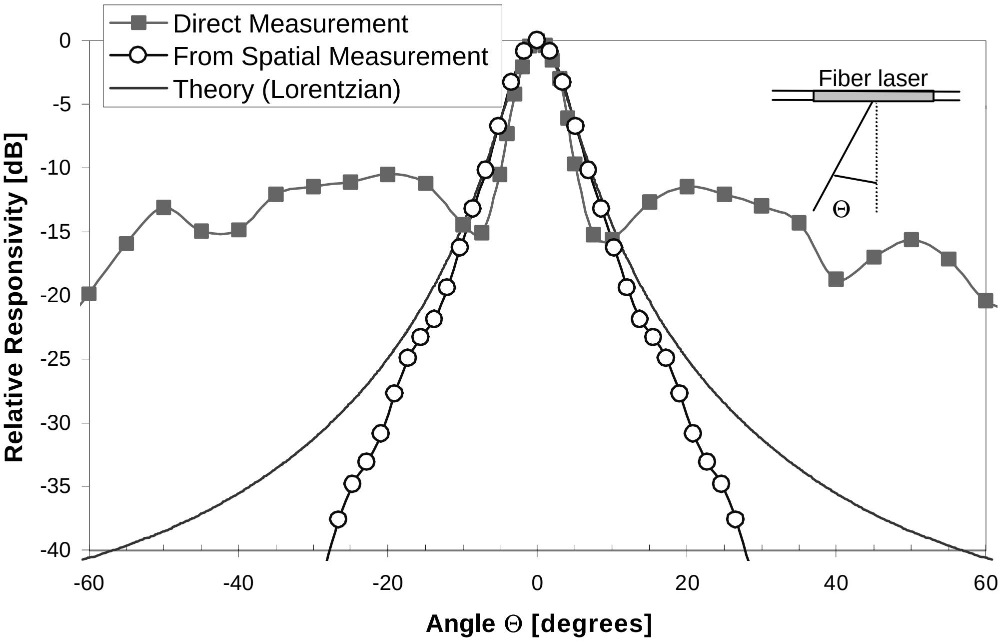

Figure 9.4. Measured and calculated angular responsivity at 800kHz. The calculations are based on the measured spatial sensitivity distribution along the fibre laser.

The side-bands in the direct angular measurements may be due to unresolved grating imperfections with high spatial frequencies (which would not be resolved by the spatial measurements), coating effects or air bubbles on the fibre.

9.3 Summary

We demonstrate for the first time a DFB fibre laser used as a hydrophone. The pressure sensitivity of the laser frequency ranges from 1 to 0.5 kHz/Pa between 400 and 800 kHz. The noise equivalent pressure was $\sim$ 93 dB rel. 1 μPa/$\sqrt{\text{Hz}}$. The angular responsivity at 800 kHz had a central lobe with a 3-dB width of 6.4°, corresponding to an effective sensitive length of approximately 6mm, which is much shorter than the laser cavity length of 5 cm.

References

[1] Koo, K.P., and Kersey, A.D., "Bragg grating-based laser sensors systems with interferometric interrogation and wavelength division multiplexing," J. Lightwave Technol., Vol. 13, pp. 1243-1249, 1995.

[2] Kringlebotn, J.T., Archambault, J.-L., Reekie, L., and Payne, D., "Er^{3+}:Yb^{3+}-codoped fiber distributed-feedback laser," Opt. Lett., Vol. 19, pp. 2101-2103, 1994.

[3] Rønnekleiv, E., Ibsen, M., Zervas, M.N., and Laming, R.I., "Characterisation of fiber DFB lasers via an index perturbation method," to be published in Appl. Opt., Vol.38, No. 21, (20. July) 1999.

[4] Culshaw, B., Davies, D.E.N., and Kingsley, S.A., "Acoustic sensitivity of optical fibre waveguides," Electron. Lett., Vol. 13, pp. 760-761, 1977.

Chapter 10

Conclusion

This chapter summarizes the most important implications of the results reported with respect to the use of Er-doped fiber DFB lasers as sensing elements or interrogation sources.

An index perturbation method for characterization of fiber DFB lasers has been demonstrated. Besides being useful for investigation of laser characteristics, such as the order of longitudinal mode operation, modal intensity distributions, grating strength, and the polarization dependence of the grating strength, the method and the associated theory reveals that the effective sensitive length of a fiber DFB laser sensor is typically only 1/5 to 1/12 of the total grating length, depending on the grating strength and the distribution of the grating phase-shift region. This allows for sensor element designs with small dimensions. The measured sensitive lengths vary between 4 and 7 mm for a grating length of 50 mm.

An important motivation for using fiber DFB lasers as sensor elements is the high resolutions obtainable in measurements of quantities that modulate the fiber strain, refractive index, or birefringence. The laser frequency and polarization beat frequency noise levels demonstrated in this thesis correspond to resolutions that are 3 to 4 orders of magnitude better than what has been achieved in the laboratory with passive sensors with comparable sensitive lengths, such as fiber Bragg gratings [1, 2]. The laser frequency and beat frequency noise measurements are summarized in Table 11.1, along with the obtained sensitivities to different measurands.

To exploit the high resolutions in practical sensor implementations it is necessary to minimize the sensitivity to disturbances that one do not want to mea-

		Laser frequency	Beat frequency
Noise floor:	@ 2 Hz	$400\ \mathrm{Hz}/\sqrt{\mathrm{Hz}}$	—
	@ 20 Hz	$140\ \mathrm{Hz}/\sqrt{\mathrm{Hz}}$	$100\ \mathrm{Hz}/\sqrt{\mathrm{Hz}}$
	@ 200 Hz	$50\ \mathrm{Hz}/\sqrt{\mathrm{Hz}}$	$30\ \mathrm{Hz}/\sqrt{\mathrm{Hz}}$
	@ 2 kHz	$20\ \mathrm{Hz}/\sqrt{\mathrm{Hz}}$	—
	@ 20 kHz	$15\ \mathrm{Hz}/\sqrt{\mathrm{Hz}}$	$3\ \mathrm{Hz}/\sqrt{\mathrm{Hz}}$
	@ 500 kHz	$1.6\ \mathrm{Hz}/\sqrt{\mathrm{Hz}}$	—
Sensitivity:	temperature	-1 MHz/mK	1.6 kHz/mK
	strain	-150 MHz/$\mu\varepsilon$	8 kHz/$\mu\varepsilon$
	hydrostatic pressure	900 Hz/Pa	(low)
	birefringence ($\Delta n/n$)	—	200 Hz/10^{-12}
	lateral force	(-1.3 ± 0.8 Hz/nN)	1.6 Hz/nN

Table 11.1. Measured fiber DFB laser frequency and polarization beat frequency noise densities, as well as sensitivities to different measurands. The polarization beat frequency of the investigated lasers were about 1 GHz.

sure, such as (depending on the application) temperature changes, vibrations, and effects of strain and bending in flexible probes. Simultaneous interrogation of the optical frequency and the polarization beat frequency from a dual polarization laser seems to be a powerful technique for reducing this problem. Careful design of the sensor housing and fiber coatings are also believed to be important in order to minimize the sensitivity to unwanted disturbances.

Instabilities due to external back reflections from discrete reflectors Rayleigh scattering in the lead fiber seems to be a potential problem for the application of fiber DFB lasers as remote sensor elements positioned far ($\gtrsim 100$ m) from the pumping and interrogation unit. In many cases, this problem can be overcome by inserting optical isolators or non-reflective wavelength selective attenuators in the lead fiber near the sensor laser. A more preferable solution would be to develope fiber DFB lasers that are more tolerable to external reflections. Important parameters in this respect are the grating reflectivity, the linewidth enhancement factor, and saturable absorber defects in the gain-medium.

The observation that single polarization fiber DFB lasers can be multiplexed along a single fiber without significant degradation of the noise performance is promising for the possibility of performing multiple point distributed sensing with fiber DFB lasers. Simulation results have also shown that the polarization mode competition at steady state is not affected significantly by serial multiplexing. It should be noted, however, that the dynamic behavior of dual polarization lasers in serially multiplexed systems still needs to be investigated.

We have focused mainly on 1480-nm pumped fiber DFB lasers with moderate output powers in the $< 500\ \mu$W range. The low laser efficiency is due to low pump absorption in the short Er-doped fiber. Considerably higher output powers can be obtained by pumping Er-Yb co-doped lasers at 980 nm, because of a much higher pump absorption. However, the high pump absorption per laser in this case does not allow for serial multiplexing of lasers. Moreover, the increased self heating associated with high power laser operation can disturb the sensor performance [3]. The output power obtained with 1480-nm pumping should be more than sufficient for accurate sensor interrogation. Sources with higher output powers can be made by using the residual pump power to pump an erbium doped fiber amplifier in an master oscillator power amplifier (MOPA) configuration.

A large portion of this work has been devoted to a theoretical and experimental investigation of polarization mode competition in fiber DFB lasers. A simple method for obtaining robust single polarization operation seems to be manipulation of the polarization dependence of the grating coupling coefficient κ, thus introducing polarization dependent losses in the laser cavity. This can be obtained by controlling the polarization of the UV light used for the grating inscription [4]. If UV post-processing is used to make the grating phase-shift, an alternative approach is to introduce a polarization dependence in the grating phase-shift [5, 6], which also leads to polarization dependent cavity losses. Pump polarization fluctuations, external back-reflections, and grating birefringence non-uniformities will also affect the laser polarization mode competition.

Sufficient control with the above mentioned parameters is also necessary to obtain robust dual polarization lasers. The results presented in Chap. 7, and also experience from other dual polarization experiments, makes us confident that this is possible. In cases where mechanically induced changes in the birefringence are to be measured, it is however important to design the force transducer mechanism carefully so that a sufficient uniform birefringence distribution is maintained along the laser length.

The low level of frequency noise and potential strain and temperature tuning capabilities of fiber DFB lasers makes them promising as sources for passive fiber Bragg grating sensor interrogation, interferometric sensor interrogation, high resolution spectroscopy, and for optical device characterization purposes. Compared to other sources with comparable frequency noise characteristics, the fiber DFB lasers have the advantages of a compact in-fiber design, easy and accurate wavelength selection during production, a large tuning range without mode-hopping, and the possibility of creating multiple wavelength sources that are pumped from a single diode pump laser, either through serial laser multiplexing, or by Moiré grating techniques [7].

The easiest method to obtain strain-tuning is by applying a tensile strain. The mechanical strength of the fiber limits the possible tuning range to ~ 10 nm in this case, corresponding to a strain of ~ 8 mε. Compression tuning allows for a larger tuning range, and mode-hop free compression tuning of a fiber DBR laser over 32 nm has already been demonstrated in the lab [8]. Major challenges in the development of a commercial compression tuned device are expected to be to ensure a sufficient uniform strain distribution to avoid longitudinal mode hopping, and at the same time avoid mechanical degradation of the fiber (due to friction or buckling). Because of the short effective cavity length, fiber DFB lasers are generally expected to be more tolerant to non-uniform strain and less prone to mode-hopping than DBR lasers.

References

[1] A. Arie, B. Lissak, and M Tur, "Static Fiber-Bragg Grating Strain Sensing Using Frequency-Locked Lasers", J. of Lightwave Technol., Vol. 17, pp. 1849–1855, 1999.

[2] B. Lissak, A. Arie, and M Tur, "Highly sensitive dynamic strain measurements by locking lasers to fiber Bragg gratings", Opt. Lett., Vol. 23, pp. 1930–1932, 1998.

[3] O. Hadeler, M. N. Zervas, E. Rønnekleiv, and M. Berendt, "Temperature distribution along DFB fibre lasers", *IEE colloquium digest on Optical Fibre Gratings*, (IEE, Box 96, M. Faraday House, Stevenage, Herts. SG1 2SD, UK), 1999.

[4] M. Ibsen, E. Rønnekleiv, G. J. Cowle, M. O. Berendt, O. Hadeler, M. N. Zervas, and R. I. Laming, "Robust high-power (>20 mW) all-fiber DFB lasers with unidirectional and truly single polarization outputs" in *Proc. to Conference on Lasers and Electro-Optics (CLEO) 1999*, pp. 245–246, paper CWE4, Baltimore, USA, 1999.

[5] H. Storøy, B. Sahlgren and R. Stubbe, "Single polarization fibre DFB laser", El. Letters, Vol. 33, pp. 56–8, 1997.

[6] J. I. Philipsen, M. O. Berendt, P. Varming, V. C. Lauridsen, J. H. Povlsen, J. Hübner, M. Kristensen, B. Pálsdóttir, "Polarisation control of DFB fibre laser using UV-induced birefringent phase-shift", El. Letters, Vol. 34, pp. 678-9, 1998.

[7] M. Ibsen, E. Rønnekleiv, O. Hadeler, G. J. Cowle, M. N. Zervas, and R. I. Laming, "Stable multiple wavelength generation in all-fibre DFB laser" in *Topical Meeting on Bragg Gratings, Photosensitivity, and Poling in Glass Waveguides*, paper FA4, Florida, USA, 1999.

[8] G. A. Ball and W. W. Morey, "Compression-tuned single-frequency Bragg grating fiber laser", Opt. Lett., Vol. 19, pp. 1979–1981, 1994.

Publication List

Journal Publications

1. E. Rønnekleiv, "Sagnac sensor for location of a disturbance", Appl. Opt., Vol. 36, pp. 2076–2083, 1997 .
2. E. Rønnekleiv, M. N. Zervas and J. T. Kringlebotn, "Modeling of Polarization Mode Competition in Fiber DFB Lasers", IEEE J. Quantum Electron., Vol. 34, pp. 1559–69, 1998.
3. E. Rønnekleiv, M. N. Zervas and J. T. Kringlebotn, "Correction to "Modeling of Polarization Mode Competition in Fiber DFB Lasers"", IEEE J. Quantum Electron., Vol. 35, pp. 1097–1100, 1999.
4. O. Hadeler, E. Rønnekleiv, M. Ibsen and R. I. Laming, "Polarimetric fiber distributed feedback laser sensor for simultaneous strain and temperature measurements", Appl. Opt., Vol. 38, pp. 1953–1958, 1999.
5. E. Rønnekleiv and O. Hadeler, "Stability of an Er-Yb-doped fiber distributed-feedback laser with external reflections", Opt. Lett., Vol. 24, pp. 617–619, 1999.
6. E. Rønnekleiv, M. Ibsen, M. N. Zervas, and R. I. Laming, "Characterization of fiber distributed-feedback lasers with an index perturbation method", Appl. Opt., Vol. 38, pp. 4558–4565, 1999.
7. S. W. Løvseth, J. T. Kringlebotn, E. Rønnekleiv and K. Bløtekjær, "Fiber DFB Lasers Used as Acoustic Sensors in Air", Appl. Opt., Vol. 38, pp. 4821–4830, 1999.
8. E. Rønnekleiv, M. Ibsen, and G. J. Cowle, "Polarization Characteristics of Fiber DFB Lasers Related to Sensing Applications", accepted (Dac. 1999) for publication in IEEE J. Quantum Electron.

Conference Proceedings

1. E. Rønnekleiv, K. Bløtekjær, and K. Kråkenes, "Distributed fiber sensor for location of disturbances," in *9th International Conference on Optical Fiber Sensors* (National Research Council of Italy, Florence, 1993), postdeadline paper PD7.

2. E. Rønnekleiv, M. Ibsen, M. N. Zervas and R. I. Laming, "Characterization of intensity distribution in symmetric and asymmetric fiber DFB lasers", in *CLEO'98, Tec. Digest,* Vol. 6, CTuE6, San Francisco 1998.

3. O. Hadeler, M. N. Zervas, E. Rønnekleiv, and M. Berendt, "Temperature distribution along DFB fibre lasers", *IEE colloquium digest on Optical Fibre Gratings*, (IEE, Box 96, M. Faraday House, Stevenage, Herts. SG1 2SD, UK), 1999.

4. E. Rønnekleiv and S. W. Løvseth, "Stability of Distributed Feedback Fiber Lasers with Optical Feedback", in *13th International Conference on Optical Fiber Sensors*, Proceedings of SPIE Vol. 3746, pp. 466–469, 1999.

5. D. Thingbø, E. Rønnekleiv and J. T. Kringlebotn, "Intrinsic Distributed Feedback Fibre Laser High Frequency Hydrophone", in *Topical Meeting on Bragg Gratings, Photosensitivity, and Poling in Glass Waveguides*, paper ThE4, pp. 57–59, Florida, USA, 1999.

6. M. Ibsen, E. Rønnekleiv, G. J. Cowle, M. O. Berendt, O. Hadeler, M. N. Zervas, and R. I. Laming, "Robust high-power (>20 mW) all-fiber DFB lasers with unidirectional and truly single polarization outputs" in *Proc. to Conference on Lasers and Electro-Optics (CLEO) 1999*, paper CWE4, pp. 245–246, Baltimore, USA, 1999.

7. M. Ibsen, E. Rønnekleiv, O. Hadeler, G. J. Cowle, M. N. Zervas, and R. I. Laming, "Stable multiple wavelength generation in all-fibre DFB laser" in *Topical Meeting on Bragg Gratings, Photosensitivity, and Poling in Glass Waveguides*, paper FA4, pp. 149–151, Florida, USA, 1999.

Presentations

1. E. Rønnekleiv and K. Bløtekjær, "Sagnac sensor system for location of disturbance", in *Norwegian Electro-Optics Meeting*, Fefor, Norway, 1993.

2. E. Rønnekleiv, "Modeling polarization mode competition in fiber DFB-lasers", in *Norwegian Electro-Optics Meeting*, Geiranger, Norway, 1997.

3. E. Rønnekleiv, D. Thingbø and J. T. Kringlebotn, "Frequency and Intensity Noise of Er-doped Fiber DFB Lasers", in *Norwegian Electro-Optics Meeting*, Balestrand, Norway, 1999.

4. S. W. Løvseth and E. Rønnekleiv, "Stability of Distributed Feedback Fiber Lasers with Optical Feedback", in *Norwegian Electro-Optics Meeting*, Balestrand, Norway, 1999.